

A STUDY ON MULTI DOPING EFFECT ON CERIA BASED MATERIALS FOR SOOT OXIDATION ACTIVITY

Thesis

Submitted in partial fulfillment of the requirements for the
degree of

DOCTOR OF PHILOSOPHY

By

ANJANA P A



DEPARTMENT OF CHEMICAL ENGINEERING
NATIONAL INSTITUTE OF TECHNOLOGY KARNATAKA
SURATHKAL, MANGALURU-575025

January – 2019

D E C L A R A T I O N

By the Ph.D. Research Scholar

I hereby *declare* that the Research Thesis entitled **A Study on Multi Doping Effect on Ceria Based Materials for Soot Oxidation Activity** which is being submitted to the **National Institute of Technology Karnataka, Surathkal** in partial fulfilment of the requirements for the award of the Degree of **Doctor of Philosophy in Chemical Engineering Department** is a *bonafide report of the research work* carried out by me. The material contained in this Research Thesis has not been submitted to any University or Institution for the award of any degree.

158022 CH15F12, ANJANA P A

Department of Chemical Engineering

National Institute of Technology Karnataka, India

Place: NITK-Surathkal

Date:

C E R T I F I C A T E

This is to *certify* that the Research Thesis entitled **A Study on Multi Doping Effect on Ceria Based Materials for Soot Oxidation Activity** submitted by **ANJANA P A** (Register Number: 158022 CH15F12) as the record of the research work carried out by her, is *accepted as the Research Thesis submission* in partial fulfilment of the requirements for the award of degree of **Doctor of Philosophy**.

Dr. Hari Prasad Dasari
Assistant Professor
Research Guide

Chairman - DRPC

Department of Chemical Engineering
National Institute of Technology Karnataka, India

ACKNOWLEDGEMENTS

First and foremost, I thank Almighty for all the blessings in my life including an opportunity to complete my PhD and during all the endeavours of my life. Special mention goes to the enthusiastic supervisor, **Dr. Hari Prasad Dasari**. My PhD has been an amazing experience because of his motivation and I thank him wholeheartedly, for his tremendous academic support and for giving me various opportunities and encouragement from the very beginning of my research work.

I thank the present Director of the NITK, **Prof. Karanam Uma Maheshwar Rao** for granting me the permission to use the institutional infrastructures. I thank **Prof. B. Raj Mohan** the former Head of the Department and **Dr. Hari Mahalingam**, the present Head of the Department, Chemical Engineering Department, NITK, for granting me the permission to use the departmental facilities throughout my research work.

I am grateful to my Research Progress Assessment Committee members, **Prof. M. B. Saidutta** and **Dr. Saumen Mandal**, for their critical evaluation and valuable suggestions during the progress of the work. I owe special thanks to **Dr. D. V. R. Murthy** for providing the encouragement from the day of my joining as research scholar in the department.

I extend my gratitude to **Prof. Jong Ho Lee** for funding the project under **KIST-IRDA** “Development of Quaternary Ceria-Based Catalysts for soot oxidation Activity” 2017-18. Also I thank **DST Inspire** “Future Materials for Solid-Oxide Fuel/Electrolysis Cells” and **DST SERB ECR** “Development of Novel SOFC Electrolyte Materials with enhanced Ionic Conductivity” for other funding. Without back support from the funding it would be impossible for me to do my research on time with quality.

My sincere thanks to **Dr. Harshini Dasari** for helping me in getting the data related to BET Surface area and pore volume and **Dr. Udhay Bhaskar Babu** for XRD data.

Also, I acknowledge **Materials Research Centre (MRC), MNIT, Jaipur** for Raman spectroscopy and X-ray Photoemission spectroscopy (XPS) analysis in their facilitation centre and provide the data. **SAIF, CUSAT, Kochi** has provided me the data related to UV-Vis DRS and TEM analysis, I thank them for their cooperation on time. I sincerely acknowledge **Mangalore university** for providing the SEM-EDS data of the samples.

Without a good peer group support, my journey would have never been this easier. I sincerely express my thanks for the timely help and support rendered by **Mrs. Irfana Shahjahn, Mrs. Sunaina Patil, Mrs. Gouri Pattanashetti, Mrs. Geethu. J, Mr. Rahul. M. R** and **Mr. Akhil Vijay**, and other B-Tech students who were part of the research group. I sincerely acknowledge all the teaching staffs including **Prof. G. Srinikethan, Prof. Vidya Shetty K** and **Dr. Keyur Raval** and non-teaching staffs including **Mr. Sadashiva, Mrs. Thrithila Shetty** and **Ms. Vijayatha** of the department for their encouraging support through my research. Also I thank all other faculties, staffs and research scholars of Department of Chemical Engineering, and other departments of NITK Surathkal.

I thank the authors of all those research publications which have been referred in preparing this thesis. I also express my gratitude to reviewers of journals for their excellent input.

I thank all my dear friends who were there to support me and help me whenever needed. I extend my gratitude to Dr. Hari Prasad Dasari's wife **Dr. Harshini Dasari** and daughter **Ms. Alankritha**. I extend my deepest and unconditional thanks to my mother **Mrs. P. N. Meenakshi**, my father **Mr. P. S. Anantharaman** and my sister **Mrs. Archana. A** and her family for their encouragement and moral support on the road to the completion of my research.

Anjana P A

Dedication

To my family for all their encouragement and inspiration and putting me through the best education as possible,

&

To all my former teachers through whom the Almighty led me to the world of knowledge and wisdom.

ABSTRACT

Ceria-based metal oxides are widely adopted as catalyst for various applications significantly due to its distinct features of cyclic redox properties, oxygen storage capacity, high metal solubility and thus, better solid solution formation. This work evaluates the impact of multi-dopants on ceria-based metal oxides for soot oxidation catalytic activity. An initial study on single metal oxides confirmed that the intrinsic nature of metal cation dictates the catalytic activity. Such that reducibility property controls the activity for redox metal oxides (CeO_2 , SnO_2 , Pr_6O_{11} , Mn_3O_4) and structural properties control for non-redox metal oxides (Gd_2O_3 , La_2O_3 , ZrO_2 , HfO_2 and Sm_2O_3).

Study on binary ceria-based metal oxide (CeO_2 - HfO_2) confirms that the structural parameter (morphology and phase stability) controls the activity over whole composition range. With increase in dopant, phase separation occurs from fluorite phase, which in turn results in a morphological modification that reduces the catalytic activity. Ternary dopant (Mn) addition to the binary metal oxide (CeO_2 - HfO_2 highest activity among binary metal oxide) at optimum composition enhances catalytic activity due to simultaneous reduction of Ce^{3+} and Mn^{4+} and improved oxygen vacancy. On further addition of dopant (Li, Ag, Ba and K) to CeO_2 - HfO_2 - Mn_2O_3 results in quaternary metal oxide that shows lowering of band gap, reactive planes and oxygen active sites that reduces active site and results in catalytic deactivation.

Ternary doped sample along with binary metal oxides show the maximum activity due to its lower optical band gap, higher F_{2g} content, higher reactive facet planes and higher reducibility ratio. Thus, it is not a single parameter that dictates the catalytic activity of ceria-based metal oxides. Intrinsic descriptors that control the activity are dopant nature, concentration and interference, apart from the extrinsic descriptor, that significantly modifies surface oxygen concentration. The thesis focuses the descriptors that actually controls the catalytic activity for multi doped ceria based metal oxides.

Keywords: Ceria; Multi Doped Metal Oxide; Soot Oxidation; Characterization; Descriptors

TABLE OF CONTENTS

DESCRIPTION		Page No.
ABSTRACT		i
TABLE OF CONTENTS		iii
LIST OF FIGURES		viii
LIST OF TABLES		xiii
ABBREVIATIONS		xv
UNITS AND NOTATIONS		xviii
1	INTRODUCTION	1
	1.1 Background	1
	1.2 Soot	1
	1.2.1. Environmental and health effects of Soot	3
	1.2.2 Soot emission Control (Diesel Particulate Filter)	3
	1.3 Ceria (CeO ₂)	4
	1.4 Scope and Objective	7
	1.5 Organization of Thesis	8
2	LITERATURE REVIEW	9
	2.1 Effect of Synthesis Method	9
	2.2 Single Metal Oxide Catalysts	12
	2.3 Ceria-Based Binary Metal Oxides	16
	2.3.1. Binary System Phase Diagram	22
	2.4 Ceria-Based Ternary Metal Oxides	24
	2.5 Ceria-Based Quaternary Metal Oxide Dopants	28
	2.6 Reaction Mechanism of Soot Oxidation Activity	32
	2.7 Conclusion	35

3	MATERIALS AND METHODS		37
	3.1	Synthesis of Ceria-Based Catalyst	37
	3.2	Physical Characterization	40
		3.2.1. X-ray Diffraction (XRD)	40
		3.2.2. Brunauer-Emmett-Teller (BET) Surface area	41
		3.2.3. Raman spectroscopy	42
		3.2.4. Scanning Electron Microscopy (SEM)	43
		3.2.5. Transmission Electron Microscopy (TEM)	43
		3.2.6. UV-Vis Diffuse Reflectance Spectroscopy (UV-Vis DRS)	44
		3.2.7. X-ray Photoemission Spectroscopy (XPS)	44
		3.2.8. Thermo Gravimetric Analyser (TGA)	45
	3.3	Soot Oxidation	46
4	STUDY ON SINGLE METAL OXIDES		47
	4.1	Single Metal Oxides	49
		4.1.1. X-ray Diffraction (XRD) Analysis	49
		4.1.2. Scanning Electron Microscopy (SEM) Analysis	53
		4.1.3. Transmission Electron Microscopy (TEM) Analysis	55
		4.1.4. X-ray Photoemission Spectroscopy (XPS) Analysis	55
		4.1.4.1 Redox Metal Oxides	55
		4.1.4.2 Non-redox Metal Oxides	62
		4.1.5. Soot Oxidation Activity	65
		4.1.5.1 Redox Metal Oxides	65

		4.1.5.2 Non-Redox Metal Oxides	68
	4.2	Conclusion	71
5		STUDY ON BINARY METAL OXIDES	72
	5.1	Ce _{1-x} Hf _x O ₂ (x=0.0-1.0) Binary Metal Oxides	72
		5.1.1 X-ray Diffraction (XRD) Analysis	73
		5.1.2. Raman Spectroscopy Analysis	75
		5.1.3. Scanning Electron Microscopy (SEM) Analysis	78
		5.1.4. Transmission Electron Microscopy (TEM) Analysis	78
		5.1.5. UV-Vis Diffuse Reflectance Spectroscopy (UV-Vis DRS) Analysis	85
		5.1.6. X-ray Photoemission Spectroscopy (XPS) Analysis	86
		5.1.7. Soot Oxidation Activity	87
	5.2	Ce _{1-x} Sm _x O ₂ (x=0.0 - 1.0) Binary Metal Oxides	93
	5.3	Ce _{0.9} M _{0.1} O ₂ (M=Sn, Hf, Zr, Gd, Sm & La) Binary Solid Solution	97
		5.3.1. X-ray Diffraction (XRD) Analysis	97
		5.3.2. Raman Spectroscopy Analysis	102
		5.3.3. Scanning Electron Microscopy (SEM) Analysis	104
		5.3.4. Transmission Electron Microscopy (TEM) Analysis	104
		5.3.5. UV-Vis Diffuse Reflectance Spectroscopy (UV-Vis DRS) Analysis	109

		5.3.6. X-ray Photoemission Spectroscopy (XPS) Analysis	110
		5.3.7. Soot Oxidation Activity	113
	5.4	Conclusion	117
6	STUDY OF MULTI DOPED METAL OXIDES		119
	6.1	Ternary And Quaternary Mixed Oxides	120
		6.1.1. X-ray Diffraction (XRD) Analysis	120
		6.1.2. Raman Spectroscopy Analysis	124
		6.1.3. Scanning Electron Microscopy (SEM) Analysis	125
		6.1.4. Transmission Electron Microscopy (TEM) Analysis	129
		6.1.5. UV-Vis Diffuse Reflectance Spectroscopy (UV-Vis DRS) Analysis	132
		6.1.6. X-ray Photoemission Spectroscopy (XPS) Analysis	134
		6.1.7. Soot Oxidation Activity	137
	6.2	Descriptors For Multi Doped Ceria Based Metal Oxides	142
		6.2.1. Reactive Planes (XRD)	142
		6.2.2. Raman Spectroscopy Analysis	144
		6.2.3. Optical Bandgap	145
		6.2.4. Reducibility and oxygen vacancy (XPS)	147
	6.3.	Conclusion	150

7	SUMMARY AND CONCLUSIONS		152
	7.1	Summary	152
	7.2	Conclusions	155
	7.3	Scope of the Work	156
APPENDIX-I			157
REFERENCES			171
PUBLICATIONS			194
BIODATA			196

LIST OF FIGURES

Figure No.	Caption	Page No.
Figure 1.1	Face centered cubic fluorite structure of ceria	5
Figure 2.1	Soot conversion profile for binary oxides	17
Figure 2.2	Temperature-composition phase diagram of ceria-hafnia binary system	23
Figure 2.3	Phase separation of ceria-hafnia binary system using XRD analysis	23
Figure 3.1	EDTA-Citrate synthesis method procedure	39
Figure 4.1	XRD pattern of single metal oxides calcined at 600°C/5h	50
Figure 4.2	SEM micrographs of (a) CeO ₂ , (b) Pr ₆ O ₁₁ , (c) Mn ₃ O ₄ , (d) ZrO ₂ , (e) HfO ₂ and (f) Sm ₂ O ₃ samples calcined at 600°C/5h	54
Figure 4.3	(a) TEM, (b) HR-TEM image and (c) SAED pattern of CeO ₂	56
Figure 4.4	(a) TEM, (b) HR-TEM image and (c) SAED pattern of La ₂ O ₃	57
Figure 4.5	XPS of (a) Ce 3d, (b) Sn 3d, (c) Pr 3d and (d) Mn 2p of the corresponding redox metal oxides	59
Figure 4.6	O 1s XPS of CeO ₂ , SnO ₂ , Pr ₆ O ₁₁ and Mn ₃ O ₄ redox metal oxides	60
Figure 4.7	XPS of (a) Gd 4d, (b) La 3d, (c) Zr 3d, (d) Hf 4f and (e) Sm 3d of the corresponding non-redox metal oxides	63
Figure 4.8	O 1s XPS of Gd ₂ O ₃ , La ₂ O ₃ , ZrO ₂ , HfO ₂ and Sm ₂ O ₃ non-redox metal oxides	64

Figure 4.9	Soot oxidation of Redox metal oxides (CeO ₂ , SnO ₂ , Pr ₆ O ₁₁ and Mn ₃ O ₄)	66
Figure 4.10	Soot oxidation of Non-Redox metal oxides (Gd ₂ O ₃ , La ₂ O ₃ , ZrO ₂ , HfO ₂ and Sm ₂ O ₃)	67
Figure 5.1	(a) XRD spectra and (b) Vegard's law of CH _x binary ceria-based metal oxides	74
Figure 5.2	Raman spectra of (a) CH0-CH30 samples and (b) CH40-CH80 samples calcined at 600°C/5h.	76
Figure 5.3	SEM images of (a) CH0, (b) CH10, (c) CH20 and (d) CH30 of CH _x binary ceria-based metal oxides	79
Figure 5.3	SEM images of (e) CH40, (f) CHM50, (g) CH60 and (h) CH70 of CH _x binary ceria-based metal oxides	80
Figure 5.3	SEM images of (i) CH80, (j) CH90 and (k) CH100 of CH _x binary ceria-based metal oxides	81
Figure 5.4	HR-TEM image of (a) CH10; (b) CH40; (c) CH80 and (d) CH100 samples	83
Figure 5.5	SAED pattern of (a) CH10; (b) CH40; (c) CH80 and (d) CH100 samples	84
Figure 5.6	Tauc's plot of CH _x binary ceria-based metal oxides	85
Figure 5.7	O 1s XPS of (a) CH0-CH30 and (b) CH40- CH100 samples	87
Figure 5.8	Soot oxidation conversion of CH _x binary ceria- based metal oxides	88
Figure 5.9	Comparison of T ₅₀ with (a) Crystallite size for CH _x ceria-based binary metal oxides	89
Figure 5.9	Comparison of T ₅₀ with (b) bandgap and (c) lattice strain for CH _x ceria-based binary metal oxides	90

Figure 5.10	Variation in lattice constant with the increase in dopant concentration for CH _x , CS _x and CG _x binary ceria-based metal oxides	96
Figure 5.11	Variation of lattice constant with the increase in ionic radius for binary ceria-based metal oxides	98
Figure 5.12	Variation of lattice strain with the increase in ionic radius for binary ceria-based metal oxides	99
Figure 5.13	Variation of lattice planes with the increase in ionic radius for binary ceria-based metal oxides	101
Figure 5.14	Variation of BET Surface area with the increase in ionic radius for binary ceria-based metal oxides	102
Figure 5.15	Variation of I _{Ov} /I _{F2g} with the increase in ionic radius for binary ceria-based metal oxides	103
Figure 5.16	SEM images of (a) C, (b) CT, (c) CH, (d) CZ samples	105
Figure 5.16	SEM images of (e) CG and (f) CS (e) CL samples	106
Figure 5.17	(a) TEM, (b) HR-TEM and (c) SAED pattern of CZ samples	107
Figure 5.18	(a) TEM, (b) HR-TEM and (c) SAED pattern of CL samples	108
Figure 5.19	Variation of Optical band gap with the increase in ionic radius for binary ceria-based metal oxides	109
Figure 5.20	Variation of (Ce ³⁺ / (Ce ³⁺ + Ce ⁴⁺)) of binary ceria-based metal oxides	111
Figure 5.21	Variation of (O _β /O _α +O _β +O _γ) for binary ceria-based metal oxides	112
Figure 5.22	Soot oxidation activity of binary ceria-based metal oxides	114

Figure 5.23	Variation in lattice constant, optical bandgap and T_{50} temperature for binary ceria-based metal oxides	116
Figure 6.1	XRD spectra of (a) CHM_x ternary and (b) CHMY quaternary ceria-based metal oxides	121
Figure 6.2	Raman spectra of (a) CHM_x ternary and (b) CHMY quaternary ceria-based metal oxides	125
Figure 6.3	SEM images of (a) CHM0 (b) CHM3, (c) CHM5 and (d) CHM7 of ternary ceria-based metal oxides	127
Figure 6.4	SEM images of (a) CHML, (b) CHMA (c) CHMB and (d) CHMK of quaternary ceria-based metal oxides	128
Figure 6.5	TEM images of (a) CHM0, (b) CHM3, (c) CHML and (d) CHMA binary, ternary and quaternary ceria-based metal oxides	130
Figure 6.5	TEM images of (e) CHMB and (f) CHMK quaternary ceria-based metal oxides	131
Figure 6.6	Tauc's plot of (a) CHM_x ternary and (b) CHMY quaternary ceria-based metal oxides	133
Figure 6.7	Ce 3d XPS of (a) CHM_x ternary and (b) CHMY quaternary ceria-based metal oxides	135
Figure 6.8	O 1s XPS of (a) CHM_x ternary and (b) CHMY quaternary ceria-based metal oxides	136
Figure 6.9	Soot Oxidation (a) CHM_x ternary and (b) CHMY quaternary ceria-based metal oxides	139
Figure 6.10	Relation between facet planes with T_{50} temperature for multi doped ceria-based metal oxides	143
Figure 6.11	F_{2g} peak variation for multi doped ceria-based metal oxides	145

Figure 6.12	Relation between optical bandgap with T_{50} temperature for multi doped ceria-based metal oxides	146
Figure 6.13	Relation between Ce reducibility with T_{50} temperature for multi doped ceria-based metal oxides	148
Figure 6.14	Relation between surface oxygen vacancy with T_{50} temperature for multi doped ceria-based metal oxides	148

LIST OF TABLES

Table No.	Caption	Page No.
Table 1.1	Elemental composition analysis of soot	2
Table 2.1	Comparison of synthesis method and reaction parameters adopted for CeO ₂ soot oxidation	11
Table 2.2	Samples synthesized by EDTA-Citrate method	12
Table 2.3	Single metal oxides as soot oxidation catalysts	14
Table 2.4	Effect of binary dopants on ceria for soot oxidation	19
Table 2.5	Effect of ternary dopants on ceria for soot oxidation	25
Table 2.6	Effect of alkali, alkaline earth and noble metal dopants on ceria for soot oxidation	30
Table 4.1	Crystallite size, lattice strain, BET Surface area, pore volume, particle size and intensity ratios of GDC samples synthesized by different methods	48
Table 4.2	I_{ov}/I_{F2g} , composition, particle size, bandgap, reducibility ratio, $(O_{\beta}/(O_{\alpha} + O_{\beta} + O_{\gamma}))$, and T_{50} of GDC samples	48
Table 4.3	Crystallographic parameters, BET surface area, pore volume, particle size, lattice strain and degree of agglomeration of single metal oxides calcined at 600°C/5h	52
Table 4.4	Bandgap, binding energy, reducibility ratio, H ₂ -TPR (T_{α}/T_{β}), Δr and T_{50} of redox metal oxides	61
Table 4.5	Bandgap, binding energy, $(O_{\beta}/(O_{\alpha} + O_{\beta} + O_{\gamma}))$, BET Surface area, lattice strain, ionic radius and T_{50} of non-redox metal oxides	64

Table 5.1	Crystallite size, lattice strain, BET surface area, pore volume, particle size, degree of agglomeration, composition, intensity ratio, optical bandgap and T_{50} temperature of CH_x samples calcined at $600^\circ\text{C}/5\text{h}$	77
Table 5.2	Crystallite size, BET surface area, pore volume, particle size, lattice strain, degree of agglomeration, composition, intensity ratio, band gap energy and T_{50} temperature of CS_x samples calcined at $600^\circ\text{C}/5\text{h}$	94
Table 6.1	Crystallite size, BET surface area, particle size, pore volume, lattice strain, intensity ratio, degree of agglomeration, bandgap, $(\text{Ce}^{3+}/(\text{Ce}^{3+} + \text{Ce}^{4+}))$, $\text{O}_\beta/(\text{O}_\beta + \text{O}_\alpha + \text{O}_\gamma)$, $\text{Mn}^{4+}/(\text{Mn}^{2+} + \text{Mn}^{3+} + \text{Mn}^{4+})$ and T_{50} temperature of CHM_x ternary and $CHMX$ quaternary ceria based metal oxides calcined at $600^\circ\text{C}/5\text{h}$	126
Table 6.2	Crystallite size, BET surface area, particle size, pore volume, lattice strain, degree of agglomeration, intensity ratio, optical bandgap, $\text{Ce}^{3+}/(\text{Ce}^{3+} + \text{Ce}^{4+})$, $\text{O}_\beta/(\text{O}_\beta + \text{O}_\alpha + \text{O}_\gamma)$, $\text{Mn}^{4+}/(\text{Mn}^{2+} + \text{Mn}^{3+} + \text{Mn}^{4+})$ and T_{50} temperature of single, binary, ternary and quaternary ceria based metal oxides calcined at $600^\circ\text{C}/5\text{h}$	149

ABBREVIATIONS

Abbreviation	Description
<i>a</i>	Lattice constant
BET	Brunauer–Emmett–Teller
CH	Ceria-Hafnium (CeO ₂ -HfO ₂) Binary metal oxide
CHM	Ceria-Hafnium-Manganese (CeO ₂ -HfO ₂ -Mn ₂ O ₃) Ternary metal oxide
CHMA	Ceria-Hafnium-Manganese-Silver (CeO ₂ -HfO ₂ -Mn ₂ O ₃ -AgO ₂) Quaternary metal oxide
CHMB	Ceria-Hafnium-Manganese-Barium (CeO ₂ -HfO ₂ -Mn ₂ O ₃ -BaO ₂) Quaternary metal oxide
CHMK	Ceria-Hafnium-Manganese-Potassium (CeO ₂ -HfO ₂ -Mn ₂ O ₃ -K ₂ O) Quaternary metal oxide
CHML	Ceria-Hafnium-Manganese-Lithium (CeO ₂ -HfO ₂ -Mn ₂ O ₃ -LiO ₂) Quaternary metal oxide
CL	Ceria-Lanthanum (CeO ₂ -La ₂ O ₃) Binary metal oxide
CM	Ceria-Managenese (CeO ₂ -Mn ₂ O ₃) Binary metal oxide
CP	Ceria- Praseodymium (CeO ₂ -Pr ₆ O ₁₁) Binary metal oxide
CZ	Ceria-Zironium (CeO ₂ -ZrO ₂) Binary metal oxide
<i>d</i>	Interplanar distance
D	Crystallite size

(Cont.)

EDTA	Ethylenediaminetetraacetic acid
FCC	Face-Centred Cubic
GDC	Gadolinium Doped Ceria
GWP	Global-Warming-Potential
IEA	International Energy Agency
$I_{F_{2g}}$	Intensity of F_{2g} peak in Raman spectroscopy
I_{Ov}	Intensity of oxygen vacancy peak in Raman spectroscopy
MvK	Mars and Van Krevelen mechanism
NO _x	Nitrous Oxides
O_{ads}	Surface adsorbed oxygen vacancy
OSC	Oxygen Storage Capacity
O_{α}	Lattice oxygen
O_{β}	Surface oxygen
O_{γ}	Oxygen in carbonates and hydroxide
PAH	Poly Aromatic Hydrocarbons
PM	Particulate Matter
RM	Redox Metal oxide
SEM-EDS	Scanning Electron Microscopy-Energy Dispersive x-ray Spectroscopy

(Cont.)

SLCP	Short-Lived Climate Pollutant
SOF	Soluble Organic Fraction
SOFC	Solid Oxide Fuel Cell
SO _x	Sulfur Oxides
T ₅₀	Temperature at 50% conversion
TEM	Transmission Electron Microscopy
TGA	Thermogravimetric analysis
TPR	Temperature Programmed Reduction
T _α	Temperature for surface CeO ₂ reduction
T _β	Temperature for bulk CeO ₂ reduction
UV-Vis DRS	UV–Visible Diffuse Reflectance Spectroscopy
V _o	Oxygen vacancy
XPS	X-ray photoelectron spectroscopy
XRD	X-ray Diffraction
Δr	Change in metal ion radius at different oxidation state
ε	Lattice strain
φ	Degree of agglomeration

UNITS AND NOTATIONS

Symbol	Description
%	Percentage
°C	Degree celsius
$\mu\text{g}/\text{m}^3$	Microgram per meter cube
Å	Armstrong
a.u.	Arbitratry unit
cm^3/g	Cubic centimeter per gram
cps	Counts per second
eV	Electron volt
m^2/g	Square meter per gram
min	Minutes
Mtoe	Metric Tonnes of oil Equivalent
nm	Nanometer
W/m^2	Watt per meter square
θ	degree
λ	Wavelength
μm	Micrometer

CHAPTER 1

INTRODUCTION

1.1. BACKGROUND

Global energy demand met by fossil fuel leads to a 1.4 % increase in carbon emission as per the International Energy Agency (IEA) reports for the year 2017 (International Energy Agency 2018). Asia accounts for two-thirds of the total global carbon emission. From 2010 to 2016, particulate matter (PM) emission report from Delhi has shown the highest global PM₁₀ emission of around 300 µg/m³ (WHO 2018). Incomplete combustion of fuel during energy production is the crucial pollutant from human-made sources which include 85% of PM and almost all of the SO_x and NO_x (International Energy Agency 2016). The Energy and Resources Institute (TERI) projection report (Advancement of Fuel Quality and Vehicle Emissions Norms to Improve Urban Air Quality in India, 2014) that the registered vehicles in India increased exponentially from 5.3 million to 159 million from 1981 to 2012 and may reach 468 million by 2031. Energy consumption in road transport sector is expected to rise from 50 Mtoe in 2010 to almost seven times (350 Mtoe) by 2031(Sharma et al. 2014).

1.2. SOOT

Organic or inorganic mixture of solid and liquid substance is the components of Particulate Matter (PM). During the incomplete combustion of fuel or bioenergy, PM is formed which is of short-lived (International Energy Agency 2016). Diesel generators, burning of fuels, transportation sectors and other industries are the principal sources of soot emission. The vehicular combustion process results in pollutant emission which depends upon the type of fuel used, engine condition and after-treatment technology (CPCB 2011; Sethi and Patil 2008; Sharma et al. 2014).

The real diesel fuel combustion deviates from ideal conditions, due to unavailability of oxygen, results in the emission of carbon monoxide (CO), hydrogen (H₂), hydrocarbon (HC) and soot apart from carbon dioxide (CO₂) and water (H₂O). The formation of soot leads to depletion of combustion efficiency, the formation of polyaromatic hydrocarbons (PAH) which are hazardous to health, also increases the radiation effect in the engine. Soot formation follows a series of steps, namely pyrolysis, nucleation, surface growth and agglomeration.

During pyrolysis, fuel at high temperature with limited oxygen produces unsaturated hydrocarbons, polyacetylenes, polycyclic aromatic hydrocarbons (PAH's) and especially acetylene which are the precursor for soot formation. In the next step of nucleation, nuclei of 1.5~2.0 nm are formed by the addition of aliphatic components to aromatic molecules. The nuclei formed provide sites for surface growth by addition of hydrocarbons onto the hot reactive surface of soot. Particles combine by the process of coalescence and agglomeration. As the individual particles stick together, agglomerates of the particles are formed. The primary particle size ranges from 20~70 nm, and agglomerates are of 0.1 μm~2 μm or sometimes even larger (Agarwala, Avinash et al. 2011). During this process, soot essentially consists of carbon-based materials apart from trace amount of other metals and impurities. The average elemental composition of commercial Printex-U soot is shown in **Table 1.1** (Tighe et al. 2016).

**Table 1.1: Elemental composition analysis of soot
(Tighe et al. (2016))**

Element	Composition (wt %)
C	91.8
H	0.6
Ash	0.1
Deficit	7.5

1.2.1 Environmental and health effects of Soot

Soot strongly absorbs visible light; hence their direct radiative force is in the range of $0.08 \sim 1.27 \text{ W/m}^2$. The high radiative effect is mainly due to the absorption and scattering of sunlight that heats up the atmosphere and inhibits sunlight to reach earth surface. Consequently, this can affect the hydrological cycle, global warming of $0.1 \sim 2.0 \text{ }^\circ\text{C}$. In effect, soot diminishes visibility, change atmospheric heat balance, interferes photosynthesis by settling on plants and block and irritate the air passageways by penetrating in human lungs (Bond et al. 2013; Setten et al. 2001). WHO has named soot along with ground-level ozone and methane as the invisible killer.

1.2.2 Soot emission Control (Diesel Particulate Filter)

Soot emission from diesel exhaust can be controlled by after treatment techniques such as Diesel Particulate Filter (DPF) that mitigates emission using particle filtration system. Diesel exhaust temperature generally lies in the range of $200 \sim 300^\circ\text{C}$ for a light duty engine and $300 \sim 450^\circ\text{C}$ for a heavy duty engine. DPF exhaust enters a channel on the wall-flow monolithic filter which works on the principle of impaction, interaction or molecular diffusion. Exhaust gas is passed through the filters, and thus, soot gets deposited on the filter surface. Due to continuous operation soot accumulates on the filter that results in back pressure development in the cylinder that reduces engine efficiency. During this process sudden filter burn off at high temperature occurs, in turn, results in melting and damage of filter itself along with engine operational issues. Normal regeneration of soot occurs at a temperature range of 600°C which cannot typically be attained inside the engine. For controlled regeneration, either filter can be heated up to ignite particulates or lower regeneration temperature with the aid of catalyst (Fino et al. 2016).

Catalysts employed in the filter reduce regeneration temperature by oxidising hydrocarbons of Soluble Organic Fraction (SOF) in PM. The catalyst must have high thermal stability since at specific hotspots inside engine temperature can rise even up to

1000°C. A variety of catalyst has been developed since 1980s such as platinum-based catalysts (Pt/CeO₂) (Wei et al. 2013), perovskites (La_{0.9}K_{0.1}Cr_{0.9}O_{3-δ}+1 wt%Pt) (Cauda et al. 2004), spinel (AB₂O₄, where A = Co & Mn, and B = Cr & Fe) (Fino et al. 2008), hydrotalcite (Co_{2.5}Mg_{0.5}Al_{1-x%}Ce_{x%}O) (Dai et al. 2012), alkali or alkaline earth metal oxides (M-Ce-Zr; M=Cu, Fe, K, Ba, Sr) (Alinezhadchamazketi et al. 2013) and transition metal oxides (Ce-M; M=Zr, Fe) (Aneggi et al. 2006). Despite all these catalysts, ceria-based catalysts are widely adopted due to their high redox properties, less expensive than noble metals, easy doping with other metals with improved stability and activity (Fino et al. 2016).

In proportion to valence change, corresponding volume change in the lattice will result during the oxygen storage and release process. With the addition of smaller ionic radius Zr into ceria lattice, volume expansion will be compensated and that facilitates valence change process further (Sobukawa 2002). Zr⁴⁺ addition prevents CeO₂ grain growth at a higher temperature and improves thermal stability and improves surface oxygen (Liu et al. 2017; Sobukawa 2002).

1.3. CERIA (CeO₂)

Cerium (Ce) with the electronic configuration of Xe 4f¹5d¹6s² is widely available element among the rare earth metals. The redox (Ce⁴⁺ / Ce³⁺) behaviour is mainly due to similar energy between 4f and 5d electronic state and also due to lower potential energy barrier to electronic density distribution in these electronic states. Ceria (CeO₂) is the most stable oxide of Ce which crystallises in face-centered cubic (fcc) fluorite lattice structure with eight oxygen atoms bonded to each Ce atom, and oxygen atoms are four-fold coordinated as shown in **Figure 1.1**. Surface or subsurface oxygen vacancy is created in ceria during the redox process. When the material is exposed to the changing environment of fluctuating composition, alternatively between oxygen-rich and lean conditions, it can donate its oxygen under the lean condition and change its oxidation state to Ce³⁺ thus, becoming Ce₂O₃.

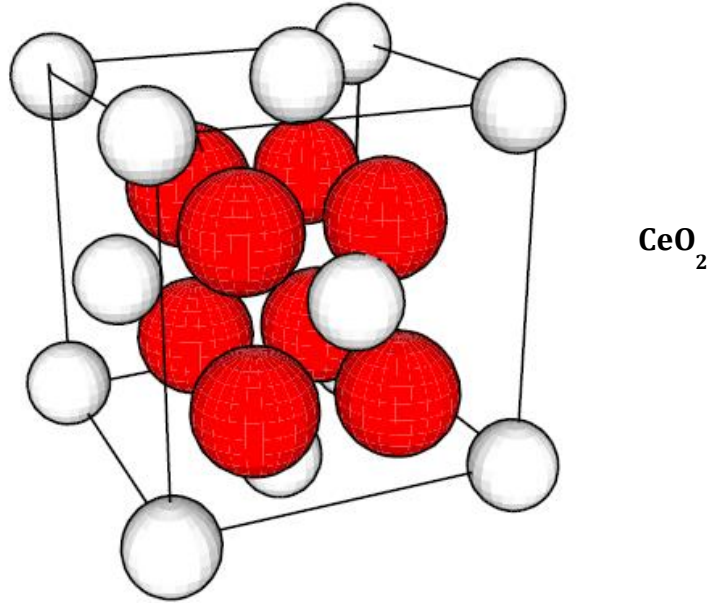


**Fig 1.1: Face-centered cubic fluorite structure of ceria
(Trovarelli et al. (1999))**

Further, it can receive oxygen under the oxidising condition and fill the vacancy created and get back to stable Ce^{4+} oxidation state and thus, becoming CeO_2 as shown in **Equation (1.1)**. Even after the oxygen removal and addition conditions, it remains in fluorite structure. Reduction of two Ce^{4+} atoms can create one oxygen vacancy. Oxygen Storage Capacity (OSC) is the total oxygen that can be stored inside the catalyst. OSC is of two types: Fast/Dynamic OSC, which relates the readily available oxygen and total OSC is the total amount of oxygen available from the catalyst. Oxygen buffering/storage property can directly affect catalytic activity especially for automobile exhaust reduction in which composition fluctuates (Boaro et al. 2000; Trovarelli et al. 1999).



Significant properties of CeO₂ that are key in a variety of applications are enhanced dispersion of support metals, enhanced precious metal interaction and promote noble metal redox behaviour, improve thermal stability, store and release oxygen and thus result in surface and bulk vacancies and readily form intermetallic compound (Trovarelli 1996). In specific, nanostructured ceria-based materials significantly improve properties like transport properties and surface to volume ratio concerning bulk volume, redox nature, defects due to the difference in oxygen partial pressure and oxygen vacancy (Reed et al. 2014; Sun et al. 2012). Critical applications of ceria as catalysts, catalyst support and SOFC materials are CO oxidation (Marbán et al. 2009), steam reforming of hydrocarbon (Patel and Pant 2007), solid oxide fuel cells (Prasad et al. 2008), sensors (Izu et al. 2007) and biomedical applications (Kumar et al. 2014).

Ceria activity is improved by doping with other metal oxides to increase OSC and oxygen mobility by creating structural deformations on ceria lattice (Reddy et al. 2008a), increase thermal stability due to presence of dopants in ceria lattice (Reddy et al. 2011) and improve surface reducibility (Vidal et al. 2000). In this context, the study focuses on developing potential catalysts for soot oxidation in specific ceria-based metal oxides with different dopants.

1.4. SCOPE AND OBJECTIVE

The scope of the work is to synthesise single metal oxides, binary, ternary and quaternary ceria-based metal oxides, characterize the metal oxides using suitable techniques and study its catalytic activity for soot oxidation. The reducibility and oxygen vacancy of all the metal oxide with composition variation and dopant addition are analysed to understand their catalytic activity using characterization tools. The variation in T_{50} with the dopant addition is analysed.

The specific objectives of the present study are:

1. To synthesis single metal oxides, binary, ternary and quaternary ceria-based (rare earth/transition) metal oxides.
2. To characterize synthesized metal oxides using various techniques such as XRD, Raman spectroscopy, BET Surface area, SEM, TEM, UV-Vis DRS and XPS.
3. To measure soot oxidation activity of all synthesized metal oxides.
4. To correlate reducibility properties with soot oxidation activity.
5. To analyse the effect of multi doping on T_{50} temperature for soot oxidation.

1.5. ORGANIZATION OF THE THESIS

The rest of this thesis is organised as follows:

Chapter 2 contains the literature review of reports on the effect of synthesis method, single metal oxides, binary ceria-based metal oxides, ternary ceria-based metal oxides, dopants for quaternary ceria-based metal oxides and reaction mechanism for soot oxidation reactions.

Chapter 3 explains the methodology and materials adopted for the synthesis of all metal oxides and details of characterization tools used for the analysis of these samples and soot oxidation reaction conditions.

Chapter 4 compares the activity of GDC solid solution obtained by EDTA-Citrate complexing and solvothermal method to confirm the synthesis method to be adopted in further. The main focus of the chapter is to analyse the activity of single metal oxides with redox (CeO_2 , SnO_2 , Pr_6O_{11} and Mn_3O_4) and non-redox (Gd_2O_3 , La_2O_3 , ZrO_2 , HfO_2 and Sm_2O_3) properties for soot oxidation using the characterization tools.

Chapter 5 discloses the activity study of binary metal oxide sample as catalysts for soot oxidation over a whole composition range for $\text{Ce}_{1-x}\text{Hf}_x\text{O}_2$ and $\text{Ce}_{1-x}\text{Sm}_x\text{O}_2$ ($x=0.0-1.0$) and at the fixed composition of $\text{Ce}_{0.9}\text{M}_{0.1}\text{O}_2$ ($\text{M}=\text{Sn}, \text{Hf}, \text{Zr}, \text{Gd}, \text{Sm}$ and La).

Chapter 6 deals with the development of ternary metal oxides ($\text{Ce}_{0.9}\text{Hf}_{0.1-0.0x}\text{Mn}_{0.0x}\text{O}_2$) ($x=0, 3, 5$ & 7) using the EDTA-Citrate method, its characterization and soot oxidation study. Also, the study on quaternary metal oxides ($\text{Ce}_{0.9}\text{Hf}_{0.07}\text{Mn}_{0.015}\text{X}_{0.015}\text{O}_2$; $\text{X}=\text{Li}, \text{Ag}, \text{Ba}$ & K) for soot oxidation activity with detailed characterization techniques are discussed. The overall study on activity with the dopant addition is concluded.

Chapter 7 contains the summary and conclusion and provides scope for the future studies.

CHAPTER 2

LITERATURE REVIEW

The background for the soot oxidation study on ceria-based materials and various objectives of the study is outlined. Reported literature for soot oxidation study is discussed in this chapter. The literature review is sub-categorised under different themes namely:

- I. Effect of synthesis method on soot activity.
- II. Single metal oxide materials for soot oxidation activity.
- III. Ceria-based binary metal oxides as soot oxidation catalyst.
- IV. Ternary metal oxides based on ceria for soot oxidation activity.
- V. Dopants for quaternary ceria-based metal oxides for soot oxidation activity
- VI. Reaction mechanism of soot oxidation activity.

The literature survey carried out under this theme is presented in the sections to follow.

2.1. EFFECT OF SYNTHESIS METHOD

Unlike other nanoparticles, nanoceria has a unique feature of lattice expansion as the particle size is small. Apart from that, the synthesis method controls the morphology, particle size and faceting of the material (Reed et al. 2014; Sun et al. 2012). A variety of synthesis methods are adopted for CeO₂ based catalyst development. Some of the most used synthesis methods are precipitation (Reddy et al. 2008a), microemulsion (Kurnatowska et al. 2014; Małecka et al. 2007), hydrothermal or solvothermal (Pan et al. 2008), sol-gel (Ansari 2010), combustion (Palmisano et al. 2006) and few more.

Table 2.1 compares the different synthesis methods adopted for CeO₂ metal oxide synthesized for soot oxidation reaction under different conditions. Piumetti et al. (2015) developed ceria nanocubes and nanorods using the hydrothermal method and mesoporous

ceria. Further, the studies of soot oxidation vary due to the variation of textural properties among the sample, and the activity is influenced by the surface properties of the samples (Piumetti et al. 2015). Microemulsion sample synthesized by Malecka et al. (2007) and Kurnatowska et al. (2014) were having different catalytic activity even though the soot oxidation reaction condition adopted in both the study were same as given in **Table 2.1**. However, the synthesis method remains constant, the crystallite size and calcination temperature variation, in turn, affects the activity of the samples (Kurnatowska et al. 2014; Małecka et al. 2007). From the preliminary literature survey, it is evident that material properties are modified with the synthesis method and thus, affects the catalytic activity. Depending upon the change in calcination temperature, synthesis method, precursor salt used, soot:catalyst contact condition and tight/loose contact the soot activity of the material varies even though the material remains constant. Thus, a single synthesis method is to be adopted for better comparison of activity in further studies. By comparing the activity of sample obtained by both EDTA-Citrate and solvothermal method a single synthesis method is adopted in further.

EDTA-Citrate complexing method or modified pechini method is the polymerised complex method adopted for CeO₂ based metal oxide synthesis. Metal ions in the solution are chelated together to form a complex which further undergoes a polyesterification reaction to form polymeric glass while heating the solution. Coprecipitation of both citrate and EDTA attains a stable chelate complex. The advantage of this synthesis methods are, hydroxo complex is not involved (Anjaneya and Singh 2017), molecular level homogeneity is achieved (Prasad et al. 2012b), easy to synthesis (Gu et al. 2007), faster reaction rates and lower energy requirements (Patra et al. 2011). Thus, the EDTA-Citrate synthesis method is a promising synthesis method that can be adopted for the metal oxide synthesis. The different materials synthesized using EDTA-Citrate complexing methods by various scientific groups and different applications are given in **Table 2.2**.

Table 2.1: Comparison of synthesis method and reaction parameters adopted for CeO₂ soot oxidation

Synthesis method	Calcination condition	Crystallite size (nm)	Surface area (m ² /g)	T ₅₀ (°C) (Tight contact)	Catalyst: Soot	Reference
Coprecipitation method	500 °C/5 h	7.3	41	522	4:1	(Reddy et al. 2008a)
Direct use of metal nitrate solution	1000 °C/2 h	140.0	2	576	4:1	(Krishna et al. 2007)
Microemulsion	400 °C/3 h	5.0	--	507	2:1	(Małecka et al. 2007)
Micro emulsion	300 °C/1 h	8.6	56	449	2:1	(Kurnatowska et al. 2014)
Hydrothermal method	550 °C/4 h	71.0	6	435	9:1	(Andana et al. 2016a)
Sol-gel method	500 °C/3 h	7.8	62	390	10:1	(Liang et al. 2008)
Hydrothermal-Nanocubes	550 °C/4 h	54.0	4	400	9:1	(Piumetti et al. 2015)
Hydrothermal-Nanorods		43.0	4	416		
Mesoporous		5.0	75	464		
Solution combustion synthesis	600 °C/ 20 min	35.0	69	476	9:1	(Piumetti et al. 2015)

Table 2.2: Samples synthesized by the EDTA-Citrate method

Sample	Crystallite size (nm)	BET Surface area (m ² /g)	Application	References
(Ce _{0.8} Gd _{0.2} O _{2-δ})	39	--	Electrolyte for IT-SOFC	(Wu et al. 2010a)
La _{1-x} Sr _x CoO _{3-δ}	29~42	4~10	Soot oxidation	(Prasad et al. 2012b)
Ce _{0.8} Sm _{0.2} O _{1.9}	30	--	Electrolyte for IT-SOFC	(Anjaneya and Singh 2017)
La _{0.8} Sr _{0.2} MnO ₃	15	33	Cathode for SOFC	(Gu et al. 2007)
(Sc ₂ O ₃) _{0.1} (ZrO ₂) _{0.9}	9	27	Electrolyte for SOFC	(Gu et al. 2007)
Ce _{0.8} RE _{0.2} O _{2-δ} (RE= Pr, Sm and Nd)	12	45~57	CO Oxidation	(Kim et al. 2017)

2.2. SINGLE METAL OXIDE CATALYSTS

Single metal oxides independently are tested as the catalyst for soot oxidation reaction without any dopant addition. As per the previous study of Neeft et al. (1996), different metals and metal oxides utilised as the catalyst for soot oxidation were tested under loose and tight contact conditions. Not only ceria, but other metal oxides also have the potential to improve oxidation reaction. Catalyst ranking differs with the variation in contact and concentration condition. They found that the order of reactivity of different metal oxides follows the trend of: Pb > Co > V > Mo > Fe > La > Mn > Sb > Bi > Ca > Cu > Ag > Ni > Cr > Zr > Ba > Zn > Ce > Mg > Nb > W > Sn > Ge. As per their study, the catalytic activity of Ce falls in the lower range, which is related to the higher mobility by surface

migration or catalyst melting and gas phase transport by high catalyst partial pressure (Neeft et al. 1996). Single metal oxides catalytic activity follows a trend of $\text{SmO}_x > \text{LaO}_x > \text{PrO}_x > \text{CeO}_2 > \text{YO}_x$. Apart from redox site available for $\text{Pr}^{3+}/\text{Pr}^{4+}$, the participation of surface peroxide like species in the reaction enhance activity for Sm^{3+} and La^{3+} (Krishna et al. 2007).

Table 2.3 summaries the single metal oxide catalyst adopted for soot oxidation by various research groups. Soot oxidation of single metal oxides (CeO_2 , TiO_2 and ZrO_2) (see **Table 2.3**) studied by Atribak et al. (2007) shown better CO_2 yield for CeO_2 compared to other catalysts. It is pointed out that depending on the metal oxide nature, and BET surface area can affect the activity directly (Atribak et al. 2007). A study by Wasalathanthri et al. (2017) synthesized a series of manganese oxide with different oxidation state and confirms that the order of catalyst activity does not follow the surface area. On the other hand, the order follows the redox activity of the material. Two-step reductions happening in these materials are due to the first reduction of MnO_2 to Mn_2O_3 and further reduction of Mn_2O_3 to MnO (Wasalathanthri et al. 2017). The study by Dernaika et al. (2003) as given in **Table 2.3** proves that rather than surface area, catalytic activity is related to active contact points with the soot (Dernaika and Uner 2003). The transition metal oxides of ZrO_2 , Al_2O_3 and TiO_2 , are active for residual hydrocarbon combustion and the samples of SiO_2 , La_2O_3 and CeO_2 are inactive since the reaction started only at around 500°C (Dernaika and Uner 2003).

Based on the literature review of single metal oxides we can conclude that the catalytic activity mainly depends upon the material selected for the study, calcination temperature and synthesis method adopted. As far as these properties are kept constant, the structural features such as active surface area and reducibility control the activity of the samples. So a similar reaction condition and synthesis method must be adopted while comparing the reactivity of the single metal oxide catalyst.

Table 2.3: Single metal oxides as soot oxidation catalysts

Samples studied	Reaction method and Calcination temperature	BET SA (m ² /g)	T ₅₀ (°C)		Remarks	Reference
			Loose contact	Tight contact		
TiO ₂ ZrO ₂ CeO ₂	Precipitation 600 °C/2 h	47 47 37	593 592 551	-- -- --	<ul style="list-style-type: none"> • CeO₂ has higher activity since it accelerates NO₂ conversion • CO to CO₂ conversion is better for CeO₂. • Calcination decreases activity 	(Atribak et al. 2007)
Co ₃ O ₄ CeO ₂ Fe ₂ O ₃ ZnO TiO ₂	Flame spray pyrolysis 500 °C/2 h	-- -- -- -- --	363 393 476 512 564	650 -- -- -- --	<ul style="list-style-type: none"> • Active oxygen available for soot oxidation is key • As heat of chemisorption for oxygen reduces, lattice oxygen mobility improves • Bond strength of oxygen in catalyst affects the reaction rate 	(Christensen et al. 2016)
Meso-Mn-A Meso-Mn ₂ O ₃ Meso-ε- Mn ₂ O ₃	Inverse micelle templating method previously 70 °C/2 h	165 88 94	-- -- --	442 436 355	<ul style="list-style-type: none"> • Redox property affects activity • Surface area doesn't influence activity • Activation energy is directly related to activity 	(Wasalathanthri et al. 2017)

Al ₂ O ₃	Commercial samples 350 °C/2 h	66	600	--	<ul style="list-style-type: none"> • Active surface in contact with catalyst and soot determines the rate of reaction, rather than the surface area. • Ease of oxygen mobility improves oxidation reaction • Metal oxide doesn't influence the activation energy 	(Dernaika and Uner 2003)
CeO ₂		3	570	--		
La ₂ O ₃		3	570	--		
SiO ₂		460	555	--		
TiO ₂		45	594	--		
CeO ₂	Nitrate heat treatment 700 °C/2 h	2	--	630	<ul style="list-style-type: none"> • Surface peroxide species participate in reaction • Samples even without redox properties showed higher activity 	(Krishna et al. 2007)
Sm ₂ O ₃		--	--	520		
PrO _x		--	--	550		
Al ₂ O ₃		--	--	560		
NiO ₂	EDTA-Citrate method 600 °C/5 h	7	--	480	<ul style="list-style-type: none"> • Metal oxide shows enhanced activity than metal itself 	(Previous study in the group)

2.3. CERIA-BASED BINARY METAL OXIDES

Modification of CeO₂ lattice by chemical doping with the aliovalent dopant (elements with different oxidation state) or isovalent (elements with the same oxidation state) results in oxygen anion vacancy creation. The vacancy creation is due to charge compensation effect of the foreign cation with a valance different than the host ion. CeO₂ easily forms solid solution with metals, such as rare earth elements and transition metals. There will be a decrease in the cell parameter when a smaller ionic radius element is substituted and thus, favours the creation of structural defects hence the oxygen mobility is modified. Also, the oxide ion diffusion energy is reduced along with lowering of lattice parameter when doping isovalent dopant with smaller ionic radius (Zr⁴⁺, Hf⁴⁺) (Trovarelli 1999).

Different rare earth metal oxides doped on ceria are studied for soot oxidation with different calcination temperature is shown in **Table 2.4**. Active oxygen for the reaction can be contributed from either oxygen in the gas phase or bulk oxygen from the catalyst surface. High activity of CeO₂ is due to its redox sites which readily exchanges gas phase oxygen and oxygen from ceria framework. Surface area, crystallite size and oxygen vacancy of the catalyst are the possible parameters that influence the activity of doped ceria. Also, the trend in oxygen vacancy is matching with soot activity (Reddy et al. 2008a).

Optimum catalyst composition determines the active oxygen production and further the active oxygen transfer depend on the particle size of the catalyst as per study of Guillén-hurtado et al. (2015). Ce_{0.5}Pr_{0.5}O₂ sample is the most active catalyst prepared using the microemulsion method. As the particle size is low, the contact area between soot and catalyst is improved, and their activity is enhanced. The results are given in **Table 2.4** (Guillén-hurtado et al. 2015).

Figure 2.1 shows the T_{50} temperature variation of binary metal oxides studied by Mukherjee et al. (2016) (see **Table 2.4**). CM (Ce-Mn) > CH (Ce-Hf) > CP (Ce-Pr) > CL (Ce-La) > CZ (Ce-Zr) > CF (Ce-Fe) > C (Ce) is the activity order for soot oxidation. Aliovalent dopant addition in CM and CP results in more oxygen vacancy creation by charge compensation. CM showing a higher degree of lattice strain improves oxygen flow, enhancement in reducibility could be related to the higher concentration of Ce^{3+} , simultaneous interaction with Ce and Mn redox couple improves the reduction reaction and all these parameters, in turn, improves the oxygen availability for soot oxidation reaction. XPS analysis confirms that CM and CH have a higher amount of surface active oxygen that easily takes part in the reaction. Amount of surface oxygen results in enhancing the activity of the samples for soot oxidation (Mukherjee et al. 2016).

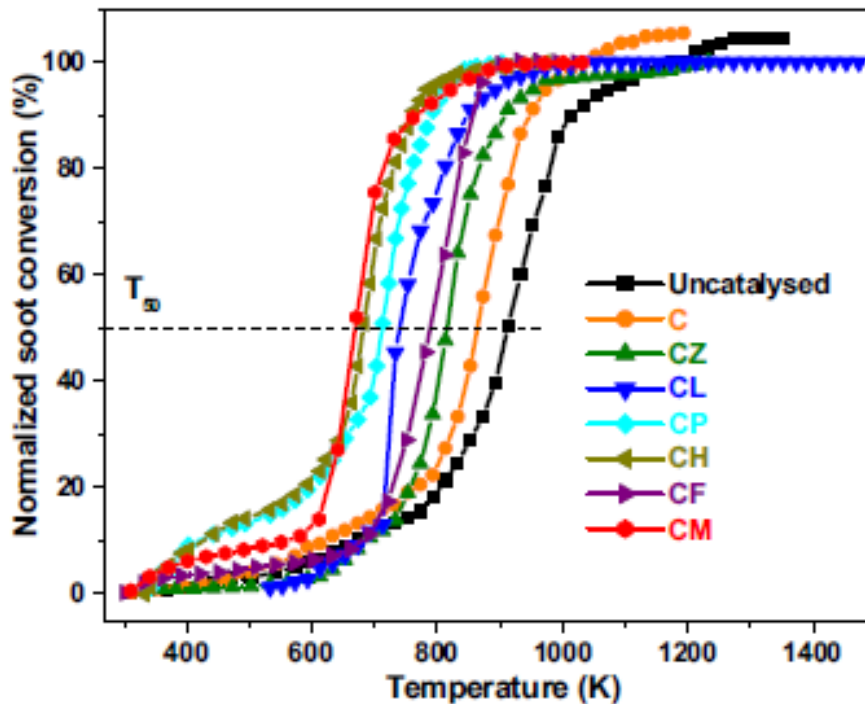


Figure 2.1: Soot conversion profile for binary oxides
(Mukherjee et al. (2016))

Krishna et al. (2007) studied the effect of doping with La and Pr on ceria lattice for soot oxidation activity. Nature and amount of dopant influence surface properties and modify catalyst activity. Dopant addition has led to decrease in crystallite size and increase in intraparticle void volume, which in turn improves catalyst mixing with soot and improve redox sites, respectively. The surface oxygen presence is a crucial factor for soot oxidation, and ceria-lanthanum metal oxide has higher oxygen vacancies with higher redox properties (Krishna et al. 2007).

Jampaiah et al. (2015) studied CM metal oxides in different compositions for soot oxidation reaction (**Table 2.4**). Synergetic effect between ceria and manganese enhances the redox properties of ceria. In comparison with pure metal oxides, doping results in enhanced surface oxygen formation and lattice distortion in the system. Facile oxygen mobility and enhanced surface reduction are the critical factors for the improved catalytic activity (Jampaiah et al. 2015).

CM series synthesized by Yu et al. (2014) using colloidal crystal template method results in three-dimensionally ordered macroporous samples. The synergistic effect of Mn and Ce is related to high oxidative properties of manganese and oxygen storage ability of ceria. Along with that, a macroporous effect enhanced the catalytic activity and improved the CO₂ selectivity. During the catalytic reaction, gaseous oxygen gets adsorbed on the catalyst surface, and further surface oxygen vacancy is created by the simultaneous valence changing the property of Mn and Ce. Active oxygen is generated from the vacancy of Mn-Ce. Hence the ratio of Mn and Ce controls the active oxygen formation that in turn affects the activity (Yu et al. 2014).

Table 2.4: Effect of binary dopants on ceria for soot oxidation

Sample studied	Reaction Method and Calcination temperature	BET SA (m ² /g)	T ₅₀ (°C) (Tight contact)	Remarks	References
Ce Ce-Zr Ce-Hf	Coprecipitation 500°C/5.0h	41 84 78	522 514 409	<ul style="list-style-type: none"> Doped samples have higher oxygen vacancy compared to pure CeO₂ Nano size enhances activity 	(Reddy et al. 2008a)
CeO ₂ Ce _{0.89} Zr _{0.11} O ₂ Ce _{0.79} Zr _{0.21} O ₂ Ce _{0.69} Zr _{0.31} O ₂ Ce _{0.59} Zr _{0.41} O ₂ Ce _{0.49} Zr _{0.51} O ₂ ZrO ₂	Nitrates mixing 1000°C/ 1.3h	2 11 18 17 17 17 19	629 480 468 458 481 471 644	<ul style="list-style-type: none"> Zr improves BET surface areas, redox properties, and thermal stability of metal oxide Zr content increases crystallite size Increased oxygen mobility within the lattice thus Ce⁴⁺ can be reduced easily. 	(Atribak et al. 2008)
CeO ₂ Ce _{0.7} Pr _{0.3} O ₂ Pr ₆ O ₁₁	Nitrates mixing 500°C/3.0h	38 25 13	430 413 455	<ul style="list-style-type: none"> Solid solution with smaller crystallite size is beneficial OSC and oxygen mobility improves with dopant addition Thermal stability is improved with dopant 	(Fan et al. 2017)

(Cont.)

Literature Review

Ce _{0.8} Zr _{0.2} O ₂	Microemulsion 500°C/5.0h	145	484	<ul style="list-style-type: none"> Nature and dopant amount are important along with particle size Composition determines active oxygen formation Particle size determines rate of active oxygen transfer 	(Guillén-hurtado et al. 2015)
Ce _{0.5} Pr _{0.5} O ₂		125	444		
Ce _{0.8} Pr _{0.2} O ₂		120	459		
Ce _{0.8} Pr _{0.2} O ₂	Coprecipitation 500°C/5.0h	70	502	(Mukherjee et al. 2016)	
Ce _{0.8} Zr _{0.2} O ₂		57	502		
Ce _{0.5} Pr _{0.5} O ₂		27	484		
CZ	Coprecipitation 500°C/5.0h	84	540		<ul style="list-style-type: none"> Surface adsorbed oxygen are key role in controlling soot oxidation CM sample has higher surface oxygen than CF Specific surface area, crystallite size, oxygen vacancy formation energy and reducibility affects the activity
CL		66	465		
CP		72	436		
CH		78	407		
CF		68	515		
CM		58	395		
Ce	Nitrates heat treatment 700°C/2.0h	57	450	<ul style="list-style-type: none"> Few surface reducible layers participate in reaction Catalyst only facilitates oxygen transfer to the soot surface without interfering reaction mechanism 	(Krishna et al. 2007)
Ce-La		48	425		
Ce-Pr		44	422		

(Cont.)

Literature Review

CeO ₂	Citric acid assisted	42	474	<ul style="list-style-type: none"> • Smaller crystallite size and higher surface oxygen vacancy improves activity • Synergetic interaction between CeO₂ and MnO_x enhanced redox properties • Improved surface reducibility and facile oxygen mobility improved catalytic activity 	(Jampaiah et al. 2015)
Ce _{0.9} Mn _{0.1} O ₂	Sol-gel	63	395		
Ce _{0.8} Mn _{0.2} O ₂	500°C/3.0h	64	390		
Ce _{0.7} Mn _{0.3} O ₂		70	352		
Ce _{0.6} Mn _{0.4} O ₂		66	400		
MnO _x		11	508		
CeO ₂	Colloidal crystal	44	393	<ul style="list-style-type: none"> • Uniform pore size and periodic voids interconnected through open windows improved contact points for soot oxidation • Strong oxidative Mn and highly reducible ceria synergistically improves the oxidation 	(Yu et al. 2014)
Ce _{0.9} Mn _{0.1} O ₂	template	--	361		
Ce _{0.7} Mn _{0.3} O ₂	550°C/4.0h	--	356		
Ce _{0.5} Mn _{0.5} O ₂		48	358		
Ce _{0.3} Mn _{0.7} O ₂		--	370		
Ce _{0.1} Mn _{0.9} O ₂		--	381		
CeO ₂	Citric acid complex	16	372	<ul style="list-style-type: none"> • Mobility and oxygen transfer affects activity • Doping enhances oxygen mobility and thus actively escape from lattice • Interstitial oxygen adjacent to Mn⁴⁺ can easily escape to the gas phase. 	(Lin et al. 2018)
Ce _{0.9} Mn _{0.1} O ₂	method	108	346		
Ce _{0.7} Mn _{0.3} O ₂	550°C/5.0h	91	345		
Ce _{0.6} Mn _{0.4} O ₂		125	299		
Ce _{0.5} Mn _{0.5} O ₂		114	304		

2.3.1. Binary System Phase Diagram

Application of ceria-based samples to different fields depends upon the phase in which they exist since the oxygen vacancy caused by internal defect sites are depending upon their phase transformation. In case of soot oxidation, the homogeneous binary solid solution in stable fluorite ceria phase is necessary with higher oxygen vacancy. As discussed earlier, a variety of binary systems are used for soot oxidation, but the phase in which they exist is critical in controlling their activity. Depending upon the variation in sensitivity of the solid samples to different analysis techniques, thermal analysis, XRD analysis or Raman analysis can be adopted for phase identification of the eutectic and peritectic systems (Montanari 2004)(Chavan and Tyagi 2006). Under normal conditions, HfO_2 exist in the monoclinic phase, with further heating in changes to tetragonal and cubic phase, respectively. Metastable-stable phase diagram of a binary ceria-hafnia system is shown in **Figure 2.2**. The stable phase boundaries are indicated as solid lines. t' and t'' represents the metastable tetragonal phase with oxygen displaced from ideal fluorite position (Fujimori et al. 2001).

Chavan et al. (2006) studied the ceria-hafnia binary series calcined at 1400 °C for 48 h, identified the stable fluorite phase of ceria up to 10 mol% Hf addition and existence of mixed cubic and fluorite phase in all further samples of higher Hf mol content using XRD analysis (see **Figure 2.3**) (Chavan and Tyagi 2006). Similarly, Raitano et al. (2015) identified the phase transformation for the ceria-hafnia binary system from pure fluorite to the mixed phase of cubic, monoclinic and tetragonal for hafnia content higher than 14 mol%. HfO_2 is confirmed to exist in the monoclinic phase (Raitano et al. 2015). Apart from the hafnia system, Grover et al. (2004) studied the phase transformation of a binary $\text{CeO}_2\text{-Gd}_2\text{O}_3$ system at 20 mol% dopant (Grover and Tyagi 2004). Artini et al. (2016) identified the phase transformation of $\text{CeO}_2\text{-Gd}_2\text{O}_3$, $\text{CeO}_2\text{-Sm}_2\text{O}_3$ and $\text{CeO}_2\text{-La}_2\text{O}_3$ at 20 mol% of dopant using XRD and Raman spectroscopy techniques (Artini et al. 2016).

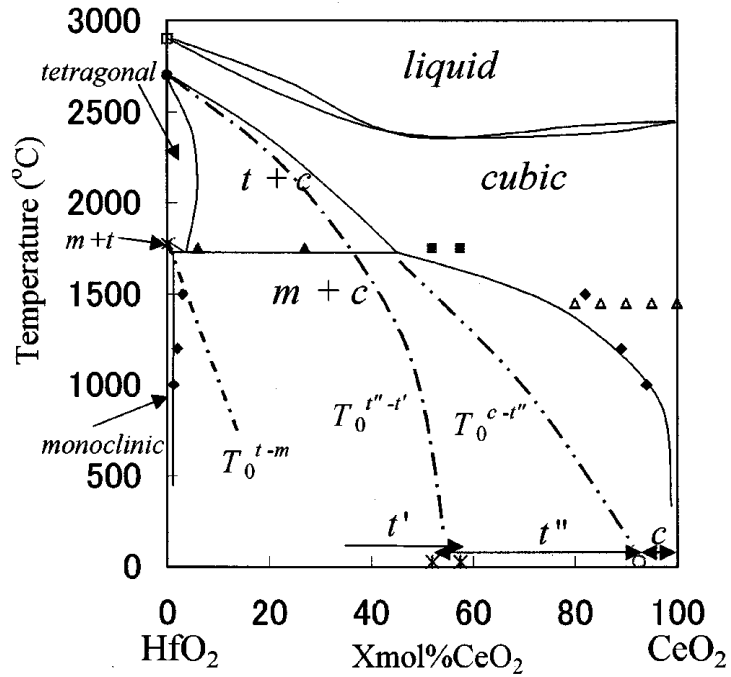


Figure 2.2: Temperature-composition phase diagram of ceria-hafnia binary system (Fujimori et al. 2001)

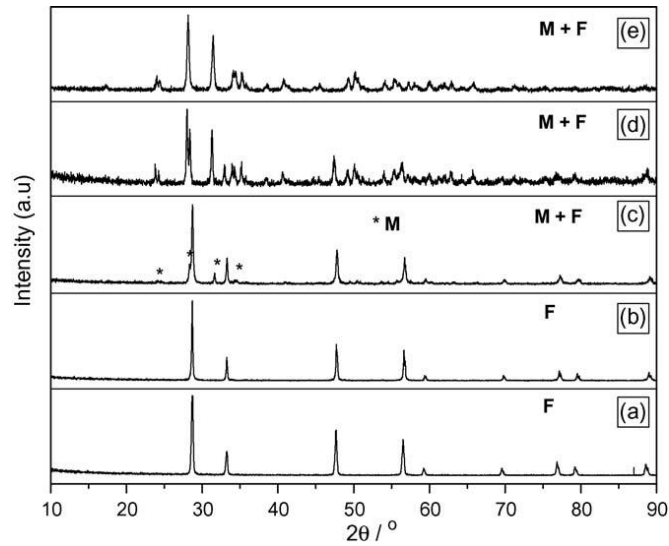


Figure 2.3: Phase separation of ceria-hafnia binary system using XRD analysis (Chavan and Tyagi 2006)

2.4. CERIA-BASED TERNARY METAL OXIDES

Aneggi et al. (2006) studied ceria doped with transition metal (Zr and Fe) and rare earth metals (La, Sm, Pr and Tb), the results are given in **Table 2.5**. The amount of surface Ce sites is higher for CZ100 and CZ75, and correspondingly these samples are active due to the better surface area, abstraction of oxygen involves mainly surface sites, with little or no participation of the bulk in the reaction. When the surface area is low or larger particle size is present, the access points for gas phase oxygen limits due to geometrical factors, the lattice oxygen contributes to the overall activity. OSC promotion in the case of rare earth metal oxides depends upon several variables such as preparation, textural and structural properties (Aneggi et al. 2006).

Vinodkumar et al. (2018) studied the co-doping system of $\text{Ce}_{0.8}\text{Eu}_{0.1}\text{M}_{0.1}\text{O}_{2-\delta}$ (M= La, Sm, Hf and Zr). **Table 2.5** gives the result of the samples. Co-doping leads to significant improvement in reduction properties and oxygen defect concentration. Aliovalent co-doped samples exhibited better catalytic activity than isovalent co-doped samples. With the presence of La as the co-dopant remarkable modification in physiochemical properties is observed that favours the catalytic activity. Since Eu and La exhibit different physical and chemical properties and are not closer members of rare earth family. On the other hand, Sm and Eu are closer members, that their characteristics also matches well and hence the activity is reduced (Vinodkumar et al. 2018).

Three-dimensionally ordered macroporous (3DOM) Ce-based catalyst was synthesized using colloidal crystal template (CCT) route by Tang et al. (2018) (see **Table 2.5**). The macroporous ceria catalyst with small interconnected pore window aids in the catalytic activity. Nd doping into the CM system enhance activity by increasing the oxygen vacancy with better Mn^{4+} content and stronger redox ability. Thermal stability improves and inactivation of catalytic activity is prevented with Nd doping (Tang et al. 2018).

Table 2.5: Effect of Ternary dopants on ceria for soot oxidation

Sample studied	Reaction Method and Calcination temperature	BET SA (m ² /g)	T ₅₀ (°C) (Tight contact)	Remarks	Reference
CeO ₂	Coprecipitation 500°C/2h	57	389	<ul style="list-style-type: none"> Oxygen storage is critical in providing an easier soot oxidation reaction Lattice oxygen of ceria is highlighted Zr addition improves thermal stability and provides reactive oxygen ions 	(Aneggi et al. 2006)
Ce _{0.47} Zr _{0.48} Fe _{0.05} O _{1.975}		106	399		
Ce _{0.48} Zr _{0.50} La _{0.02} O _{1.99}		93	414		
Ce _{0.48} Zr _{0.50} Pr _{0.02} O _{1.99}		99	410		
Ce _{0.48} Zr _{0.50} Sm _{0.02} O _{1.99}		92	411		
Ce _{0.48} Zr _{0.50} Tb _{0.02} O _{1.99}		96	414		
CeO ₂	Nitrate precursor heating 1000°C/90 min	2	575	<ul style="list-style-type: none"> Zr promotes cerium-rich surfaces; Y hinders the accumulation of cerium on the surface Addition of Y doesn't affect its activity due to Y accumulation on the surface and thus hindering the active components For loose contact, activity depends upon surface area 	(Atribak et al. 2009)
Ce _{0.99} Y _{0.01} O ₂		2	540		
Ce _{0.94} Y _{0.06} O ₂		3	545		
Ce _{0.88} Y _{0.12} O ₂		2	564		
Ce _{0.85} Zr _{0.15} O ₂		11	471		
Ce _{0.85} Zr _{0.15} Y _{0.01} O ₂		13	456		
Ce _{0.80} Zr _{0.15} Y _{0.05} O ₂		12	470		
Ce _{0.75} Zr _{0.15} Y _{0.10} O ₂		10	470		

(Cont.)

Literature Review

CeO ₂	Coprecipitation 500°C/5h	41	604	<ul style="list-style-type: none"> Ease of release of substantial amount of oxygen in co-doped ceria-based materials at low temperature rather than doped samples yields in better activity Coexistence of Eu and La modifies structural properties and enhances catalytic activity Trivalent co-doped CE sample exhibits higher oxygen vacancy than tetravalent 	(Vinodkumar et al. 2018)
Ce _{0.9} Eu _{0.1} O _{2-δ}		63	487		
Ce _{0.8} Eu _{0.1} La _{0.1} O _{2-δ}		96	446		
Ce _{0.8} Eu _{0.1} Sm _{0.1} O _{2-δ}		84	471		
Ce _{0.8} Eu _{0.1} Hf _{0.1} O _{2-δ}		79	470		
Ce _{0.8} Eu _{0.1} Zr _{0.1} O _{2-δ}	94	483			
CeO ₂	Solution combustion synthesis 650°C	15	451	<ul style="list-style-type: none"> Uncoordinated planes enhance activity due to instability of the atoms Activity enhances by bulk oxygen anion mobility and electrical conductivity 	(Andana et al. 2016b)
Ce _{0.80} Zr _{0.20} O ₂		23	469		
Ce _{0.80} Pr _{0.20} O ₂		16	457		
Ce _{0.80} Pr _{0.10} Zr _{0.10} O ₂		38	444		
CeO ₂	Cation complexing 750°C/1h	3	470	<ul style="list-style-type: none"> Active oxygen at low temperature was created Reducible Pr enhances redox potential than non-reducible Zr Dynamic OSC is high for high surface area samples 	(Imanaka et al. 2009)
Ce _{0.64} Zr _{0.16} Bi _{0.20} O _{1.90}		11	407		
Ce _{0.48} Pr _{0.30} Bi _{0.22} O _{1.840}		7	376		
Ce _{0.47} Pr _{0.21} Bi _{0.32} O _{1.840}		5	358		
Ce _{0.46} Pr _{0.12} Bi _{0.42} O _{1.840}		2	381		

(Cont.)

Literature Review

CeO ₂	Emulsion polymerization 550°C/4h	29	401	<ul style="list-style-type: none"> • Co-doped sample with enhanced oxygen vacancy and oxygen adsorption results in stronger redox ability and surface Mn⁴⁺ • Nd promotes thermal stability of the sample • Nd doping prevents phase separation and sintering. Maintains partial low-temperature redox capacities after ageing. 	(Tang et al. 2018)
Ce _{0.9} Mn _{0.1} O _{2-δ}		51	394		
Ce _{0.8} Mn _{0.2} O _{2-δ}		52	376		
Ce _{0.7} Mn _{0.3} O _{2-δ}		54	353		
Ce _{0.6} Mn _{0.4} O _{2-δ}		37	360		
Ce _{0.5} Mn _{0.5} O _{2-δ}		34	367		
Ce _{0.8} Nd _{0.1} Mn _{0.1} O ₂		55	374		
Ce _{0.7} Nd _{0.1} Mn _{0.2} O ₂		57	356		
Ce _{0.6} Nd _{0.1} Mn _{0.3} O ₂		57	331		
Ce _{0.5} Nd _{0.1} Mn _{0.4} O ₂		40	340		
Ce _{0.4} Nd _{0.1} Mn _{0.5} O ₂	33	349			
Ce _{0.85} Mn _{0.15} O ₂	Citric acid aided sol-gel method 500°C/5h	18	535	<ul style="list-style-type: none"> • Thermal stability is improved with Al₂O₃ addition • Phase prevention and sintering are reduced • Redox property and activity are directly related 	(Wu et al. 2011)
Ce _{0.85} Mn _{0.15} O ₂ :Al ₂ O ₃ = 2:1		130	575		

2.5. CERIA-BASED QUATERNARY METAL OXIDE DOPANTS

Alkali or alkaline earth metals can enhance the catalytic activity by improving the mobility with the formation of a low melting or eutectic systems with other catalyst components and thus, favours the catalytic activity for soot oxidation since contact points are critical in this type of reactions. Alkali metal may be present on catalyst surface or lies within the surface. In that case, the activity can be improved by modification in electron-donor properties, the formation of eutectics and sometimes the phase change (Jakubek et al. 2015). Alkali metals influence catalytic activity either by carbonate assisted mechanism or by redox mechanism (Aneggi et al. 2008). With the presence of alkali and alkaline earth metals, CO₂ selectivity improves (Castoldi et al. 2009). Deactivation of ceria metal oxides is reduced by adding suitable precious metals on ceria lattice. Higher surface reducibility on silver-ceria interface affects catalytic activity positively. Apart from that, silver can form active oxygen and peroxide species (Castoldi et al. 2015).

Li improves the electronic properties of the catalyst due to its high electropositive nature (Jakubek et al. 2015). Ruiz et al. (2012) report that catalyst supported with Li shows better activity compared to other alkali metal oxides due to the variation in reaction mechanism with which they react (Ruiz et al. 2012). With addition of Li into a perovskite system, activity likely increased by improving electro-neutrality and thus, obtain higher active oxygen sites for reaction to take place (Fino et al. 2006) On the other hand study by Shangguan et al. (1998) shows that the activity and selectivity of catalyst doped with Li is much lower than other alkali metal doped samples (Shangguan 1998).

Silver metal oxides are reported to be highly reactive for soot oxidation. One feature of Ag₂O is that it gets converted to metallic Ag after the reaction. Thus, they are generally doped with other metals to enhance their activity (Neeft et al. 1996). The lower activation energy, easy superoxide formation and higher oxygen reducibility are the reason for enhanced activity of Ag-Ce (Liu et al. 2016; Shimizu et al. 2010). Preda et al. (2011) studied the soot oxidation mechanism for Ag-Ce state that interface between Ag and Ce

results in active oxygen species formation and thus take part in soot oxidation reaction (Preda and Pacchioni 2011). Silver particles are reported to show enhanced mobility that ensures good soot catalyst contact (Castoldi et al. 2015; Gardini et al. 2016; Liu et al. 2016). **Table 2.6** reports the various Ag based catalysts studied for soot oxidation activity. The gaseous oxygen on the surface of Ag results in the formation of active oxygen at the interface of metals and result in forming O_n^{x-} species that migrate to soot surface and take part in reaction (Yamazaki et al. 2011).

Barium reduces crystal sintering that ensures the stability even with ageing. Triggering effect of the nitrate aids in enhancing the activity of barium doped Mn-CeO₂ samples. On addition of Ba into a system, perovskite-based catalyst are formed during high-temperature calcination that acts as a limitation of Ba dopant (XiaodongWu et al. 2011). As the Ba covers the surface, the redox property reduces since the surface covers with Ba which limits the active oxygen reactivity (XiaodongWu et al. 2011). Ba based catalyst reported having lower catalytic activity when compared to K based catalyst as per the study of Matarrese et al. (2016) due to lower redox property of Ba (Matarrese et al. 2016). Some of the Ba based catalyst results are given in **Table 2.6**.

Potassium-containing catalysts are reports improved soot and catalyst contact by improving the surface mobility. K having high electropositivity leads to improved catalytic activity due to enhanced electron donation capacity of the element (Castoldi et al. 2009) (Li et al. 2016). K can improve the chemisorbed oxygen on the catalyst surface. The K activity can be improved by forming carbonate intermediates. Soot oxidation using K₂O is reported to occur at a temperature around 300 °C (An and McGinn 2006). Enhanced activity of potassium doped sample is mainly due to redox cycle along with cerium that improves the oxygen transfer between the dopants and correspondingly takes part in soot oxidation. Lower electronegativity of dopant, in turn, results in easy dissociation of oxygen chemisorption. Lower agglomeration ensures higher dispersion due to stronger electrostatic attraction with surface oxygen (Aneggi et al. 2008). **Table 2.6** gives the soot oxidation activity of K based catalysts.

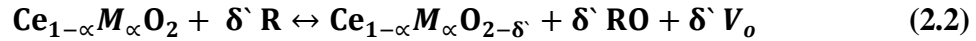
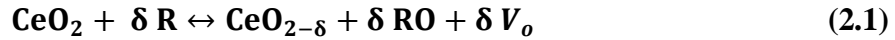
Table 2.6: Effect of alkali, alkaline earth and noble metal dopants on ceria for soot oxidation

Sample studied	Reaction Method and calcination temperature	BET SA (m ² /g)	T ₅₀ (°C)	Remarks	Reference
Cu,K/CeO ₂	Precipitation method	--	313	<ul style="list-style-type: none"> • Low melting point of K improves the contact point of catalyst-soot • Higher resistance to sulfur deactivation 	(Weng et al. 2008)
K/Al ₂ O ₃	Calcination of metal acetate loaded alumina	180	450	<ul style="list-style-type: none"> • Activity depends upon the electronegativity of the alkali metals • Mobility of surface species control activity along with reactivity 	(Castoldi et al. 2009)
K-CeO ₂	Wetness impregnation	20	367	<ul style="list-style-type: none"> • Lower electronegativity of dopant improves dissociative chemisorption of oxygen 	(Aneggi et al. 2008)
K/CeO ₂	Mixing and heating	--	400	<ul style="list-style-type: none"> • Higher surface oxygen from CeO₂ and higher mobility of K improves activity • Carbonate intermediate mechanism with the presence of K 	(Miró et al. 1999)

Ag-Ba/CeO ₂	Wetness impregnation	31	470	<ul style="list-style-type: none"> • Instead of Ba and Sr presence, Ag presence significantly influence activity • CO₂ selectivity is high for the sample • Superoxide formation by Ag enhances catalytic activity 	(Castoldi et al. 2015)
Ag-Sr/CeO ₂		20	460		
Ag/CeO ₂	Wetness impregnation	10	376	<ul style="list-style-type: none"> • Catalyst deactivation is due to lesser (O₂⁻) presence • Ag enhances superoxide (O₂⁻) formation than peroxide (O⁻) • Reverse transformation of superoxide to metallic oxide improves 	(Liu et al. 2016)
Ba-Ce	Sol-gel method	58	480	<ul style="list-style-type: none"> • Mn^{x+} and Ce^{x+} sites coordinated to Stable bidentate or monodentate nitrates 	(Wu et al. 2010b)
Ba-Mn		153	400		
Ba-Mn-Ce		81	390		
Ba-Cu-Ce	Sol-gel method	60	395	<ul style="list-style-type: none"> • Ba restrains the deterioration of the catalyst by inhibiting the sintering of ceria and copper oxide crystallites 	(Lin et al. 2011)

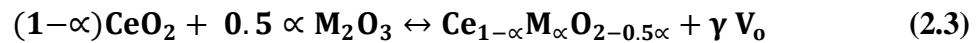
2.6. REACTION MECHANISM OF SOOT OXIDATION ACTIVITY

The reaction of CeO₂ during external doping has been studied, as per the findings; an intrinsic vacancy is created during the redox reaction of CeO₂ when a reductant molecule such as soot is in contact. The equation is as given by **Equation (2.1)**. This kind of reaction can be promoted either by noble metal dispersion or by chemical doping with dopants (Trovarelli 1999). Here we are discussing only dopant addition on CeO₂ lattice, and it is as given in **Equation (2.2)**.



Where R is the reductant (Soot), RO is the gaseous product (CO/CO₂), M is the isovalent dopant (Zr⁴⁺, Hf⁴⁺), α is the mole fraction of dopant added and, V_o is the oxygen anion vacancy.

Ceria modification by an aliovalent (M²⁺/M³⁺) element leads to oxygen anion vacancy creation by charge compensating the effect of foreign cations with a lower valance than that of host cation (Trovarelli 1999). The substitution with a di or trivalent cation leads to the reaction as shown in **Equation (2.3)** and **Equation (2.4)**:

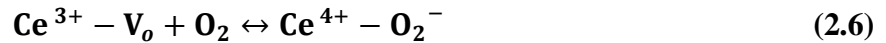


The reaction mechanism for soot oxidation generally reported are discussed here. Gaseous O₂ spills over the catalyst surface by adsorption and forms O_xⁿ⁻ through **Equation (2.5)**:



The high density of Ce^{3+} and V_o leads to the surface capping oxygen (O^{2-}) formation (Liu et al. 2017)

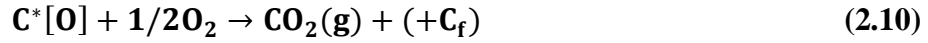
The soot oxidation activity is explained by the reaction as shown in **Equation (2.6)**. Gaseous phase oxygen fills the oxygen vacancy created during oxidation of soot which leads to the active oxygen species (O^{2-}) creation. This active oxygen is responsible for the reaction. Thus, the ceria and soot interface plays an essential role for rapid surface oxygen species transfer over soot and improve soot oxidation rate (Sudarsanam et al. 2016).



Where, V_o is the oxygen vacancy and O^{2-} is the active oxygen.

Spillover oxygen is vital in controlling the active centre formation and regeneration and also serves as a reactant. Thus, the active oxygen makes soot oxidation efficient. The soot oxidation mechanism follows two redox processes as per Mars-van Krevelen (MvK) mechanism: injection of electrons into the catalyst and extraction of electrons from the oxide. This process can occur spontaneously when the highest occupied molecular orbital of hydrocarbon is above the unoccupied conduction band (CB), allows transfer of electrons from soot to the catalyst, and when the empty molecular orbitals of O_2 must be level with the occupied valence band to ensure transfer from the solid. Thus, the electronic property is essential in oxidation reaction (Piumetti et al. 2016c).

A stepwise reaction undergone during soot oxidation is given in **Equation (2.7)-Equation (2.10)**. Initially, when catalyst comes into contact with gaseous oxygen, it gets adsorbed on its surface **Equation (2.7)**. Further the reaction between the adsorbed oxygen and carbon results in active intermediate, **Equation (2.8)**. This intermediate reacts with either adsorbed oxygen or gaseous oxygen and forms CO_x and leave active C site on soot, **Equation (2.9 and 2.10)** (Shangguan et al. 1997).



Soot reduces ceria at the interface between carbon and catalyst surface results in CO₂ formation. Gaseous O₂ refilled on oxygen vacancies reacts with reduced ceria and forms superoxides/peroxides. The active oxygen migrates to the carbon surface and reacts to form CO₂ efficiently. A new contact point between soot and ceria is established, and the cycle repeats (Soler et al. 2016).

2.6 CONCLUSION

From the literature review, the following inferences are obtained:

- Properties of materials are influenced by the synthesis method adopted. Apart from that, the calcination temperature also controls the structural properties and thus, modifies the reaction condition of the sample.
- A single synthesis method is essential for better comparison of the catalytic activity. Thus, EDTA-Citrate method is a potential synthesis method that can be adopted for this study.
- A detailed study on single metal oxide as catalysts for soot oxidation activity is necessary as per the preliminary literature search. Since, with the variation in nature metal oxide, properties that affect structural features may differ.
- Doping of ceria lattice with the metal such as rare earth and transition metal oxides improves the catalytic activity for soot oxidation. The influence of binary metal oxides over whole composition range is still not yet reported for soot oxidation, and the variation in properties with the different composition can be studied in detail. The optimum composition of metal oxide is critical to study.
- The binary metal oxides with fixed composition and different dopant metal can be studied to confirm the active dopant for ceria-based metal oxides.
- Ternary dopant addition on binary metal oxide may result in improved catalytic activity due to the multiple active sites influence on ceria lattice that has potential in improving redox properties and oxygen diffusion within the sample. Thus, the highest catalytic activity is expected for these samples.
- Alkali, alkaline earth and noble metals are reported to show enhanced activity due to higher electropositivity, lower sintering temperature and higher mobility that

enhance contact points for soot oxidation. These metal oxides are potential in studying as quaternary metal oxide dopants.

As per the conclusions are drawn from the literature survey the objectives of this research are guided. Formulated objectives address few issues of importance specifically to improve the ceria-based materials catalytic activity for soot oxidation activity and are presented in **Chapter 1**.

The detailed synthesis steps, characterization techniques adopted for analysing the synthesized metal oxides and the soot oxidation reaction conditions are outlined in the next chapter.

CHAPTER 3

MATERIALS AND METHODS

Single metal oxide samples and binary, ternary and quaternary ceria-based metal oxide samples used in this study are synthesized using the EDTA-Citrate method. Further, the synthesized metal oxides are characterized using various characterization techniques and adopted as a catalyst for soot oxidation reaction.

3.1. SYNTHESIS OF CERIA-BASED CATALYSTS

In this work, ceria-based nano-materials are synthesized using the EDTA-Citrate complexing method (Prasad et al. 2012b). The EDTA-Citrate method has the advantage above other synthesis methods due to the selective chelating agents added during the synthesis that quickens the reaction into completion in a single step. The energy requirement for the reaction is lesser for these reactions. The chelating agents added during the process are citric acid as primary chelating agent and EDTA (Ethylene Diamine Tetra Acetic acid) as the secondary chelating agent with higher complexing ability. The metal ion chelates with the chelating agent and forms metal complex during the reaction. EDTA-Citric acid-metal complex is highly stable due to the formation of 5-membered strong ring structure during the synthesis. Unbound metal ions are reduced during the synthesis that confirms homogeneous precursor solution and thus confirms metal binding into solution. The metal complex chelate undergoes a polyesterification reaction in further that result in the polymeric glass with metal ions uniformly distributed. Despite the nature of metal ions, they form a cage-type complex with EDTA resulting in molecular level metal ion mixing. Similarly, citric acid can also form the metal complex with different metal ions. The metal-EDTA complex is immobilised with the help of secondary chelation of citric acid with the metal ions.

Various metal nitrate precursor salts used for synthesis of corresponding metal oxides are Cerium nitrate hexahydrate $[\text{Ce}(\text{NO}_3)_3 \cdot 6\text{H}_2\text{O}] \geq 99\%$ (SRL chemicals), Stannous chloride dehydrate ($\text{SnCl}_2 \cdot 2\text{H}_2\text{O}$) 98% (Loba), Praseodymium nitrate hexahydrate $[\text{Pr}(\text{NO}_3)_3 \cdot 6\text{H}_2\text{O}]$ 99.9% (Sigma), Gadolinium nitrate hexahydrate $[\text{Gd}(\text{NO}_3)_3 \cdot 6\text{H}_2\text{O}]$ 99.9% (Sigma), Lanthanum nitrate hexahydrate $[\text{La}(\text{NO}_3)_3 \cdot 6\text{H}_2\text{O}]$ 99% (Sigma), Zirconyl nitrate hydrate $[\text{ZrO}(\text{NO}_3)_2 \cdot 6\text{H}_2\text{O}]$ 99.5% (Acros), Hafnium chloride (HfCl_4) (Aldrich), Manganese nitrate hydrate 98% $[\text{Mn}(\text{NO}_3)_2 \cdot x\text{H}_2\text{O}]$ (Sigma) and Samarium nitrate hexahydrate $[\text{Sm}(\text{NO}_3)_3 \cdot 6\text{H}_2\text{O}]$. EDTA (Ethylenediaminetetraacetic acid) and Citric acid were used as chelating agents. Ammonium hydroxide solution NH_4OH (25% ammonia) (spectrum reagents) is used to adjust the pH. Initially, the stoichiometric amounts of metal nitrate were dissolved in a specific amount of distilled water. The pre-calculated quantity of EDTA is mixed with the metal nitrate solution under stirring and further dissolved using NH_4OH solution. In further, the stoichiometric quantity of citric acid is added to the metal-EDTA solution. The mole ratio of total metal ions to EDTA and citric acid was 1:1:1.5. The final solution of pH is maintained at ~ 9 by adding NH_4OH solution, and the solution is heated at 100°C along with stirring. The resulting gel obtained by thickening the solution is further heat-treated in an oven at 150°C for 24 h which results in a solid precursor. It is further undergone two-stage calcination at 350°C for 12h and 600°C for 5h in a muffle furnace to obtain the final metal nano-powder product. The schematic representation of the synthesis method is as shown in **Figure 3.1**.

$\text{Ce}_{0.9}\text{Ge}_{0.1}\text{O}_2$ (GDC) sample was synthesized using the Solvothermal method to compare the activity with EDTA-Citrate sample. A stoichiometric amount of respective metal chloride precursor salts were mixed with 4% octadecylamine dissolved in ethanol solution under continuous stirring condition. Ethylenediamine was added to the obtained solution to regulate the viscosity and to adjust the pH ($\sim 9-10$). Once the mixture is completely dissolved, the solution was transferred to a 500 ml Teflon-lined autoclave and sealed. A solid solution was obtained by heating the solution in the autoclave at $150^\circ\text{C}/72$ h. The solid precursor was calcined at $600^\circ\text{C}/5$ h (Sun et al. 2005).

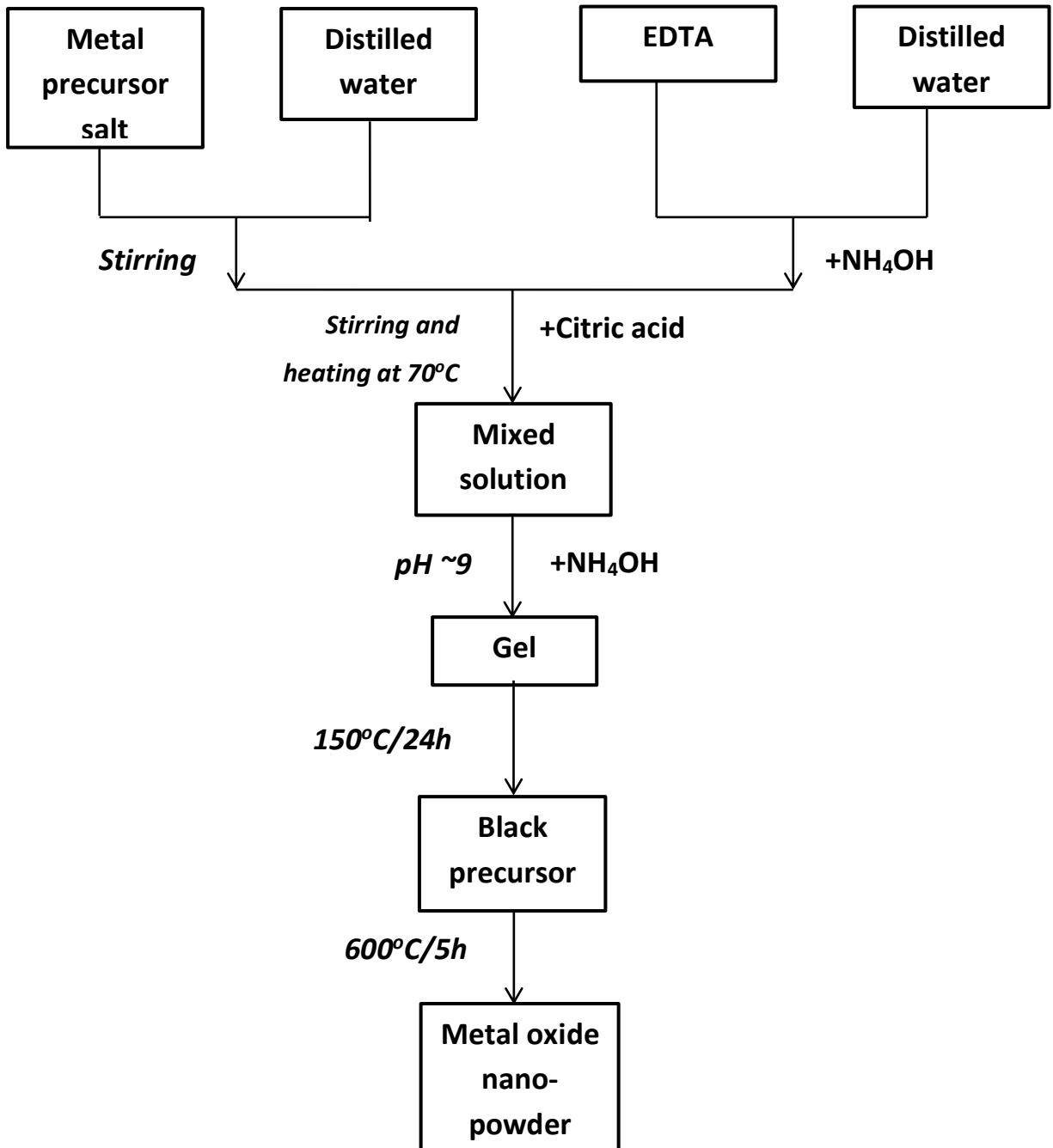


Figure 3.1: EDTA-Citrate method synthesis procedure

The metal oxide samples synthesized were characterized using various characterization techniques such as X-Ray Diffraction (XRD) to understand the sample crystallinity, to identify phase of formation and calculate lattice parameters, Brunauer-Emmett-Teller (BET) Surface area to find the surface area available for the reaction, Pore volume analysis to find the pore volume on the sample surface, Raman spectroscopy to understand the metal-oxygen bonding and to identify secondary phase, Scanning Electron Microscopy (SEM) and Transmission Electron Microscopy (TEM) to analyse morphological details of the samples, UV-Vis Diffusive Refractive Spectroscopy (UV-Vis DRS) to calculate the bandgap values of the samples and X-ray Photoelectron Spectroscopy (XPS) to calculate the metal oxidation state, reducibility and surface oxygen concentration of the sample. The obtained metal oxides are adopted as a catalyst for soot oxidation activity using standard soot.

3.2. PHYSICAL CHARACTERIZATION

The various characterization tools adopted in this study are explained here:

3.2.1. X-Ray Diffraction (XRD)

Bulk composition along with the crystalline structure of the nanomaterials is identified using XRD technique. Elastic scattering of X-rays by electrons (Thomson scattering) leads to electron-like Hertz dipole oscillation at the incoming beam frequency, which is the dipole radiation source. The x-ray diffraction structural investigations are undergone using the Thomson component of x-rays. XRD measurement was done using XPERT Pro diffractometer with operating parameters of 20-80° 2θ range, 0.02 step size and 2s as step time at 40 kV and 30 mA. The radiation source used for the X-ray Diffraction (XRD) measurement was Cu Kα (0.154 nm). Debye-Scherrer equation given in **Equation (3.1)** was used to calculate the crystallite size (D) of the material.

$$D = \frac{0.94\lambda}{\beta \cos\theta} \quad (3.1)$$

Where, λ is the x-ray wavelength, β is the line width in radians and θ is the Bragg angle relative to the primary x-ray.

$$d_{hkl} = \frac{a}{\sqrt{h^2 + k^2 + l^2}} \quad (3.2)$$

Lattice constant (a) is calculated using **Equation (3.2)** for cubic lattices. This relation is developed based on the consideration that the interplanar spacing (d_{hkl}) depends on the Miller indices (h,k,l) and unit cell parameter a .

$$2d_{hkl} \sin \theta = \lambda \quad (3.3)$$

Equation (3.3) is called the Bragg equation, where λ is the x-ray wavelength and θ is the Bragg angle relative to the primary x-ray. The generalisation is easily performed by just inserting the interplanar spacing d_{hkl} of the crystal lattice under investigation (Mario Birkholz 2006). The lattice strain (ϵ) of the samples are calculated from the corresponding diffraction peak as given in **Equation (3.4)**.

$$\epsilon = \frac{\beta}{4 \tan \theta} \quad (3.4)$$

The reactive facet plane is quantitatively analysed by intensity ratios of the corresponding peaks in the XRD spectrum. The intensity ratio of (200)/(111) is calculated as the ratio of the intensity of (200) peak to the intensity of (111) peak obtained from XRD spectrum. Similarly, (220)/(111) intensity ratio is calculated as the ratio of the intensity of (220) and (111) peaks, respectively obtained from XRD spectrum.

3.2.2. Brunauer-Emmett-Teller (BET) Surface area

Quantitative analysis of surface area was undergone using SMARTSORB-92/93 instrument operating at 230 V AC and 50 Hz. Single point Brunauer-Emmett-Teller (BET) method using N₂ physisorption technique is used to analyse the surface area of the sample. Initially, the sample is regenerated for 60 min at 200 °C to remove the adsorbed gases and moisture. N₂ in the gas mixture (30% N₂ and 70% helium) gets adsorbed as a single molecular layer on the surface of the sample while passing it through the sample. The adsorption isotherm is obtained by measuring the gas adsorbed across a wide range of relative pressure at a constant

temperature of 77K. The adsorbed N₂ was allowed to desorb, and the volume of nitrogen adsorbed is obtained from the isotherm was used in single point BET equation based on Brunauer-Emmett-Teller theory to calculate the surface area of the sample (Hwang and Barron 1987). The BET equation used to calculate the surface area is given in **Equation (3.5)**

$$\frac{1}{X\left[\left(\frac{P}{P_0}\right)-1\right]} = \frac{1}{X_m C} + \frac{C-1}{X_m C} \left(\frac{P}{P_0}\right) \quad (3.5)$$

Where X is the weight of nitrogen adsorbed at a given relative pressure (P/P₀), X_m is related to the volume of gas adsorbed at STP, which is the monolayer capacity, and C is constant.

Particle size is calculated using the BET surface area is expressed by **Equation 3.6**.

$$\text{Particle size from BET surface area} = \frac{6}{\rho \times \text{BET Surface area}} \quad (3.6)$$

Where ρ is the density of the metal oxide.

The degree of agglomeration is calculated as the ratio of particle size calculated using BET surface area and crystallite size (D) calculated using the Scherrer equation from XRD (Ayastuy et al. 2010).

3.2.3. Raman spectroscopy

Information about the nanocrystalline microstructures can be obtained from Raman spectroscopy due to its interaction between ions. Identification of chemical structure and physical form of samples are undergone using Raman spectroscopy, along with that the characteristic spectra features identify the substances of a sample, and to calculate the amount of substance quantitatively or semi-quantitatively in a sample. Bruker: RFS 27 model Raman spectrometer was used to measure the Raman spectra of the samples using a conventional backscattering geometry with a charged-couple device (CCD) detector consisting of a triple polychromator. Diode laser source used is of

the near-infrared 785nm laser with a nominal output of 12.5 mW. As the light interacts with the molecule, virtual sites that are of short-lived states are formed by polarising the electron cloud around the nuclei. These unstable state results in photon re-radiation and this energy changes are detected by vibrational spectroscopy (Mukherjee et al. 2017; Smith and Dent 2005). Using the obtained Raman spectra, the relative oxygen concentration is calculated from the ratio of the intensity of oxygen vacancy peak to the intensity of the fluorite peak of CeO₂.

3.2.4. Scanning Electron Microscopy (SEM)

Morphology and size of the materials are analysed by using electron microscopy. When a primary electron beam is bombarded on a specimen, secondary or backscattered electrons are created. Morphological analyses of the samples are obtained from SEM analysis. SEM of the samples is analysed in a CARL ZEISS SIGMA instrument for the microstructural and compositional analysis of the samples. Before the analysis sputtering was undergone. Due to electron vacancy created during the electron ejection from the atom, an x-ray is emitted to balance the energy difference created in the atom (Voutou and Stefanaki 2008; Zaera and Ma 2006).

3.2.5. Transmission Electron Microscopy (TEM)

The basic operation of TEM is that when the electron beam falls on a thin specimen, it penetrates through it without any interaction and then appropriate lens helps in imagining the sample. Ultrastructure and crystal defects of the metals can be evaluated using TEM analysis. Diffraction is created during the interaction of electron by crystal, and the crystal lattice information is obtained by the patterns of spots created on the screen during the diffraction. High-resolution Transmission Electron Microscopy (TEM) of the samples are analysed in Joel/JEM 2100. Particle size is calculated from suitable TEM image by fitting histogram plot of the particle size and counts by Gaussian peak fitting.

3.2.6. UV-Vis Diffuse Reflectance Spectroscopy (UV-Vis DRS)

Spectroscopy in the electromagnetic region of ultraviolet (UV), visible (Vis) and near-infrared (NIR) aids in transferring electrons from low energy to high energy or molecular orbitals when the material is irradiated with light is called as electronic spectroscopy. Diffuse Reflectance Spectroscopy can analyse the material in the range of visible to near-infrared (400-2500 nm) and mid-infrared range (2500-25000 nm) (Weckhuysen 2004). Diffuse reflected light from the solid sample can be collected using DRS technique which gives information about the outer shell orbital electron of the metal. The UV-Vis DRS measurements were performed over the wavelength range 200–800 nm, using a UV-Vis NIR spectrometer (Cary 5000) with an integration sphere diffuse reflectance attachment. From the absorbance data obtained from UV-Vis DRS spectra, a plot is made between $(h\nu)$ Vs $[(\alpha h\nu)^2]$ moreover, the x-axis intercept is obtained as the optical bandgap value.

3.2.7. X-ray Photoemission Spectroscopy (XPS)

The chemical state of the dopant and host ions on the surface, quantity surface composition, surface adsorbed oxygen species concerning lattice oxygen and weakly bonded oxygen species that is having a direct relationship with OSC were studied using XPS technique. Irradiation of sample with monoenergetic x-rays results in electron emission due to the surface interaction by the photoelectric effect. The kinetic energy of the emitted electron is analysed. Each element has a unique elemental spectrum. The electron binding energy versus a number of electrons is obtained as the spectrum of the sample. The peak height and area under each peak can be used for quantitative analysis of the sample; peak position and peak separation values can find the elemental chemical states. A monoenergetic soft X-ray is irradiated on the sample, the energy of emitted electrons are investigated. XPS analysis was performed in Omicron ESCA+ instrument under ultra-high vacuum condition using Al K α (1486.6 eV) excitation anode source (25 W and 15kV) with a background pressure of 6.7×10^{-8} Pa. An X-ray spot size of 100 μm diameter and energy calibration scale of C1s core level peak at 284.6 eV was used for the analysis. Shirley background subtraction and Gaussian-Lorentzian peak fitting were done

for all core level spectra for deconvolution of peaks using Casa XPS software (Wagner et al. 1978). The Ce reducibility ratio is calculated using **Equation 3.7** and the oxygen concentration using **Equation 3.8**. The ratios are represented as a percentage and compared with other samples.

$$\text{Ce reducibility ratio} = [\text{Ce}^{3+} / (\text{Ce}^{3+} + \text{Ce}^{4+})] \quad (3.7)$$

$$\text{Oxygen concentration} = [\text{O}_\beta / (\text{O}_\alpha + \text{O}_\beta + \text{O}_\gamma)] \quad (3.8)$$

3.2.1. Thermogravimetric Analyser (TGA)

Thermogravimetry Analysis (TGA) is a thermal analysis technique in which the weight loss of the sample is examined with as a function of time (constant temperature) or increasing temperature (constant heating rate), in a specified environment is programmed. The gas environment can be well maintained within the instrument during the experiment. The physical or chemical properties of the materials can be monitored with temperature. The micro-thermobalance measures the weight changes in the sample mass due to adsorption of oxygen, thermal degradation, oxidation or other heterogeneous reactions. Weight loss analysis of the sample is undertaken in a TGA instrument (TG/DTA 6300) over a temperature range of 30-650°C at 10°C/min heating rate using 100 ml/min flow of air.

3.3 SOOT OXIDATION ACTIVITY

Soot oxidation reaction was undergone by using widely adopted standard soot (PrintexU, Orion Engineered Chemicals Ltd. (“Printex ® U Properties Unit” 2009)). The synthesized metal oxide samples are used as catalysts. The mixture of soot and catalyst at a weight ratio of 1:4 was mixed in a mortar and pestle for 30 min under a tight contact condition (Krishna et al. 2007). The sample was preheated at 200°C to remove the bound moisture in the sample mixture. The oxidation reaction is undergone in a TG-DTA 6300 Thermo Gravimetric analysis (TGA) instrument using air as a purge gas at a flow rate of 100 ml/min, heating at a rate of 10°C/min, from room temperature to 600°C. Weight loss of soot with time is analysed from the TG data, and it is converted regarding conversion (%). T₅₀ (temperature at which 50% conversion is observed) temperature was obtained from the graph and used further to compare different catalyst samples. The weight loss obtained from TGA is converted regarding conversion by applying **Equation (3.6)**.

$$\text{Conversion (\%)} = \frac{\text{Initial weight} - \text{weight at any instance}}{\text{Initial weight} - \text{Final weight}} \times 100 \quad (3.6)$$

The repeated cycle was undergone to confirm the repeatability of the sample.

CHAPTER 4

STUDY ON SINGLE METAL OXIDES

Before the study on multi doping effect of ceria-based metal oxides; the synthesis method to be adopted for the development of all metal oxide needs to be fixed. Since the synthesis method affects the activity significantly due to variation in surface structure, weakly bound oxygen, reactive planes and reducibility that has potential in modifying the catalytic activity for soot oxidation. The descriptor that varies with the variation in synthesis method is initially studied. In further, the single metal oxides that can potentially be adopted along with CeO₂ are analysed and tested for soot oxidation activity. Based on the single metal oxide study, the descriptors that are intrinsic to metal cation can be concluded. This can help in selecting the possible dopant for future research on multi doping effect on ceria lattice.

Depnding upon the synthesis method adopted, both intrinsic (oxygen availability) and extrinsic (surface contact points) descriptors control the catalytic activity. The various properties calculated for GDC sample synthesised using EDTA-Citrate method and solvothermal method is given in **Table 4.1** and **Table 4.2** (Anantharaman et al. 2018a). From the data it is evident that GDC synthesised by EDTA-Citrate method is a promising synthesis method that can be adopted for ceria-based metal oxides, due to better surface properties that enhance surface oxygen mobility. Since it is essential to find the primary descriptor that controls the catalytic activity, the descriptor that is potentially involved due to synthesis method, such as, precursor salt, reaction conditions and calcination temperature is limited in the further study by adopting a single synthesis method of EDTA-Citrate complexing method (Anantharaman et al. 2018a).

Table 4.1: Crystallite size, lattice strain, BET Surface area, pore volume, particle size and intensity ratios of GDC samples synthesized by different methods (Anantharaman et al. 2018a)

Synthesis method	Crystallite size ^a (nm)	Lattice strain ^b	BET surface area (m ² /g)	Pore volume (cm ³ /g)	Intensity ratio ^c (%)	
					(200)/(111)	(220)/(111)
EDTA-Citrate	10	0.015	45	0.0601	34.2	51.2
Solvothermal	26	0.006	43	0.0530	30.8	45.4

^a- Calculated from intense XRD peak using Debye-Scherrer equation; ^b- Calculated from intense XRD peak and ^c- Calculated from intensity ratio of XRD

Table 4.2: I_{ov}/I_{F2g} , composition, particle size, bandgap, reducibility ratio, ($O_{\beta} / (O_{\alpha} + O_{\beta} + O_{\gamma})$), and T_{50} of GDC samples (Anantharaman et al. 2018a)

Synthesis method	I_{ov}/I_{F2g} ^a (%)	EDS Composition (%)		Particle size ^b (nm)	Band gap ^c (eV)	Ratio of reducibility ^d (%)	O_{β} binding energy ^e (eV)	T_{50} ^f (°C)
		Ce	Gd					
EDTA-Citrate	9.5	90	10	10.3	2.99	45.4	528.8	468
Solvothermal	8.7	91	9	24.8	3.13	31.2	529.1	500

^a- Calculated using intensity ratio of Raman peak; ^b- Calculated using TEM image; ^c- Calculated using Tauc's plot; ^d- Calculated using Ce 3d XPS peak; ^e- Calculated using O 1s XPS peaks and ^f- Temperature at 50% conversion of soot occurs

4.1 SINGLE METAL OXIDES

From the fundamental study of synthesis method, EDTA-Citrate method is used for the synthesis of all metal oxides in further. The study by Neeft et al. (1996) proved that a large number of metal oxides under tight contact condition are active for soot oxidation (Neeft et al. 1996). To understand the reaction mechanism variation with the change in dopant metal and dependency of another descriptor on catalytic activity, single metal oxide study is adopted. Also, the potential catalyst that can be used as dopant materials for the ceria-based catalyst is also resolved. Thus, a series of single metal oxides are selected in such a way that, few are having multiple oxidation states (redox) and other show single oxidation state (non-redox). Single redox metal oxides (CeO_2 , SnO_2 , Pr_6O_{11} and Mn_3O_4) and non-redox metal oxides (Gd_2O_3 , La_2O_3 , ZrO_2 , HfO_2 and Sm_2O_3) are synthesized using the EDTA-Citrate complexing method. The characterization of the metal oxide is carried out using XRD, BET surface area, pore volume analyser, SEM, TEM, UV-Vis DRS and XPS. The obtained results are illustrated and discussed further. The soot oxidation activity of all metal oxides are analysed under tight contact conditions, and the effect of different parameters on activity is further studied in detail.

4.1.1 X-ray Diffraction (XRD) Analysis

Structural properties of all the metal oxides are initially analysed using XRD analysis. **Figure 4.1** demonstrates the XRD patterns of the synthesized single metal oxides. From the XRD patterns of CeO_2 and SnO_2 samples, all the major peaks related to cubic fluorite structure (Atribak et al. 2008) and tetragonal structure (Chen et al. 2008) are noticeable, respectively. Pr_6O_{11} and Mn_3O_4 correspond to tetragonal structure (Li et al. 2013). Gd_2O_3 samples revealed major peaks that are related to the cubic fluorite structure (Du et al. 2015; Khan et al. 2014).

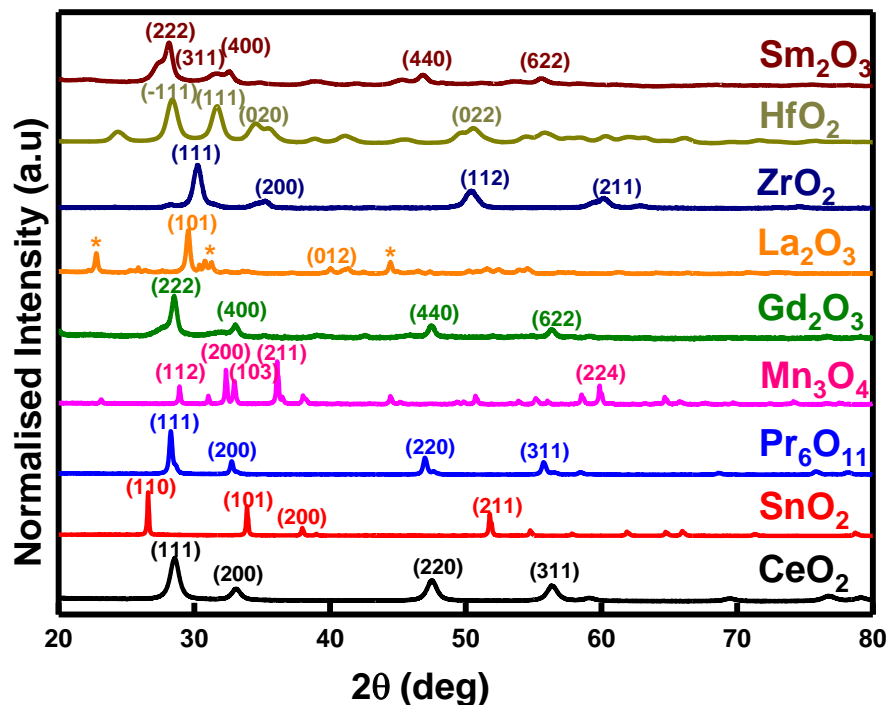


Figure 4.1: XRD pattern of single metal oxides calcined at 600°C/5h.
(* indicates $\text{La}_2\text{O}_2\text{CO}_3$)

La_2O_3 sample showed hexagonal structure (with (101) and (012) planes) along with some impurity in the monoclinic phase corresponding to lanthanum oxycarbonate ($\text{La}_2\text{O}_2\text{CO}_3$). One reason for the impurity phase formation might be due to continuous exposure of the sample in the air atmosphere since La_2O_3 sample is highly unstable in an air atmosphere and can readily adsorb CO_2 and transform into an impurity phase (Ghiasi and Malekzadeh 2015; Neeft et al. 1996). ZrO_2 sample displayed peaks corresponding to the tetragonal structure from XRD plot (Keramidas and White 1974). Similarly, HfO_2 shows their characteristic peaks corresponding to the monoclinic structure (Ho et al. 2003) and Sm_2O_3 sample confirms the cubic phase from the peaks obtained (Sun et al. 2007). Except for La_2O_3 sample, all other samples demonstrated corresponding metal oxides and

didn't contain any impurities. The impurity presence in La_2O_3 may affect its activity since the active sites availability due to impurity presence can act as intermediate and thus aid or suppress the activity.

Table 4.3 shows the physical properties of the metal oxides related to phases, lattice constant (a) (\AA), crystallite size (D) (nm), BET surface area (m^2/g), pore volume, particle size (nm) calculated from BET Surface area, lattice strain (ϵ) and degree of agglomeration (ϕ). For the metal oxides, the crystallite size is in the range of 7-56 nm in which Sm_2O_3 sample showed lowest crystallite size (~ 7 nm) and SnO_2 showed highest crystallite size (~ 56 nm). CeO_2 sample showed the highest surface area (~ 41 m^2/g) and SnO_2 showed the lowest surface area (~ 0.8 m^2/g). The surface area of all other samples is within this range. Pore volume in the range of $0.0006 \sim 0.0552$ cm^3/g , lowest for SnO_2 and highest for Gd_2O_3 .

The particle size calculated from the BET surface area of samples lie in the range of 1107 \sim 19 nm with SnO_2 having the largest and CeO_2 with the lowest value. The particle size of all other sample is within this range. The lattice strain values of the samples vary from 0.002 \sim 0.02. Highest strain value is obtained for Sm_2O_3 , and the lowest value is for Gd_2O_3 . The particle size calculated from the BET surface area is larger than the crystallite size calculated from the XRD peaks. This reflects that the particles are agglomerated, and the degree of agglomeration (ϕ) (ratio of crystallite size obtained from XRD and the particle size obtained from BET surface area) is in the range of 2 \sim 36, which indicates that all the samples are agglomerated. The lowest and highest degree of agglomeration is obtained for CeO_2 and La_2O_3 samples, respectively.

Table 4.3: Crystallographic parameters, BET surface area, pore volume, particle size, lattice strain and degree of agglomeration of single metal oxides calcined at 600°C/5h

Metal oxide	Phase	Lattice constant ^a (Å)	Crystallite size ^b (nm)	BET Surface area (m ² /g)	Pore volume (cm ³ /g)	Particle size ^c (nm)	Lattice strain ^d (ε)	Degree of agglomeration ^e (φ)
CeO ₂	Cubic	a=b=c=5.4	10.6	41.2	0.0545	17	0.0125	2
SnO ₂	Tetragonal	a=b=4.7 c=3.2	55.9	0.8	0.0006	1107	0.0028	20
Pr ₆ O ₁₁	Cubic	a=b=c=5.5	28.5	3.6	0.0059	221	0.0052	8
Mn ₃ O ₄	Tetragonal	a=b=5.5, c=10.1	46.9	1.8	0.0067	652	0.0025	14
Gd ₂ O ₃	Cubic	a=b=c=10.8	16.3	4.6	0.0552	177	0.0092	11
La ₂ O ₃	Hexagonal	a=b= 4.1, c=5.8	29.9	0.9	0.0033	1084	0.0054	36
ZrO ₂	Tetragonal	a=b=5.1, c= 5.2	12.3	7.2	0.0245	147	0.0112	12
HfO ₂	Monoclinic	a=5.1 b=5.2 c=5.2,β=99.1°	9.6	21.1	0.0392	30	0.0157	3
Sm ₂ O ₃	Cubic	a=b=c=11.1	7.2	8.4	0.0514	95	0.0190	13

^a- Calculated from XRD using Miller indices and Bragg's equation; ^b- Calculated from intense XRD peak using Debye-Scherrer equation; ^c- Calculated from BET Surface area; ^d- Calculated from intense XRD peak and ^e- Calculated as the ratio of Particle size and crystallite size

The influence of surface area and crystallite size on the soot oxidation activity of these metal oxides will be discussed later. In general, with the increase in surface area, the active sites for the catalytic activity also increases thus showing an enhancement in the catalytic efficiency (Liang et al. 2007). This statement may not hold good for all the catalytic reactions, in some cases like soot oxidation, the surface area may or may not be the key factor that affects the catalytic activity. Thus it is critical to comprehend the fundamental properties which profoundly influence the soot oxidation conversion (Aneggi et al. 2012). The metal oxides synthesized have a broad range of surface area which can be due to specific surface nature. The pore volume of the sample is relatively low compared to other reported values (Krishna et al. 2007).

4.1.2. Scanning Electron Microscopy (SEM) Analysis

SEM analysis helps in understanding the surface structure of these metal oxides. **Figure 4.2** illustrates the morphology of CeO_2 , Pr_6O_{11} , Mn_3O_4 , ZrO_2 , HfO_2 and Sm_2O_3 samples. SEM image in **Figure 4.2 (a)** for CeO_2 has flaky agglomerates (Zhang et al. 2016) and whereas from **Figure 4.2 (b)** Pr_6O_{11} sample have ovoid agglomerates with spherical particles (Chellappan and Sanjeeviraja 2014). Mn_3O_4 (Chudobova et al. 2013) sample displayed spherical agglomerate structure as shown in **Figure 4.2 (c)**. ZrO_2 SEM micrograph from **Figure 4.2 (d)** has a plate-like agglomerate structure (Nezhad et al. 2013). From **Figure 4.2 (e)** of HfO_2 also (Nezhad et al. 2013), the plate-like agglomerated structure is evident. **Figure 4.2 (f)** shows micrograph of Sm_2O_3 as aggregated particles.

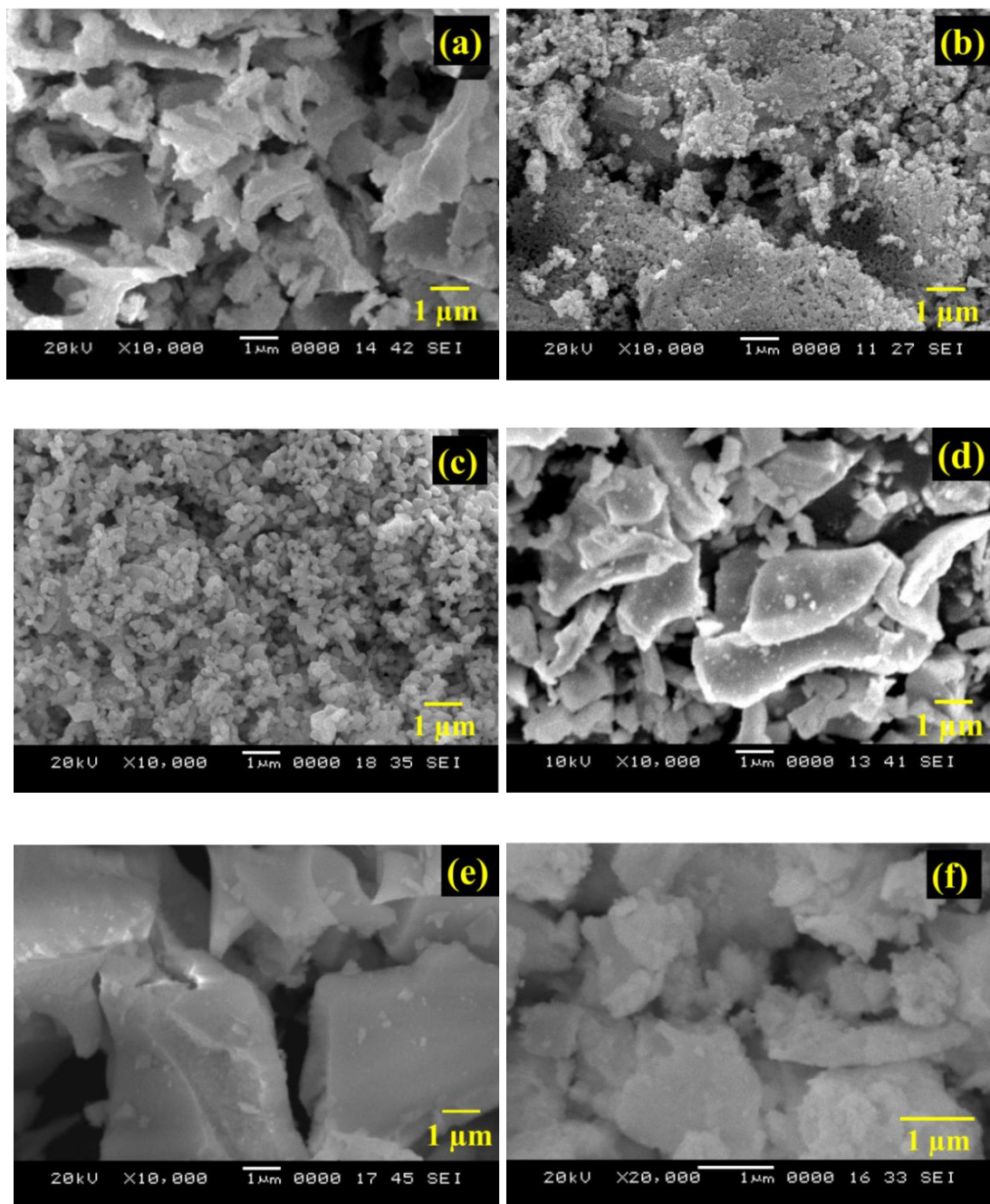


Figure 4.2: SEM micrographs of (a) CeO₂, (b) Pr₆O₁₁, (c) Mn₃O₄, (d) ZrO₂, (e) HfO₂ and (f) Sm₂O₃ samples calcined at 600°C/5h

4.1.3. Transmission Electron Microscopy (TEM) Analysis

Figure 4.3 depicts the TEM image of CeO₂ sample. The nanoparticle size in **Figure 4.3 (a)** TEM image is within the range of 6 ~ 11 nm. The interplanar distance obtained from the HR-TEM image (**Figure 4.3 (b)**) is 3.13 Å, and it corresponds to (111) plane of CeO₂ sample. The average particle size is ~11 nm for CeO₂ sample (Crystallite size from XRD, D= 11.7 nm). **Figure 4.3 (c)** depicts the SAED pattern in which each ring corresponds to each plane and their interplanar distance matches with the corresponding planes in XRD results (Kumar et al. 2013). **Figure 4.4** demonstrates the TEM morphology of La₂O₃ sample. From **Figure 4.4 (a & b)**, it is tough to identify the nano-particle nature, and from XRD patterns (**Figure 4.1**) of La₂O₃ sample it hints that the impurity phase (La₂O₂CO₃) dominates the morphology (**Figure 4.4 (a & b)**) of La₂O₃ sample. The SAED patterns (**Figure 4.4 (c)**) Bragg spots instead of rings which confirms the impurity in La₂O₃ as observed in XRD results.

4.1.4 . X-ray Photoemission Spectroscopy Analysis

4.1.4.1. Redox metal oxides

The surface elemental analysis and oxidation state can be identified effectively using XPS analysis (Mukherjee et al. 2016). The redox samples (CeO₂, SnO₂, Pr₆O₁₁ and Mn₃O₄) are analysed by XPS analysis to determine the multiple oxidation states and O1s bonding. **Figure 4.5** and **Figure 4.6** shows metal spectra of Ce 3d, Sn 3d, Pr 3d and Mn 2p and O1s spectra of CeO₂, SnO₂, Pr₆O₁₁, and Mn₃O₄, respectively. All the peaks are fitted using Gaussian profiles, and C corrected using CasaXPS. Ce 3d peak in **Figure 4.5 (a)** shows a broad range of spectrum confirming multiple oxidation states. Designation of 3d_{3/2} and 3d_{5/2} indicates two sets of spin-orbital contributions that are represented in the figure as u and v respectively. The peaks shown as u', u, v'', v' and v corresponds to Ce⁴⁺ oxidation state and u₀, and v₀ corresponds to Ce³⁺ oxidation states (Mukherjee et al. 2016). These peaks confirm the presence of multiple oxidation states of Ce (Damyanova et al. 2008).

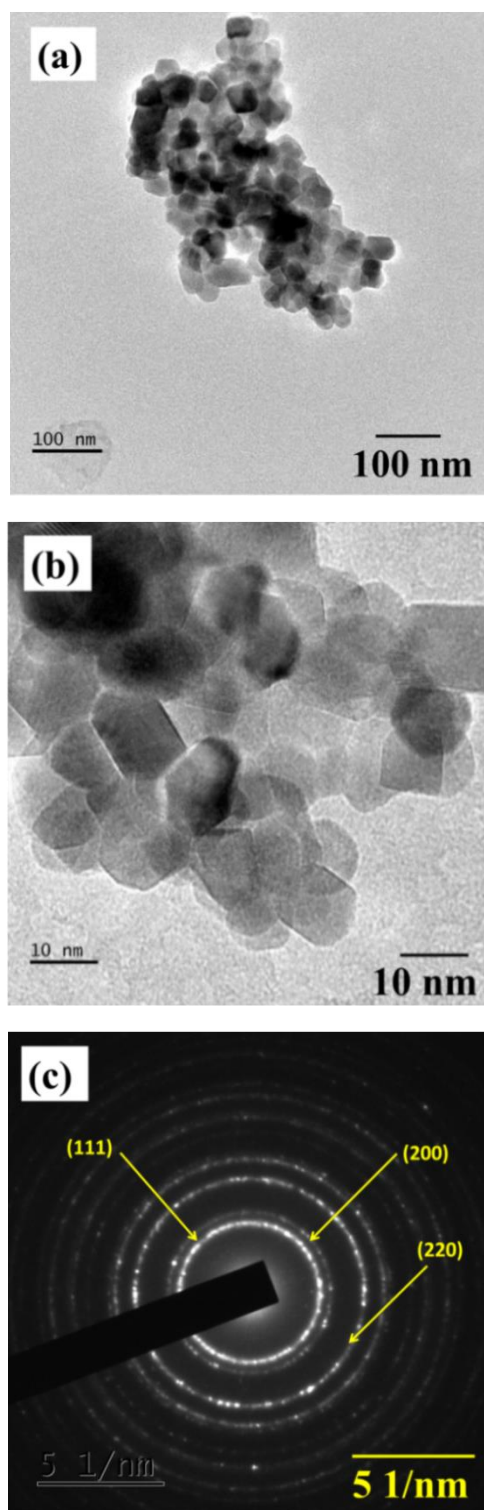


Figure 4.3: (a) TEM, (b) HR-TEM image and (c) SAED pattern of CeO₂

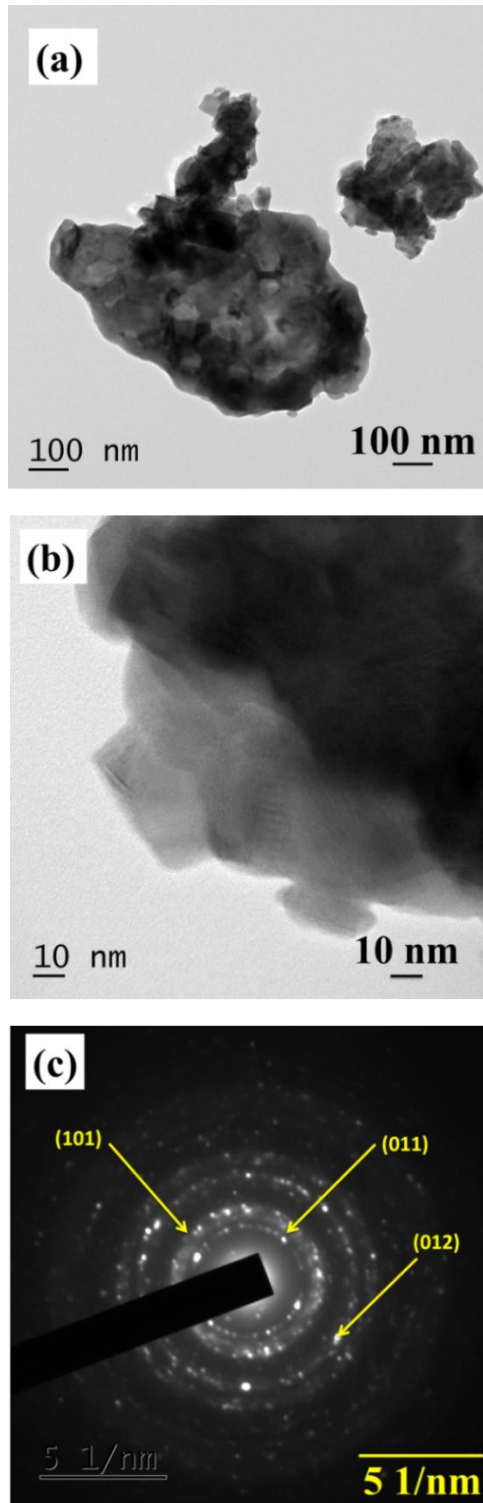


Figure 4.4: (a) TEM, (b) HR-TEM image and (c) SAED pattern of La_2O_3

Peaks in **Figure 4.5 (b)** depicts the XPS peaks of SnO₂ sample and the peaks corresponding to 3d_{3/2} and 3d_{5/2} at 495 and 486 eV, respectively represent Sn⁴⁺ oxidation state and shoulder peaks at 494, and 485 eV corresponds to Sn²⁺ oxidation state (Ayastuy et al. 2014). Similarly, for Pr₆O₁₁ sample (**Figure 4.5 (c)**), the presence of 3d_{3/2} and 3d_{5/2} spin orbitals at 934 and 950 eV represent the Pr⁴⁺ oxidation state and the shoulder peaks at 929 and 955 eV represent Pr³⁺ oxidation state. Corresponding binding energy confirms the existence of Pr₆O₁₁ in different oxidation state as Pr^{3+/4+} (Mukherjee et al. 2016). From **Figure 4.5 (d)**, the XPS plot of Mn₃O₄ sample confirms the multiple Mn oxidation states (Mn²⁺, Mn³⁺ and Mn⁴⁺). The 2p_{1/2} and 2p_{3/2} peaks at 652 and 640 eV corresponds to Mn³⁺, and the shoulder peaks at 650 and 639 eV corresponds to Mn⁴⁺ and Mn²⁺, respectively (Zhan et al. 2015). From the XPS data, it can be confirmed that the selected metal oxides exist in multiple oxidation states.

The ratio of $(\text{Ce}^{3+} / (\text{Ce}^{3+} + \text{Ce}^{4+}))$, $(\text{Pr}^{3+} / (\text{Pr}^{3+} + \text{Pr}^{4+}))$, $(\text{Sn}^{2+} / (\text{Sn}^{2+} + \text{Sn}^{4+}))$ and $(\text{Mn}^{3+} / (\text{Mn}^{4+} + \text{Mn}^{3+} + \text{Mn}^{2+}))$ indicate the reducibility ratio of the redox sample, and it is calculated from the XPS plots by integrated areas under lower oxidation state to that of the total area of all the peaks. The area ratio for the redox samples (RM \equiv CeO₂, SnO₂, Pr₆O₁₁ and Mn₃O₄) are given in **Table 4.4**. From this data, it is evident that the Mn₃O₄ sample has a better degree of reducibility, which in turn enhances the oxygen vacancy concentration (Venkataswamy et al. 2016) than compared to other redox samples and may result in better soot oxidation activity. H₂-TPR data from the literature (Ayastuy et al. 2014; Du et al. 2015; Zhan et al. 2015; Zhang et al. 2016) for the current redox samples (see **Table 4.4**) also reveals that the Mn₃O₄ reduces at much lower temperature than compared to other samples, and it is in concurrence with the reducibility data obtained from XPS analysis.

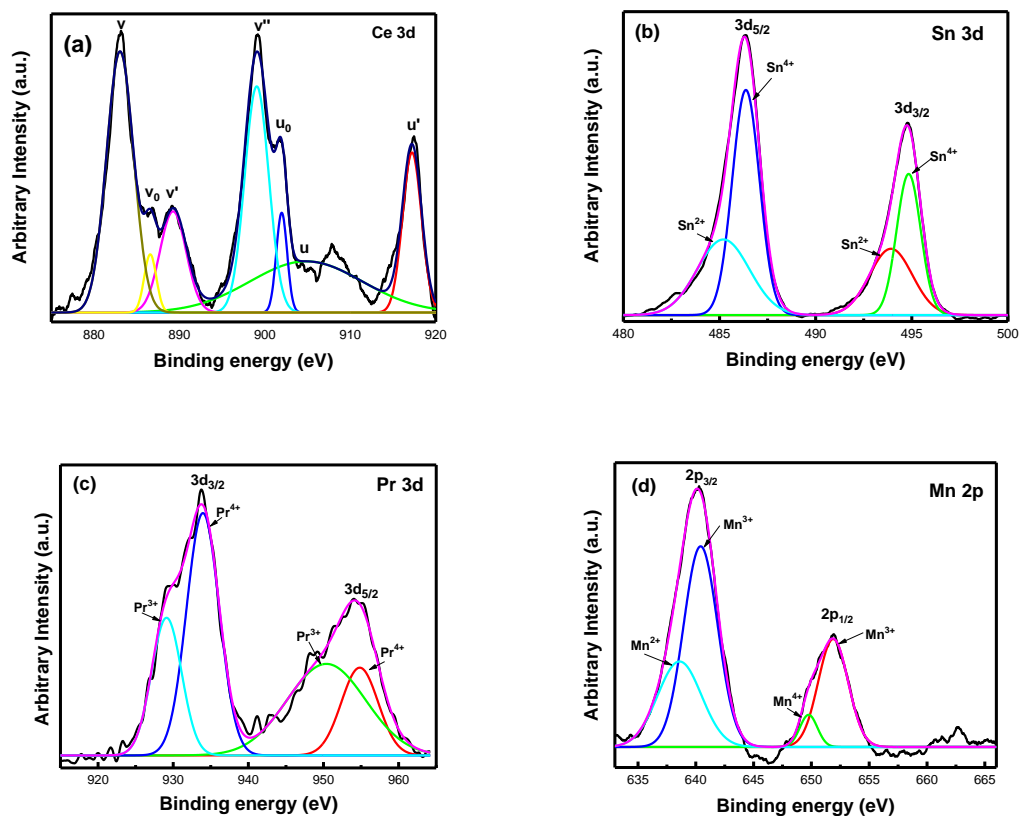


Figure 4.5: XPS of (a) Ce 3d, (b) Sn 3d, (c) Pr 3d and (d) Mn 2p of the corresponding redox metal oxides

Further, for a better understanding of oxygen species that are in association with redox metal, O 1s XPS analysis of all the redox samples are obtained and compared with each other. The O 1s peak of CeO₂, SnO₂, Pr₆O₁₁ and Mn₃O₄ samples in **Figure 4.6** confirm peaks corresponding to O_α (lattice oxygen), O_β (surface adsorbed oxygen) and O_γ (oxygen present due to hydroxyls, chemisorbed water and carbonates), respectively (Mukherjee et al. 2016).

Table 4.4 depicts the corresponding binding energies. Consideration of binding energy values of different peak leads to better comparative study. Lower the binding energy of O_β peak, easier the release of surface adsorbed oxygen and thus take part in reaction efficiently (Mukherjee et al. 2016). From the data of binding energy, it is evident that

Pr_6O_{11} has the lowest surface oxygen binding energy and then Mn_3O_4 , followed by CeO_2 . SnO_2 has higher binding energy value which can drop their catalytic activity compared to other samples. Thus, Pr_6O_{11} and Mn_3O_4 are expected to show better catalytic activity compared to CeO_2 and SnO_2 . From XPS data, it is apparent that the Mn_3O_4 sample has higher reducibility compared to other redox samples (Pr_6O_{11} , CeO_2 and SnO_2) and it may aid in soot oxidation activity since higher reducibility directly leads higher oxygen buffering capability (Trovarelli 1999). From **Table 4.4** it can be noticed that the Δr (ionic size difference of the corresponding metal oxides at different oxidation states) is small for the Mn_3O_4 sample followed by Pr_6O_{11} sample than compared to other redox samples (CeO_2 and SnO_2). The survey scan XPS spectra of CeO_2 given in **Figure S4.1, Appendix I** confirms the presence of Ce, O and C without any other impurity elements.

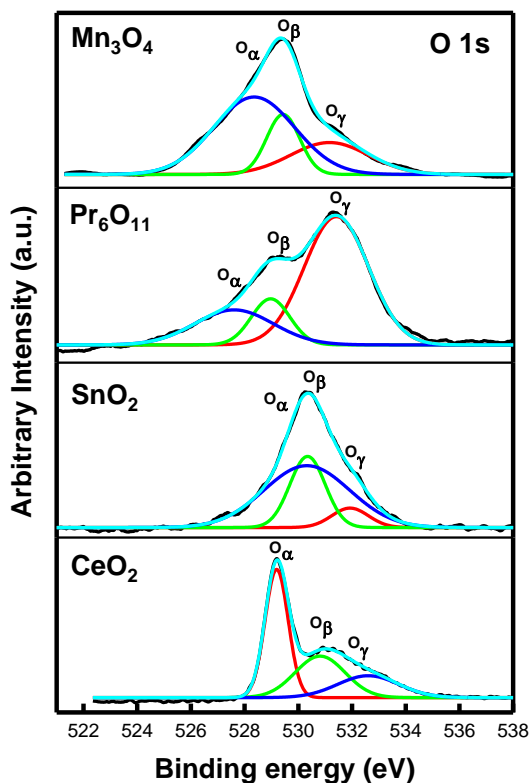


Figure 4.6: O 1s XPS of CeO_2 , SnO_2 , Pr_6O_{11} and Mn_3O_4 redox metal oxides

From H₂-TPR studies obtained from literature (Ayastuy et al. 2014; Du et al. 2015; Zhan et al. 2015; Zhang et al. 2016), the reduction temperatures T_α (surface metal reduction) and T_β (bulk metal reduction) are much lower for the Mn₃O₄ sample followed by the Pr₆O₁₁ sample than compared to the other redox samples (CeO₂ and SnO₂). From the viewpoint of easy reducibility, lower reduction temperature and smaller Δr value, Mn₃O₄ and Pr₆O₁₁ samples may lead to better soot oxidation activity than compared to CeO₂ and SnO₂ samples. The redox metal oxides show the multiple oxidation states which aids for soot oxidation reactions. The non-redox metal oxides that have shown enhanced surface properties similar to that of redox metal oxides also may have enhanced catalytic activity which is discussed in detail in a further section.

Table 4.4: Bandgap, binding energy, reducibility ratio, H₂-TPR (T_α/T_β), Δr and T₅₀ of redox metal oxides

Metal oxide	Band gap ^a (eV)	Binding energy ^b (eV)			Reducibility ratio ^c (%)	H ₂ -TPR (T _α /T _β) ^d (°C)	Δr ^e (Å)	T ₅₀ ^f (°C)
		O _α	O _β	O _γ				
CeO ₂	3.1	529	530	532	30	500/750 ¹	0.17	530
SnO ₂	3.3	530	530	532	42	550/800 ²	0.37	576
Pr ₆ O ₁₁	1.5	528	529	531	33	512/550 ³	0.17	482
Mn ₃ O ₄	1.7	528	529	531	70	317/350 ⁴	0.09 & 0.05	484

^a- Calculated using Tauc's plot; ^b- Calculated from O 1s XPS; ^c- Calculated from Ce 3d XPS; ^d- T_α/T_β surface/bulk ceria reduction temperature obtained using H₂-TPR from references [¹- (Zhang et al. 2016); ²- (Ayastuy et al. 2014); ³- (Du et al. 2015) and ⁴- (Zhan et al. 2015)]; ^e- Obtained from standard reference (Shannon 1976) and ^f- Temperature for 50% conversion of soot

4.1.4.2. Non-Redox metal oxides

Figure 4.7 demonstrates the metal core level XPS spectra of Gd 4d, La 3d, Zr 3d, Hf 4f and Sm 3d of the non-redox metal oxide samples (Gd_2O_3 , La_2O_3 , ZrO_2 , HfO_2 and Sm_2O_3) and the corresponding O 1s peaks are depicted in **Figure 4.8**. For Gd_2O_3 sample, the spin-orbital doublet of $4d_{5/2}$ and $4d_{3/2}$ at 141.4 and 146.7 eV, respectively confirms the presence of Gd^{3+} oxidation state (Durgasri et al. 2014). For La_2O_3 sample, La $3d_{5/2}$ displayed multiple peaks at 834.9 and 838.4 eV with a 3.5 eV binding energy split. From literature (Mukherjee et al. 2016), the binding energy split for the same is ~ 4.0 eV, and this confirms the presence of the impurity phase and is identified as $La_2O_2CO_3$ from XRD data.

For ZrO_2 and HfO_2 samples, the peaks at 181.5 eV (Zr $3d_{5/2}$) and 183.9 eV (Zr $3d_{3/2}$) confirms the presence of Zr^{4+} oxidation state and the peaks at 16.8 eV (Hf $4f_{5/2}$) and 18.6 (Hf $4f_{7/2}$) confirms the presence of Hf^{4+} oxidation state, respectively (Mukherjee et al. 2016). In the case of Sm 3d XPS, a significant peak at around 1083 eV is attributed to $3d_{5/2}$ ionization of Sm^{3+} . Charge transfer effect of 4f electrons that are unpaired in Sm results in a shoulder peak at lower binding energy. These results indicate the existence of Sm in the +3 oxidation state on the surface of the Sm_2O_3 sample (Kuntaiah et al. 2013).

Similar to the O 1s spectra of redox metal oxides, non-redox metal oxides O 1s spectra are deconvoluted into different species based on binding energy values as, O_α (lattice oxygen), O_β (surface adsorbed oxygen) and O_γ (oxygen present due to hydroxyls, chemisorbed water and carbonates), respectively (Mukherjee et al. 2016). From **Figure 4.8**, the relative percentage of surface oxygen (O_β) to the total oxygen ($O_\alpha + O_\beta + O_\gamma$) is calculated and shown in **Table 4.5**. The decreasing order of relative surface oxygen to the total oxygen is in the order: Sm_2O_3 (64 %) > HfO_2 (58 %) > La_2O_3 (53 %) > ZrO_2 (8 %) > Gd_2O_3 (4 %). Surface oxygen is critical in controlling the soot oxidation activity and will be discussed later.

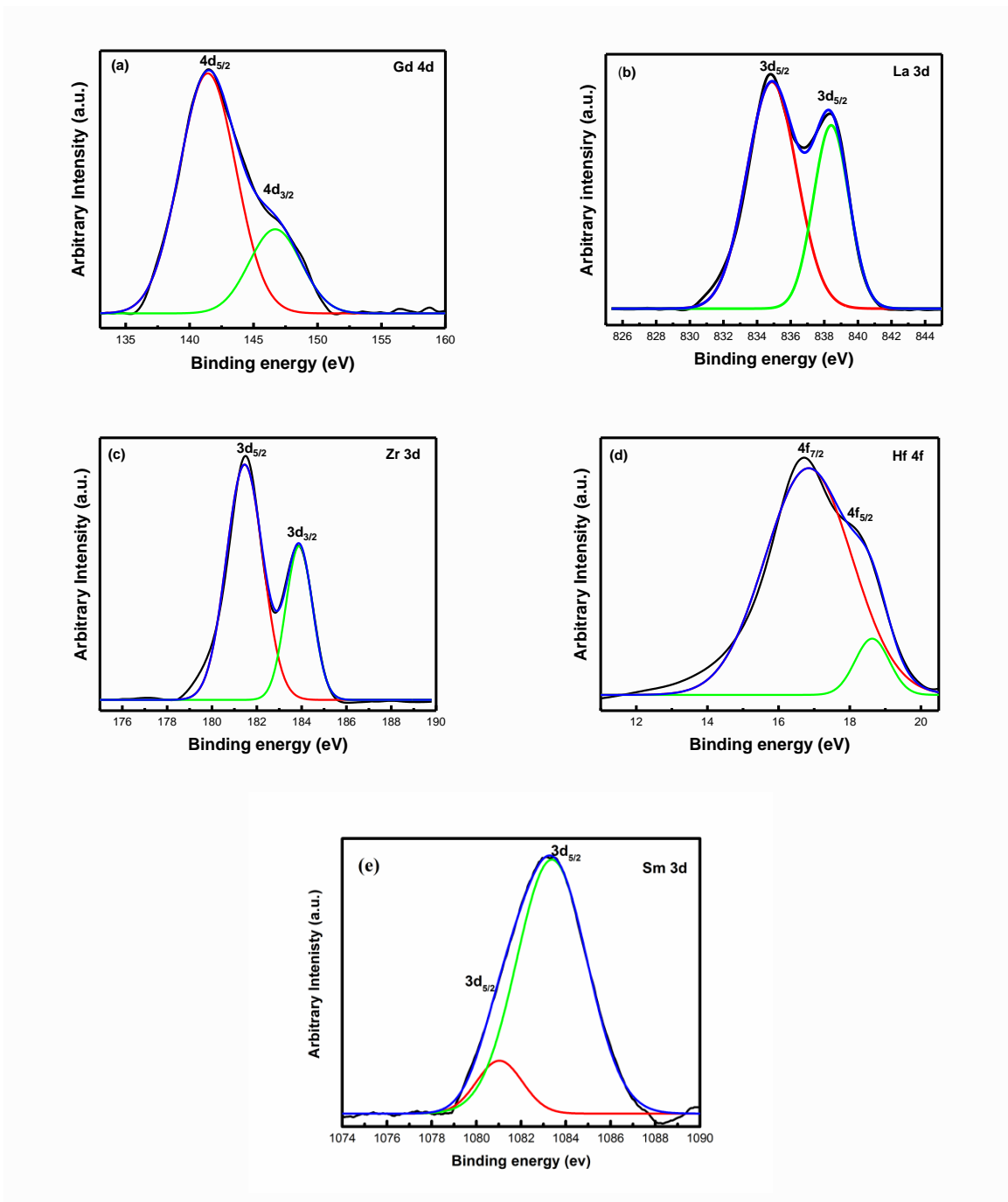


Figure 4.7: XPS of (a) Gd 4d, (b) La 3d, (c) Zr 3d, (d) Hf 4f and (e) Sm 3d of the corresponding non-redox metal oxides

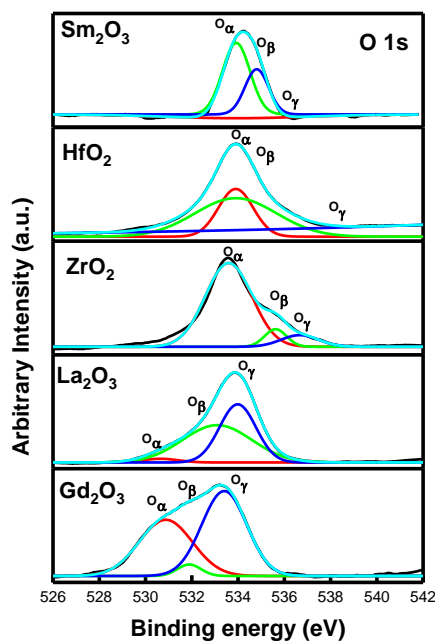


Figure 4.8: O 1s XPS of Gd₂O₃, La₂O₃, ZrO₂, HfO₂ and Sm₂O₃ non-redox metal oxides

Table 4.5: Bandgap, binding energy, ($O_{\beta}/(O_{\alpha} + O_{\beta} + O_{\gamma})$), BET surface area, lattice strain, ionic radius and T₅₀ of non-redox metal oxides

Metal oxide	Band gap ^a (eV)	Binding energy ^b (eV)			$O_{\beta}/(O_{\alpha}+O_{\beta}+O_{\gamma})$ ^b (%)	BET Surface area (m ² /g)	Lattice strain	Ionic radius ^c (Å)	T ₅₀ ^d (°C)
		O _α	O _β	O _γ					
Gd ₂ O ₃	5.0	530	532	533	4	4.6	0.0092	1.05	533
La ₂ O ₃	5.4	531	533	534	53	0.9	0.0054	1.16	505
ZrO ₂	4.8	534	536	537	8	7.2	0.0112	0.84	494
HfO ₂	5.3	531	534	537	58	21.1	0.0157	0.83	483
Sm ₂ O ₃	5.1	533	534	535	41	8.4	0.0190	1.08	537

^a- Calculated using Tauc's plot; ^b- Calculated from O 1s XPS; ^c- Obtained from standard reference (Shannon 1976) and ^d- Temperature for 50% conversion of soot

4.1.5. SOOT OXIDATION ACTIVITY

4.1.5.1.Redox metal oxides

According to the soot oxidation mechanism proposed by Shangguan et al. (1997) the redox reaction ensures the cyclic reduction and oxidation steps in metal oxide catalyst (Shangguan et al. 1997). This mechanism is applicable to metal and metal oxide catalyst (Aneggi et al. 2006; Shangguan et al. 1997). The following steps are involved in this mechanism (Mukherjee et al. 2016)



Where, $\mathbf{M_{red}}$ and $\mathbf{M_{oxd}-O_{ads}}$ represent the reduced and oxidised metal, respectively. $\mathbf{O_{gas}}$ and $\mathbf{O_{ads}}$ represent the gaseous and surface adsorbed oxygen species, respectively. $\mathbf{C_f}$ denotes the surface active site of carbon or free site on carbon surface, and \mathbf{SOC} represents the surface carbon–oxygen complex. As the gaseous oxygen gets adsorbed on the catalyst surface and the atomic species ($\mathbf{O_{ads}}$) reacts with free carbon site, intermediate active oxygen are formed. The reaction between the intermediate active oxygen or $\mathbf{O_{ads}}$ or the gaseous oxygen forms $\mathbf{CO/CO_2}$ (Shangguan et al. 1997).

Figure 4.9 demonstrates the soot oxidation activity of the redox metal oxides. T_{50} temperature (Temperature at which at least 50% of soot conversion takes place) is used as a reference point to evaluate the performance of catalysts. $\mathbf{Mn_3O_4}$ and $\mathbf{Pr_6O_{11}}$ catalysts showed much better soot oxidation activity followed by $\mathbf{CeO_2}$ and $\mathbf{SnO_2}$ catalysts when compared to bare soot oxidation activity. The observed T_{50} temperatures for the redox catalysts, $\mathbf{Mn_3O_4}$, $\mathbf{Pr_6O_{11}}$, $\mathbf{CeO_2}$, and $\mathbf{SnO_2}$ are 483, 485, 530 and 576 °C, respectively (see **Table 4.4**) indicating that the soot oxidation activity order is: $\mathbf{Mn_3O_4} > \mathbf{Pr_6O_{11}} > \mathbf{CeO_2} > \mathbf{SnO_2}$.

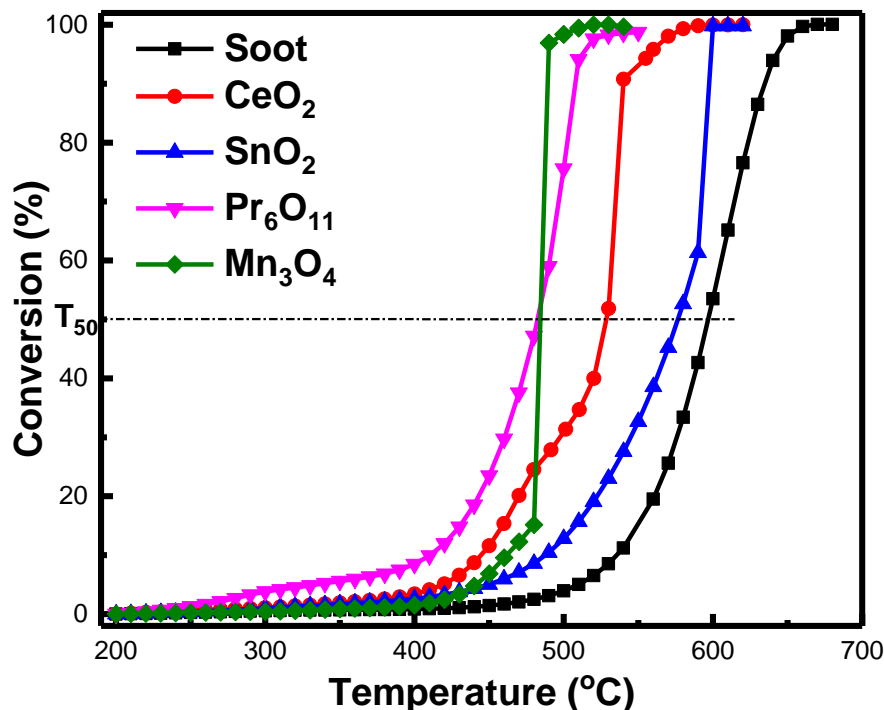


Figure 4.9: Soot oxidation of Redox metal oxides

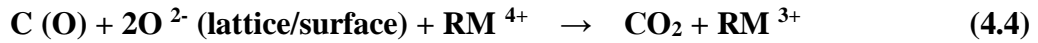
(CeO₂, SnO₂, Pr₆O₁₁ and Mn₃O₄)

From the proposed mechanism of soot oxidation, it implies that the formation of the metal-oxide bond ($M_{\text{oxd}}-O_{\text{ads}}$) is essential, indicating that the active presence of surface adsorbed oxygen (O_{β}) in the metal oxides (Christensen et al. 2016). Based on bandgap and O 1s XPS spectra, we can see that Mn₃O₄ and Pr₆O₁₁ samples have the lowest bandgap and binding energy values.

From the XPS analysis, it is also worthwhile to mention that the Mn₃O₄ sample has higher reducibility than compared to other samples indicating that the sample can readily undergo reduction ($M_{\text{red}} + \text{SOC}$). Apart from this, the Δr is smallest for Mn₃O₄ sample than compared to other samples. In general, the soot oxidation reaction mechanism of

MnO_x is through Mars-van-Krevelen (MvK) mechanism. Surface defects and oxygen mobility are significant as per the mechanism for soot oxidation.

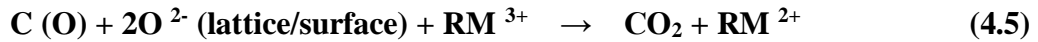
In this mechanism, the oxygen vacancy reacts with SOCs at the soot-catalyst interface as per **Equation (4.4)**. The interaction is facilitated by catalyst reduction by transfer of oxygen from the bulk to its surface (Mul et al. 1998; Wasalathanthri et al. 2017).



RM is redox metal (Ce, Sn, Pr and Mn)

For RM ≡ Ce, Sn and Pr, the oxidation of SOCs occur at the interface of soot and catalyst using surface adsorbed oxygen, **Equation (4.4)**.

Whereas, for RM = Mn, Mn³⁺ can be further reduced to Mn²⁺ due to its multiple step reduction behaviours which facilitates further the SOCs to react with lattice/surface oxygen ions (**Equation (4.5)**) and enhance the overall soot oxidation reaction



From this, it is evident that the multiple redox steps (Mn⁴⁺ → Mn³⁺ → Mn²⁺) can further enhance the soot oxidation activity than compared to single redox step (RM⁴⁺ → RM³⁺, RM ≡ Ce, Sn and Pr).

From the present results it can infer that, for redox catalysts, the presence of surface adsorbed oxygen at lower binding energies, higher reducibility and smaller Δr govern the soot oxidation activity rather than the large surface area, greater pore volume and smaller crystallite size.

4.1.5.2. Non-Redox metal oxides

Figure 4.10 illustrates the soot oxidation activity of non-redox metal oxides. The profile indicates that HfO_2 and ZrO_2 showed much better soot oxidation activity than La_2O_3 , Gd_2O_3 and Sm_2O_3 . The T_{50} temperatures are 483, 494, 505, 533 and 537 °C for HfO_2 , ZrO_2 , La_2O_3 , Gd_2O_3 and Sm_2O_3 respectively, indicating the soot oxidation activity order is $\text{HfO}_2 > \text{ZrO}_2 > \text{La}_2\text{O}_3 > \text{Gd}_2\text{O}_3 > \text{Sm}_2\text{O}_3$. **Table 4.5** manifests that the increase in BET surface areas, lattice strain and a decrease in ionic radius follows the order: $\text{HfO}_2 > \text{ZrO}_2 > \text{Gd}_2\text{O}_3 > \text{La}_2\text{O}_3 > \text{Sm}_2\text{O}_3$. Dopant with +4 oxidation state is significantly better than +3 oxidation state as per the results obtained for the samples.

In general, the smaller ionic radius of the cation (Rao and Mishra 2003) and higher lattice strain improves the oxygen mobility and thus helps in oxygen migration (Mukherjee et al. 2016; Rushton et al. 2013). Larger surface area leads to more number of active sites for soot oxidation and thus enhance the soot oxidation activity (Liang et al. 2007). The order of T_{50} temperature for soot oxidation activity follows the order of surface oxygen vacancy, surface area, lattice strain and ionic radius expect for the La_2O_3 sample. This variation may be because of the presence of impurity ($\text{La}_2\text{O}_2\text{CO}_3$) in La_2O_3 sample which enhances the soot oxidation activity by a carbon-intermediate mechanism (Aneggi et al. 2007). Thus, in the case of non-redox samples other than the La_2O_3 sample, surface features may improve the catalytic activity which benefits in surface oxygen that can be availed for soot oxidation reaction by spillover mechanism (Mul et al. 1998).

It is noteworthy to mention that the Gd_2O_3 sample showed the highest pore volume ($0.0552 \text{ cm}^3/\text{g}$) (See **Table 4.3**) than compared to other samples. Which may help in the better interaction between Gd_2O_3 and the soot particles in direct contact by enhancing the transfer of the surface oxygen on the soot surface at the interface of catalyst, and further the gas phase oxygen occupies the vacancies and thus enhance the light-off (T_{10}) performance. In case of non-redox metal oxides (Gd_2O_3 , La_2O_3 , ZrO_2 , HfO_2 and Sm_2O_3) surface oxygen has a vital role since the transfer of surface oxygen at the soot-catalyst

interface takes place by spillover mechanism and form SOCs. This kind of surface mechanism is mainly aided through the higher surface area, higher lattice strain and smaller ionic radius rather than multiple oxidation states of host cations.

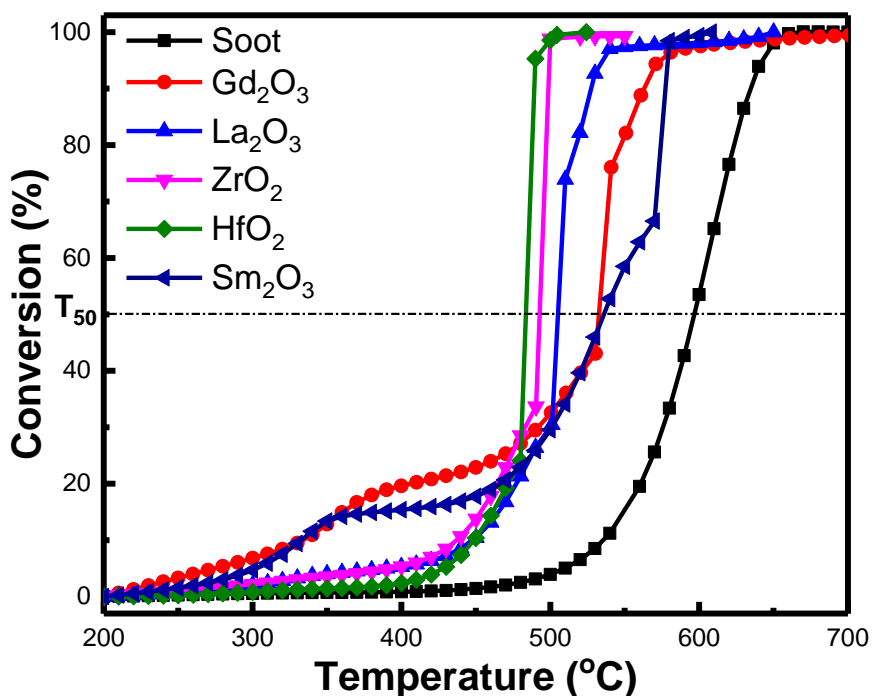


Figure 4.10: Soot oxidation of Non-Redox metal oxides (Gd₂O₃, La₂O₃, ZrO₂, HfO₂ and Sm₂O₃)

Based on the soot oxidation activity study for redox and non-redox metal oxides, the overall catalytic activity of the sample is controlled by different parameters depending upon the nature of the host cation material. The summary of the catalytic activity and its effect by various parameters are concluded for both redox and non-redox metal oxides in **Appendix I Figure S4.2**. For samples having redox properties, higher reducibility, lower binding energy for surface oxygen and smaller ionic radius difference at different

oxidation states of host ion control its activity. However, for non-redox metal oxide samples, higher surface area, higher lattice strain and smaller ionic radius aids the soot oxidation activity of the catalyst. Apart from that, the current study concludes that non-redox metal ions with +4 oxidation state (Hf and Zr) showed significant activity. The principal descriptor for the catalytic activity is the nature of metal itself, which in turn is controlling the metal-oxygen and oxygen-oxygen distance, and thus affects the oxygen mobility and active contact points. From the results obtained in the study, further research focuses on binary and ternary ceria-based metal oxides doped with other metal having redox and non-redox properties that showed better activity as single metal oxide catalyst for soot oxidation reaction.

4.2 CONCLUSION

The synthesis method adopted for catalyst development controls the surface and structural properties of the sample and thus influence the catalytic activity for soot oxidation reactions. To restrict the influence of reaction parameters as catalytic descriptor, a single synthesis method of EDTA-Citrate complexing method is adopted in comparison with solvothermal method. The enhanced activity of GDC sample synthesized by the EDTA-Citrate method is due to smaller crystallite size and bandgap and higher lattice strain, reactive facet planes, surface oxygen and Ce³⁺ reducibility. Thus all the metal oxides in further are synthesized only using the EDTA-Citrate method and thus restrict the descriptor that influences the activity due to change in synthesis procedure.

Analysis of single metal oxide with redox and non-redox properties confirms that the first and foremost descriptor for catalytic activity is the nature of metal cation. The activity of metals with multiple oxidation state is affected by the redox properties such as metal reducibility, surface oxygen binding energy and smaller ionic radius difference between different oxidation states which are intrinsic in nature. Similarly, for non-redox metal oxide the properties that controls the catalytic activity are, surface oxygen vacancy and transport that affects the activity with the higher surface area, higher lattice strain and smaller ionic radius. Non-redox metal ions with +4 oxidation state (Hf and Zr) showed significant activity compared to other non-redox (La, Gd and Sm) samples and almost equivalent to redox metal oxides such as Mn₃O₄ and Pr₆O₁₁. The nature of metal cation further modifies the oxygen mobility for oxidation reaction. Another way to further modify the descriptor and thus the catalytic activity is the modification of host lattice. Thus, doping the ceria lattice with suitable metal can further alter the descriptor which may possibly enhance its activity.

CHAPTER 5

STUDY ON BINARY METAL OXIDES

The study of single metal oxides for soot oxidation confirms that the descriptor primarily influencing the catalytic activity is the nature of the dopant whether it is redox or non-redox. Further study aims in improving the catalytic activity of ceria by suitable modification using dopants. Thus the ceria lattice is suitably modified by dopant addition to form binary metal oxide that results in modifying the host structure, phase and active sites which further results in modification of oxygen vacancy and mobility and thus the activity may be affected. However, the amount with which the dopant is to be added is not well analysed. Based on this inference, the binary ceria-based metal oxide combination of CeO₂-HfO₂ with redox and non-redox metals over the whole composition is developed, and the optimum composition along with the descriptor that varies with the dopant addition is studied in detail. Once the composition is fixed, the binary metal oxide dopant effect is analysed by varying the dopant metal and tested for soot oxidation activity.

5.1 Ce_{1-x}Hf_xO₂ (x=0.0 - 1.0) BINARY METAL OXIDES

Based on the preliminary study on single metal oxides, it is apparent that non-redox metal oxide such as HfO₂ showed significant activity equivalent to that of other redox metal oxides. Thus, the study on binary metal oxide is initially focused on the combination of non-redox HfO₂ with redox CeO₂ over the whole composition range. Ce_{1-x}Hf_xO₂ (CH_x) (x varies from 0-100 mol%) binary metal oxide over whole composition range is successfully synthesized using the EDTA-Citrate method. The characterization of full range binary metal oxides is carried out using XRD, BET surface area, pore volume analyser, Raman spectroscopy, SEM, TEM, UV-Vis DRS and XPS analysis. The obtained results are illustrated and discussed in detail. The soot oxidation activity of all the metal oxides are

analysed under tight contact conditions, and the effect of different parameters on the activity are studied in detail.

5.1.1. X-ray Diffraction (XRD) Analysis

Pre-calcined CH10 sample synthesized by the EDTA-Citrate method, oven dried at 150°C / 24h using TG-DTG analysis (see **Appendix II Figure S5.1**) to find the decomposition behaviour with the rise in temperature before the characterization of the sample. XRD spectra of the CH_x binary sample series is depicted in **Figure 5.1 (a)**. CH0-CH90 samples demonstrate the peak corresponding to fluorite (F) phase of CeO₂ (Atribak et al. 2008) CH100 exists in monoclinic phase (M phase) of HfO₂ (Ramadoss et al. 2012), and the monoclinic peak is evident from CH80 onwards in trace amounts. From the preliminary XRD study, multi-phase is present among the selected sample series, that is F phase (CH0~CH70), hybrid phase of F and M (CH80~CH90) and M phase (CH100), respectively. The lattice constant is calculated using Bragg's law for F phase (CH0-CH90) and M phase (CH100).

Figure 5.1 (b) shows the plot of the cubic root of lattice volume with the dopant concentration in mol%. The lattice constant is decreasing linearly with the increase in dopant content due to the smaller ionic radius of Hf⁴⁺ when compared to Ce⁴⁺ (Zhou and Gorte 2008). However, the slope of the line varies from CH70 onwards which indicates the solid solution is formed only up to CH70 sample as per Vegard's rule (Vegard 1921). Further, with the increase in dopant content, it is no more soluble in the host lattice. Instead, it segregates as a secondary phase. This result corroborates with the peak identified from the diffraction pattern (Chavan and Tyagi 2006). **Table 5.1** gives the value of crystallite size (D) and lattice strain (ε), BET surface area, particle size using BET surface area, pore volume and degree of agglomeration (φ) calculated for CH_x samples. Crystallite size (D) and lattice strain (ε) value are in the range of 7.4 ~ 11.5 nm and 0.011 ~ 0.019, respectively. Samples with smaller crystallite size may have better oxygen diffusion along with the increase in lattice strain (Rushton et al. 2013).

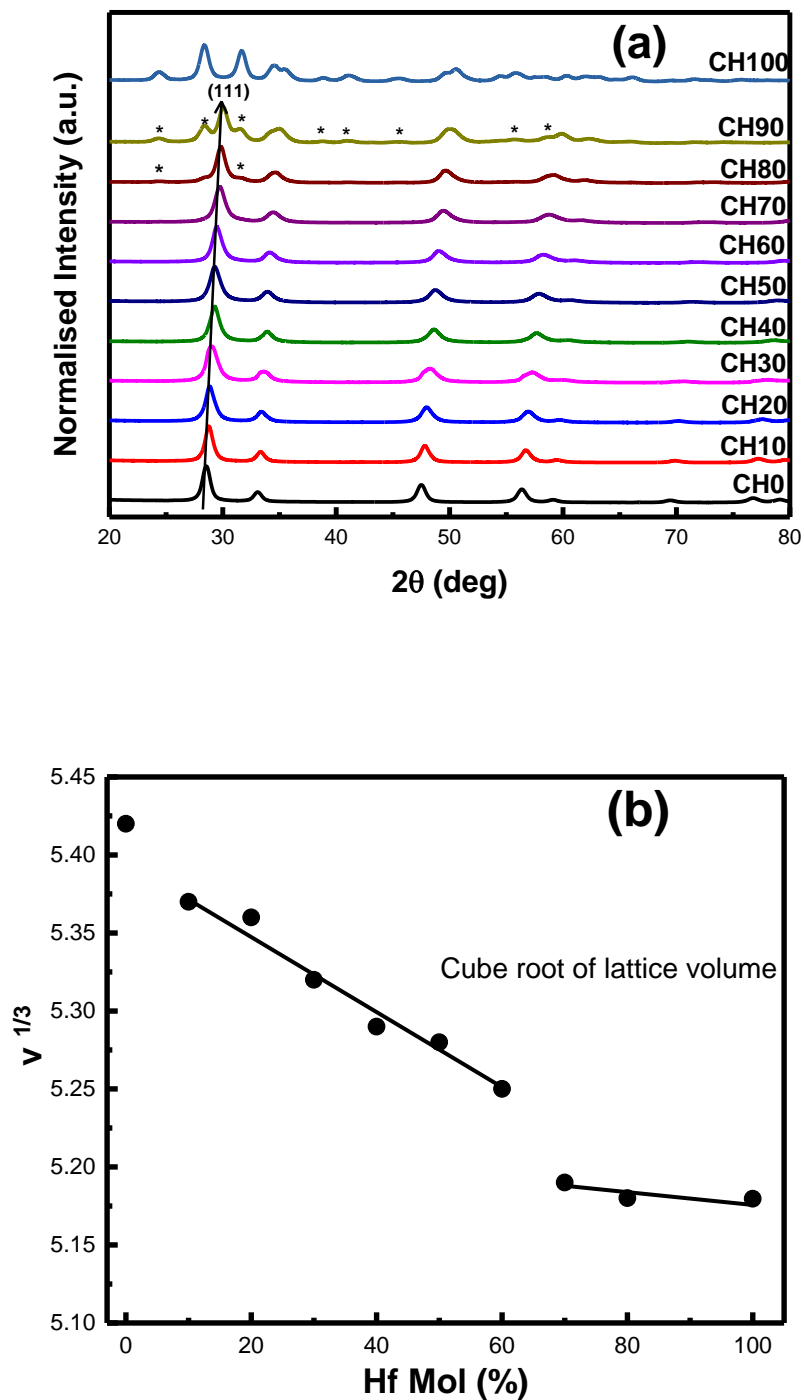


Figure 5.1: (a) XRD spectra and (b) Vegard's law of CH_x binary ceria-based metal oxides

BET surface area of the sample is around 18 ~ 41 m²/g. Among the solid solution sample range obtained from XRD, CH10 showed the highest surface area compared to other samples. Particle size is in the range of 19 ~ 40 nm. The pore volume of the sample is in the range of 0.027 ~ 0.054 cm³/g. Pore volume decreases up to CH20 sample, further addition of dopant leads to an increase in pore volume. Influence of pore volume on soot activity can be neglected since the pore size in this range can no longer accommodate the bigger soot particles (Krishna et al. 2007). 1.6 ~ 5.0 is the degree of agglomeration (ϕ) value range of CH_x samples. Lesser agglomerated particles ensure efficient surface to volume ratio and thus enhance the catalytic activity (Sun et al. 2007). CH10 showed the lower degree of agglomeration value among the solid solution sample of CH10 ~ CH60. A solid solution metal oxide showed enhanced thermal stability with enhanced reducibility compared to secondary phase segregated non-homogeneous mixed oxide sample (de Leitenburg et al. 1995).

5.1.2. Raman Spectroscopy Analysis

From the Raman spectroscopy results obtained, the whole composition is divided into three regions based on the phase in which they exist. The Raman spectra obtained for CH_x samples are provided in **Figure 5.2**. The dominant peak at 462.8 cm⁻¹ (F_{2g}) owing to the symmetric stretching mode of F phase CeO₂ is evident in CH0 sample (Weber et al. 1993). Thus, CH10 ~ CH30 in **Figure 5.2 (a)** is considered to exist in a single F phase since there is no presence of any other impurity phases. Reduction in Raman peak intensity for higher dopant content samples could be related to the difference in polarizability of Ce and Hf due to the difference in size (Artini et al. 2016).

The Raman spectra of the CH40 ~ CH80 sample shown in **Figure 5.2 (b)** have peaks at around 260 cm⁻¹ and 630 cm⁻¹, which is an indication of the presence of M phase (P2₁) apart from the F_{2g} peak seen in initial samples with the single phase (Jayaraman et al. 2017). Co-existence of peaks corresponding to both F phase CeO₂ and M phase HfO₂ confirms the formation of a hybrid phase among the selected region of CH40 ~ CH80. Raman band corresponding to vibration mode of monoclinic HfO₂ are evident in **Figure**

S5.2 (Appendix II) for CH90 and CH100 samples (Jayaraman et al. 2017). However, only CH100 exist in pure M phase since the CH90 sample exhibits both F and M phase as shown in XRD results. The intensity ratio of F_{2g} and oxygen vacancy ($I_{OV}/I_{F_{2g}}$) is calculated and the values are given in **Table 5.1** for the specific sample range in which F_{2g} peak is visible. The ratio provides a correlation of relative lattice oxygen defects available in the binary metal oxide (Guo et al. 2011). Chavan et al. (Chavan and Tyagi 2006) and Izu et al. (2007) have synthesized Ce-Hf series at varying concentration and found that $Ce_{0.85}Hf_{0.15}O_2$ sample onwards monoclinic phase of HfO_2 starts appearing (Izu et al. 2007). Also, weak monoclinic phase starts segregating from $Ce_{0.74}Hf_{0.26}O_2$ onwards as per study the Raitano et al. (2015) (Raitano et al. 2015). However, in the present work, the hybrid phasic metal oxide in fluorite and monoclinic phase starts from CH40 based on the secondary peak from Raman result.

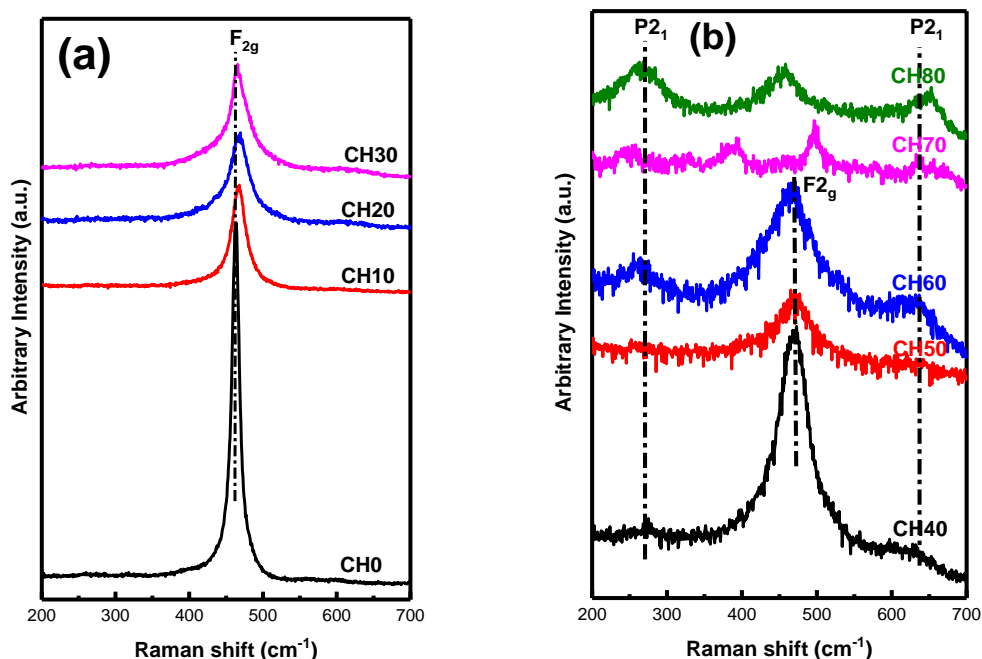


Figure 5.2: Raman spectra of (a) CH0-CH30 samples and (b) CH40-CH80 samples calcined at 600°C/5h

Table 5.1: Crystallite size, lattice strain, BET surface area, pore volume, particle size, degree of agglomeration, composition, intensity ratio, optical bandgap and T₅₀ temperature of CH_x samples calcined at 600°C/5h

Metal oxide	Crystallite size ^a (nm)	Lattice strain ^b (ε)	BET Surface area(m ² /g)	Particle size ^c (nm)	Pore volume (cm ³ /g)	Degree of agglomeration ^d (φ) [^]	Composition using EDS (%)		I _{ov} /I _{F2g} ^e (%)	Band gap ^f (eV)	O _β / (O _α +O _β +O _γ) ^g (%)	T ₅₀ temperature (°C)
							Ce	Hf				
CH0	10.6	0.013	41	16.8	0.054	1.6	100	0	--	3.08	41	530
CH10	9.6	0.014	29	26.5	0.043	2.8	92	8	6	2.97	44	430
CH20	8.4	0.016	19	39.8	0.027	4.7	82	18	18	2.93	34	435
CH30	7.4	0.019	24	30.7	0.034	4.1	76	24	14	2.88	36	435
CH40	8.1	0.016	18	40.2	0.032	4.9	65	35	21	2.71	58	455
CH50	7.6	0.018	21	32.2	0.035	4.2	52	48	34	2.70	36	460
CH60	8.1	0.016	20	33.7	0.033	4.1	47	53	--	2.73	32	475
CH70	7.8	0.017	25	25.9	0.043	3.3	35	65	--	2.78	43	475
CH80	8.8	0.015	20	31.9	0.043	3.6	26	74	--	2.83	36	510
CH90	11.3	0.011	25	25.2	0.036	2.2	11	89	--	2.94	45	540
CH100	9.6	0.015	21	30.1	0.039	3.1	0	100	--	5.30	54	483

^a- Calculated from intense XRD peak using Debye-Scherrer equation; ^b-Calculated from intense XRD peak; ^c- Calculated from BET Surface area; ^d- Calculated as the ratio of particle size and crystallite size; ^e- Calculated using intensity ratio of Raman peak; ^f- Calculated using Tauc's plot and ^g- Calculated using XPS O 1s peaks using CasaXPS software

The significant variation in phase boundaries might be due to the difference in calcination temperature, crystallite size and surface area that are influenced by the adopted synthesis method. Since the secondary phase is confirmed, the effect of structural morphology upon a change in phase is analysed in further.

5.1.3. Scanning Electron Microscopy (SEM) Analysis

Figure 5.3 shows the SEM morphology of CH_x sample series. All the samples have agglomerated particles. **Figure 5.3 (a)** confirms the flaky agglomerated particles of CH0 sample (Zhang et al. 2016). The flaky morphology is consistent in the case of CH10 (**Figure 5.3 (b)**), CH20 (**Figure 5.3 (c)**) and CH30 (**Figure 5.3 (d)**) samples that exist in single F phase. However, for CH40 sample in **Figure 5.3 (e)**, the morphology is changed considerably with the appearance of layers of flakes, which can be directly correlated to the phase variation. As the dopant content is increased further, there is not much variation in the morphology of the sample as evident for CH40 ~ CH100 sample in **Figure 5.3 (e)** to **Figure 5.3 (k)**, respectively.

Apart from the phase separation from the crystallographic and vibrational analysis, morphological classification is confirmed from the SEM image as F phase, hybrid phase (F+M) and M phase in the range of CH10 ~ CH30, CH40 ~ CH90 and CH100, respectively. The EDS composition of all the samples was analysed and tabulated in **Table 5.1** asserts that the theoretical and actual composition of the samples is almost similar.

5.1.4. Transmission Electron Microscopy (TEM) Analysis

HR-TEM images in **Figure 5.4** shows the lattice fringes corresponding to each plane. CH10 and CH40 sample fringes correspond to the *d* spacing of (111) plane in F phase as indicated in **Figure 5.4 (a)** and **Figure 5.4 (b)**, respectively. CH10 has an additional presence of more reactive facet plane of (200). These planes may be formed by defect creation while doping that may aid in the active site availability (Bharali et al. 2012).

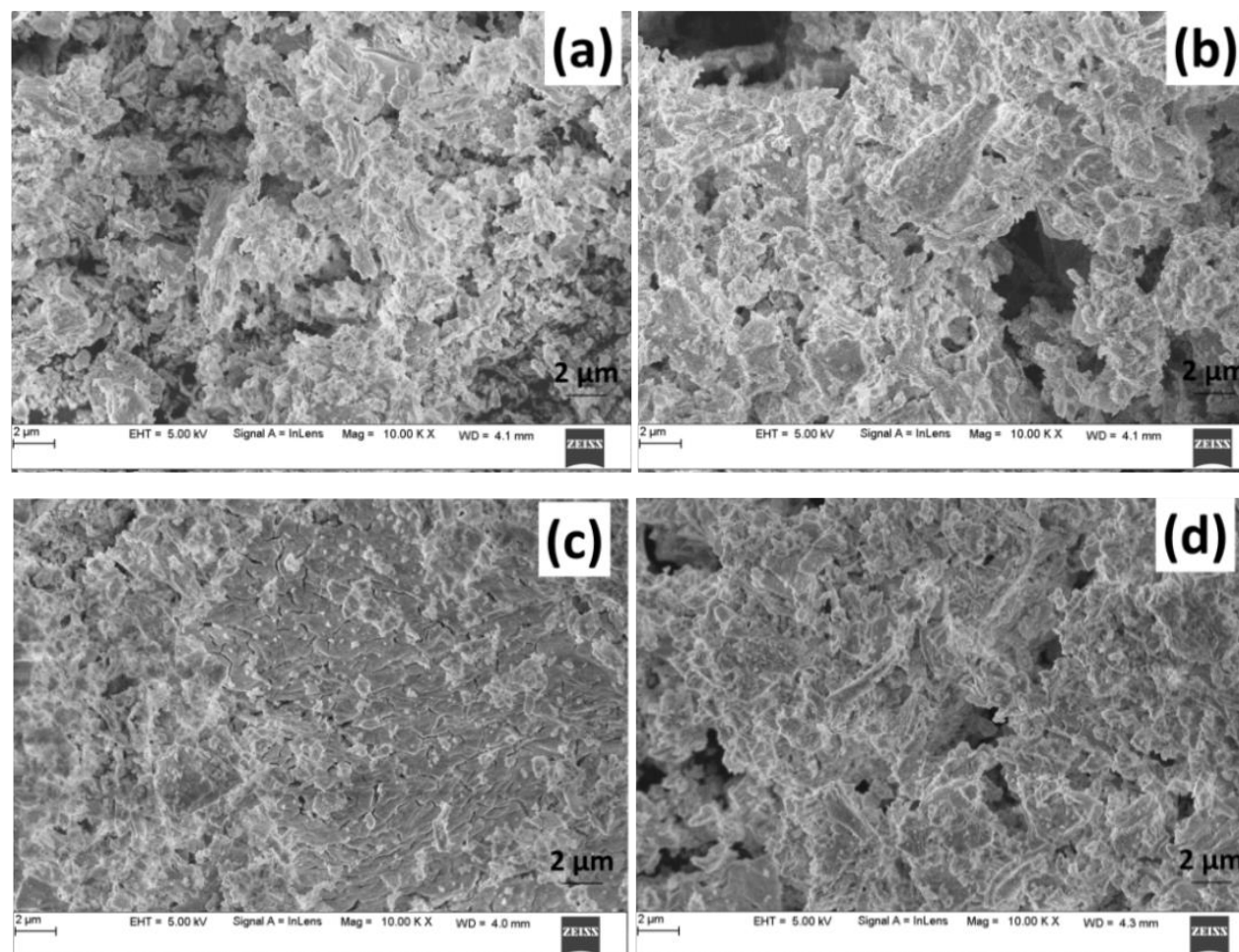


Figure 5.3: SEM images of (a) CH0, (b) CH10, (c) CH20 and (d) CH30 of CH_x binary ceria-based metal oxides

(Contd.)

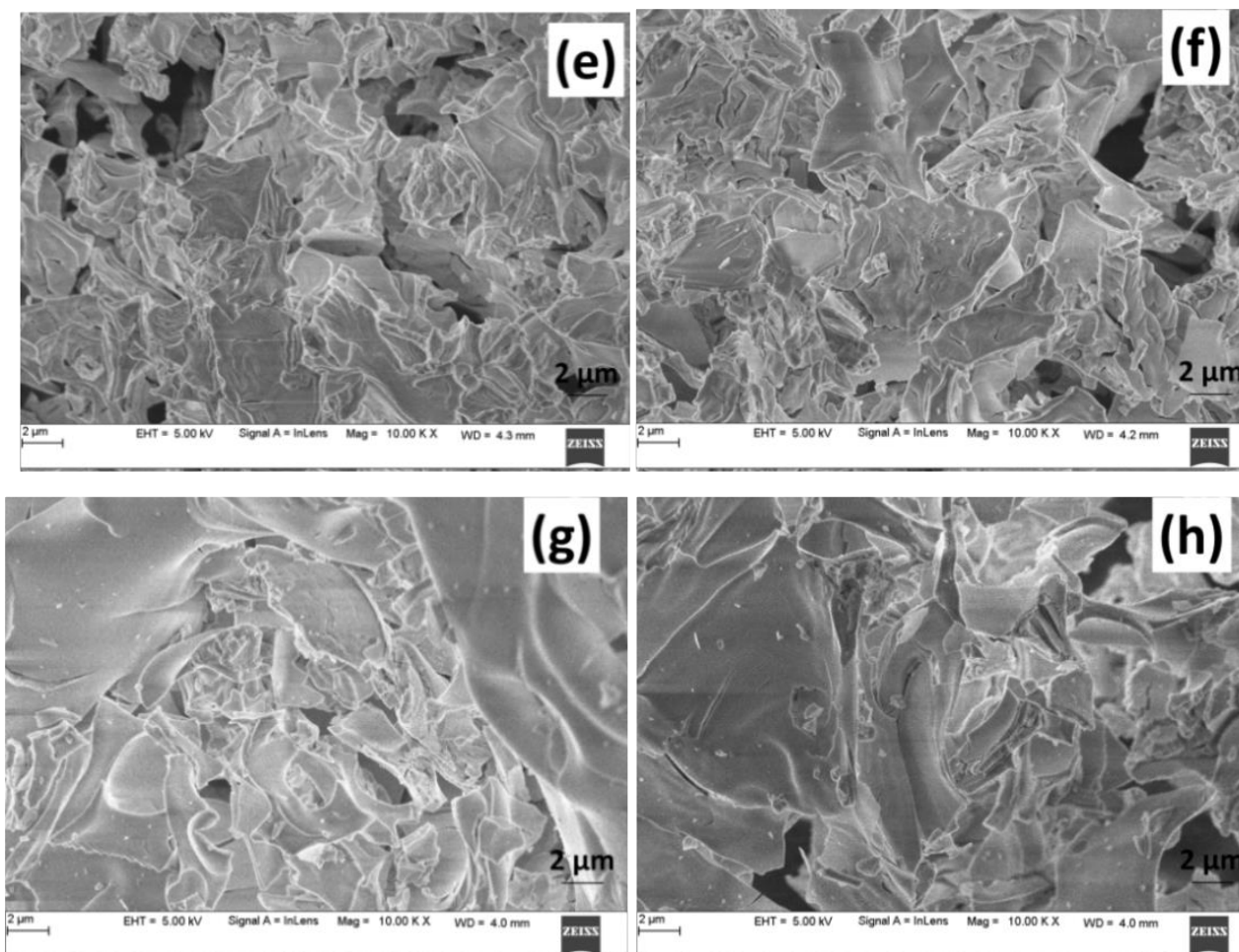


Figure 5.3: SEM images of (e) CH40, (f) CH50, (g) CH60 and (h) CH70 of CH_x binary ceria-based metal oxides

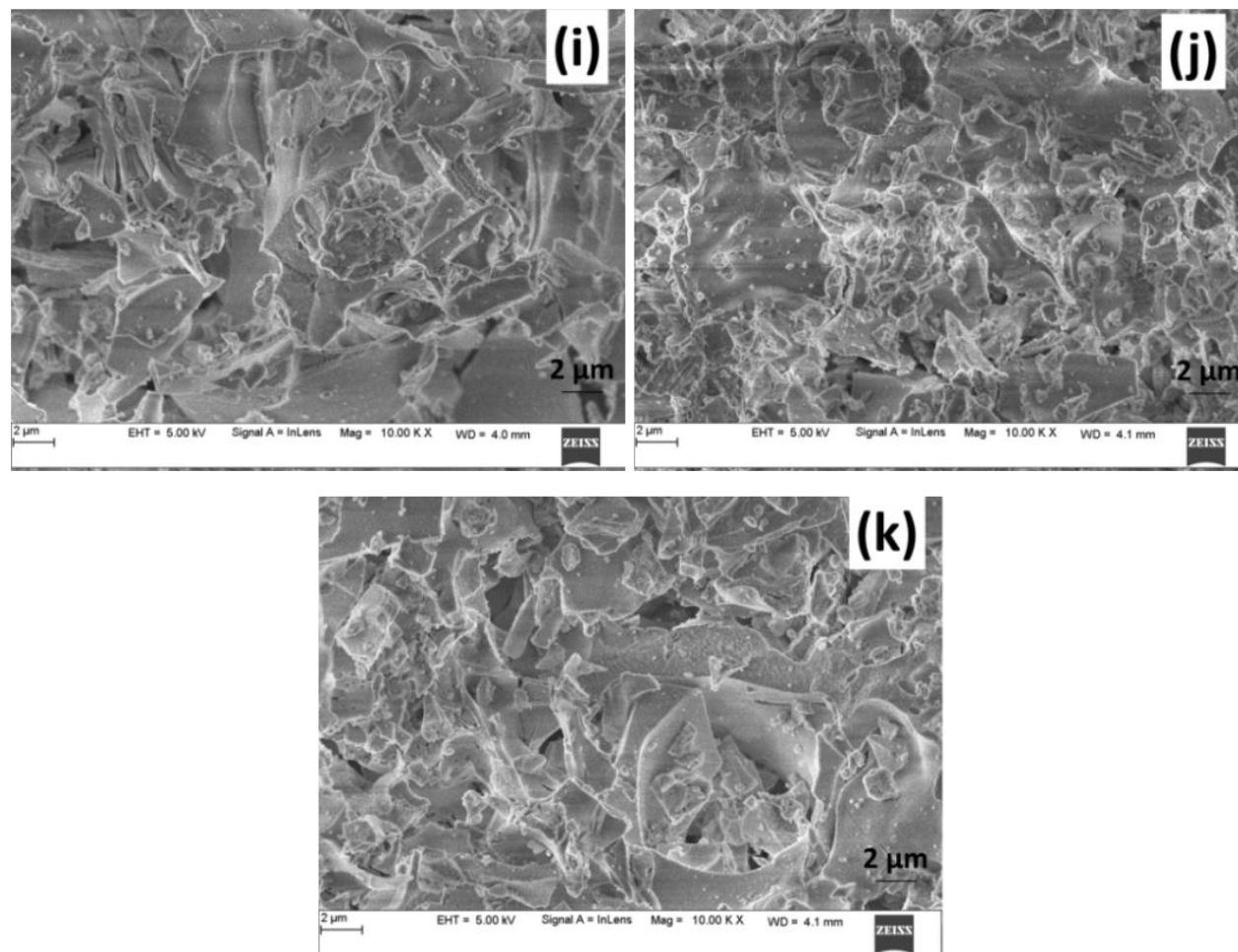


Figure 5.3: SEM images of (i) CH80, (j) CH90 and (k) CH100 of CH_x binary ceria-based metal oxides

CH80 in **Figure 5.4 (c)** shows the lattice fringes corresponding to the d spacing of intense peaks in both F and M phase, which strongly confirms the existence of hybrid phase in this sample. However, CH100 indicates only the planes in M phase as shown in **Figure 5.4 (d)**.

SAED pattern confirms the polycrystalline nature of the sample (see **Figure 5.5**). CH10 sample in **Figure 5.5 (a)** with clear concentric smooth rings confirm fluorite phase of CeO_2 as calculated from XRD result with each circle corresponding to each plane (Shantilal Gangrade et al. 2017). For CH40 sample, **Figure 5.5 (b)**, few spots start appearing in the ring pattern corresponding to the monoclinic phase of HfO_2 (Brezesinski et al. 2005). However, the rings are not precise; instead, crystals are seen as spots of almost similar size to that of CH10. Apart from larger spots, some smaller spots are also evident which may correspond to that of dopant. On observing the SAED pattern of CH80 sample in **Figure 5.5 (c)** the spot size reduction occurs which are similar to smaller spots in CH40 sample. The crystals are not well arranged in ring form. CH100 sample in **Figure 5.5 (d)** shows spot similar to that of CH80, but of lesser in number, the ring structure is not well maintained in this case.

Thus, it is clear from the electron diffraction images that CeO_2 exist in ring pattern with larger spots and HfO_2 maintains the spot pattern with smaller size spot (Mikhlin et al. 2009; Shantilal Gangrade et al. 2017). In the case of CH40 sample, ring pattern is almost maintained with both larger and smaller spots corresponding to host and dopant, respectively, confirms the hybrid phase. The hybrid phase formation affects surface morphology as evident in SEM result is consistent with the results obtained from SAED images.

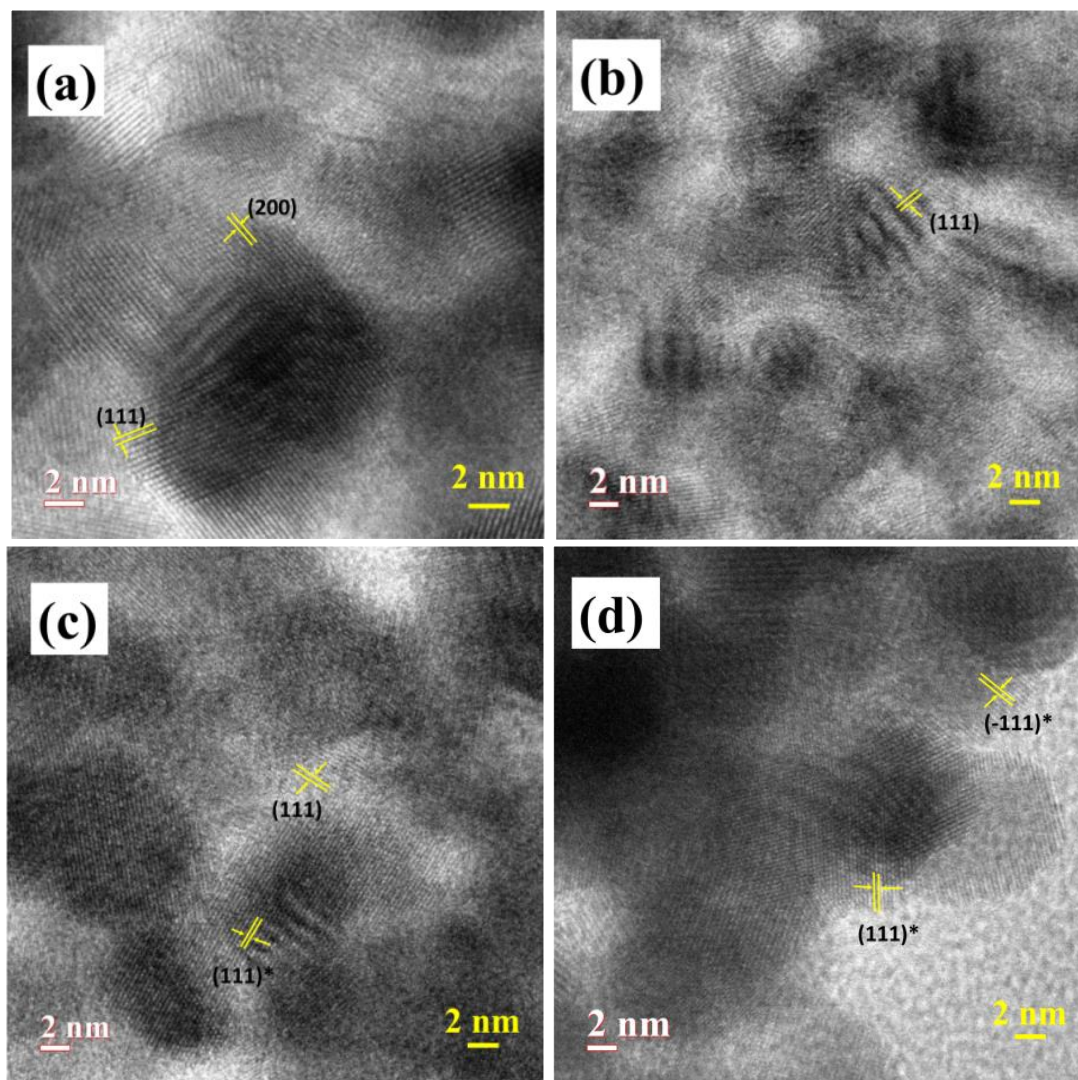


Figure 5.4: HR-TEM image of (a) CH10; (b) CH40; (c) CH80 and (d) CH100 samples (*-Monoclinic phase of HfO₂)

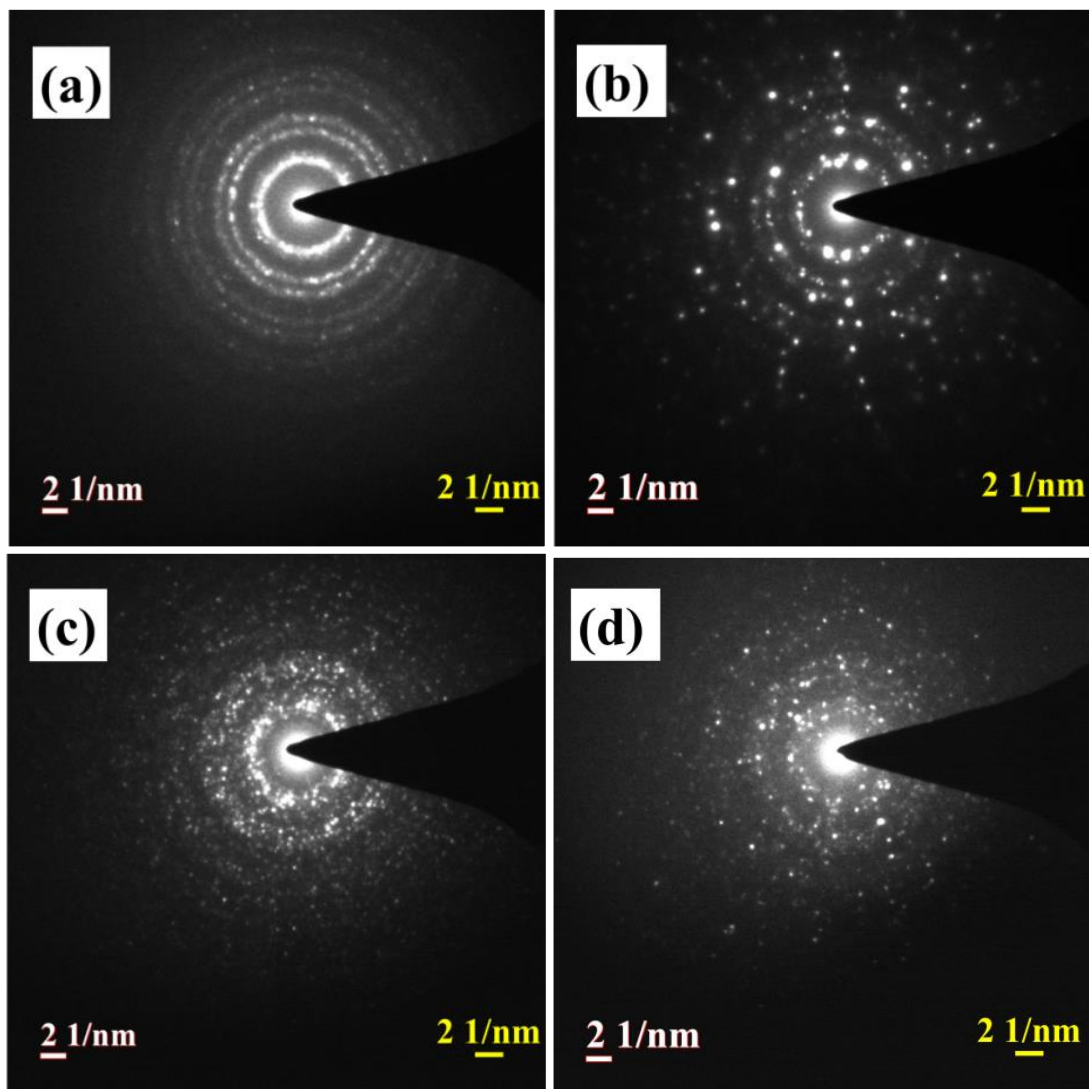


Figure 5.5: SAED pattern of (a) CH10; (b) CH40; (c) CH80 and (d) CH100 samples

5.1.5. UV-Vis Diffuse Reflectance Spectroscopy (UV-Vis DRS) Analysis

To study the optical bandgap and electronic structure of metal ions, UV-Vis DRS analysis is used. Based on the UV-Vis DRS results obtained (see **Appendix II, Figure S5.3**), all sample (except CH100) shows two peaks around 270 and 345 nm in CH0 spectra corresponding to charge transfer transition and interband transition as per the literature (Ansari et al. 2014; Babitha et al. 2015). Absorption peak in UV region at around 245 nm is only seen in the CH100 sample that substantially corresponds to HfO_2 (Padma Kumar et al. 2015). Dopant (Hf^{4+}) substitution into ceria lattice results increase in strain due to a reduction in symmetry at the Ce sites (Babitha et al. 2015; Reddy et al. 2008b). Using Tauc's plot (Tauc et al. 1966), the bandgap value for all CH_x samples are calculated as shown in **Figure 5.6** and tabulated in **Table 5.1**.

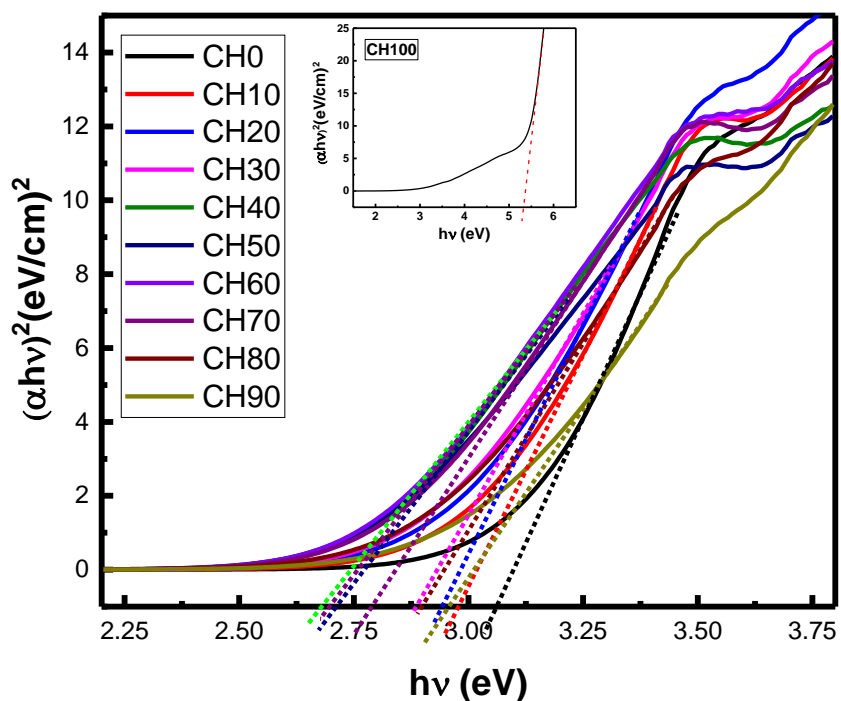


Figure 5.6: Tauc's plot of CH_x binary ceria-based metal oxides

Optical bandgap has a direct correlation with the oxygen vacancy, lattice distortion and surface defects (Xiao and Weber 2011). Concerning the variation in phase formation, the effect of optical bandgap may also change.

5.1.6. X-ray Photoemission Spectroscopy (XPS) Analysis

The O 1s spectra of CH_x samples in the single phase (CH0-CH30) and hybrid phase (CH40-CH90) obtained from XPS data is shown in **Figure 5.7 (a)** and **Figure 5.7 (b)**, respectively. The peaks obtained in O 1s matches well with the literature (Dupin et al. 2000). The O 1s peak corresponds to lattice oxygen (O_α), surface oxygen (O_β) and oxygen due to hydroxyls (O_γ) (Zhang et al. 2016).

Using CasaXPS software, the peaks were deconvoluted, and the ratio of surface oxygen concentration to the total oxygen concentration, i.e., $(O_{\beta}/(O_{\alpha} + O_{\beta} + O_{\gamma}))$ is obtained and tabulated in **Table 5.1**. For the F phase samples (CH10~CH30) and hybrid (F + M) phase (CH40 ~ CH90), the $(O_{\beta}/(O_{\alpha} + O_{\beta} + O_{\gamma}))$ is obtained in the range of (34 ~ 44 %) and (32 ~ 58 %), respectively. Among the F phase samples CH10, and hybrid phase CH40 showed better $(O_{\beta}/(O_{\alpha} + O_{\beta} + O_{\gamma}))$ values, and it may also influence the soot oxidation activity (Bueno-López et al. 2005) apart from phase, surface morphology and bandgap.

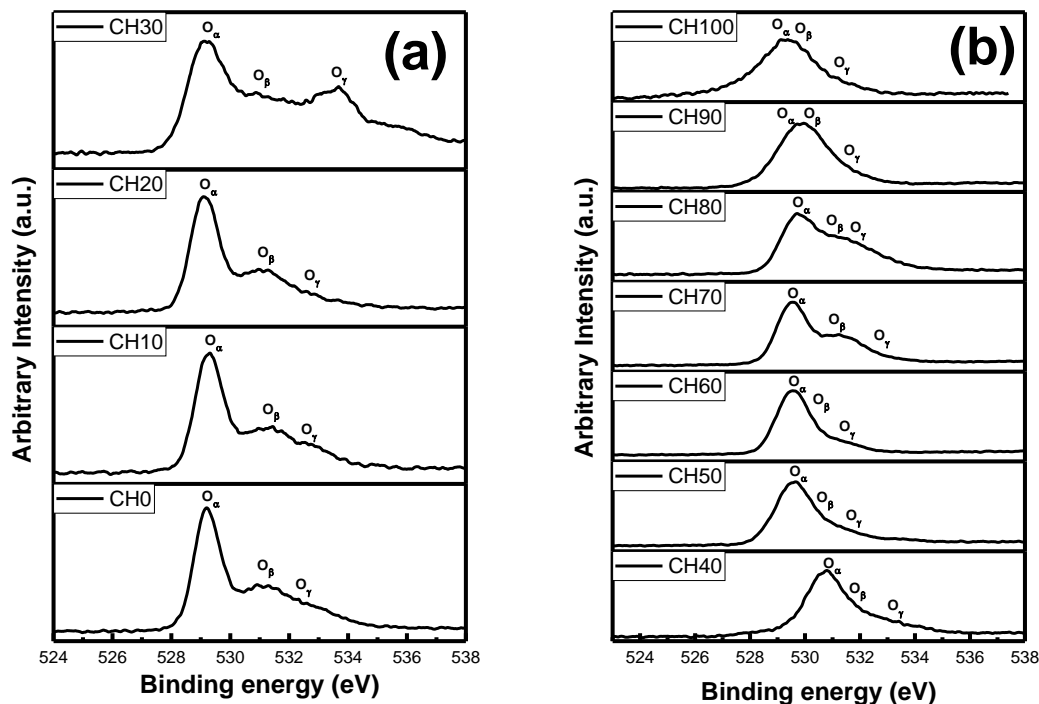


Figure 5.7: O 1s XPS of (a) CH0-CH30 and (b) CH40-CH100 samples

5.1.7. Soot Oxidation Activity

Figure 5.8 depicts the soot conversion profile of all the samples with the rise in temperature and Table 5.1 provides the T_{50} temperature data corresponding to each sample. From the conversion plot, it is evident that the activity is relatively higher for F phase (CH10 ~ CH30) samples rather than the hybrid (F+M) phase and M phase samples. Among F phase samples, CH10 (430 °C) displayed the lowest T_{50} temperature followed by CH20 and CH30 respectively. Also the order of catalytic activity in hybrid phase samples are CH40 > CH50 > CH60 ~ CH70 > CH80 > CH90 respectively. A preliminary characterization study, such as XRD and Raman spectroscopy and also the surface morphology study using SEM and SAED analysis has proved the evidence of hybrid phase from CH40 sample onwards. From this study, it is concluded that the catalytic activity

depends initially upon the metal oxide composition and sample structural morphology. As the morphology of the catalyst varies, the active contact site for soot oxidation is reduced, and thus it affects the activity of the sample. Apart from that, phase formation also affects the active contact points for the soot oxidation reaction.

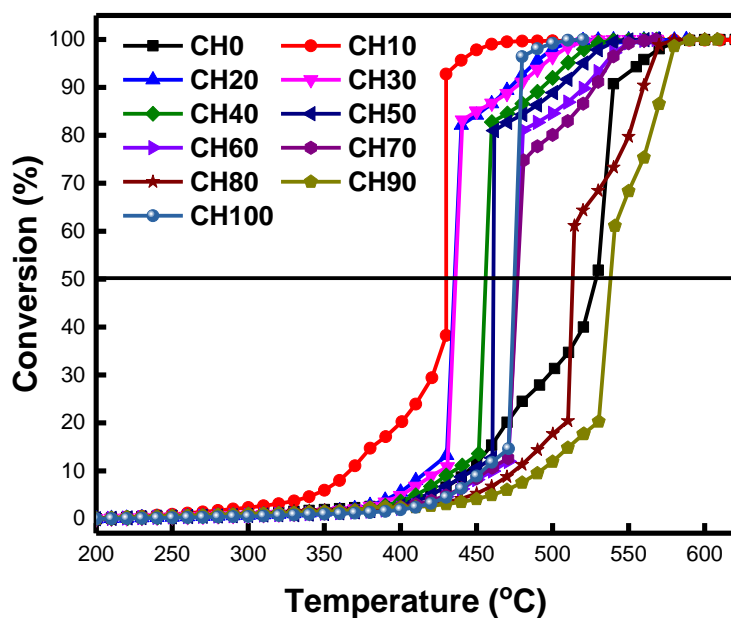


Figure 5.8: Soot oxidation conversion of CH_x binary ceria-based metal oxides

Figure S5.4 (Appendix II) shows the effect of contact mode (tight and loose) on soot oxidation activity of CH0 sample, and tight contact mode resulted in better catalytic activity than the loose contact mode. When the catalyst is in tight contact with the soot, the intrinsic property of the catalyst controls the reaction and results in better catalytic activity than compared to loose contact mode (Krishna et al. 2007; Su and McGinn 2014). **Figure S5.5 (Appendix II)** shows the effect of soot to catalyst ratio (1:4 and 1:10) on the soot oxidation activity of CH10 sample in tight contact mode. As the soot to catalyst ratio varies from 1:4 to 1:10, an increase in catalytic activity is observed, and this is related to

enhancement in the contact points of the soot and catalyst sample (Leistner et al. 2012). As the soot to catalyst ratio is changed from 1:4 to 1:10, the catalytic activity is increased by only 9°C.

Figure 5.9 (a), **Figure 5.9 (b)** and **Figure 5.9 (c)** show the variation in T_{50} temperature with the deviation in crystallite size, optical bandgap and lattice strain, respectively. From the trend, it is clear that the activity is nearly similar to the variation in these parameters in the hybrid (F+M) phase region. The lowering of catalytic activity points out the substantial influence of structural properties instead of intrinsic properties apart from the hybrid phase existence.

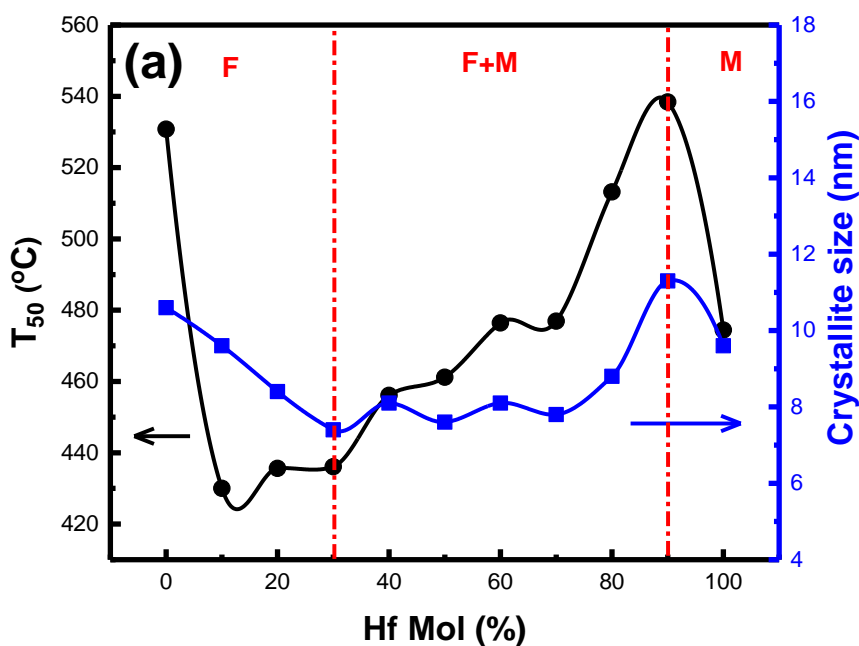


Figure 5.9: Comparison of T_{50} with (a) Crystallite size of CH_x ceria-based binary metal oxides

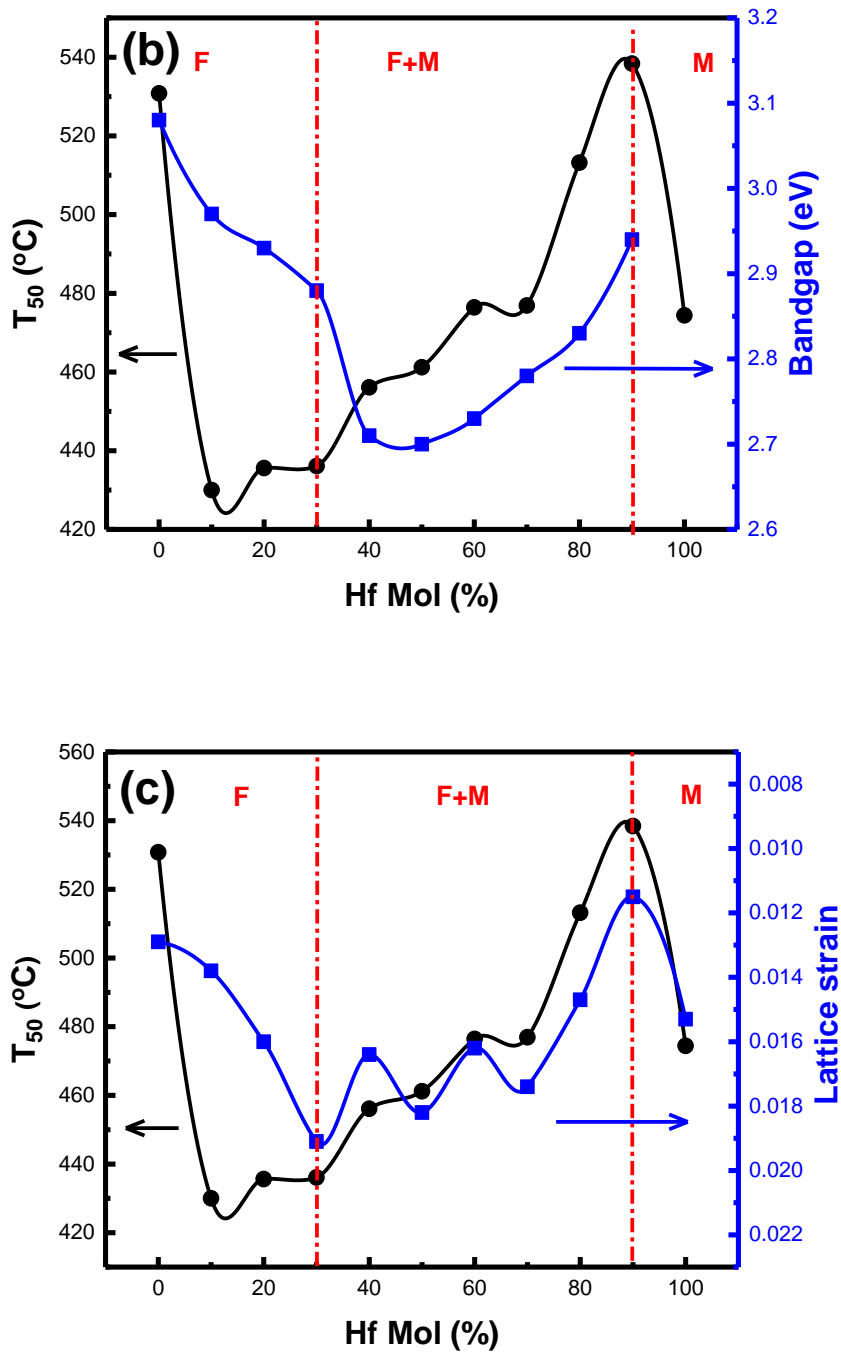


Figure 5.9: Comparison of T_{50} with (b) bandgap and (c) lattice strain for CH_x ceria-based binary metal oxides

Reddy et al. (Reddy et al. 2008a) synthesized CeO₂-HfO₂ of 80:20 mole ratio using coprecipitation method under a calcination temperature of 500 °C/5 h obtained a soot activity at 409 °C as T₅₀ temperature which is quite lower when compared to the same composition (435 °C) prepared in this study. This might be due to the difference in synthesis method, calcination temperature which resulted in lower crystallite size (5 nm) and higher surface area (78 m²/g) of those samples compared with the sample prepared in the present study.

Morphology of the sample significantly varies along with the secondary phase formation. Thus, the active sites on the catalyst surface are depleted for soot oxidation due to the hindering of redox (Ce) ions by the non-redox (Hf) ions. Lattice strain developed in the crystal decreases since the defect creation in host lattice is reduced due to decrease in dopant available within the crystal structure. As the lattice strain decreases, the oxygen mobility within the catalyst is reduced that results in a decrease in catalytic activity (Ma et al. 2014; Rushton et al. 2013). With the reduction in crystallite size lower reducibility energy is achieved (Duprez et al. 2001). Conversely, in the case of solid solution samples, CH10 with the minimum dopant content shown enhanced activity. CH10 showed the highest surface area, smaller particle size, lower degree of agglomeration and higher ($O_{\beta} / (O_{\alpha} + O_{\beta} + O_{\gamma})$) value within F phase samples (CH10 ~ CH30) that aids in improving surface properties of the samples which in turn enhances the catalytic activity.

Figure S5.6 (Appendix II) shows the graphical abstract of soot oxidation activity for CH_x binary metal oxides series. Soot oxidation study under tight contact condition of CH_x sample series confirms that the catalytic activity is higher for solid solution samples in F phase CH10 ~ CH30 (430 ~ 435 °C) rather than the hybrid phase CH40 ~ CH100 samples (450 ~ 560 °C). The textural and structural properties support the catalytic activity of F phase samples. The T₅₀ temperature, as low as 430°C is obtained for CH10, which is due to enhanced structural properties such as high surface area, low particle size, a low degree of agglomeration and high surface oxygen concentration that improves the contact points,

apart from stable morphology and phase. As far as soot oxidation is concerned, the descriptors that control the catalytic activity for CH_x samples can be generalised as stable solid solution formation with the stable host structure, optimum dopant concentration and stable structural properties. Soot oxidation being significantly controlled by structural properties, improvement in structural features is critical in enhancing the activity.

The CH_x binary metal oxides characterized by XRD analysis confirms the existence of different phases based on peaks and Vegard's rule (lattice constant (5.15 ~ 5.41 Å)) as fluorite (F), hybrid (F+M) and monoclinic (M) phases. Raman spectroscopy asserts the phase boundary of the hybrid phase from CH40. With the change in phase from single to hybrid, the morphology of the sample also varies substantially as per SEM morphological analysis. It is further supported by the variation in the SAED pattern of the samples. Soot oxidation study under tight contact condition confirms that the catalytic activity is higher for solid solution samples in F phase CH10 ~ CH30 (430 ~ 435 °C) rather than the hybrid phase CH40 ~ CH100 samples (450 ~ 560 °C). The textural and structural properties support the catalytic activity of F phase samples. As far as soot oxidation is concerned, the descriptors that control the catalytic activity for CH_x samples can be generalised as stable solid solution formation with the stable host structure, optimum dopant concentration and stable structural properties. Soot oxidation being significantly controlled by structural properties, improvement in structural features is critical in enhancing the activity.

5.2. Ce_{1-x}Sm_xO₂ (x=0.0-1.0) BINARY METAL OXIDES

Based on the study of CeO₂-HfO₂ binary metal oxide series, phase stability along with surface morphology modifies with the addition of dopant that result in reduced catalytic activity. To confirm the effect of phase on catalytic activity, a similar system of CeO₂-Sm₂O₃ is studied. Similar to CH_x series, Ce_{1-x}Sm_xO₂ (CS_x) (x varies from 0-100 mol%) binary metal oxide over the whole composition range is synthesized using the EDTA-Citrate method. From XRD, Raman analysis and UV-vis DRS analysis of CS_x, samples exists in three phases: (CS10–CS30 (Fluorite), CS40–CS90 (hybrid (Fluorite+Cubic)) and CS100 (Cubic phase)) depending on the dopant content. The various properties of the series calculated using different characterization techniques are given in **Table 5.2** (Anantharaman et al. 2018b). The CS_x samples in fluorite (F) phase displayed high surface area, low degree of agglomeration, low band gap energy and high oxygen vacancies than compared to the CS_x samples in hybrid-phasic (F+C) and cubic (C) phase. Among the CS_x samples, CS10 sample displayed high surface area (38 m²/g), a low degree of agglomeration ($\phi=0.36$), low band gap energy (3.04 eV) and high oxygen vacancy concentration (64.4 %). This factors resulted in enhancing its soot oxidation activity (T₅₀=480 °C) (Anantharaman et al. 2018b).

Table 5.2: Crystallite size, BET surface area, pore volume, particle size, lattice strain, degree of agglomeration, composition, intensity ratio, bandgap and T₅₀ temperature of CS_x samples calcined at 600°C/5h (Anantharaman et al. 2018b)

Metal oxide	Crystallite size ^a (nm)	BET Surface area (m ² /g)	Particle size ^b (nm) [#]	Lattice strain ^c (ε)	Degree of agglomeration ^d (φ) [^]	Composition using EDS (%)		I _{ov} /I _{F2g} ^e (%)	Band gap ^f (eV)	Ce ³⁺ reducibility ^g (%)	O _β / (O _α +O _β +O _γ) ^g (%)	T ₅₀ temperature (°C)
						Ce	Sm					
CS0	10.6	41	17	0.013	1.6	100	0	--	3.08	30	41	530
CS10	08.2	38	23	0.018	2.8	94	6	5	3.04	25	64	480
CS20	08.0	45	19	0.018	2.4	82	18	12	3.06	41	45	500
CS30	07.9	35	24	0.018	3.0	73	27	20	3.07	4	34	511
CS40	06.9	29	29	0.021	4.2	63	37	35	3.06	25	12	502
CS50	06.7	24	35	0.022	5.2	53	47	51	3.09	16	07	512
CS60	05.6	18	46	0.026	8.2	40	60	--	3.10	--	08	531
CS70	05.1	16	50	0.029	9.8	32	68	--	3.10	--	10	537
CS80	04.6	14	58	0.032	12.6	22	78	--	3.12	35	06	542
CS90	04.4	10	77	0.033	17.5	12	88	--	3.15	05	34	538
CS100	07.2	08	95	0.019	13.2	0	100	--	5.06	--	54	537

^a- Calculated from intense XRD peak using Debye-Scherrer equation; ^b- Calculated from BET Surface area; ^c- Calculated from intense XRD peak; ^d- Calculated as the ratio of particle size and crystallite size; ^e- Calculated using intensity ratio of Raman peak, ^f- Calculated using Tauc's plot and ^g. Calculated using XPS Ce 3d or O 1s peaks using CasaXPS software

The binary metal oxide systems over the whole composition range were studied for different dopants such as CeO₂-HfO₂ (CH_x), CeO₂-Sm₂O₃ (CS_x) and CeO₂-Gd₂O₃ (CG_x). From the study, it is significantly evident that only up to 30 mol% all the system exists in a stable solid solution form. Secondary phase starts segregating with the dopant addition that affects various physiochemical properties of the system, which in turn hinders the active sites on the catalyst surface that has the potential in reducing the catalytic activity. The secondary phase of monoclinic in the case of CH_x and cubic in the case of CS_x and CG_x are evident from the lattice constant calculation from 30 mole % dopant onwards. **Figure 5.10** shows the lattice constant variation of CH_x, CS_x and CG_x system with the rise in dopant content. The lattice is constant for CH_x decreases with increase in dopant content, which confirms the smaller ionic radius of the dopant ion (Hf⁴⁺). Similarly, the lattice constant increases for larger ionic radius dopants of Sm³⁺ and Gd³⁺. Based on the phase segregation, a concentration lower than 30 mol% is optimum for the activity study.

The catalytic activity study of CH_x and CS_x sample series confirm that phase stability is the critical descriptor for both the sample series despite the variation in dopant nature. Isovalent (Hf⁴⁺) dopant modifies the structural (morphology) properties. However, the catalytic activity of aliovalent (Sm³⁺) doped samples are influenced by the electronic (optical bandgap) properties of the sample. Thus, it can be concluded that the dopant nature is a critical descriptor in catalytic activity not only for single metal oxides but also for binary ceria-based system. However, the descriptor that is influenced with the change in dopant for binary system is the host structure, phase stability, morphology and oxygen mobility. For further study, the host structure variation, phase change and surface morphology modification are restricted by choosing suitable composition in such a way that the solid solution is confirmed without any hybrid phase formation. Thus the other descriptors that possibly influence oxygen vacancy can be studied in detail.

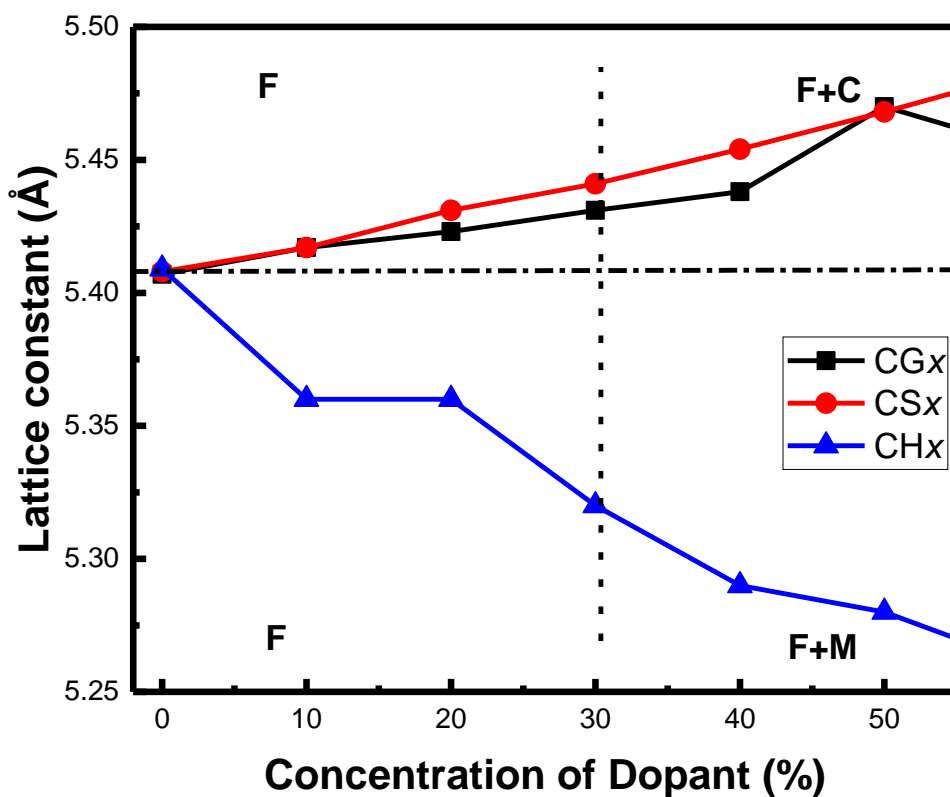


Figure 5.10: Variation in lattice constant with the increase in dopant concentration for CH_x, CS_x and CG_x binary ceria-based metal oxides

5.3. Ce_{0.9}M_{0.1}O₂ (M=Sn, Hf, Zr, Gd, Sm & La) BINARY SOLID SOLUTION

Based on the preliminary study of binary metal oxides over whole composition range, the optimum composition is selected as 90:10 molar ratio of ceria: dopant, since the solid solution formation is confirmed for both the series in this range and also the highest catalytic activity is obtained. Maintaining the composition at optimum, dopant material is changed to find the variation in descriptors for catalytic activity. CeO₂ (C), Ce_{0.9}Sn_{0.1}O₂ (CT), Ce_{0.9}Hf_{0.1}O₂ (CH), Ce_{0.9}Zr_{0.1}O₂ (CZ), Ce_{0.9}Gd_{0.1}O₂ (CG), Ce_{0.9}Sm_{0.1}O₂ (CS) and Ce_{0.9}La_{0.1}O₂ (CL) were synthesized using the EDTA-Citrate method and characterized using various techniques, and further soot oxidation activity is analysed. Since the composition remains the same, the effect of host structure variation among the samples and thus the secondary phase formation which deteriorates the catalytic activity can be neglected. In specific, binary ceria-based metal oxides are classified based on the ionic radius of dopant added since the dopant metal nature influences the catalytic activity as per the previous study. The binary metal oxides in this study are classified as larger ionic radius and smaller ionic radius samples. Cations with radius smaller than Ce⁴⁺ (0.97 Å), such as Hf⁴⁺ (0.83 Å), Zr⁴⁺ (0.84 Å) and Sn⁴⁺ (0.81 Å) (Shannon 1976) are categorised as smaller ionic radius dopants. Similarly, dopants with ionic radius higher than Ce⁴⁺ are categorised as larger ionic radius samples (Gd³⁺ (1.05 Å), Sm³⁺ (1.08 Å) and La³⁺ (1.16 Å) (Shannon 1976). Again, smaller ionic radius dopants fall under the classification of isovalent since the charge of dopant and host cation remains the same. Similarly, the larger ionic radius samples are classified as aliovalent dopants due to the difference in charge between host and dopant cation. The effect of various dopants on catalytic activity is tested using different characterization tools and used for soot oxidation.

5.3.1. X-ray Diffraction (XRD) Analysis

The synthesized binary ceria-based metal oxides are initially characterized using XRD analysis for phase identification. Diffraction peaks are obtained for all the samples and shown in **Figure S5.7 (Appendix II)**. All samples (C, CT, CH, CZ CG, CS and CL)

displayed peak analogous to the cubic fluorite structure of CeO₂ (Atribak et al. 2008). Apart from fluorite phase peaks of CeO₂, CT alone shows rutile type tetragonal phase of SnO₂ in a trace that confirms the hybrid phase formation. With the presence of the secondary phase, the activity may be hindered for CT sample since the active sites need not be readily available for the reaction (Katta et al. 2010). Lattice constant, crystallite size, lattice strain and facet plane ratio are calculated from the corresponding diffraction peaks, and their values are given in **Table S5.1 (Appendix II)** along with BET surface area, pore volume and particle size calculated from BET surface area. **Figure 5.11** displays lattice constant variation with the change in dopant ionic radius for all the binary metal oxide samples. It is evident from the variation in values that smaller and larger ionic radius samples have lower and higher lattice constant, respectively in comparison with the C sample (Zhu et al. 2010).

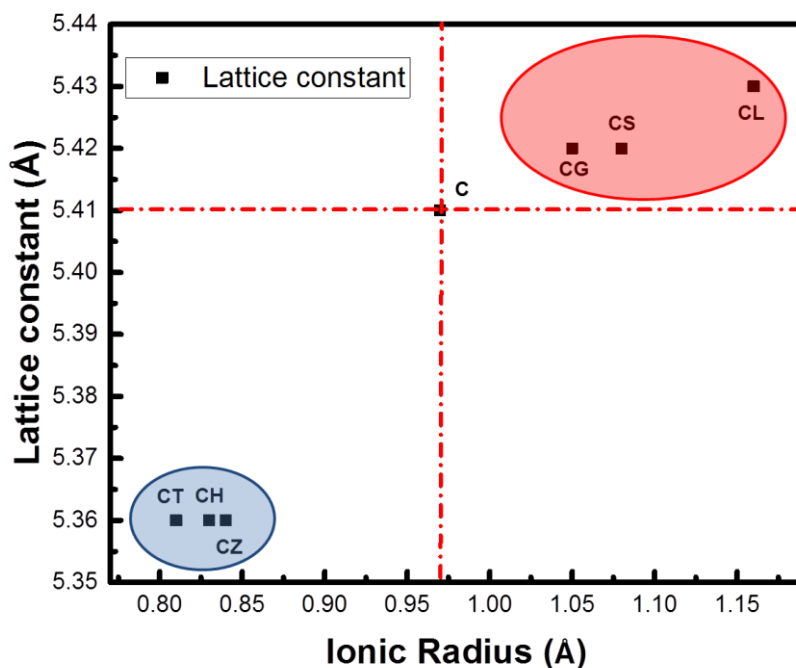


Figure 5.11: Variation of lattice constant with the increase in ionic radius for binary ceria-based metal oxides

The higher lattice constant observed for CL is due to the higher ionic radius of La^{3+} . According to Reddy et al. (2008b), oxygen vacancy formation energy and reducibility depend upon the dopant ionic radius, and thus the catalytic activity varies with the variation in cation radius (Reddy et al. 2008b). Dopants of larger and smaller ionic radius may influence soot oxidation activity differently. **Figure 5.12** confirms that all doped samples show higher lattice strain than C and thus higher oxygen diffusion may result in these samples. With the improved lattice strain, oxygen migration smoothens, and thus the oxidation reaction occurs quickly (Rushton et al. 2013). Hence, in the present study, all doped ceria-based binary metal oxides may have better catalytic activity than C.

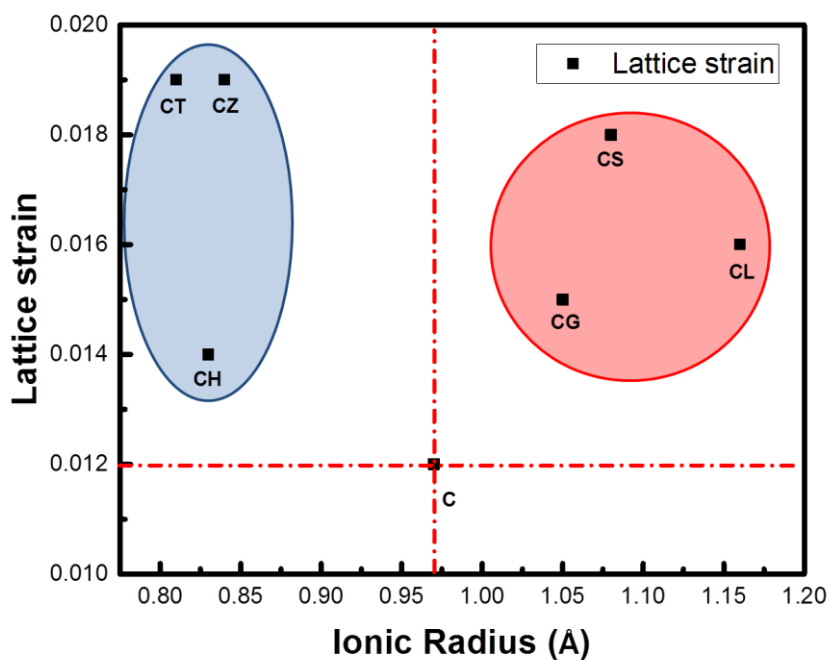


Figure 5.12: Variation of lattice strain with the increase in ionic radius for binary ceria-based metal oxides

The intensity ratio of the reactive facet planes of (220)/(111) and (200)/(111) are calculated from the diffraction peaks and plotted with the change in dopant ionic radius and are given in **Figure 5.13**. Doped samples show almost the same or higher (200)/(111) ratio than pure C sample. On the other hand, for (220)/(111) planes, CH, CZ, CG and CL has almost higher ratio than C. Aneggi et al. (2014) reported a direct correlation between soot oxidation and exposed surface planes due to higher reactivity of (200) and (220) planes with (200) being more reactive (Aneggi et al. 2014). A study by Shen et al. (2015) states that the reactive plane availability improves oxygen migration from the bulk and thus effectively enhance the catalytic activity (Shen et al. 2015). Planes of (200) which is more reactive than (220) in doped samples has the potential to improve the catalytic activity. As per the values of (200) intense planes and lattice strain, doped samples enhance the catalytic activity compared to C.

BET surface area variation with ionic radius is given in **Figure 5.14**, which confirms that the EDTA-Citrate method results in surface area value in the range of 25 ~ 45 m²/g. A direct relation between surface area and activity holds good for morphologically modified ceria samples studied by Aneggi et al. (Aneggi et al. 2014). On the other hand, a study by Piumetti et al. (Piumetti et al. 2016), Thrimurthulu et al. (Thrimurthulu et al. 2012) and Guillén-Hurtado et al. (Guillén-Hurtado et al. 2012) confirms that surface area does not control the activity. Instead, actual points where catalyst and soot are in contact determines the catalyst performance (Guillén-Hurtado et al. 2012; Piumetti et al. 2016b; Thrimurthulu et al. 2012). Since the synthesis method adopted and composition remains the same for binary metal oxides, the variation in morphology may be limited. Particle size and degree of agglomeration of ceria-based metal binary oxide samples are also calculated and given in **Table S5.1 (Appendix II)**. The particle sizes are higher than the crystallite size of the corresponding sample that confirms the agglomeration of particles. Also, the degree of agglomeration confirms that all doped samples are more agglomerated than C.

Intrinsic structural descriptors that may affect the soot oxidation activity of ceria-based binary metal oxides as per XRD results are solid solution formation (Katta et al. 2010),

dopant ionic radius (Reddy et al. 2008b), lattice strain (Rushton et al. 2013) and reactive (200) plane (Aneggi et al. 2014). On the contrary, the surface area may not be a descriptor in this study. Raman spectroscopy is carried to find the metal-oxygen bond and lattice defects in the binary oxide samples.

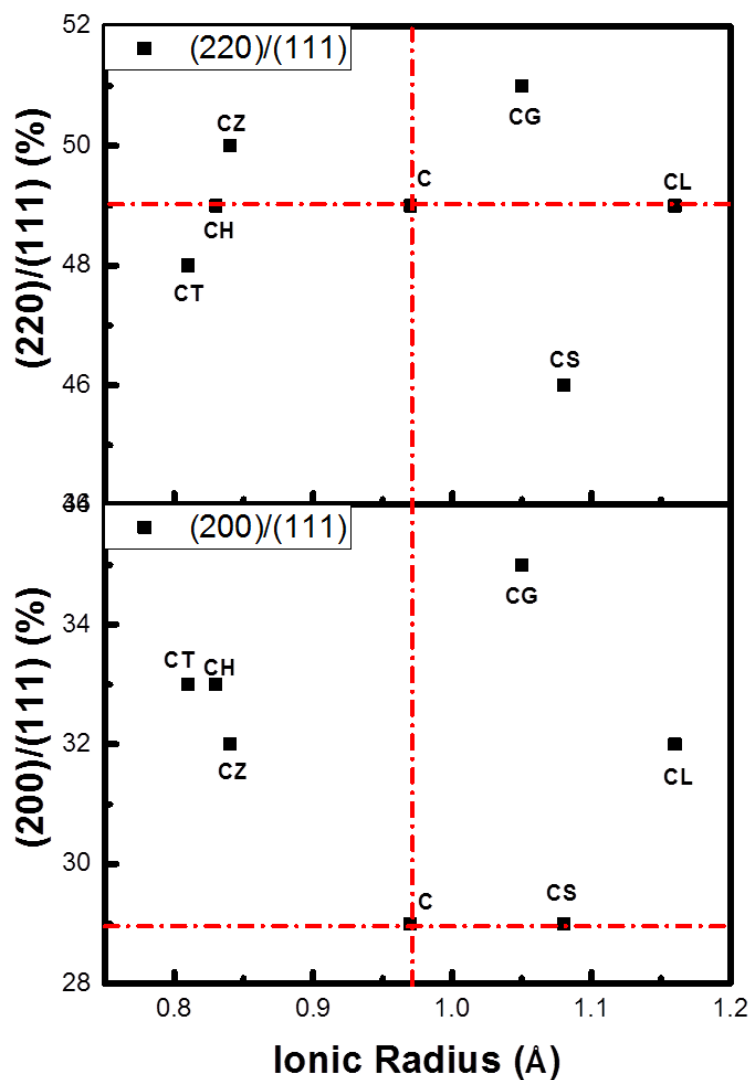


Figure 5.13: Variation of lattice planes with the increase in ionic radius for binary ceria-based metal oxides

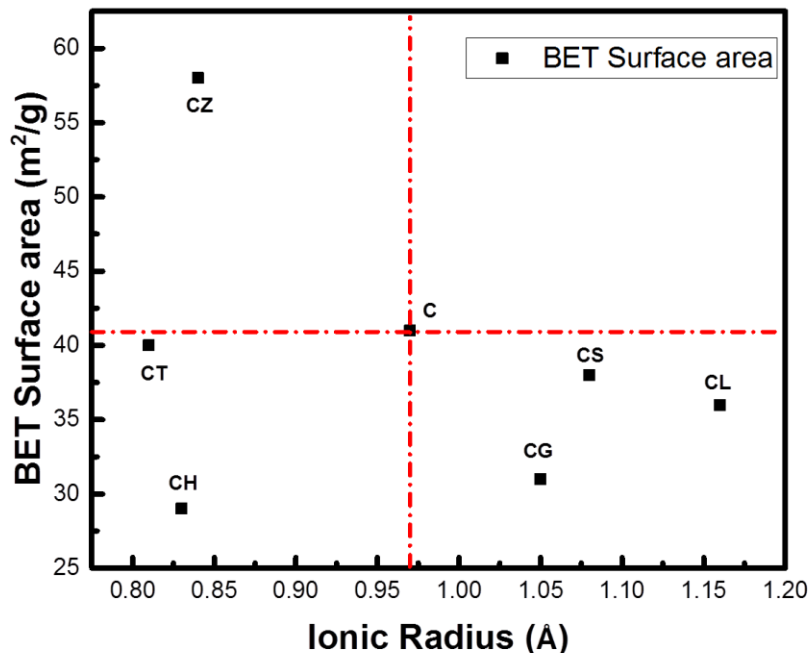


Figure 5.14: Variation of BET Surface area with the increase in ionic radius for binary ceria-based metal oxides

5.3.2. Raman Spectroscopy Analysis

Raman spectra of all binary metal oxide samples are given in **Figure S5.8**. The F_{2g} peak analogous to ceria in the fluorite phase is evident in all samples (Weber et al. 1993). Blueshift is observed in the F_{2g} peak for samples with smaller ionic radius and redshift for larger ionic radius samples (Mukherjee et al. 2017). Apart from F_{2g} peak oxygen vacancy is observed in all the samples with the existence of a shoulder peak at $560 \sim 610 \text{ cm}^{-1}$ (Vinodkumar et al. 2013). The ratio of the intensity of oxygen vacancy to F_{2g} peak represented as $(I_{OV}/I_{F_{2g}})$ confirms the availability of total oxygen within the lattice (Sarkar et al. 2017). **Figure 5.15** illustrates the $I_{OV}/I_{F_{2g}}$ variation with the ionic radius. Higher ratios are observed for CH and CL samples than C and lower for CT, CZ, CG and CS samples than C.

Aliovalent dopant addition leads to a difference in charge between dopant (Gd^{3+} , Sm^{3+} and La^{3+}) and host cation (Ce^{4+}), which in turn results in charge compensation and thus enhance oxygen vacancy formation (Sudarsanam et al. 2014). The Raman intensity ratio calculated using the data reflects the lattice oxygen from the bulk (Guo et al. 2011). If lattice oxygen has the potential in dictating the soot oxidation activity, then the larger ionic radius CL may have better catalytic activity than the smaller ionic radius samples. Oxygen vacancy is critical descriptor in controlling the catalytic activity due to their involvement in enhancing the oxidation reaction of soot (Lin et al. 2018). However, the property that controls the mobility and creation of oxygen vacancy may vary upon dopant nature. In further, the variation in sample morphology with the dopant addition to ceria lattice is studied using SEM and TEM analysis.

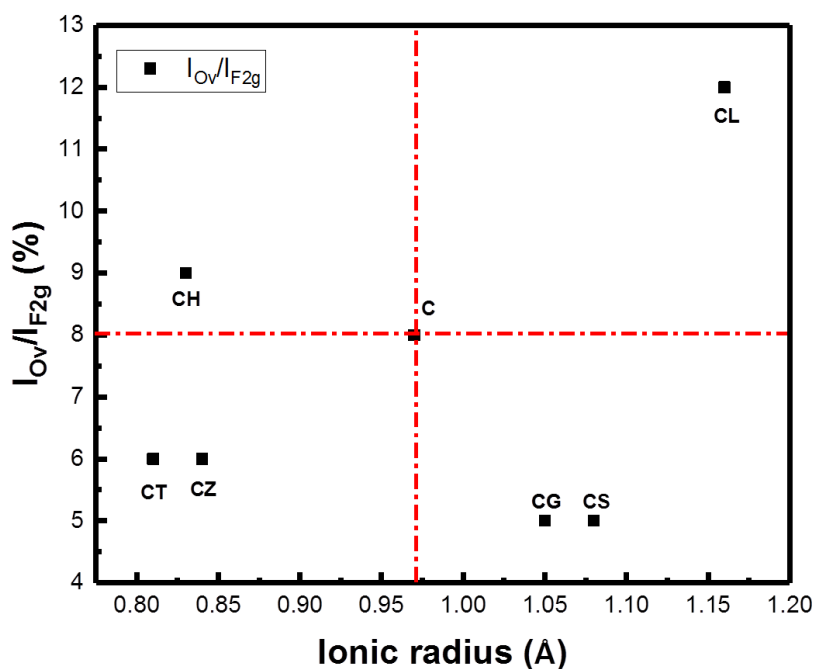


Figure 5.15: Variation of I_{Ov}/I_{F2g} with the increase in ionic radius for binary ceria-based metal oxides

5.3.3. Scanning Electron Microscopy (SEM) Analysis

The SEM images of the samples are displayed in **Figure 5.23**. Sample morphology confirms the agglomerated flaky nature without any specific shape. **Figure 5.23 (a)** to **Figure 5.16 (e)** confirms the flaky nanoparticles for the entire binary oxide samples (Zhang et al. 2016). Not much deviation in morphology is evident from the SEM image of the samples. This could be related to the solid solution formation as confirmed by the XRD results which is specific to the selected composition. Higher resolution TEM analysis is further utilised to confirm the SEM results of constant morphology.

5.3.4. Transmission Electron Microscopy (TEM) Analysis

TEM micrographs of CZ and CL samples are given in **Figure 5.17** and **Figure 5.18**, respectively. TEM image in **Figure 5.17 (a)** and **Figure 5.18 (a)** for CZ and CL samples confirm particles without any specific shape. **Figure 5.17 (b)** and **Figure 5.18 (b)** shows HR-TEM image of CZ and CL samples, with the interplanar distance of lattice fringes that corresponds to intense (111) plane in both the samples. Similarly, the SAED pattern of CZ and CL in **Figure 5.17 (c)** and **Figure 5.18 (c)** corresponds to the plane calculated from the XRD results of the respective samples.

Surface morphology significantly influences the soot oxidation activity due to structural modifications (Aneggi et al. 2014; Zhang et al. 2016). With the synthesis procedure for all the binary metal oxides remaining the same, the structural morphology does not vary with the dopant addition. The effect of morphology can be neglected along with BET surface area for soot oxidation activity. In further, the effect of the optical bandgap is analysed using UV-Vis DRS analysis of the samples.

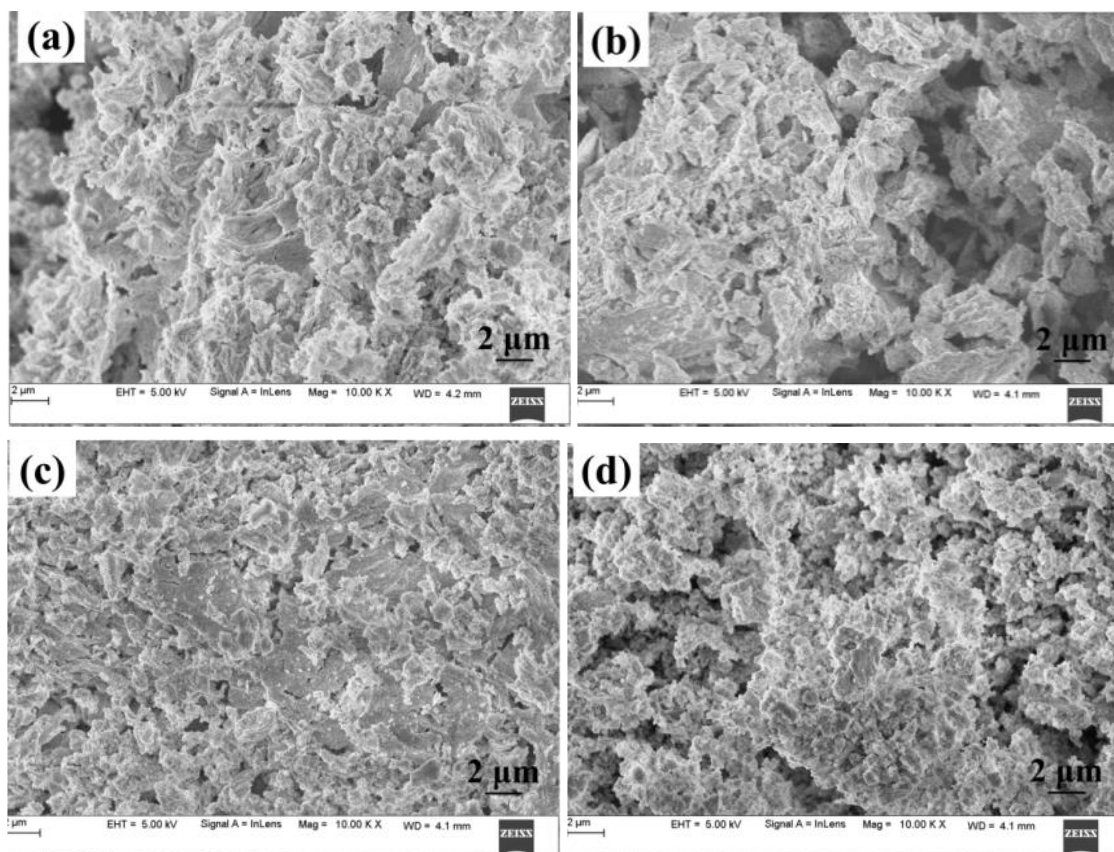


Figure 5.16: SEM images of (a) C, (b) CT, (c) CH and (d) CZ samples

(Contd.)

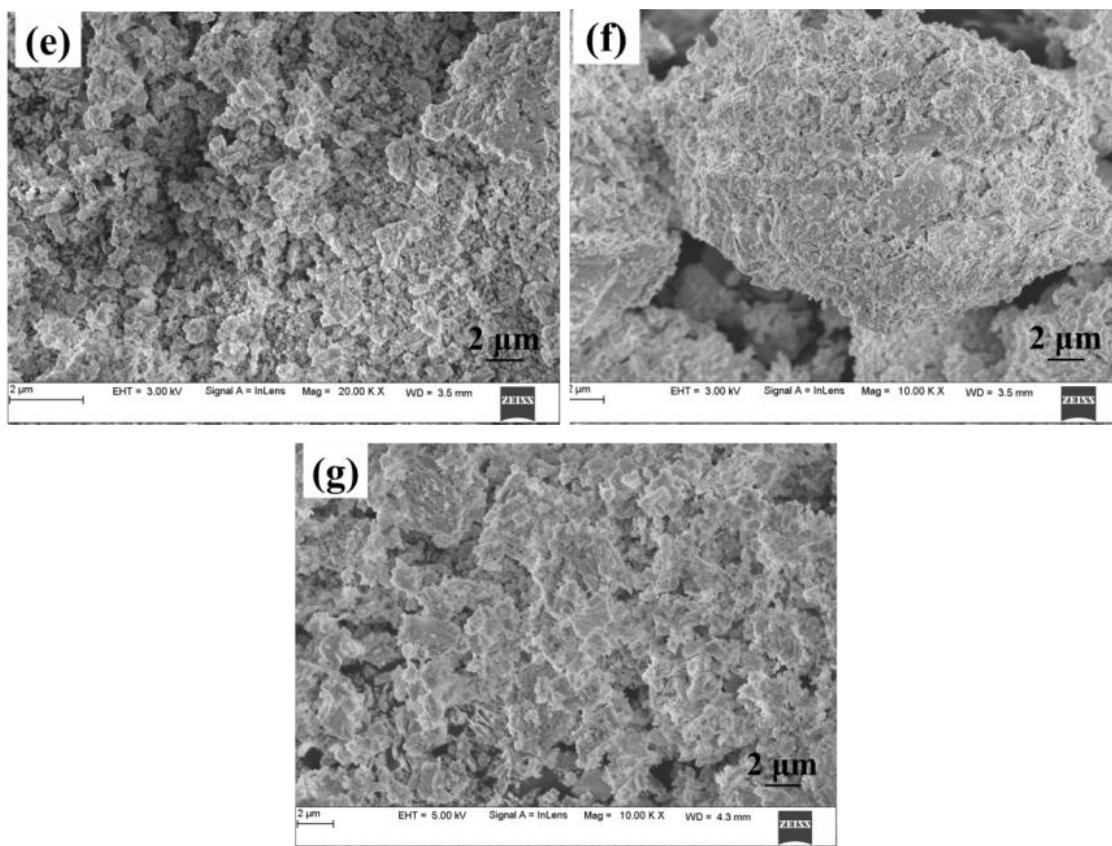


Figure 5.16: SEM images of (e) CG, (f) CS and (g) CL samples

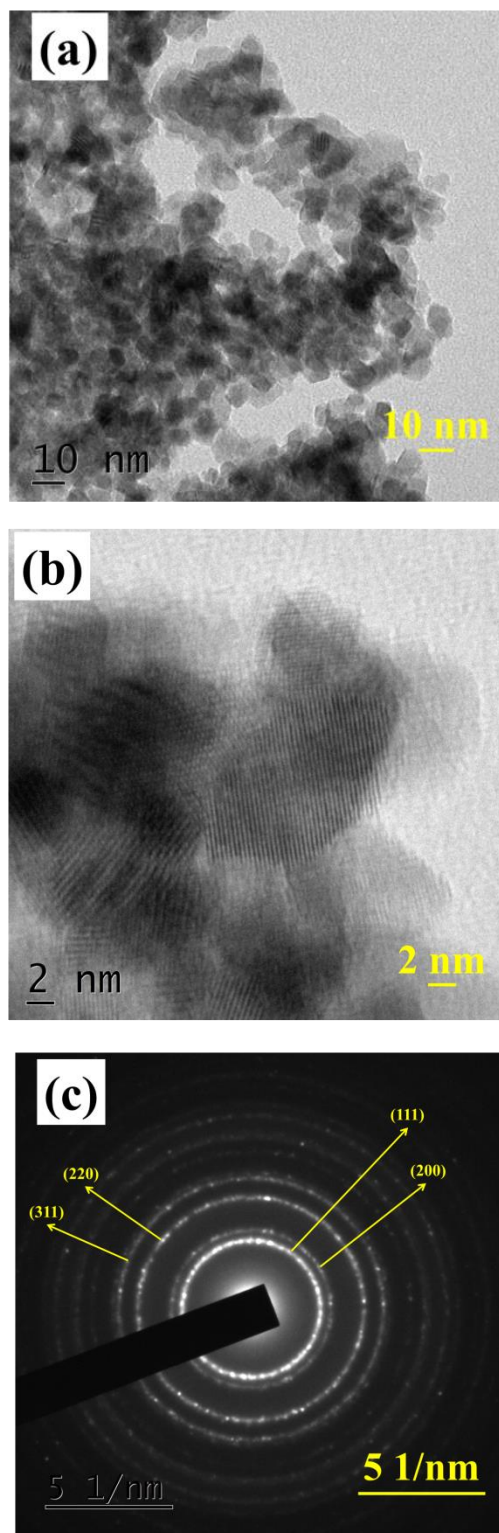


Figure 5.17: (a) TEM, (b) HR-TEM and (c) SAED pattern of CZ sample

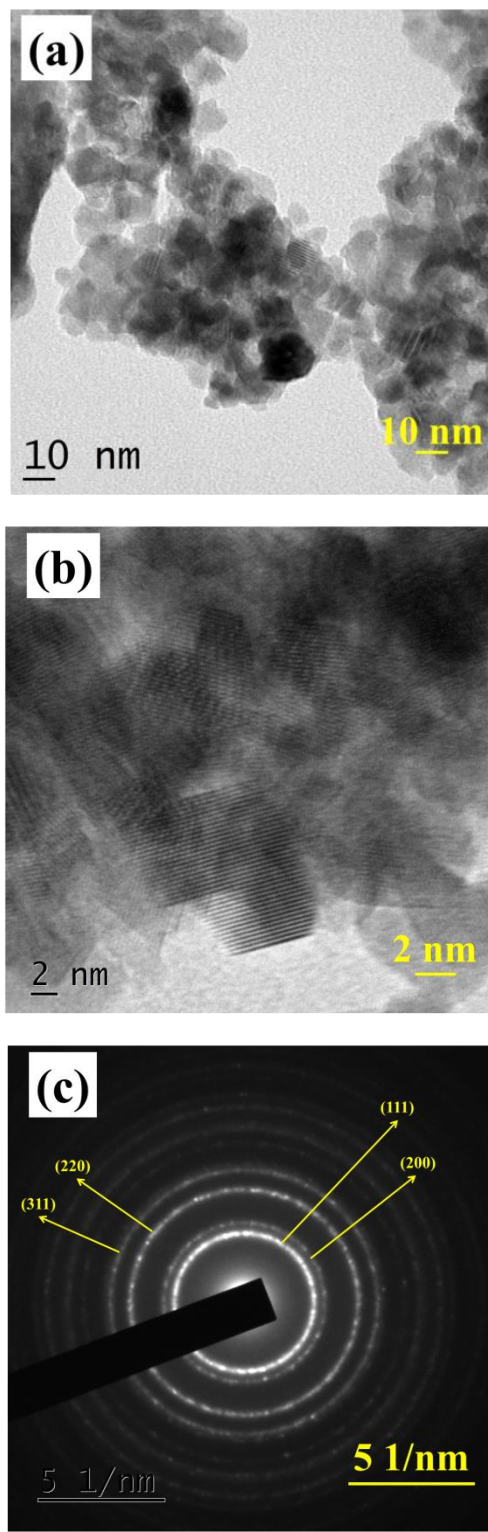


Figure 5.18: (a) TEM, (b) HR-TEM and (c) SAED pattern of CZ sample

5.3.5. UV-Vis Diffuse Reflectance Spectroscopy (UV-Vis DRS) Analysis

The absorbance spectra in UV and Visible range of respective samples obtained are given in **Figure S5.9** in **Appendix II**. Peaks corresponding to the charge transaction and interband transaction matches well in all the samples (Calvache-Muñoz et al. 2017). The direct bandgap is calculated from the absorbance peaks using Tauc's plot (see **Appendix II Figure S5.10**) (Tauc et al. 1966). **Figure 5.19** shows the optical bandgap of both smaller and larger ionic radius samples. Bandgap values obtained matches with the literature values reported (Ansari et al. 2014). Smaller ionic radius samples with a smaller lattice constant have lower bandgap values, and on the other hand, larger ionic radius has a higher bandgap value. Apparent relation holds between the ionic radius and optical bandgap for the samples (Getsoian et al. 2014).

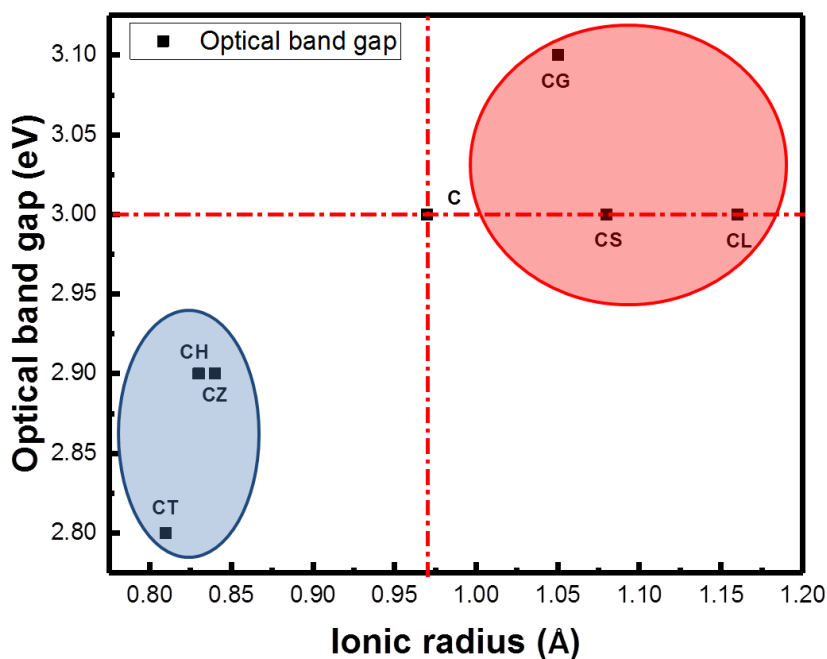


Figure 5.19: Variation of Optical bandgap with the increase in ionic radius for binary ceria-based metal oxides

The bandgap variation is directly proportional to the lattice constant due to the change in metal interaction (Mia et al. 2017). Intermediate level with vacant sites are formed with the lowering of the bandgap, that may enhance the rate of soot oxidation reaction. Bandgap values decrease with the improvement in defect density (Filtschew et al. 2016) and Ce³⁺ concentration (Ansari et al. 2014). Mukherjee et al. (Mukherjee et al. 2017) showed a decrease in bandgap for doped samples, due to the increase in oxygen defect density calculated from Raman analysis (Mukherjee et al. 2017). With the reduction in bandgap values, the defect sites are formed easily that results in enhancing the oxygen vacancy formation and thus improves the catalytic activity. In this light, the optical bandgap along with oxygen vacancy from Raman study may be a critical intrinsic descriptor that has potential influencing the soot oxidation activity apart from the structural descriptor. Based on the results obtained, the trend in I_{Ov}/I_{F2g} matches well with the obtained optical bandgap specifically for smaller ionic radius samples. In contrary, for larger ionic radius binary metal oxides, CL with higher I_{Ov}/I_{F2g} did not show a higher optical bandgap value. This may be because Raman spectra account only lattice oxygen vacancy. The change in oxygen vacancy formation mechanism for isovalent and aliovalent might be the reason for the difference in optical bandgap trend. Further, the Ce³⁺ concentration and surface oxygen concentration are calculated using XPS analysis.

5.3.6. X-ray Photoemission Spectroscopy (XPS) Analysis

The elemental oxidation state of the sample is analysed using XPS analysis of Ce 3d and O 1s shown in **Figure S5.11 (a)** and **Figure S5.11 (b)** (**Appendix II**), respectively. XPS is a surface characterization that helps in understanding the surface features of the catalyst at which soot essentially oxidise (Turishchev and Kashkarov 2008). Spin-orbital multiplets of Ce 3d_{5/2} and 3d_{7/2} contribute to the multiple oxidation states of Ce³⁺ and Ce⁴⁺ (Andana et al. 2016; Thrimurthulu et al. 2012). Reducibility ratios are calculated based on the deconvoluted peaks as $(Ce^{3+} / (Ce^{3+} + Ce^{4+}))$ and are plotted for all the samples with the increase in ionic radius (see **Figure 5.20**) (Devaiah et al. 2015). From the figure, it is well evident that the reducibility ratio is higher for smaller ionic radius samples rather than for

larger ionic radius samples. Samples having higher reducibility shows better catalytic activity due to improved redox cycle for soot oxidation reaction (Fang et al. 2008). Lower reducibility ratio for larger ionic radius samples could be due to reduced redox cycle since they form mostly lattice oxygen as per the Raman analysis (Krishna et al. 2007).

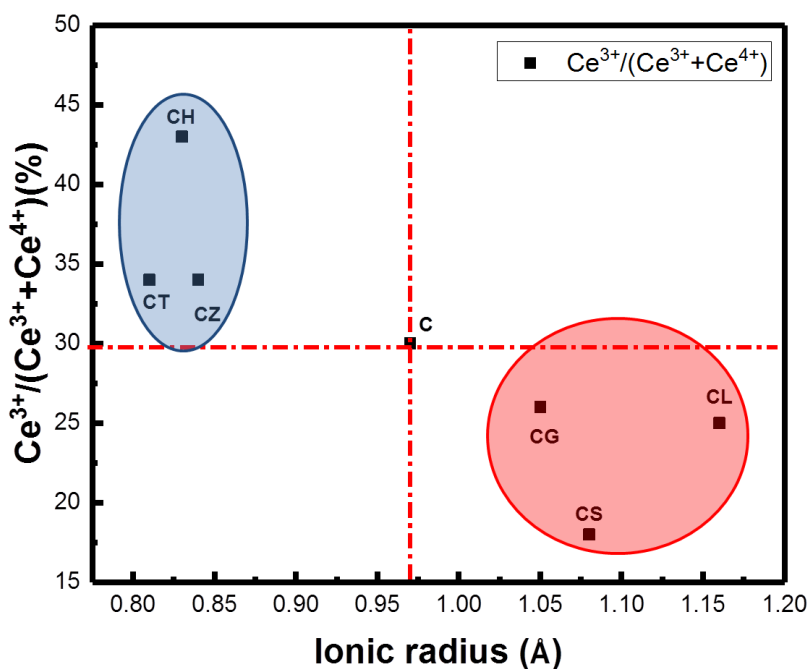


Figure 5.20: Variation of $(\text{Ce}^{3+} / (\text{Ce}^{3+} + \text{Ce}^{4+}))$ for binary ceria-based metal oxides

On deconvoluting the peaks for O 1s, three oxygen peaks are seen that corresponds to lattice oxygen (O_α), surface oxygen (O_β) and weakly bound oxygen (O_γ), respectively (Devaiah et al. 2015; Guo et al. 2011). The relative ratio of surface oxygen to the total oxygen ($\text{O}_\beta / (\text{O}_\alpha + \text{O}_\beta + \text{O}_\gamma)$) plot with the increase in ionic radius shown in **Figure 5.21**, relates the surface oxygen mobility of the sample (Devaiah et al. 2015). The surface oxygen vacancy concentration for both smaller and larger ionic radius samples is almost in similar range. Despite better $I_{\text{ov}}/I_{\text{F2g}}$ ratio from Raman results for aliovalent CL, surface oxygen vacancy calculated from XPS is low. This could be related to higher lattice oxygen

(O_α) in bulk rather than surface oxygen (O_β) for CL that results from charge difference between dopant and host cations. Even lattice oxygen in CL can involve in the oxidation reaction and may affect the catalytic activity. Thus, the critical descriptor defined for soot oxidation reaction is oxygen vacancy as per initial characterization study. Whether it is surface oxygen (Gao et al. 2017; Mukherjee et al. 2017) or lattice oxygen (Zhu et al. 2007) depends on the dopant ionic radius. Due to the lowering of lattice oxygen diffusion than surface oxygen, a corresponding lowering in the activity might be seen in catalytic activity for CL sample (Krishna et al. 2007). The catalytic activities for soot oxidation reaction are studied further, and the detailed analyses of different descriptors are discussed.

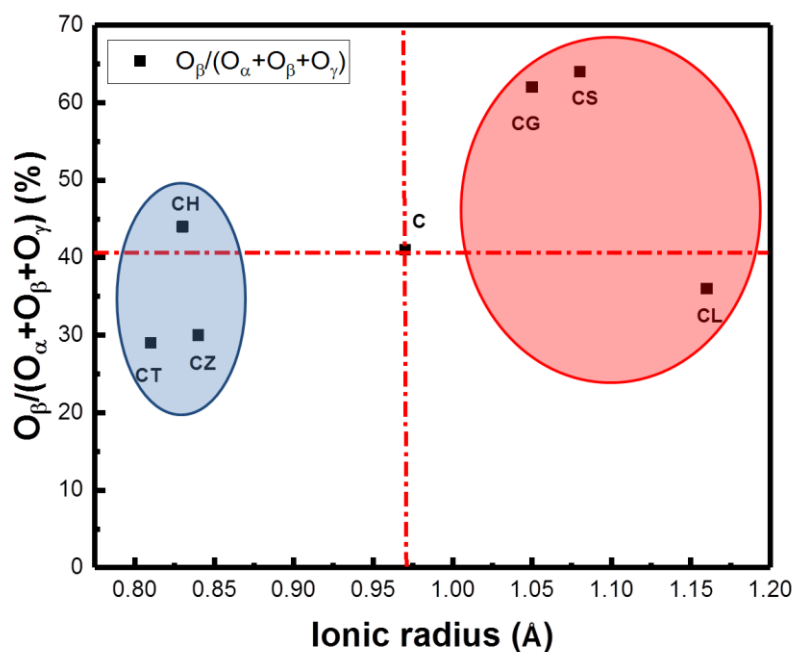


Figure 5.21: Variation of ($O_\beta / (O_\alpha + O_\beta + O_\gamma)$) for binary ceria-based metal oxides

5.3.7. Soot Oxidation Activity

The soot conversion profile of binary metal oxides are shown in **Figure S5.12 (Appendix II)** and **Figure 5.22** show the variation in T_{50} temperature with the ionic radius. It is evident that the T_{50} temperatures of doped samples are lower than C due to the improved lattice strain and (200) planes as studied from XRD. Among the smaller ionic radius samples (CT, CH and CZ), CT has significantly lower activity ($T_{50}=450$ °C) due to secondary phase formation as evident from XRD peaks which hinders the active site contact. Almost similar T_{50} temperature obtained for CH and CZ (430 °C and 425 °C respectively) could be due to the similar dopant ionic radius with the same oxidation state of +4 between host and dopant ion. While smaller ionic radius dopants are added to ceria lattice, lattice constant decreased, and lattice strain increased that confirm the incorporation of dopants into ceria lattice.

Highly reactive (200) and (220) plane availability in higher quantity for CH and CZ may result in reducing the energy for oxygen vacancy formation and results in lower T_{50} temperature. Even though CZ has a higher surface area, correspondingly T_{50} temperature variation is not evident that indicates the surface area is not directly influencing soot oxidation activity of samples in this study. I_{Ov}/I_{F2g} which indicates the lattice oxygen concentration is higher specifically for CH and so the activity is improved significantly. However, optical bandgap has reduced while doping C with smaller ionic radius dopants. As the bandgap reduced, defect sites are formed that lowers oxygen vacancy formation energy. Isovalent Hf⁴⁺ and Zr⁴⁺ create defect sites due to ionic radius difference between host and dopant cation that improves the oxygen migration within the ceria lattice and thus aids the soot oxidation reaction. Doping smaller ionic radius sample has reduced the optical bandgap, which is critical for defect site creation that could be a primary descriptor for catalytic activity.

The cations with +3 oxidation state are doped in ceria lattice with larger ionic radius (CG, CS and CL) which are of different charge than the host Ce⁴⁺ (aliovalent dopants). These

samples display a higher T_{50} temperature than the smaller ionic dopant as shown in **Figure 5.22**. CL shows the lowest T_{50} temperature of 450 °C compared to CG and CS with a T_{50} temperature of 490 °C and 480 °C, respectively.

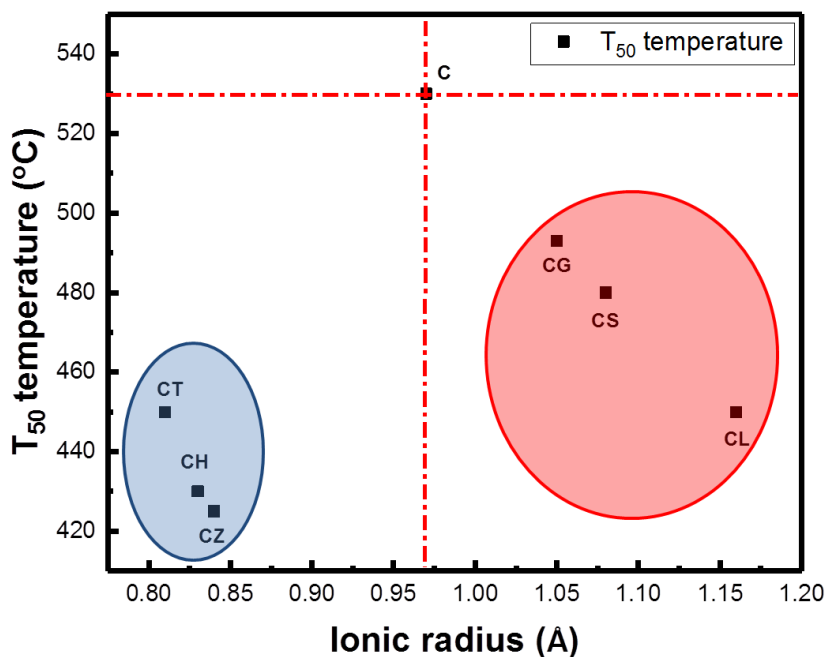


Figure 5.22: Soot oxidation activity of binary ceria-based metal oxides

The lattice constant is higher for CL than C samples due to the higher ionic radius of the dopants. Highly reactive facet planes of (200) and (220) in CG and CL improves the oxidation reaction by reducing the oxygen vacancy formation energy. Oxygen concentration calculated for larger ionic radius samples using Raman spectroscopy shows a higher content of oxygen vacancy for CL compared to CG and CS. this is due to the addition of highest ionic radius La having a charge of +3 which is different from host Ce of +4 charge, that results in charge compensation mechanism. The optical bandgap is higher for CG and almost similar for CS and CL samples. Instead of defect sites taking part in oxidation reaction for smaller ionic radius samples, oxygen vacancy formed due to

charge compensation mechanism controls the oxidation reaction for larger ionic radius samples.

Even though catalytic activity does not directly correlate with surface area, a minimum value is necessary to ensure sufficient contact between soot and catalyst (Piumetti et al. 2016). Despite having a very high surface area (84 m²/g) for CZ with 80:20 composition ratio synthesized by coprecipitation method studied by Mukherjee et al., (2016) lower activity (T₅₀ ~ 540 °C) is justified due to low surface oxygen vacancy for the sample (Mukherjee et al. 2016). Similarly for CL and CH samples T₅₀ temperature of ~465 °C and ~407 °C, respectively are obtained that are considerably lower than the value obtained in our study (Mukherjee et al. 2016), could be due to the difference in synthesis method, calcination conditions and sample composition.

The increase of bandgap lowers the catalytic activity of larger ionic radius samples, and among these samples, it is the lattice oxygen vacancy formed due to largest ionic radius dopant (CL) addition that shows improved catalytic activity. The dependency of soot oxidation activity of samples with the dopant ionic radius (lattice constant) and in turn the optical bandgap values are depicted in **Figure 5.23**. Thus the soot activity is highly dependent on the ionic properties of dopant added to the ceria lattice as per the study. CZ nanoparticles with 90:10 composition synthesized by hydrothermal method having the same composition as the current study has shown a T₅₀ temperature of ~491 °C (Piumetti et al. 2016b) which is considerably higher than the T₅₀ temperature (~425 °C) obtained in this study, this might be because of lower surface area (~2 m²/g) obtained by the study.

Oxidation of soot occurs by utilising the surface adsorbed oxygen on the sample. However, the primary descriptors that can potentially influence the catalytic activity are the nature of the dopant (isovalent or aliovalent), ease of solubility with host structure (solid solution or hybrid phase), dopant ionic radius (smaller or larger) and optical bandgap (lower or higher). However, all these descriptors further affect the oxygen vacancy formation which is controlling the overall oxidation reaction of soot. Thus the

critical descriptor that needs to be improved is the surface oxygen vacancy concentration by varying different structural and intrinsic properties. Isovalent dopants of the smaller ionic radius can directly influence defect site formation which enhances the oxidation reaction by forming an intermediate level with lower energy, and thus the oxygen defect sites can be formed easily. Defect sites or active oxygen site further take part in oxidation reaction (Katta et al. 2010). If the larger ionic radius dopant is aliovalent, charge difference exist between host ion and cation and further charge compensation mechanism leads to vacant oxygen sites that smoothly involve in oxidation reaction (Sudarsanam et al. 2014). With the variation in dopant size and charge, the reaction mechanism varies, so does the T_{50} temperature also.

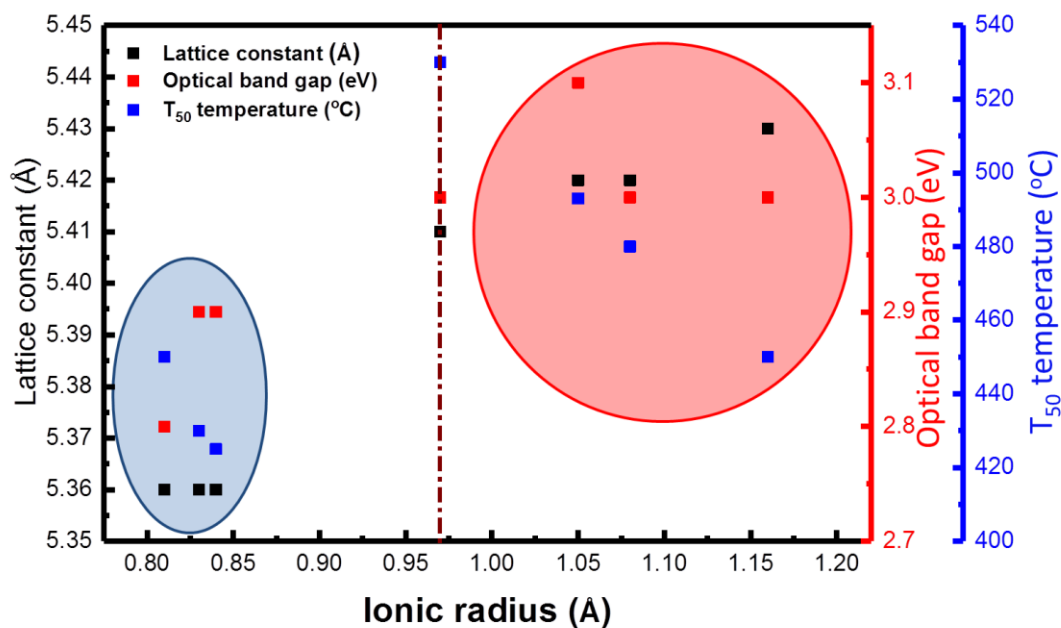


Figure 5.23: Variation in lattice constant, optical bandgap and T_{50} temperature for binary ceria-based metal oxides

5.4. CONCLUSION

Due to the variation in phase of different metal oxides, such as fluorite for CeO₂, monoclinic for HfO₂, phase segregation occurs on addition of the dopant to ceria lattice. For CeO₂ - HfO₂ (CH_x) single phase of fluorite (F) is observed only till 30 mol% dopant addition. On further addition of the dopant, hybrid phase formation results that have potential in deteriorating the catalytic activity due to the reduction in active site contact points. With the modification in phase, corresponding phase change is observed for CH_x series. Out of the solid solution samples studied for CH_x and CS_x series, higher catalytic activity is observed for 10 mol% dopant concentration. CH_x and CS_x activity depend upon the structural properties such as surface area, degree of agglomeration and surface oxygen concentration. A single phase with uniform morphology of CH_x sample results in enhanced catalytic activity compared to hybrid phase samples of non-uniform morphology.

By comparing the activity of CH10 with CS10 and CG10, CH10 has a higher activity due to its smaller ionic radius and isovalent nature in combination. The primary descriptor for the activity over whole composition range is significantly phase co-operation without secondary phase, uniform morphology, surface area and surface oxygen concentration. However, the descriptor will be much specific if the study focuses on specific composition since the dopant metal nature controls the activity further and not the structural parameters.

As the dopant composition of 10 mol% is fixed from the preliminary study over the whole composition, the further focus is on the variation in dopant metal on the catalytic activity. The selected metal cations for the study contain both smaller ionic radius dopants that are isovalent and larger ionic radius dopants that are aliovalent. The soot oxidation study confirms that the smaller ionic radius dopant results in better activity than larger ionic radius dopants due to higher reactive (200) and (220) planes, lower optical bandgap and higher surface oxygen concentration. Larger ionic radius dopant samples activity is

comparatively lower than smaller ionic radius dopants significantly due to variation in dopant size and charge. Among these samples, CL showed the highest activity due to higher lattice oxygen concentration created with the charge compensation mechanism.

The reduction in activity of larger ionic radius dopants can be related to lower diffusion of lattice oxygen than surface oxygen which takes part in the oxidation reaction and in turn increase in the bandgap values. With the change in dopant nature, the soot oxidation reaction mechanism also changes. In case of smaller ionic radius it is the defect site creation, and for larger ionic radius samples it is by charge compensation mechanism. As the structural difference is limited here, the descriptor that controls the activity is indeed specific to dopant nature and they are optical dopant ionic radius (smaller or larger), dopant charge (isovalent or aliovalent), bandgap (decrease or increase), reducibility (increase or decrease), oxygen vacancy concentration (surface oxygen or bulk oxygen) and oxygen vacancy creation mechanism (defect creation or charge compensation).

CHAPTER 6

STUDY OF MULTI DOPED METAL OXIDES

Based on the multi dopant literature studies for ceria-based metal oxides and the previous study on binary metal oxides, further improvement of binary series with dopants to form ternary and quaternary ceria-based mixed oxides are analysed for soot oxidation activity. Initial study on binary series has confirmed that Ce-Hf system has the highest catalytic activity due to the significant structural properties in comparison with the corresponding single metal oxides. Thus the host structure modification with the addition of dopant significantly improves the catalytic activity of ceria. The non-redox Hf, substituted in binary series, is partially replaced with redox Mn to form ternary metal oxide. Combined effect of redox (Mn) and non-redox (Hf) is tested in ternary series so that the reducibility and oxygen defect sites may be affected simultaneously. The total dopant concentration is maintained as 10 mol% based on the whole compositional analysis. Ce-Hf-Mn ternary samples with varying Mn concentration are developed using the EDTA-Citrate method.

The effect of further modification of ternary metal oxides using different dopants are analysed to understand the ability of ceria lattice to withstand the dopants and enhance catalytic activity. The dopants selected explicitly for quaternary series are reported to have high mobility and high electron donor ability in binary or ternary metal oxides. The modifications of ternary metal oxides by various dopants are studied for the catalytic activity of soot oxidation. The overall catalytic activities of single, binary, ternary and quaternary ceria-based mixed oxides are compared by using different characterization techniques. The descriptor that controls the catalytic activity of the multi doped metal oxides is discussed in detail by comparing the different characterization results obtained for the mixed oxides samples.

6.1. TERNARY AND QUATERNARY MIXED OXIDES

$\text{Ce}_{0.90}\text{Hf}_{1-0.90-x}\text{Mn}_x\text{O}_{2-\delta}$ ($x=0.00, 0.03, 0.05$ and 0.07) ternary metal oxides at different Mn concentration are synthesized using EDTA-Citrate method and it is represented in further as CHM_x ($x= 0, 3, 5, 7$). Also, quaternary metal oxides of $\text{Ce}_{0.90}\text{Hf}_{0.07}\text{Mn}_{0.015}\text{Y}_{0.015}\text{O}_{2-\delta}$ ($\text{Y}=\text{Li, Ag, Ba}$ and K) synthesized using EDTA-Citrate Complexing method is represented as CHML, CHMA, CHMB and CHMK, respectively and generally represented as CHMY ($\text{Y}=\text{L, A, B}$ and K). The quaternary metal oxides are arranged according to the increasing ionic radius of the dopant metal ion. That is, CHML ($\text{Li}= 0.92 \text{ \AA}$), CHMA ($\text{Ag}= 1.28 \text{ \AA}$), CHMB ($\text{Ba}= 1.42 \text{ \AA}$) and CHMK ($\text{K}= 1.51 \text{ \AA}$), respectively. The synthesized metal oxides are characterized initially using XRD, Raman Spectroscopy, SEM, TEM, UV-Vis DRS and XPS to understand the structural and intrinsic properties of the samples. The influence of these parameters on the catalytic activity is tested under tight contact condition. The variation in catalytic activity with the increase in dopant from ternary to quaternary mixed oxide is discussed in detail.

6.1.1. X-Ray Diffraction (XRD) Analysis

CHM_x ($x= 0, 3, 5$ and 7) ternary and CHMY ($\text{Y}=\text{L, A, B}$ and K) quaternary ceria-based mixed oxides are initially characterized using the XRD analysis for structural parameters identification, and the corresponding diffractograms are depicted in **Figure 6.1 (a)** and **Figure 6.1 (b)**, respectively. XRD spectra show the peak analogous to single phase fluorite structure of CeO_2 in all the mixed oxide samples (Aneggi et al. 2014). The absence of any distinct peak for secondary phase or impurities in the diffraction pattern confirms the formation of the fluorite phase solid solution. The specific range of diffraction pattern given in **Figure S6.1 (a)** for ternary metal oxide indicates a considerable shift of (111) peak towards the lower angle with the dopant addition, which in turn reflects an increase in lattice constant values.

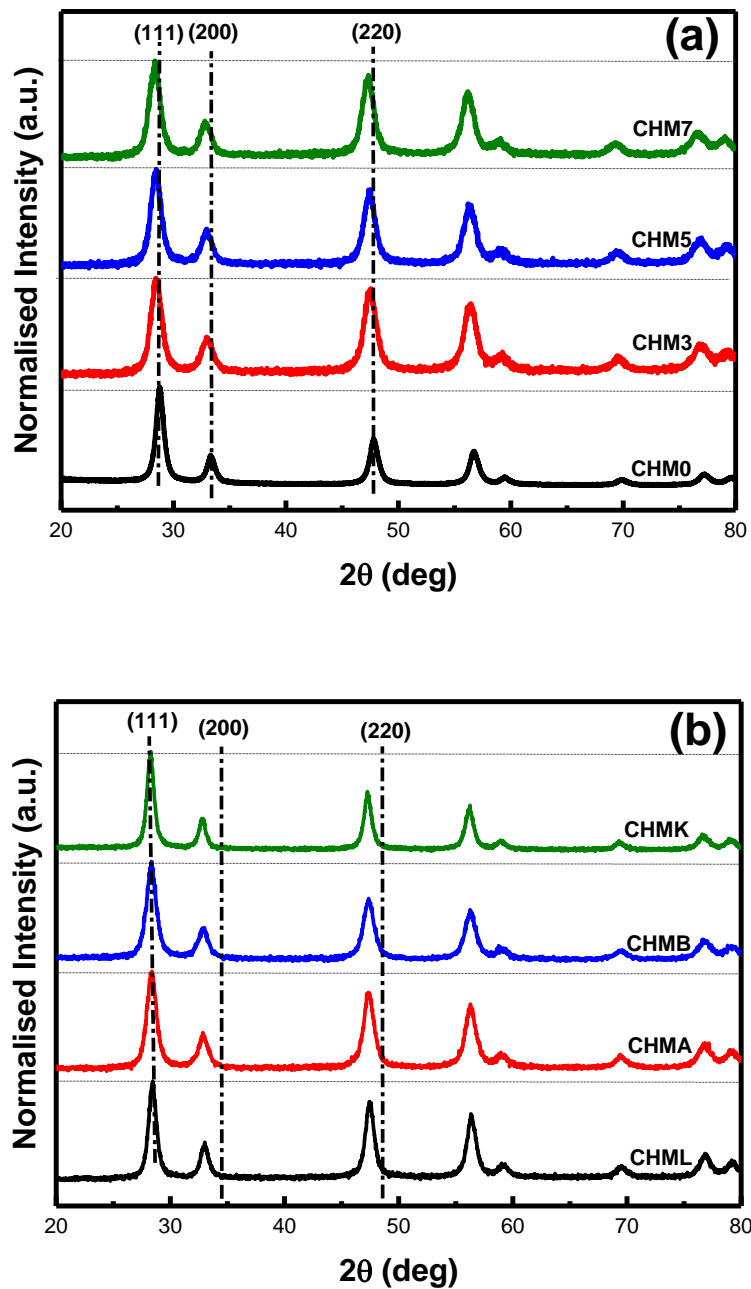


Figure 6.1: XRD spectra of (a) CHM_x ternary and (b) CHMY quaternary ceria-based metal oxides

With Mn addition to Ce-Hf lattice, the unit cell expansion is observed due to larger ionic radius Mn²⁺ (0.96 Å (Shannon 1976)) (Mesnard et al. 2006). Similarly, peak broadening is confirmed for Mn-doped samples (CHM3, CHM5 and CHM7) in comparison with Ce-Hf binary system (CHM0) that reflects a decrease in crystallite size value (Jampaiah et al. 2015).

Table 6.1 reports the information related to crystallographic parameters, surface area, particle size, pore volume and degree of agglomeration of the ternary and quaternary mixed oxides. The lattice constant and crystallite size values reported in the table corroborates with the change in peak in XRD spectra (see **Figure S6.1 (a)** and **Figure S6.1 (b)**). From the table it is evident that the presence of Mn as an additional dopant in the Ce-Hf system resulted in decrease in crystallite size and particle size and increase in lattice constant, lattice strain, plane intensity ratios ((200)/(111) and (220)/(111)), and surface area. There is no particular trend for the pore volume and degree of agglomeration. According to the literature (Aneggi et al. 2012, 2014; Rangaswamy et al. 2015; Rushton et al. 2013) for ceria-based systems, a decrease in crystallite size (Rangaswamy et al. 2015) and increase in lattice stain (Rushton et al. 2013) and plane intensity ratios ((200)/(111) and (220)/(111)) (Aneggi et al. 2012, 2014) showed a positive effect for soot oxidation activity. It is also important to note that the structural descriptors like host structure (crystallite size), defect sites (lattice strain, reactive planes), phase cooperation and metal-oxygen bond have prominent role in catalytic activity for soot oxidation reactions (Capdevila-Cortada et al. 2016). Among the ternary (CHM_x) system, increase in Mn concentration has shown no significant effect on crystallite size, lattice strain, (200)/(111) intensity ratio and the degree of agglomeration is in between 2~3 (see **Table 6.1**).

CHM3 displayed a better (220)/(111) intensity ratio. Among the different planes of ceria-based systems, (200) and (220) planes are less stable and hence highly reactive for soot oxidation reactions due to enhanced oxygen migration. If the intensity ratio of these planes is high, then it may enhance the soot oxidation activity also (Aneggi et al. 2012, 2014).

Aneggi et al. (Aneggi et al. 2012), obtained high-intensity ratio of (200)/(111) and (220)/(111) for ceria and ceria-zirconia system and resulted in higher soot oxidation activity due to lowering of oxygen vacancy formation energy in these highly reactive planes (Aneggi et al. 2012).

The ceria nanoparticles may contain surface termination in different planes of (111), (220) and (200), out of which the latter two planes are more reactive than the former one. With the variation in the appearance of planes, the electronic property also varies. The highly reactive planes of (200) and (220) results in lowering the surface vacancy formation energy, and in further enhances the intrinsic defect sites that result in enhanced oxygen storage capacity and thus improves the soot oxidation activity (Capdevila-Cortada et al. 2016). Grasselli et al. (2002) postulated seven pillars (phase cooperation, host structure, metal-oxygen bond, lattice oxygen, redox, site location and multifunctional nature of the active sites) to describe the activity of the cerium oxide, especially for oxidation reactions (Grasselli 2002). The experimental and theoretical mapping of the seven pillars proposed by Grasselli et al. (2002) is compiled by M. Capdevila-Cortada et al. (2016) and suggested that the impact of surface energy facets ((100) and (110)) of ceria as one of the descriptors which influence the intrinsic properties (Capdevila-Cortada et al. 2016; Grasselli 2002).

The specific diffraction pattern of quaternary CHMY samples in **Figure S6.1 (b)** shows only a slight shift towards lower angle in comparison with ternary metal oxides, which could be due to addition of negligible dopant concentration (1.5 mol%). Among the CHMY samples, CHMK showed greater shift followed by CHMB, CHMA and CHML, which can be correlated to the increase in ionic radius ($\text{Li}^{1+} = 0.92 \text{ \AA}$, $\text{Ag}^{1+} = 1.28 \text{ \AA}$, $\text{Ba}^{2+} = 1.42 \text{ \AA}$ and $\text{K}^{1+} = 1.51 \text{ \AA}$ (Shannon 1976)). This observation correlates with the lattice constant calculated and are given in **Table 6.1**. From **Table 6.1** it is also evident that, on addition of dopant (Li, Ag, Ba, K) to Ce-Hf-Mn results in quaternary (CHMY) system, shows decrease in lattice strain, (200)/(111) and (220)/(111) intensity ratios and surface area when compared to CHM3 sample. An increase in crystallite size, particle size, pore

volume and degree of agglomeration is also noticed. The observed trend in the descriptors, host structure (crystallite size) and defect sites (lattice strain, reactive planes) studied so far gives a hint that the quaternary (CHMY) system may show an adverse effect on the soot oxidation activity.

6.1.2. Raman spectroscopy Analysis

Figure 6.2 (a) and **Figure 6.2 (b)** demonstrate the Raman spectra of ternary CHM_x and quaternary CHMY mixed samples. F_{2g} mode fluorite structure Raman spectra of CeO_2 is confirmed with the presence of the characteristic peak at around 460 cm^{-1} in both CHM_x and CHMY, ternary and quaternary spectra, respectively, that correspond to oxygen symmetric breathing around cerium cations (Luo et al. 2006). Second-order Raman feature of CeO_2 is evident at $\sim 240 \text{ cm}^{-1}$ as a weak peak in CHM_x ternary metal oxides spectra (Weber et al. 1993). Another peak at $\sim 600 \text{ cm}^{-1}$ (O_v) corresponds to intrinsic oxygen vacancy created in the ceria lattice due to the defective structure in both CHM_x and CHMY ternary and quaternary spectra, respectively (Jiaxiu et al. 2013). The intensity ratio of peaks representing the oxygen vacancy and fluorite structure, that is, $I_{\text{O}_v}/I_{\text{F}_{2g}}$ relates the amount of total lattice oxygen concentration available in the sample (Sarkar et al. 2017).

Table 6.1 gives the intensity ratios calculated for all the samples. The oxygen vacancy peak intensity increases with Mn dopant addition to Ce-Hf system. Further dopant (Li, Ag, Ba, K) addition into the ternary Ce-Hf-Mn system (CHMY) shows negligible variation in ratio except for CHMA. The higher ratio of CHMA among quaternary metal oxides could be related to multiple oxidation states of Ag with +1, +2 and +3 that creates charge imbalance and hence produces vacant oxygen sites. However, $I_{\text{O}_v}/I_{\text{F}_{2g}}$ from Raman spectra interprets the bulk oxygen vacancy and their influence on catalytic activity can be neglected due to lower diffusion of bulk oxygen in comparison with surface oxygen that takes part in oxidation reaction (Sarkar et al. 2017).

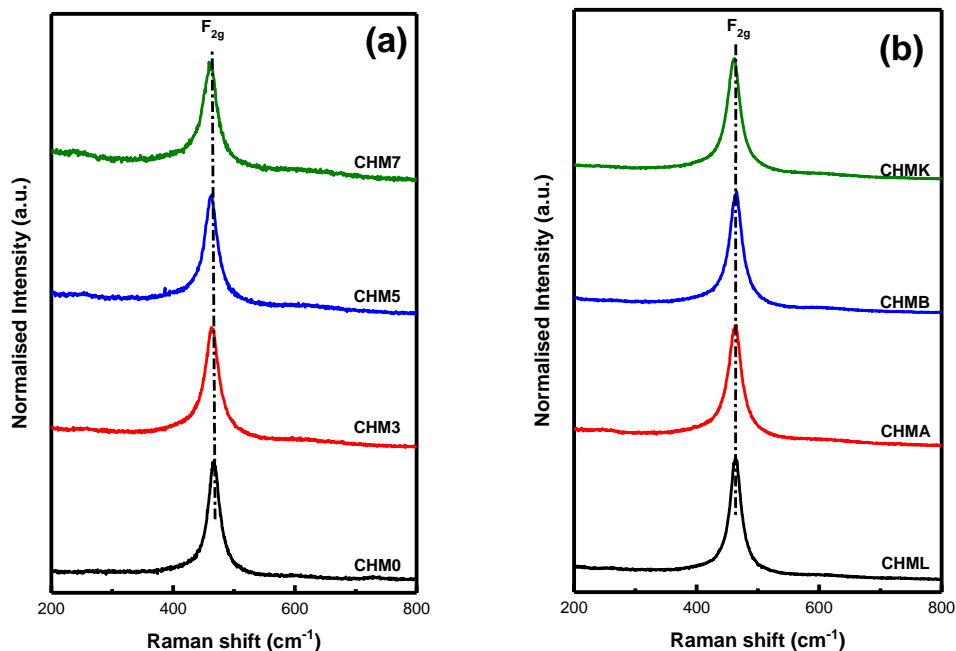


Figure 6.2: Raman spectra of (a) CHM_x ternary and (b) CHMY quaternary ceria-based metal oxides

6.1.3. Scanning Electron Microscopy (SEM) Analysis

Figure 6.3 and **Figure 6.4** show the SEM images of CHM_0 binary, CHM_x ($x=3, 5$ and 7) ternary and CHMY ($Y=L, A, B$ and K) quaternary mixed oxides of the Ce-Hf-Mn system, respectively. From the SEM image of CHM_x ternary system in the current study (see **Figure 6.3**), it is noticed that there is no change in surface morphology between CHM_0 binary system and $\text{CHM}_3 \sim \text{CHM}_7$ ternary system. Further, it can also be noticed that the CHMY quaternary system in **Figure 6.4** also displayed similar surface morphology as the binary and ternary system.

Table 6.1: Crystallite size, BET surface area, particle size, pore volume, lattice strain, intensity ratio, degree of agglomeration, bandgap, ($Ce^{3+} / (Ce^{3+} + Ce^{4+})$), $O_{\beta} / (O_{\beta} + O_{\alpha} + O_{\gamma})$, $Mn^{4+} / (Mn^{2+} + Mn^{3+} + Mn^{4+})$ and T_{50} temperature of CHM_x ternary and $CHMX$ quaternary ceria based metal oxides calcined at $600^{\circ}C/5h$

Metal oxide	Crystallite size ^a (nm)	BET Surface area (m ² /g)	Particle size ^b (nm) [#]	Pore volume (cm ³ /g)	Lattice strain ^c (ϵ)	Intensity Ratio ^d (%)		Degree of agglomeration ^e (ϕ) [^]	I_{ov} / I_{F2g} ^f (%)	Band gap energy ^g (eV)	$Ce^{3+} / (Ce^{3+} + Ce^{4+})$ ^h (%)	$O_{\beta} / (O_{\beta} + O_{\alpha} + O_{\gamma})$ ^h (%)	$Mn^{4+} / (Mn^{2+} + Mn^{3+} + Mn^{4+})$ ^h (%)	T_{50} temperature (°C)
						(200)/(111)	(220)/(111)							
CHM0	9.6	29	26	0.043	0.014	33	49	3	6	2.97	37	44	--	430
CHM3	7.3	36	21	0.042	0.020	46	90	2	11	2.77	67	88	23	426
CHM5	7.5	35	23	0.067	0.020	45	81	3	13	2.77	32	26	8	446
CHM7	7.3	48	16	0.069	0.020	45	87	2	16	2.77	45	18	9	433
CHML	9.9	23	36	0.073	0.015	43	81	4	6	2.89	52	35	--	460
CHMA	8.3	23	35	0.071	0.018	44	81	4	10	2.79	70	10	--	460
CHMB	7.9	28	29	0.065	0.014	39	66	4	6	2.83	49	13	--	460
CHMK	10.8	36	36	0.065	0.016	36	62	3	7	2.87	85	7	--	480

^a- Calculated from intense XRD peak using Debye-Scherrer equation; ^b- Calculated from BET Surface area; ^c- Calculated from intense XRD peak; ^d- Intensity ratio of intense planes in XRD; ^e- Calculated as the ratio of particle size and crystallite size; ^f- Calculated using intensity ratio of Raman peak; ^g- Calculated using Tauc's plot and ^h- Intensity ratio calculated from XPS using CasaXPS software

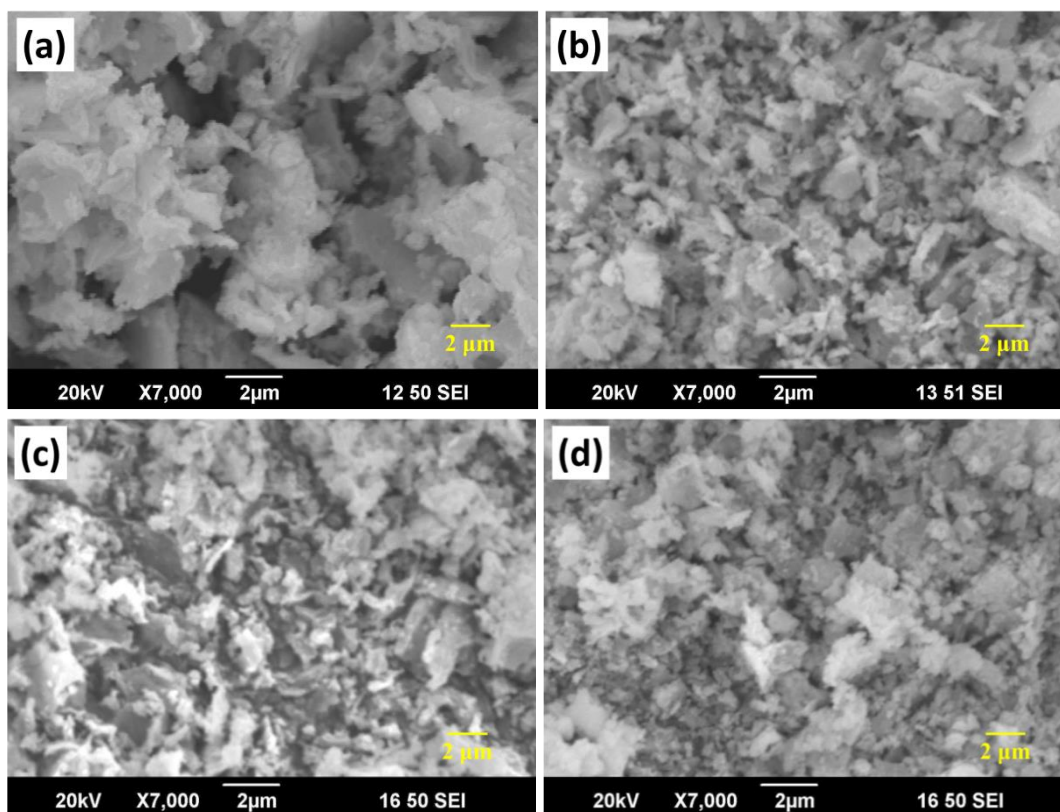


Figure 6.3: SEM images of (a) CHM0, (b) CHM3, (c) CHM5 and (d) CHM7 of ternary ceria-based metal oxides

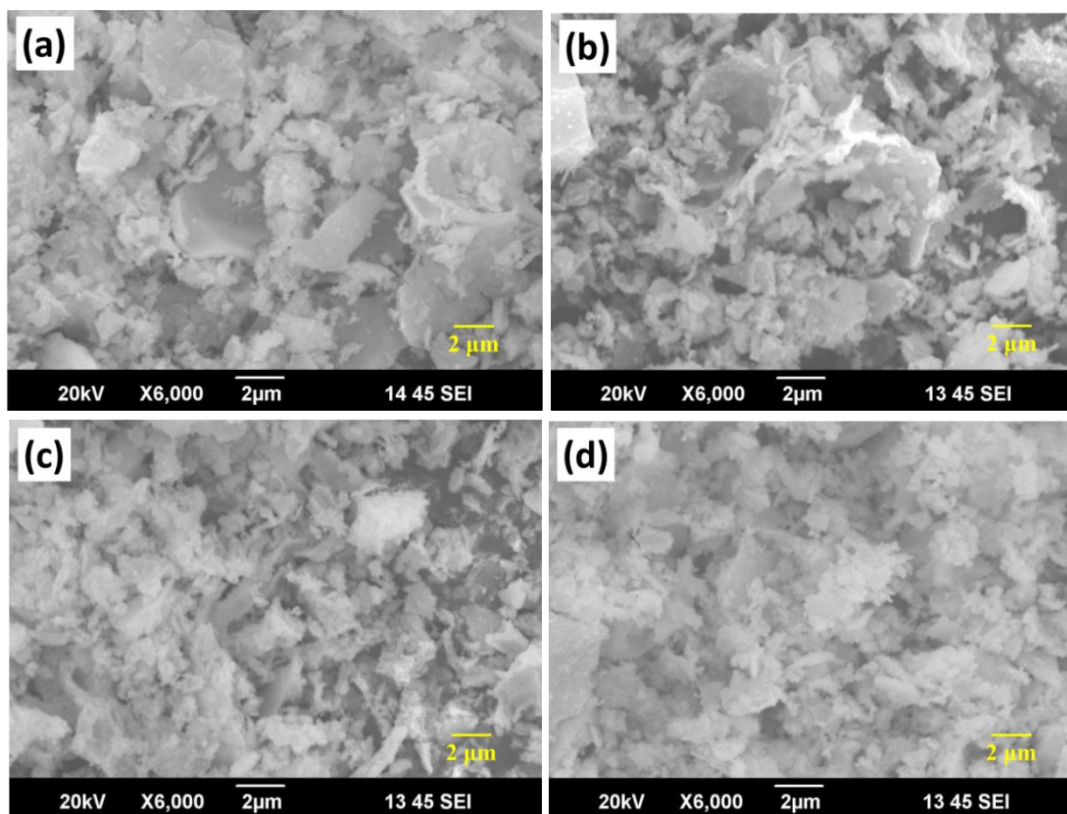


Figure 6.4: SEM images of (a) CHML, (b) CHMA (c) CHMB and (d) CHMK of quaternary ceria-based metal oxides

The reason for similar surface morphology for the Ce-Hf binary, ternary and quaternary systems is that the samples displayed a single phase solid-solution (from XRD data) since the total dopant concentration in all the samples are maintained as 10 mol%, that confirms the phase and structural stability of the sample. Studies on Ce-Hf (CH_x) binary system showed that the sample morphology significantly varies with the secondary phase formation at higher Hf content (for Hf > 30 mol% in the Ce-Hf binary system) and thus resulted in decline in catalytic activity as discussed in **Chapter 5.1**. Ceria rich single fluorite phase resulted in enhanced soot oxidation activity

6.1.4. Transmission Electron Microscopy (TEM) Analysis

Figure 6.5 shows the TEM images of the binary CHM0, ternary CHM3 and quaternary CHMY mixed oxides. From the TEM image of CHM0 (**Figure 6.5 (a)**) binary system and CHM3 (**Figure 6.5 (b)**) ternary system, it can be noticed that Mn as the additional dopant decreased the particle size from 11 nm to 8 nm. From the TEM images of the CHMY (**Figure 6.5 (c)** to **Figure 6.5 (f)**) quaternary system, it is interesting to observe that the particle size has been increased (~ 11 nm) in all the samples with the addition of dopant (Li, Ag, Ba and K) into CHM3 ternary system despite the change in dopant metal. The variation in particle size with the dopant addition from binary to quaternary sample correlates with their corresponding crystallite size calculated from XRD. With the lowering of particle size as observed from the TEM image of CHM3, the catalytic activity may improve due to enhanced contact points for soot activity (Andana et al. 2016). However, further dopant addition has resulted in increasing the particle size and crystallite size that may lead to deterioration in the catalytic activity of quaternary CHMY samples. The dopants (Li, Ag, Ba and K) added to CHM3 to form CHMY quaternary system can also act as sintering aids when doped in the Ce-Hf systems.

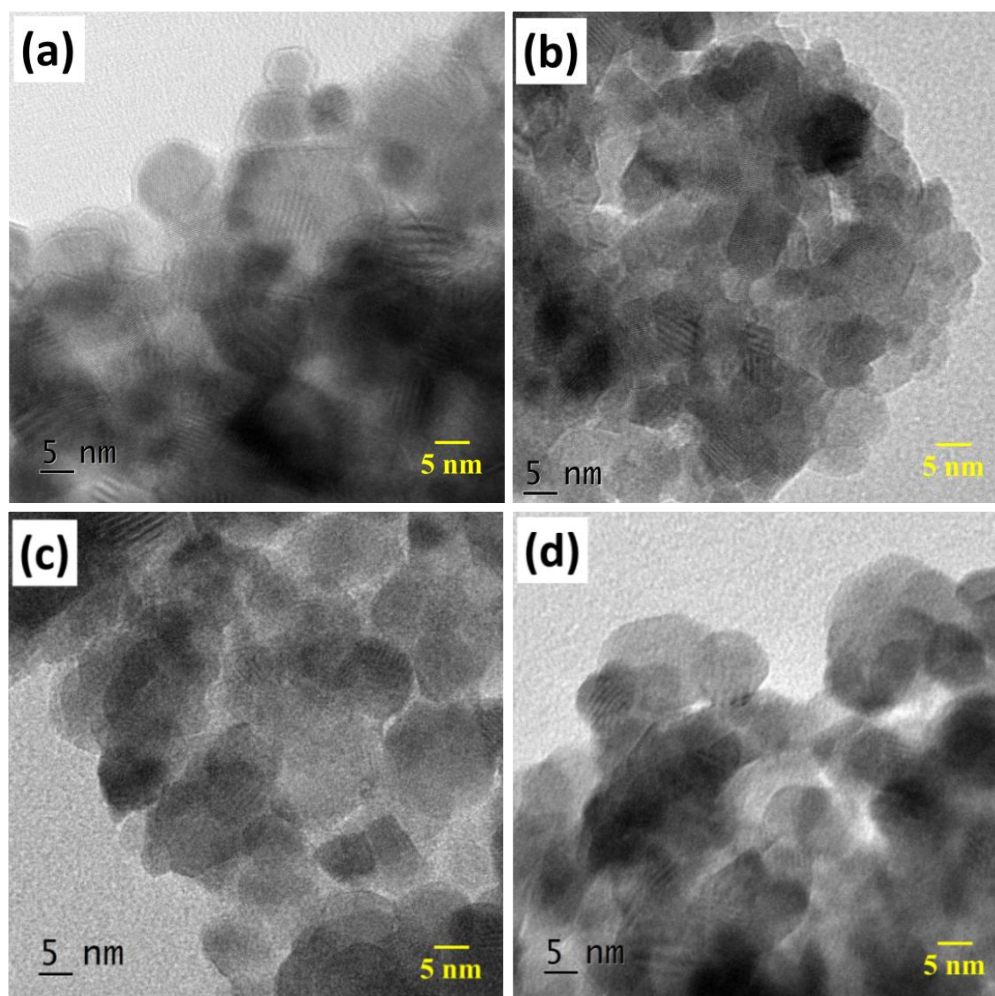


Figure 6.5: TEM images of (a) CHM0, (b) CHM3, (c) CHML and (d) CHMA binary, ternary and quaternary ceria-based metal oxides

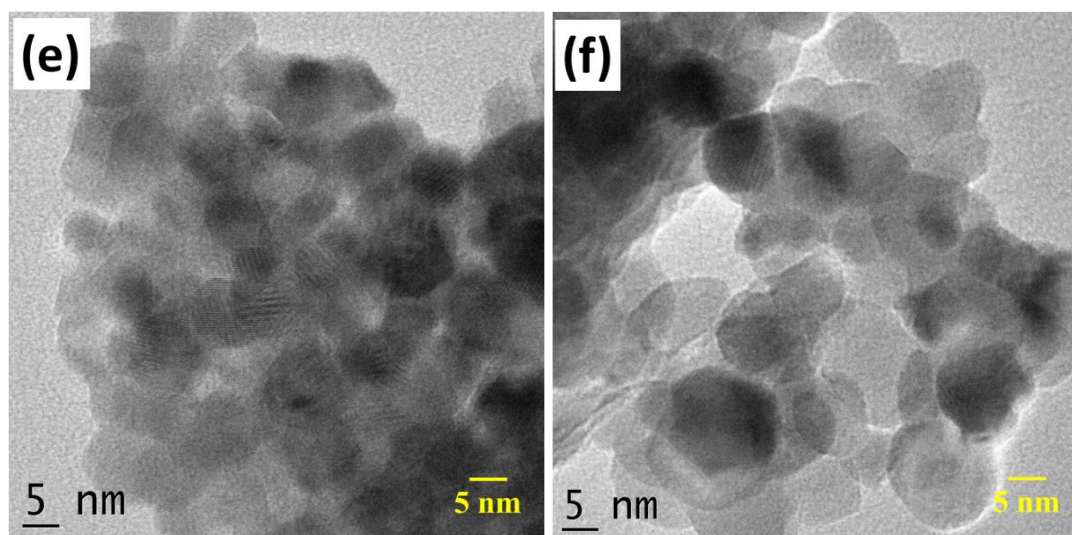


Figure 6.5: TEM images of (e) CHMB and (f) CHMK quaternary ceria-based metal oxides

Nicholas et al. (2007) successfully predicted and evaluated the sintering aids for ceria-based system using Vegard's Slope equation and identified the undersized acceptor dopants that result in decreasing the sintering temperature of the ceria-based system through either liquid phase sintering or heterogeneous doping (Nicholas and Jonghe 2007). In the present study, from the TEM image of the CHM_x and CHMY systems it can be interpreted that there is a drastic increase in the particle size for the quaternary systems, and it can be due to either liquid phase sintering (Y = Li and Ag) or heterogeneous doping (Y = Ba and K). At this point, it is not clear on the particle size growth mechanism, but it is evident that the particle size has increased for the quaternary system. The rise in particle size leads to sintering of nanoparticle that affects the structural properties of CHMY quaternary series. It can eventually affect the host structure and can have an impact on the structural descriptors as observed in XRD such as, facet ratio ((200) / (111) and (220)/(111)), lattice strain and surface area which affects the catalytic activity.

6.1.5. UV-Vis Diffuse Reflectance Spectroscopy (UV-Vis DRS) Analysis

Figure S6.2 (a) and **Figure S6.2 (b)** shows the UV-Vis DRS spectra of CHM_x ternary and CHMY quaternary mixed oxides with peaks significantly in 200 ~ 500 nm range. The spectral feature appearing as a single broad peak at around 280 nm assigns to both Ce³⁺-O²⁻ and Ce⁴⁺-O²⁻ charge transfer transaction (Ranga Rao and Sahu 2001). Apart from that, the interband transaction at 350 nm is evident. Optical bandgap calculated using Tauc's plot method for ternary CHM_x and quaternary CHMY mixed oxides are depicted in **Figure 6.6 (a)** and **Figure 6.6 (b)**, respectively and the values are given in **Table 6.1**. In comparison with CHM0 binary sample, ternary CHM3 sample has significantly reduced bandgap value with the addition of Mn dopant which correlates the improvement in the intrinsic property. Sample with higher Mn content of CHM5 and CHM7 had almost the same bandgap which might be due to the enhanced d-d interband transaction with Mn addition (Liu et al. 2011).

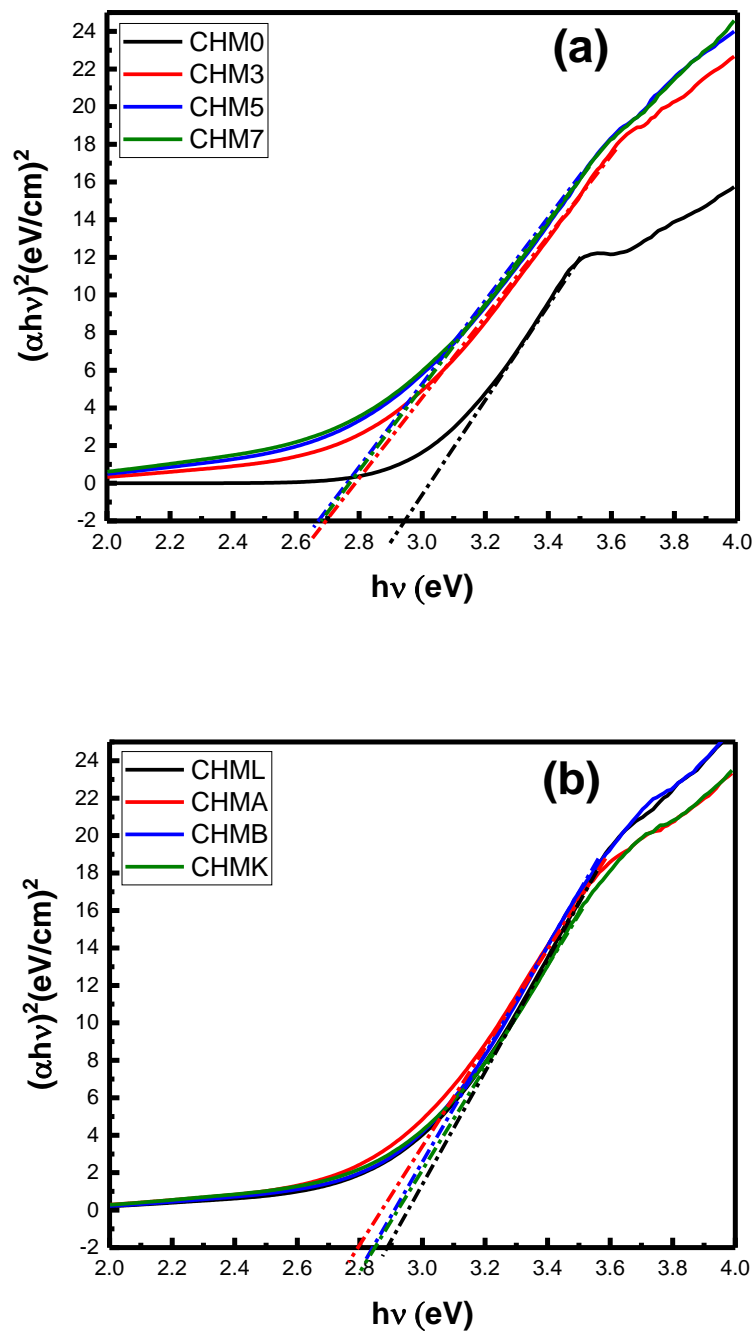


Figure 6.6: Tauc's plot of (a) CHM_x ternary and (b) CHMY quaternary ceria-based metal oxides

Similar to the limited change in the lattice parameter, the optical bandgap almost remain constant for CHM3-CHM7 samples that suggest a correlation between optical bandgap and lattice constant (Katta et al. 2012; Mia et al. 2017). However, for quaternary CHMY sample (2.79 ~ 2.89 eV) with an additional dopant than ternary (2.77 eV) system, optical bandgap increased. It is evident that with even trace addition of dopant to the quaternary system, a significant change in structural parameters and optical properties are evident in contrast to the constant structural properties for ternary series. Thus, the reactive facet planes and also optical bandgap has the potential in influencing the oxygen storage capacity, surface reduction, vacancy formation energy, oxygen basicity and intrinsic defect formation that in turn results in modifying the soot oxidation activity (Capdevila-Cortada et al. 2016).

6.1.6. X-ray Photoemission Spectroscopy (XPS) Analysis

Figure 6.7 (a) and **Figure 6.7 (b)** shows the Ce 3d core level XPS spectra and **Figure 6.8 (a)** and **Figure 6.8 (b)** shows the O 1s spectra of CHM_x ternary and CHMY quaternary mixed samples, respectively. Multiple oxidation states of Ce³⁺ and Ce⁴⁺ are confirmed on deconvoluting the peaks using CasaXPS software, and their position are represented in the corresponding spectra (Devaiah et al. 2015). The peak area calculated as $(\text{Ce}^{3+} / (\text{Ce}^{3+} + \text{Ce}^{4+}))$ on deconvoluting the peaks correspond to Ce³⁺ reducibility ratio (Devaiah et al. 2015). Similarly, the O 1s XPS of the samples confirms the presence of three peaks with each corresponding to lattice oxygen (O_α), surface oxygen (O_β) and weakly bound oxygen species (O_γ), respectively (Mukherjee et al. 2016). The area ratio of $(\text{O}_{\beta} / (\text{O}_{\alpha} + \text{O}_{\beta} + \text{O}_{\gamma}))$ calculated on deconvoluting the O 1s spectra indicates the surface oxygen concentration in the sample. The ratios of $(\text{Ce}^{3+} / (\text{Ce}^{3+} + \text{Ce}^{4+}))$ and $(\text{O}_{\beta} / (\text{O}_{\alpha} + \text{O}_{\beta} + \text{O}_{\gamma}))$ for CHM_x ternary and CHMY quaternary mixed samples are specified in **Table 6.1**. Hf 4f metal XPS spectra for ternary CHM_x and quaternary CHMY mixed samples are illustrated in **Figure S6.3 (a)** and **Figure S6.3 (b)**, respectively. Hf in the single oxidation state of +4 is confirmed from the spectra with a binding energy

difference of ~ 1.5 eV (Ramadoss et al. 2012). Multiple oxidation states of Mn^{2+} , Mn^{3+} and Mn^{4+} are confirmed from Mn 2p spectra for CHM_x ternary series in **Figure S6.4 (a)** and **Figure S6.4 (b)**, respectively (Nesbitt and Banerjee 1998). On further deconvolution of Mn 2p, the area ratio of $(\text{Mn}^{4+} / (\text{Mn}^{2+} + \text{Mn}^{3+} + \text{Mn}^{4+}))$ corresponds to Mn reducibility ratio and the values are reported in **Table 6.1**.

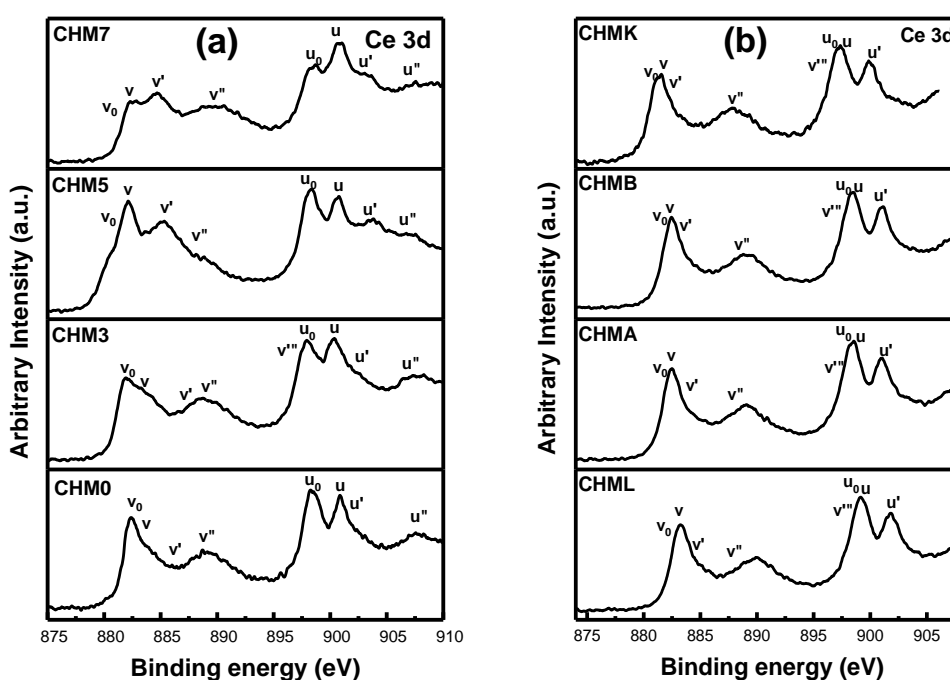


Figure 6.7: Ce 3d XPS spectra of (a) CHM_x ternary and (b) CHMY quaternary ceria-based metal oxides

Table 6.1 shows the information related to reducibility properties of the ternary and quaternary mixed oxides along with optical bandgap. From the table it is evident that, with the addition of Mn as dopant in the Ce-Hf system, CHM3 sample showed higher $(\text{Ce}^{3+} / (\text{Ce}^{3+} + \text{Ce}^{4+}))$, $(\text{Mn}^{4+} / (\text{Mn}^{2+} + \text{Mn}^{3+} + \text{Mn}^{4+}))$ and $(\text{O}_\beta / (\text{O}_\alpha + \text{O}_\beta + \text{O}_\gamma))$ ratio and lower optical bandgap. According to the literature (Devaiah et al. 2015; Nesbitt and Banerjee 1998; Rushton et al. 2013), for ceria-based systems, higher ratio of Ce^{3+} reducibility (Devaiah et al. 2015), Mn^{4+} reducibility (Nesbitt

and Banerjee 1998) and surface oxygen vacancy (Devaiah et al. 2015) and lower optical bandgap (Rushton et al. 2013) results in improved catalytic activity due to enhanced cyclic oxidation/reduction reaction that leads to formation of oxygen vacancy and defect site (Tang et al. 2018). Among the ternary series, CHM3 with the highest Ce³⁺ and Mn⁴⁺ reducibility and surface oxygen concentration and lower optical bandgap results in reduced oxygen vacancies formation that improves the cyclic oxidation reaction by forming defect sites and has improved active site availability. With the enhanced oxygen vacant site availability, soot oxidation reaction takes place in a much easier manner (Filtschew et al. 2016; Tang et al. 2018).

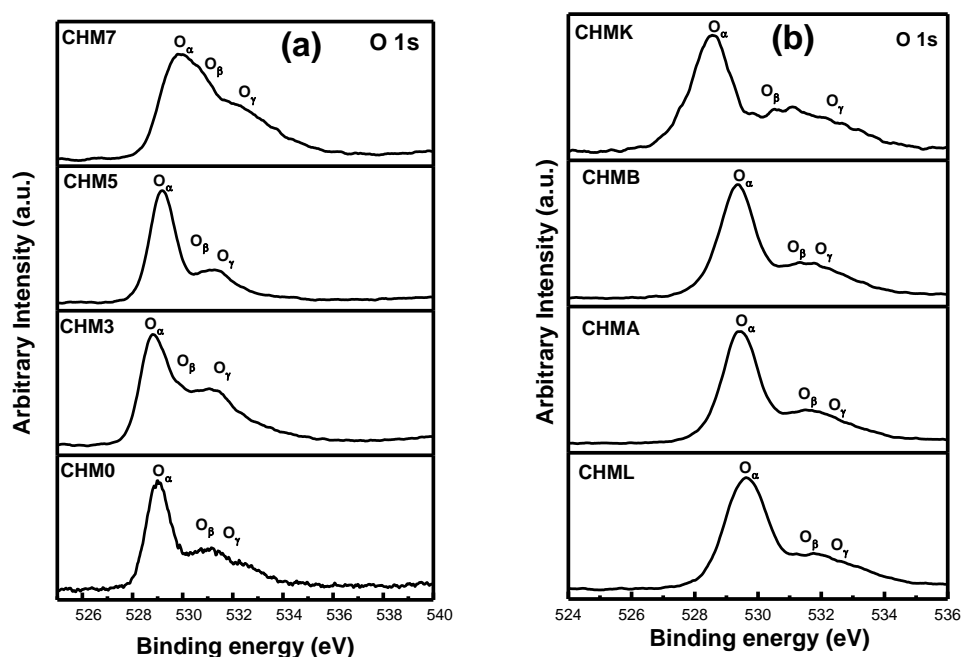


Figure 6.8: O 1s XPS spectra of (a) CHM_x ternary and (b) CHMY quaternary ceria-based metal oxides

From **Table 6.1** it is also noticed that with the addition of quaternary elements (Li, Ag, Ba, K) to CHM3 sample, there is a decrease in $(\text{Ce}^{3+} / (\text{Ce}^{3+} + \text{Ce}^{4+}))$, $(\text{O}_\beta / \text{O}_\alpha)$

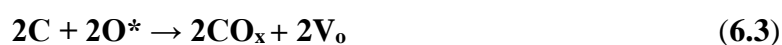
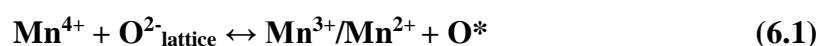
+ O_{β} + O_{γ}) and (I_{ov}/I_{F2g}) ratio and increase in optical bandgap. The observed trend in the descriptors of redox (Ce^{3+} and Mn^{4+} reducibility) and active sites (surface oxygen and optical bandgap) studied so far gives a further hint apart from the descriptors of host structure (crystallite size), oxygen vacancy (lattice strain, reactive planes), phase cooperation and metal-oxygen bond (see **Table 6.1**) that the addition of quaternary elements (Li, Ag, Ba and K) in the Ce-Hf-Mn system may show an adverse effect on the soot oxidation activity. The catalytic activity of the samples are discussed in detail in further section.

6.1.7. Soot oxidation activity

Ternary CHM_x and quaternary CHMY samples are tested as the catalyst for soot oxidation activity, and **Figure 6.9 (a)** and **Figure 6.9 (b)** provides their conversion profile, respectively. **Table 6.1** shows the T_{50} temperature of the samples. Among the ternary doped samples (**Figure 6.9 (a)**), CHM3 with the minimum dopant content showed the highest catalytic activity with a T_{50} temperature of 426 °C. However, on further addition of dopant, a drop in catalytic activity is observed, this indicates that optimum dopant concentration is reached at CHM3. Based on the XRD characterization study, it is reported that the structural parameters are not modified among the ternary CHM_x sample series. Reactive (200) and (220) planes are highly available in CHM3 sample in comparison with other ternary samples that potentially reduce the energy for surface oxygen vacancy formation. Also, the intrinsic properties such as Ce^{3+} and Mn^{4+} reducibility, surface oxygen vacancy and optical bandgap are reported higher for CHM3 that shows a positive impact on the catalytic activity.

In the presence of soot, Mn^{4+} reduces to lower oxidation states of Mn^{3+}/Mn^{2+} that leads to the creation of oxygen vacancy. Similarly, Ce^{3+} undergoes an oxidation reaction that results in forming an active vacant site. Simultaneous electron transfer between Ce^{3+} and Mn^{4+} readily forms a redox cycle between Mn and Ce (Huang et

al. 2017; Zhao et al. 2017). With this effect, an efficient oxidation reaction can be expected since the oxygen vacancy is improved during the cyclic reduction/oxidation reaction (Devaiah et al. 2015). In further, oxygen mobility also increases, that leads to the enhanced catalytic activity of the sample due to the reduction in bandgap value that aids in forming vacant defect sites (Huang et al. 2017)(Yu et al. 2014). These steps are explained in **Equation 6.1 - 6.3**. The reduction of Mn^{4+} and oxidation of Ce^{3+} are shown in **Equation 6.1** and **6.2**, respectively. During this reaction, active oxygen species are created that is represented as O^* . In the presence of active species, soot oxidation takes place much easier due to its easy migration towards soot surface and thus results in the formation of carbon oxides. The rate-limiting step during the soot oxidation reaction in the presence of metal oxides are generally reported to be **Equation 6.3**, that is the oxygen migration step from the catalyst surface to soot (Krishna et al. 2007; Nascimento and Serra 2016). The factor determining soot oxidation activity rate is thus the oxygen migration and vacancy formation as far as the structural factors are negligible. Higher oxygen vacancy with improved mobility enhances the participation of active sites for soot oxidation reaction.



Soot conversion of CHMY quaternary samples in **Figure 6.9 (b)** shows a considerable reduction in activity irrespective of the dopant elements (Li, Ag, Ba and K) in comparison with the ternary CHM3 sample. **Table 6.1** provides the 50 % conversion temperature (T_{50} temperature) of CHMY sample series.

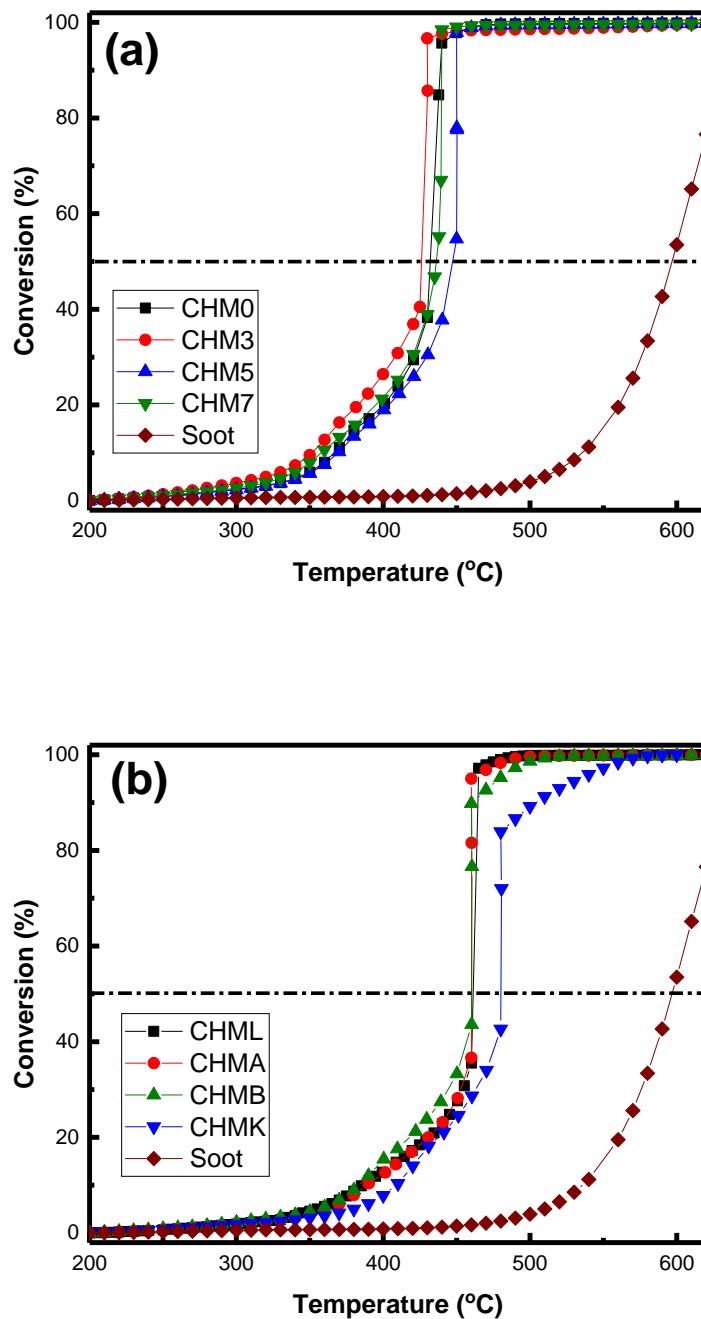


Figure 6.9: Soot Oxidation of (a) CHM_x ternary and (b) CHMY quaternary ceria-based metal oxides

CHML, CHMA and CHMB (~460 °C) showed almost similar activity, and CHMK (~480 °C) has comparatively lower activity. However, the T_{50} temperatures for CHMY are higher than the ternary CHM3 sample (~426 °C). It is evident from the results that the catalytic deactivation occurs even with the trace addition of dopants (1.5 mol%) into the ternary system. XRD results confirm that the crystallite size increased and BET surface area decreased for CHMY samples that diminish the contact points (Rangaswamy et al. 2015). In line with the decrease in crystallite size, the particle size also decreased as evident from the TEM image. The modification in particle size even with traces of dopant elements can be related to the sintering of nanoparticles (Nicholas and Jonghe 2007). Enhanced particle sintering with the dopant addition to ternary series result in active contact point hindering and lowers the reducibility, thus declines the catalytic activity (Andana et al. 2016; Tang et al. 2018).

CHMY quaternary series has a reduced lattice strain, (220) and (200) reactive plane, optical bandgap, Ce^{3+} reducibility ratios and surface oxygen concentration which affects the electronic properties more than the structural properties. The oxygen vacancy formation energy, vacant defect sites and oxygen migration reduces with the reduction in lattice strain and highly reactive (200) and (220) planes, and increase in the bandgap. Further, the reducibility is affected due to the decline in oxygen storage capacity that deteriorates the catalytic activity in further (Capdevila-Cortada et al. 2016). The soot oxidation reaction improves with the oxygen diffusion within the catalyst lattice that improve the oxygen mobility for the reaction (Boaro et al. 2000). Even though the structural descriptors (phase stability, morphology) are controlled by limiting the dopant concentration to 10 mol%, the catalytic activity has reduced due to the predominance of other structural (crystallite size, particle size, surface area, lattice strain and particle sintering) descriptors and electronic (reactive planes, optical bandgap, reducibility and surface oxygen) descriptors for quaternary series.

From the previous study on single and binary metal oxides, it has been witnessed an increase in activity with the addition of dopant. That is, the T_{50} temperatures of single metal oxides of CeO_2 , HfO_2 and Mn_3O_4 are 530 °C, 483 °C, 484 °C, respectively. For a binary system of $\text{Ce}_{0.9}\text{Hf}_{0.1}\text{O}_2$ (CHM0), minimum T_{50} temperature obtained was 430 °C that confirms a significant improvement in catalytic activity with the binary dopant addition. An additional dopant results in the reduction of T_{50} temperature to 426 °C for Ce-Hf-Mn (CHM3) ternary metal oxides with the improvement in redox and oxygen vacancy properties. However, for the system of quaternary metal oxides of Ce-Hf-Mn-Y (Y=Li, Ag, Ba and K), catalyst deactivation is evident in comparison with ternary metal. The structural and intrinsic descriptors influences the catalytic activity which further enhances the oxygen vacancy formation and mobility that aids in soot oxidation reaction.

6.2. DESCRIPTORS FOR MULTI DOPED CERIA BASED METAL OXIDES

Previous study on single, binary, ternary and quaternary ceria-based metal oxides as catalysts for soot oxidation activity has confirmed that the descriptors that influence the catalytic activity changes with the change in the system under study. However, a comparative study on activity with the dopant addition is required, which is focused in this section. A correlation is developed for the catalytic activity with the addition of dopant to ceria lattice using basic characterization techniques such as XRD, Raman spectroscopy, TEM, UV-Vis DRS and XPS. For that, the single metal oxide (CeO_2 , C) binary metal oxide ($\text{Ce}_{0.9}\text{Hf}_{0.1}\text{O}_2$, CH10) ternary metal oxide ($\text{Ce}_{0.9}\text{Hf}_{0.07}\text{Mn}_{0.03}\text{O}_2$, CHM3) and quaternary metal oxide ($\text{Ce}_{0.9}\text{Hf}_{0.07}\text{Mn}_{0.015}\text{Li}_{0.015}\text{O}_2$, CHML) was selected such that these are the samples that showed the highest catalytic activity among the studied metal oxides. Also, the samples are confirmed to exist in single phase of solid solution without any secondary phase since the dopant concentration is maintained to be 10 mol% in all the case. Thus all the samples exist in fluorite phase of CeO_2 . Since the phase change is limited, morphology change and structural modification are limited as evident from the SEM image of the samples. Even though significant change in TEM morphology is also not observed for most of the samples, quaternary metal oxides resulted in nanoparticle sintering that clearly leads to rise in particle size. Thus the descriptors such as phase cooperation, host structure and site isolation are restricted to not influence the catalytic activity. The other critical descriptor that influence the activity is dopant nature, based on the previous study. The intrinsic descriptor that influence the activity is analysed using various characterization tools in further and discussed in detail.

6.2.1. Reactive Planes (XRD)

The important parameters that influence the soot oxidation activity as per XRD analysis are crystallite size, lattice strain and reactive planes. The values for different metal oxides are given in **Table 6.2**. From the data, it is confirmed that the CHM3 has a smaller crystallite size, higher lattice strain and higher reactive plane intensity

ratios, compared to all other samples, even higher than highly doped quaternary metal oxide. Smaller crystallite size ensures the enhanced contact points and thus may impact the catalytic activity (Andana et al. 2016). With the increase in lattice strain, oxygen diffusion within the lattice improves, and further, the activity enhances (Rushton et al. 2013). Lower oxygen vacancy formation energy in reactive planes of (200) and (220) have shown higher catalytic activity than stable (111) plane which benefits the catalytic activity (Aneggi et al. 2012). The relation of reactive plane ratios with T_{50} temperature is shown in **Figure 6.10**.

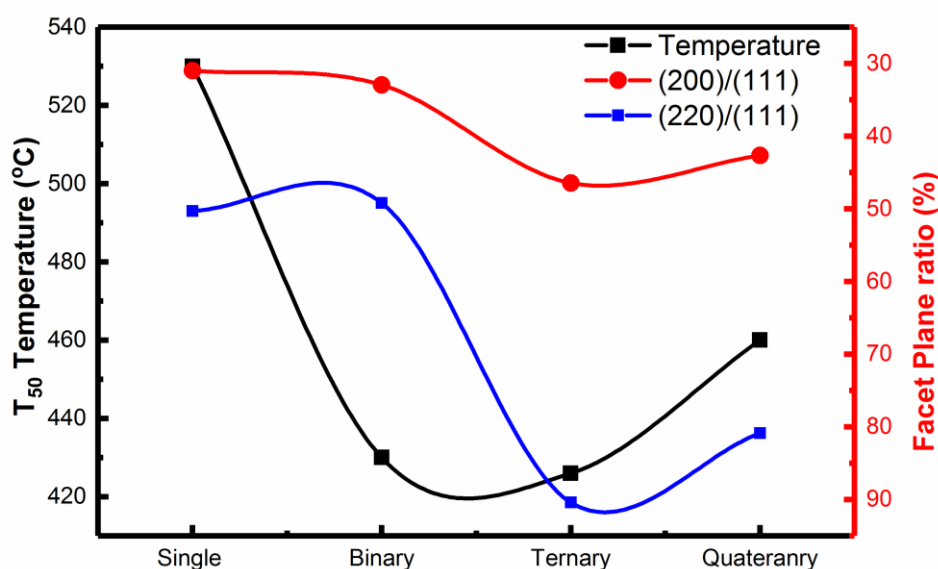


Figure 6.10: Relation between facet planes with T_{50} temperature for multi doped ceria-based metal oxides

From the result it is evident that both the planes of (200) and (220) show almost the same trend in values with the dopant. Hf dopant addition to CeO_2 to form CH10 binary metal oxide doesn't influence the reactive planes significantly. However, on addition of Mn to CH10 results in higher reactive plane intensity for CHM3 ternary metal oxide. Further dopant addition results in lowering the intensity of reactive planes. The trend in reactive plane follows the activity trend which confirms that the reactive planes are critical in controlling the catalytic activity. The highest activity of CHM3 ternary metal oxides can be related to the smaller crystallite size, higher

lattice strain, and higher reactive plane availability. The descriptor that controls the activity based on XRD analysis are host structure with smaller crystallite size and oxygen mobility by enhanced lattice strain and reactive plane intensity.

6.22. Raman Spectroscopy Analysis

The Raman spectra of specific samples which showed the highest activity among single, binary, ternary and quaternary metal oxides are given in **Figure 6.11**. From the figure, it is well evident that the intense peak that corresponds to F_{2g} vibration of CeO_2 varies its intensity. Apart from F_{2g} peak, the sample also has peak corresponding to oxygen vacancy (O_v). The ratio of oxygen vacancy to the F_{2g} peak intensity ($I_{O_v}/I_{F_{2g}}$) gives the quantity of lattice oxygen available in the bulk of the sample. The ratios of the corresponding samples are given in **Table 6.2**. From the values, it is evident that the maximum ratio is observed for ternary metal oxide and further dopant addition leads to lowering the ratio. However, the ratio corresponds to lattice oxygen which has lower diffusion in comparison with surface oxygen that easily takes part in soot oxidation reaction.

While comparing the intensities of the F_{2g} peak, a quaternary ceria-based metal oxide with the maximum number of dopant showed the highest intensity, followed by single metal cerium oxide, ternary ceria-based metal oxide and binary ceria-based metal oxide, respectively. From the preliminary literature study, it was proved that (Prasad et al. 2013), with the decrease in F_{2g} peak intensity, oxygen mobility and redox properties are increased due to the deformation created with the dopant addition. The result obtained in this study also matches well with the literature. The lower F_{2g} intensity of binary and ternary ceria-based metal oxides lead to improved catalytic activity due to enhanced redox properties compared to single and quaternary ceria-based metal oxides having higher intensity ratios. Thus the descriptor that influence the activity based on Raman spectroscopy study are redox and oxygen mobility which needs to analysed in further using XPS analysis.

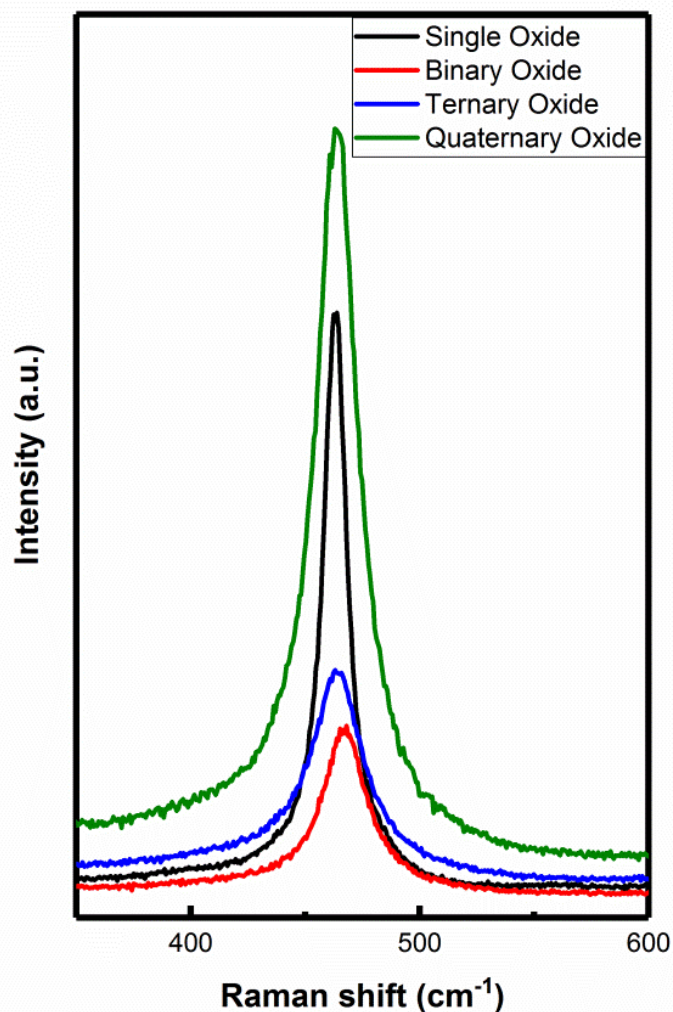


Figure 6.11: F_{2g} peak variation for multi doped ceria-based metal oxides

6.2.3. Optical Bandgap

Lowering of bandgap value is related to the point defect creation in the intermediate level due to oxygen vacancies (Sarkar et al. 2017). Even though the bandgap is in the range of 3.1 eV for pure CeO₂ single metal oxide and around 3.0 eV for Ce-HfO₂ binary metal oxide, with the addition of Mn to form a Ce-Hf-MnO₂ ternary metal oxide, the bandgap reduced significantly to 2.75 eV. A decrease in the bandgap of around 0.1 eV is caused by the addition of Hf to form binary oxide and the bandgap decrease of around 0.25 eV is observed even with the trace addition of Mn to form ternary metal oxides, which shows the influence of multiple oxidation states of Mn.

Thus it is confirmed that oxidation state of dopant has an impact on the bandgap values and hence on the oxygen vacancy that enhances the catalytic activity of ternary metal oxides (Sarkar et al. 2017). On further addition of dopant to form the quaternary metal oxide, bandgap value increased and hence the catalytic activity drops down significantly due to lowering of defect sites. Overall, the activity of single, binary, ternary and quaternary metal oxides are precisely related to the bandgap values obtained since the oxygen vacancy has a direct correlation with these values. Bandgap being the intrinsic property, with the decline in bandgap, oxygen vacancy is directly correlated that is the critical descriptor for the soot oxidation activity.

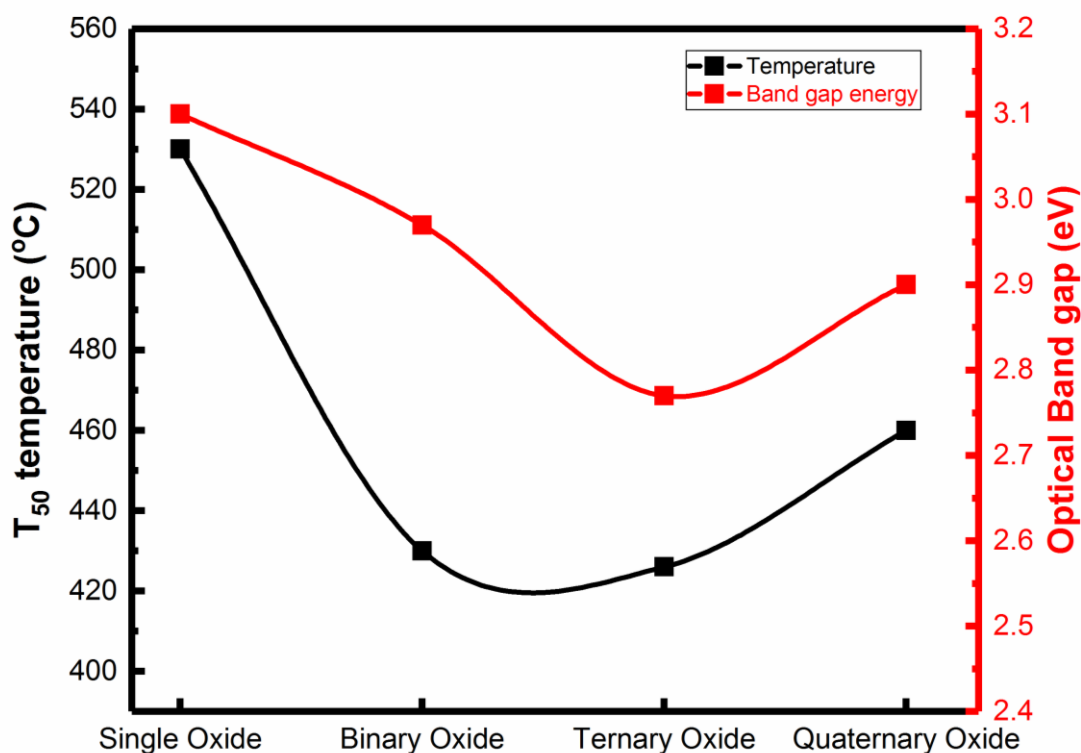


Figure 6.12: Relation between optical bandgap with T_{50} temperature for multi doped ceria-based metal oxides

6.2.4. Reducibility and oxygen vacancy (XPS)

With the addition of dopants into ceria lattice, the reducibility of Ce^{3+} is expected to improve that in turn results in enhanced catalytic activity (Puigdollers et al. 2017). The reducibility ratio obtained for all the samples are given in **Table 6.2** and depicted in **Figure 6.13**. The reducibility ratio increases with the addition of dopant till ternary metal oxide, and on further the reducibility ratio and catalytic activity drops for quaternary metal oxide. The role of surface oxygen is well studied for the catalytic activity since it is the surface oxygen that takes part in the soot oxidation reaction by forming active sites (Liu et al. 2017). Similar to Ce^{3+} reducibility ratio, Mn^{4+} reducibility is calculated for CHM, and CHML samples that contain Mn cation and the values are given in **Table 6.2**. Reduction in value is observed for quaternary CHML sample in comparison with CHM ternary metal oxide that confirms the lowering of Mn reducibility that in turn declines the catalytic activity.

The ratio of surface oxygen to the total oxygen that interprets the surface oxygen concentration and its variation with the T_{50} temperature is displayed in **Figure 6.14**. Similar to reducibility, the surface oxygen also increases up to ternary metal oxides and further decreases for quaternary metal oxide. With the rise in intensity of reactive planes ((200) and (220)), the energy for surface oxygen vacancy formation reduces that is the critical descriptor for the soot oxidation reaction. Also, the defect site formation improves with the reduction in bandgap values, which again enhances the active oxygen vacancy sites. With further enhancement in reducibility, the redox reaction enhances and thus the surface oxygen vacancy increase which results in improved oxidation reaction.

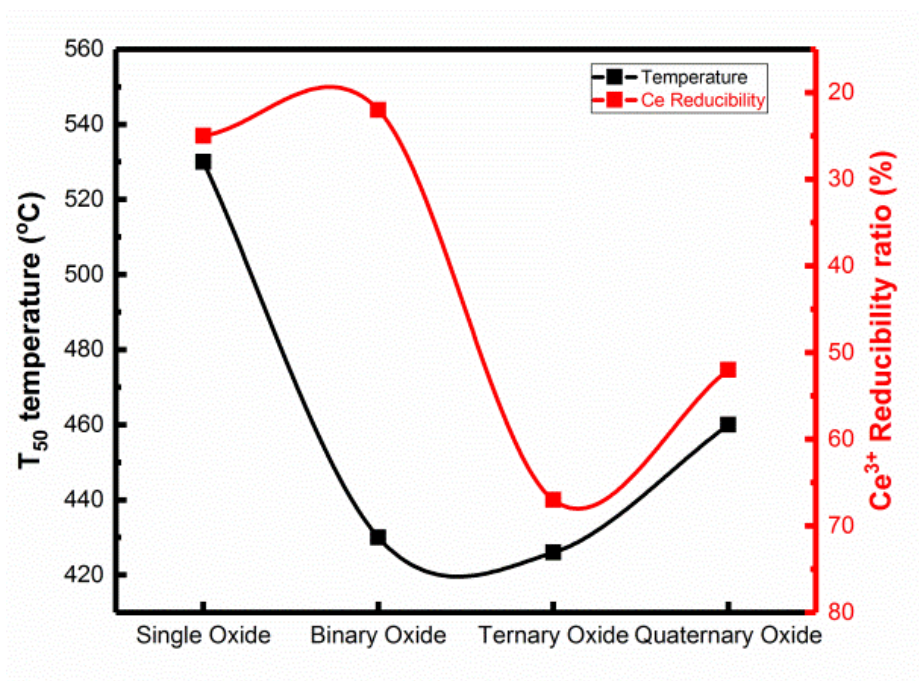


Figure 6.13: Relation between Ce reducibility with T₅₀ temperature for multi doped ceria-based metal oxides

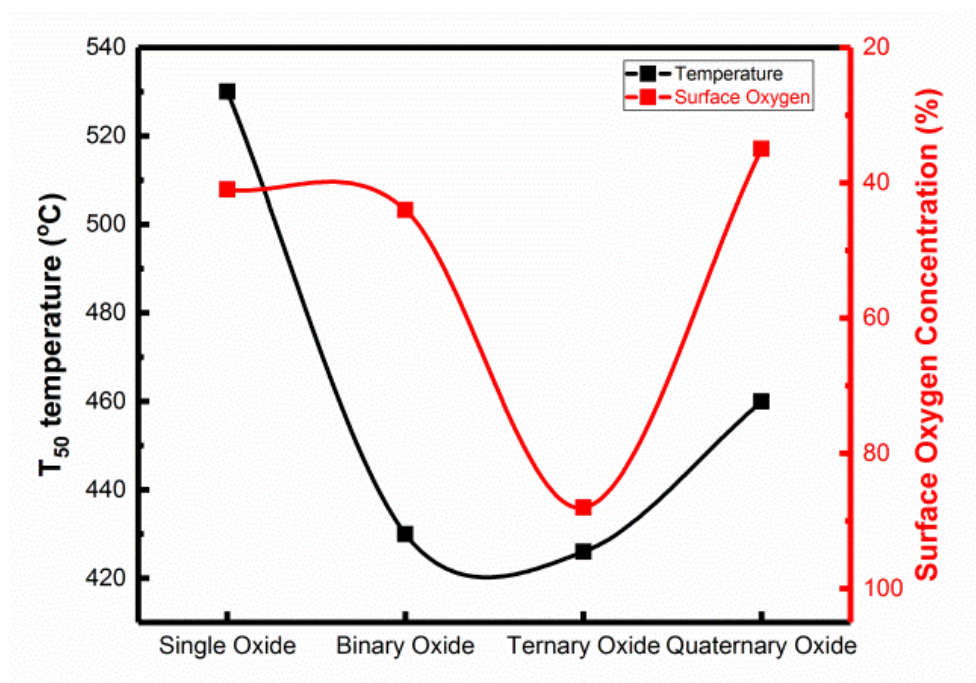


Figure 6.14: Relation between surface oxygen vacancy with T₅₀ temperature for multi doped ceria-based metal oxides

Table 6.2: Crystallite size, BET surface area, particle size, pore volume, lattice strain, degree of agglomeration, intensity ratio, optical bandgap, $Ce^{3+}/(Ce^{3+} + Ce^{4+})$, $O_{\beta}/(O_{\beta} + O_{\alpha} + O_{\gamma})$, $Mn^{4+}/(Mn^{2+} + Mn^{3+} + Mn^{4+})$ and T_{50} temperature of single, binary, ternary and quaternary ceria based metal oxides calcined at 600°C/5h

Metal oxide	Crystal lite size ^a (nm)	BET Surface area (m ² /g)	Particle size ^b (nm) [#]	Pore volume (cm ³ /g)	Lattice strain ^c (ε)	Intensity Ratio ^d (%)		Degree of agglomeration ^e (φ) [^]	I _{ov} /I _{F2g} ^f (%)	Optical band gap ^g (eV)	Ce ³⁺ / (Ce ³⁺ + Ce ⁴⁺) ^h (%)	O _β /(O _β + O _α + O _γ) ^h (%)	Mn ⁴⁺ /(Mn ²⁺ + Mn ³⁺ + Mn ⁴⁺) ^h (%)	T ₅₀ temperature (°C)
						(200)/(111)	(220)/(111)							
C	10.6	41	17	0.054	0.013	31	50	2	--	3.08	25	41	--	530
CH	9.6	29	26	0.054	0.014	33	49	3	6	2.97	22	44	--	430
CHM3	7.3	36	21	0.042	0.020	46	90	2	11	2.77	67	88	23	426
CHML	9.9	23	36	0.073	0.015	43	81	4	6	2.89	52	35	19	460

^a- Calculated from intense XRD peak using Debye-Scherrer equation; ^b- Calculated from BET Surface area; ^c- Calculated from intense XRD peak; ^d- Intensity ratio of intense planes in XRD; ^e- Calculated as the ratio of particle size and crystallite size; ^f- Calculated using intensity ratio of Raman peak; ^g- Calculated using Tauc's plot and ^h- Intensity ratio calculated from XPS using CasaXPS software;

6.3. CONCLUSION

The catalytic activity for soot oxidation activity of CHM_x ternary and CHMY quaternary mixed oxides are compared using preliminary characterization techniques. The structural parameters obtained using XRD shows that the ternary samples have lower crystallite size and particle size and higher lattice strain, reactive facet planes of (220) and (200) and surface area. With the improvement in reactive planes, the oxygen vacancy formation energy reduces by forming defect sites which in turn enhances the reducibility and surface oxygen vacancy. With respect to change in reactive planes, the corresponding reduction in optical bandgap and improvement in Ce³⁺ and Mn⁴⁺ reducibility is observed along with higher surface oxygen vacancy concentration. Among CHM_x samples, CHM3 (T₅₀= 426 °C) showed the highest activity due to improvement in the intrinsic properties such as reactive planes, optical bandgap, metal reducibility and surface oxygen concentration.

On addition of dopants (Li, Ag, Ba and K) to CHM3 (quaternary mixed oxide), catalytic activity reduced (T₅₀ = 460 ~ 480 °C) significantly due to the increase in particle / crystallite size because of the nanoparticle sintering that reduces the active contact points for the reaction. Consequently, reactive planes, lattice strain and surface area are reduced which confirms a declination in structural parameters that consequently affects the catalytic activity by increasing the optical bandgap and reducing the reducibility ratio and surface oxygen concentration, which are the intrinsic properties of the samples. In effect, with the nanoparticle sintering process during the dopant addition, both structural and intrinsic properties are declined that deactivates the catalyst. Thus, the catalytic activity of ternary metal oxide is better than the binary metal oxide sample. However, the activity drastically reduced on further dopant addition to form quaternary metal oxides. The effect of structural and intrinsic descriptors on catalytic activity depends on the dopant nature. In this particular study the nanoparticle sintering has negative effect of descriptors.

On comparing the catalytic activity of single, binary, ternary and quaternary ceria-based metal oxides, the descriptors that affect the activity can be concluded. The key descriptors for catalytic activity can be (a) contact points- enhanced by lower crystallite size and particle size, (b) oxygen vacancy/mobility- improved for a sample with higher lattice strain, lower F_{2g} peak intensity, lower optical bandgap, and (c) redox sites- improved by enhanced reducibility and surface oxygen vacancy. Among these descriptors, contact point is the structural descriptor which can be modified by changing the structural features of the sample. However, oxygen vacancy or mobility and redox are the intrinsic descriptor that can be modified by changing the dopant metal, addition of further dopant and

CHAPTER 7

SUMMARY AND CONCLUSIONS

7.1. SUMMARY

Summary drawn from the research with respect to multi doping effect on ceria-based metal oxides are discussed in this section.

The effect of single metal oxide samples on soot oxidation activity and the descriptors that controls the activity are:

- EDTA-Citrate complexing method is confirmed to have the enhanced catalytic activity in comparison with solvothermal method and thus it is adopted for the synthesis of all the samples
- Redox single metal oxide metal oxides has higher activity than non-redox single metal oxides due to enhanced surface oxygen availability due to reducibility of the metal oxide. Non-redox metal oxide activity is controlled by the surface properties such as surface area, lattice strain and ionic radius.
- The prime descriptor that controls the activity is the nature of the metal cation itself
- Non-redox HfO_2 ($T_{50}= 483^\circ\text{C}$) has shown activity equivalent to that of redox metal oxides such as Pr_6O_{11} ($T_{50}= 482^\circ\text{C}$) and Mn_3O_4 ($T_{50}= 484^\circ\text{C}$), thus HfO_2 is adopted for further studies

To evaluate the catalytic activity of binary ceria-based metal oxide samples with various dopants over the whole composition range and to find the effect of change in dopant with the activity at fixed composition

- CeO₂-HfO₂ and CeO₂-Sm₂O₃ binary metal oxide over the whole composition confirms the prime descriptor for this specific system is phase stability. For the system of CeO₂-HfO₂ phase change influences the change in morphology and for CeO₂-Sm₂O₃ it is bandgap that is modified with the phase change
- Both the sample series confirms the highest activity at minimum dopant concentration of 10 mol% due to high surface area, lower degree of agglomeration, high surface oxygen that enhances the contact points
- At the optimum composition, the binary system with varying dopants are analysed and confirmed that the dopant nature, whether larger or smaller ionic radius and isovalent or aliovalent dictates primarily the catalytic activity
- Surface oxygen vacancy formation for smaller ionic radius is defect site formation and charge compensation mechanism for larger ionic radius samples. Smaller ionic radius dopant sample such as HfO₂ (T₅₀= 430°C) and ZrO₂ (T₅₀= 425°C) showed enhanced activity in comparison with larger ionic radius dopant samples La₂O₃ (T₅₀= 450°C), Sm₂O₃ (T₅₀= 480°C) and Gd₂O₃ (T₅₀= 493°C). Thus the non-redox metal dopant with smaller ionic radius and isovalent is tested further for higher doped samples.

To develop ternary ceria-based metal oxides and quaternary ceria based metal oxides based on the results obtained for binary metal oxides

- Binary metal oxide (CeO₂-HfO₂) showing highest activity is further doped with redox Mn₂O₃ to analyse the combined effect of redox and non-redox dopants into

ceria lattice. The synergistic effect of both the dopants improve the activity by enhanced reducibility properties that improves the reactive facet planes, surface oxygen, that in turn enhances the oxygen mobility

- On further addition of various dopants into ternary metal oxides to form quaternary ceria based metal oxides, reduction in catalytic activity is observed due to increase in bandgap, reduction in reactive planes, reduction in surface oxygen that reduces the catalytic activity in comparison with ternary metal oxides. More than that, a significant change in particle size variation is observed which confirms the sintering due to quaternary dopant addition which in turn reduces the active sites and thus affects the activity.

To compare the overall performance of ceria based materials as catalysts for soot oxidation with the addition of different types of dopants

- On addition of dopant in CeO_2 ($T_{50} = 530$ °C) to form binary metal oxide ($T_{50} = 426$ °C), activity is improved due to improvement in reactive planes, reduction in F_{2g} peak intensity, reduction in bandgap and increase in Ce reducibility.
- Increase in activity with the presence of redox metal oxide in ternary metal oxide $\text{CeO}_2\text{-HfO}_2\text{-Mn}_2\text{O}_3$ ($T_{50} = 530$ °C) is correlated to improved reactive facet planes, F_{2g} peak intensity, bandgap value, reducibility and oxygen vacancy which improves the oxygen mobility
- Quaternary metal oxide reduces the activity due to reduction in surface properties along with the modification in particle size that confirms the sintering of metal oxide which reduces the active sites for catalytic activity

7.2. CONCLUSIONS

The thesis concentrates on multiple doping effect on ceria-based metal oxides for soot oxidation activity. For this, the metal oxide at different level of dopants such as single metal oxides (without any dopant), binary ceria-based metal oxide (over whole composition range and optimum composition with different dopant), ternary ceria-based metal oxide (at different composition of ternary dopant) and quaternary ceria-based metal oxide (varying quaternary dopant metal at fixed composition) are developed and analysed using various characterization tools and tested for soot oxidation activity. A single synthesis method of EDTA-Citrate complexing, is adopted for all the metal oxide development. With the variation in dopant metal nature, the descriptor that controls the activity also modifies significantly.

Different structural and surface characterization techniques are adopted to analyse the metal oxides developed and further correlate the various parameters on catalytic activity of the samples. The study confirms the effect of different descriptors at different level of dopant and their influence on catalytic activity.

7.3. SCOPE OF THE WORK

- Further synthesized samples can be tested for real time Diesel Particulate Filter and analyse the catalytic activity and their efficiency
- Understand the sintering mechanism of quaternary metal oxides which resulted in catalytic deactivation
- Alternatives for dopants, such as rare earth metals can be added in quaternary metal oxides and can be analysed for catalytic activity

APPENDIX- I

Study On Single Metal Oxides

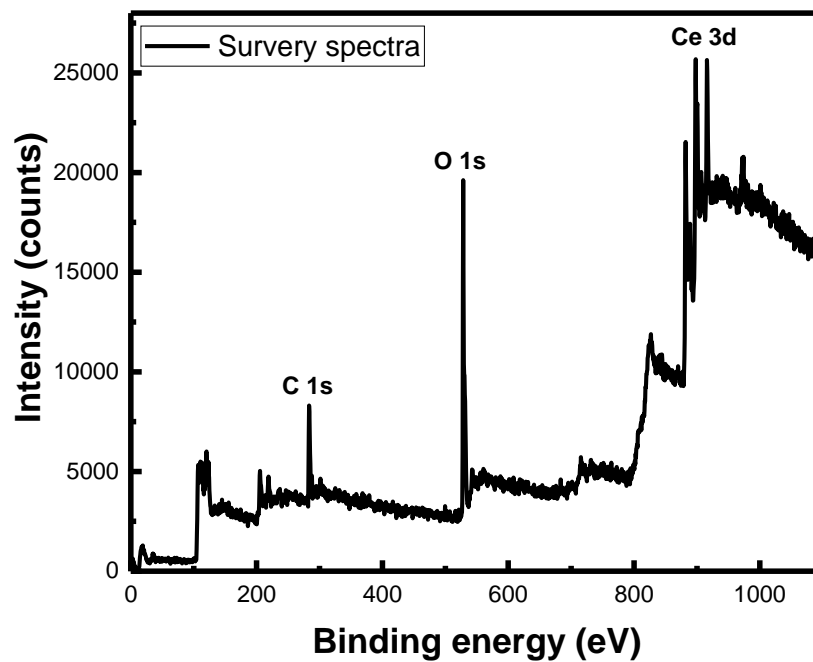


Figure S4.1: Survey spectrum of Ce 3d XPS

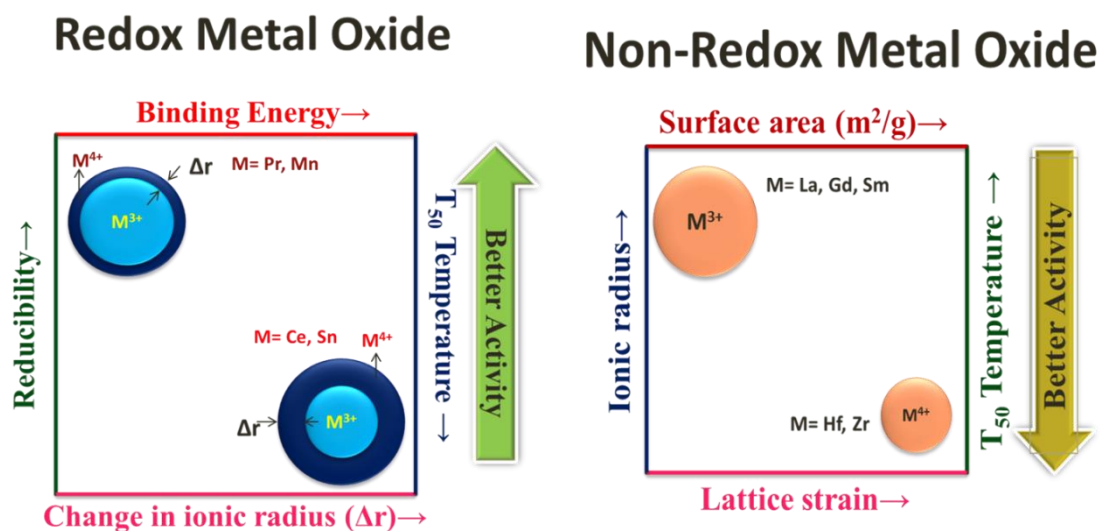


Figure S4.2: Graphical Abstract of Single Metal Oxides (Redox and Non-Redox) catalytic activity on soot oxidation

APPENDIX- II

Study On Binary Metal Oxides For Soot Oxidation Activity

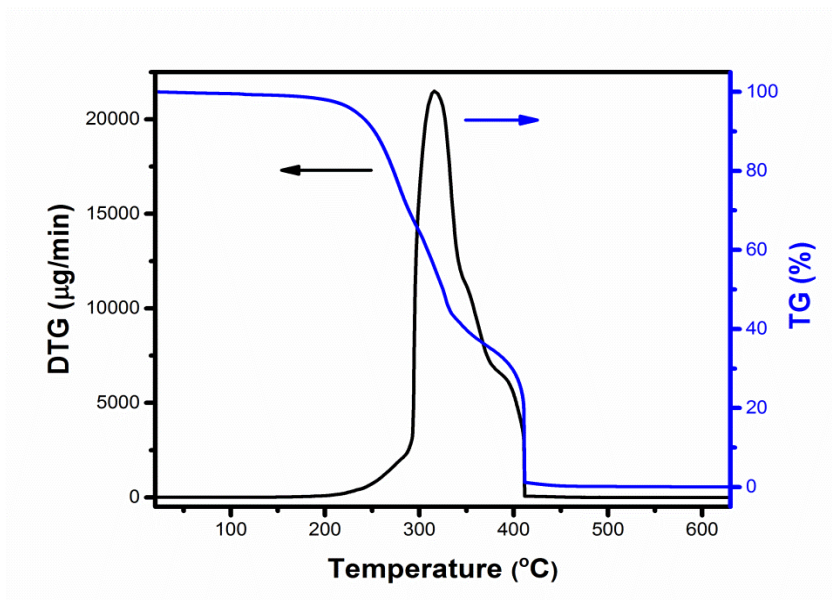


Figure S5.1: TG plot of CH10 sample before calcination

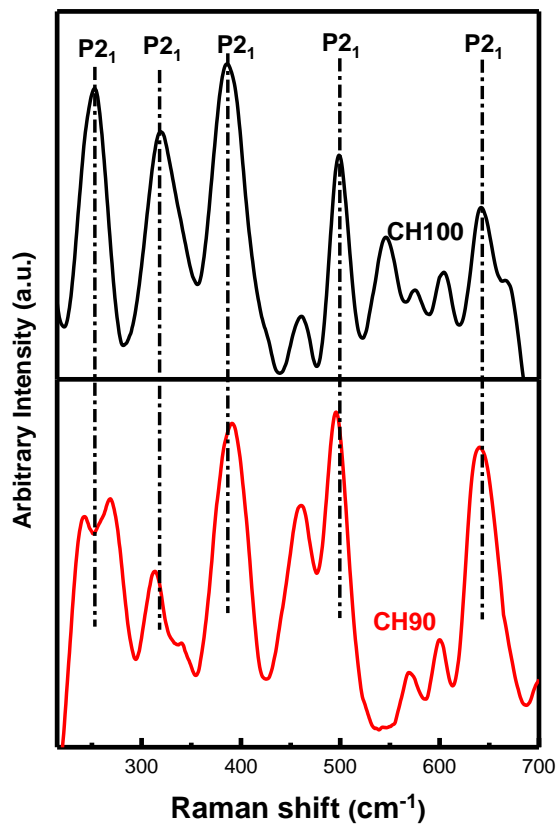


Figure S5.2: UV-Vis DRS of CH90 and CH100 binary metal oxides

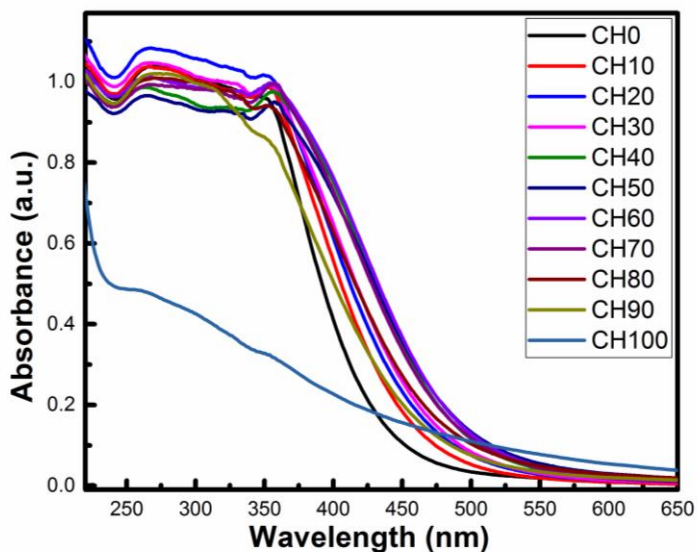


Figure S5.3: UV-Vis DRS of CH_x binary metal oxides

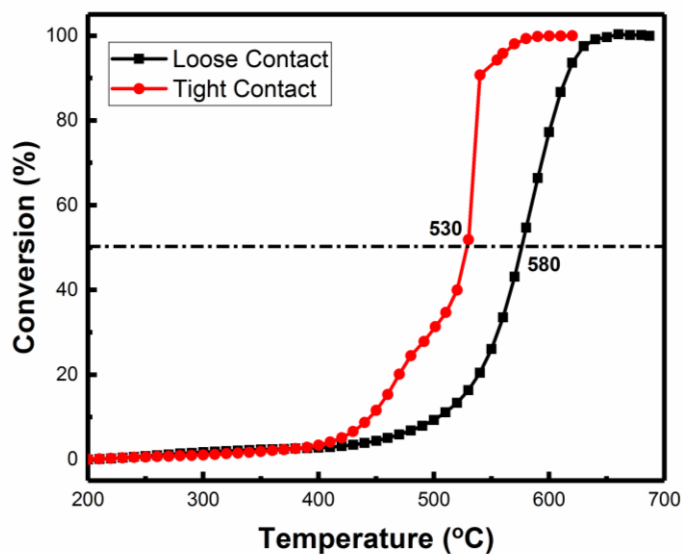


Figure S5.4: Soot oxidation activity of CH₁₀ under loose and tight contact

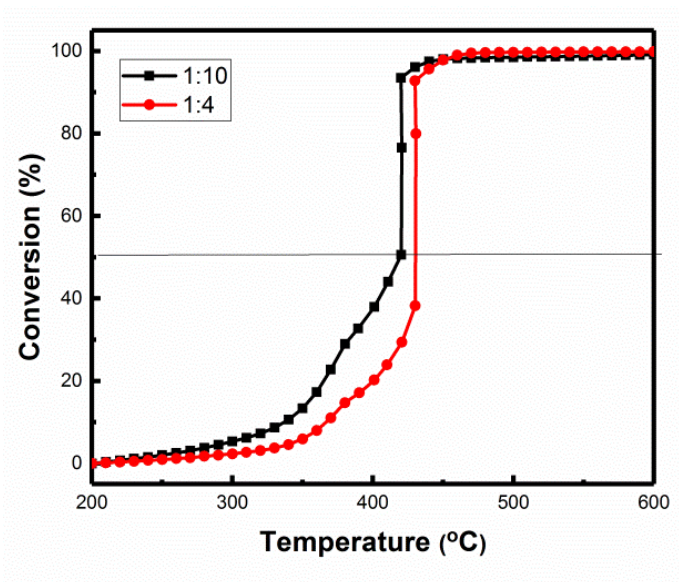


Figure S5.5: Soot oxidation activity of CH10 sample at different soot to catalyst ratio (1:4 and 1:10)

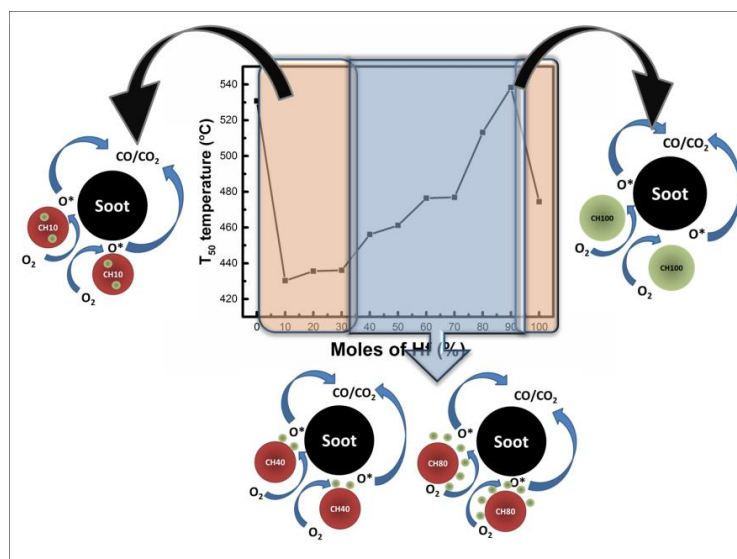


Figure S5.6: Graphical Abstract of Binary Metal Oxide catalysts activity on soot oxidation

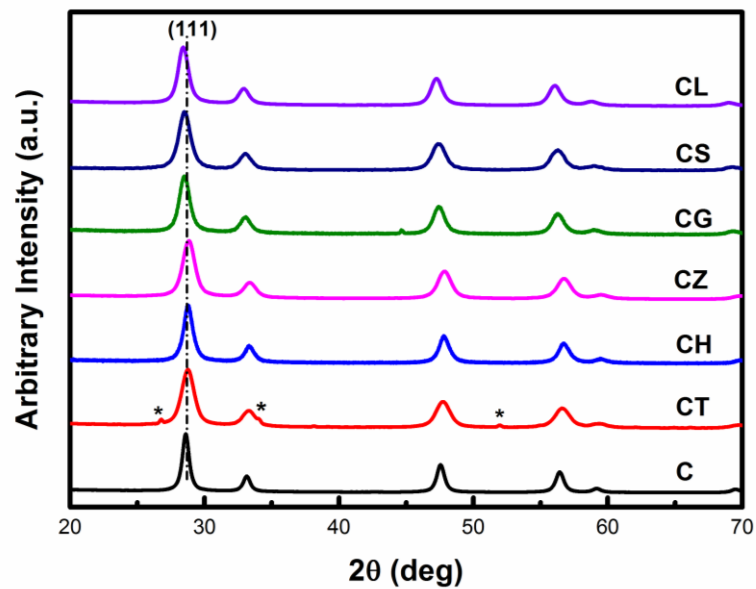


Figure S5.7: XRD spectra of ceria based binary metal oxides

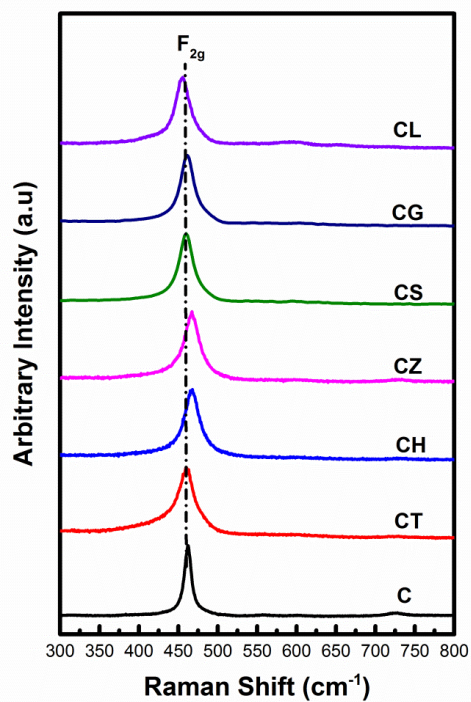


Figure S5.8: Raman spectra of ceria based binary metal oxides

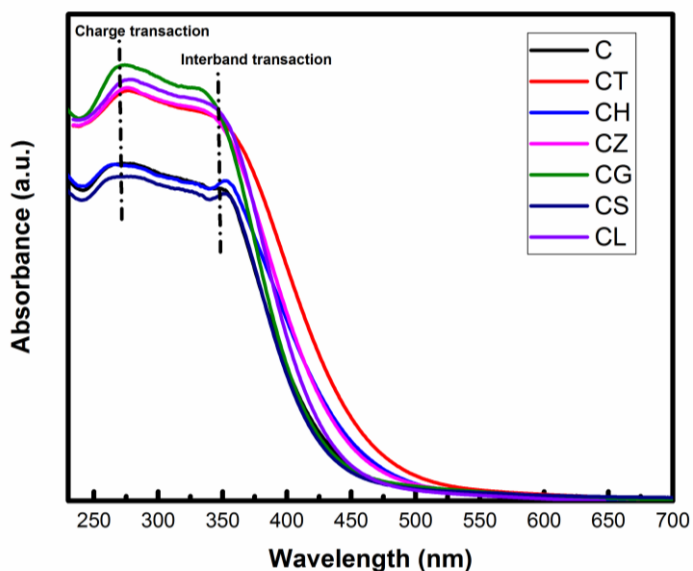


Figure S5.9: UV-Vis DRS spectra of ceria based binary metal oxides

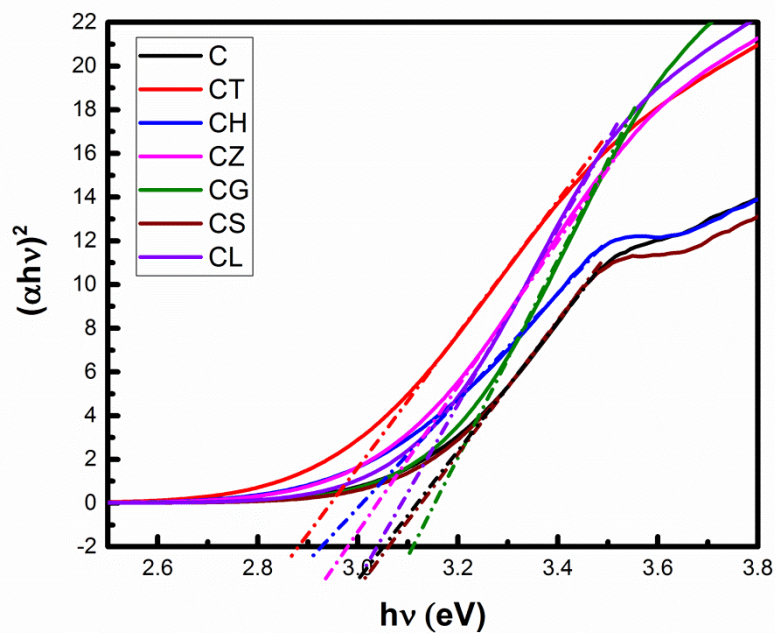


Figure S5.10: Tauc's plot of ceria based binary metal oxides

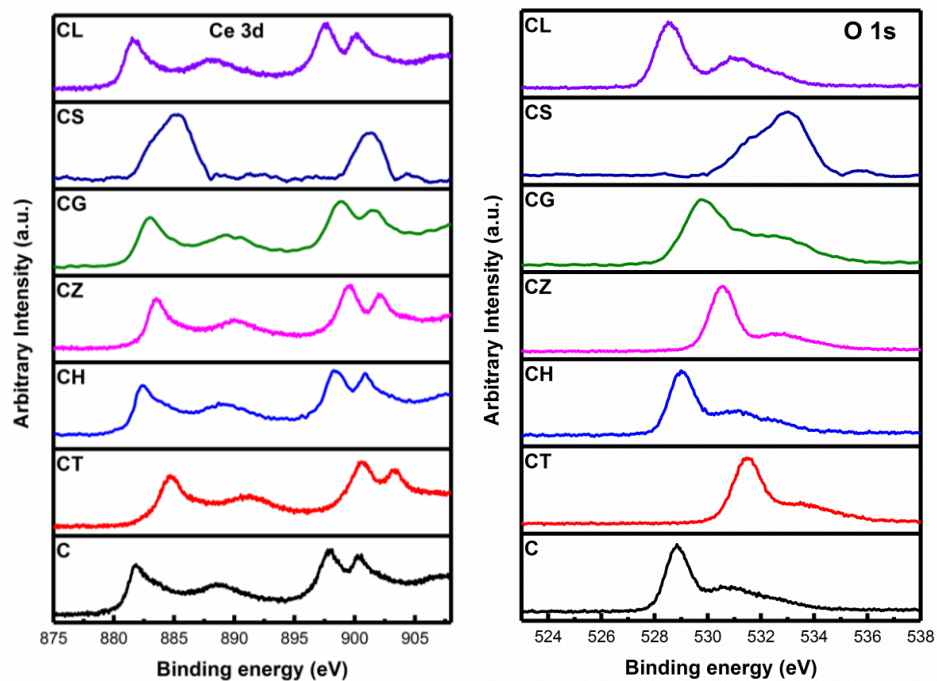


Figure S5.11: (a) Ce 3d and (b) O 1s XPS spectra of ceria based binary metal oxides

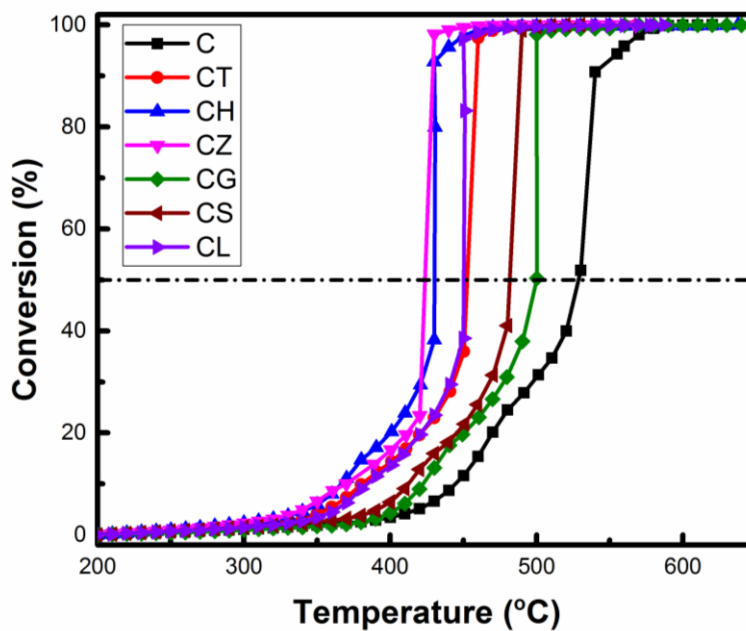


Figure S5.12: Soot oxidation activity of ceria based binary metal oxides

Table S5.1: Crystallite size, BET surface area, particle size, lattice strain and degree of agglomeration of Ce-Me binary metal oxides calcined at 600°C/5h.

Metal oxide	Lattice constant^a (Å)	Crystallite size^b (nm)	Lattice strain^c (ε)	BET Surface area^e (m²/g)	Particle size^f (nm)	Degree of agglomeration^g (φ)
C	5.41	11.7	0.012	41	20	1.5
CT	5.38	8.9	0.019	40	21	2.8
CH	5.36	9.6	0.014	29	26	2.8
CZ	5.36	7.7	0.019	58	15	1.9
CG	5.42	9.9	0.015	31	28	2.8
CS	5.42	8.2	0.018	38	23	2.8
CL	5.43	8.9	0.016	36	23	2.6

APPENDIX- III

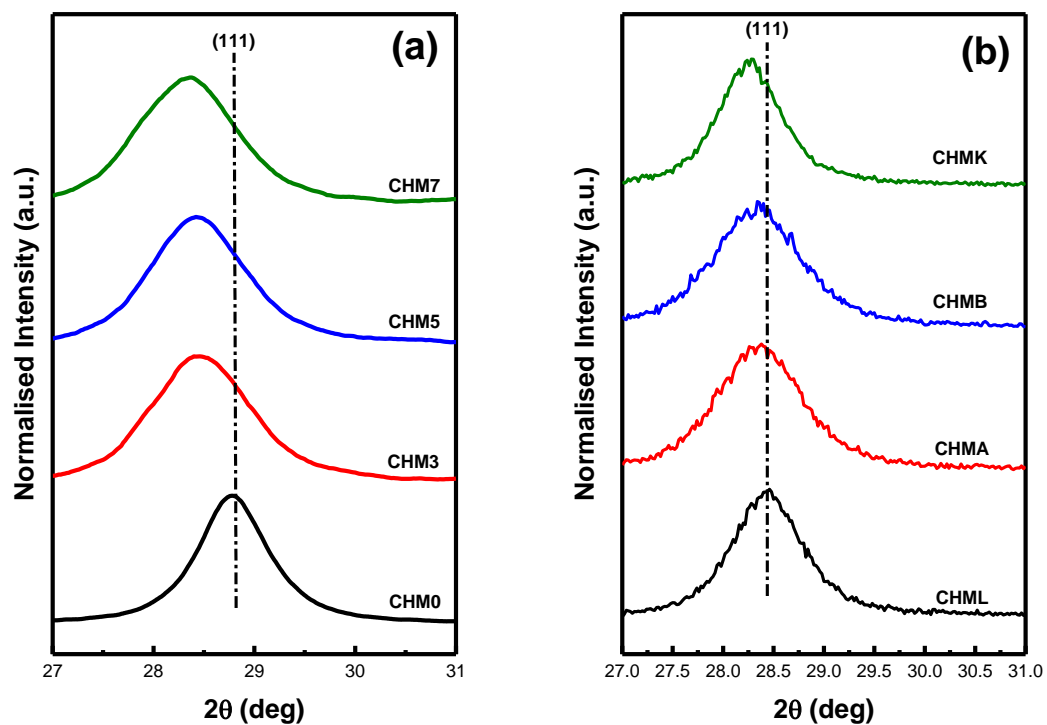


Figure S6.1: Specific XRD spectra of (a) CHM_x ternary and (b) CHMY quaternary ceria-based mixed oxides

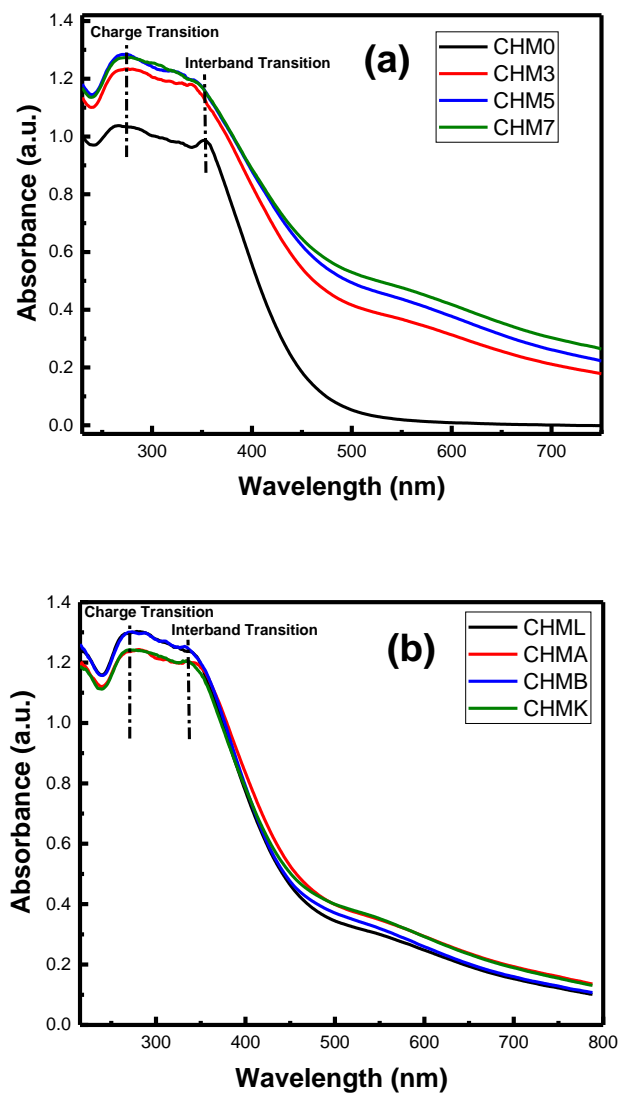


Figure S6.2: UV-Vis DRS of (a) CHM_x ternary and (b) CHMY quaternary ceria-based mixed oxides

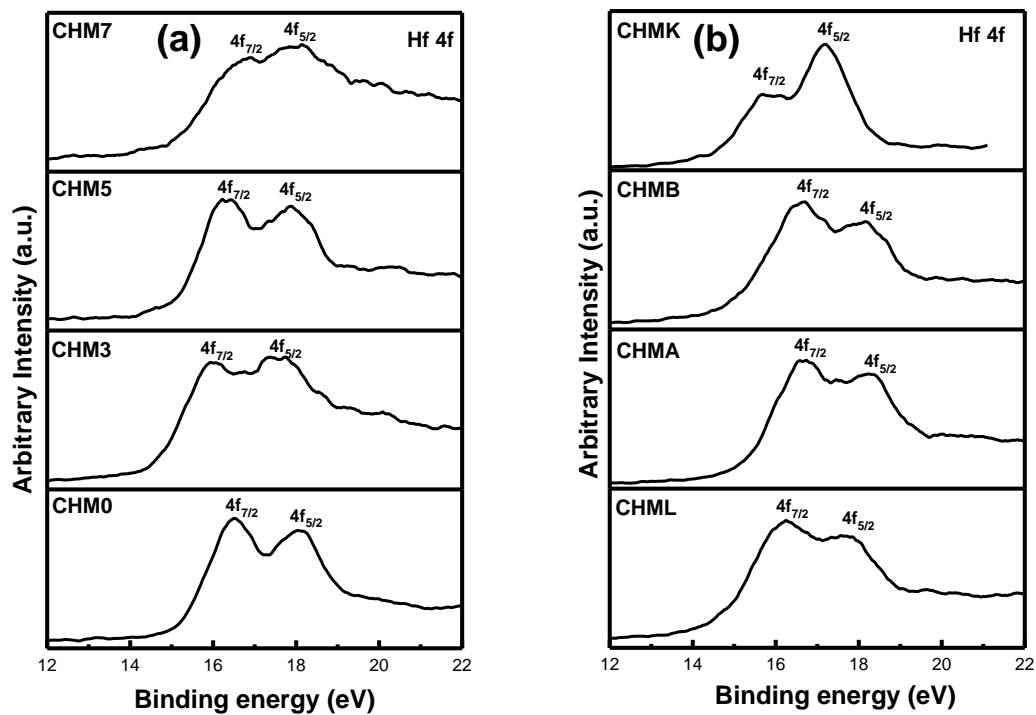


Figure S6.3: Hf 4f XPS of (a) CHM_x ternary and (b) CHMY quaternary ceria- based mixed oxides

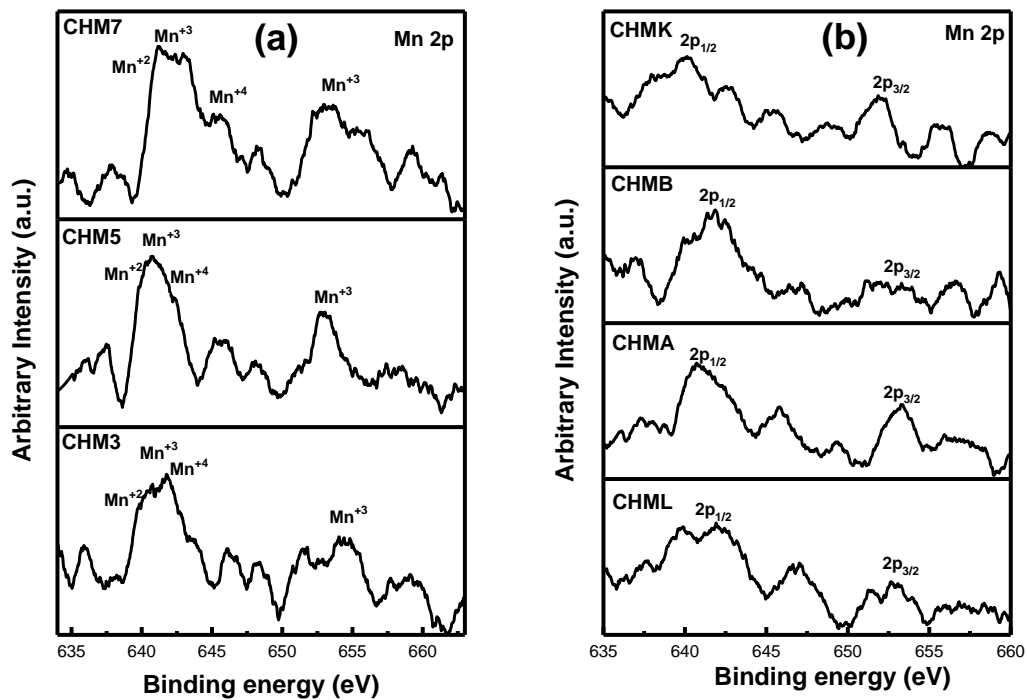


Figure S6.4: Mn 2p XPS of (a) CHM_x ternary and (b) CHMY quaternary ceria-based mixed oxides

REFERENCES

Agarwala, Avinash, K., Gupta, T., and Kothari, A. (2011). "Particulate emissions from biodiesel vs diesel fuelled compression ignition engine." *Renew. Sustain. Energy Rev.*, 15, 3278–3300.

Alinezhadchamazketi, A., Khodadadi, A. A., Mortazavi, Y., and Nemati, A. (2013). "Catalytic evaluation of promoted CeO₂-ZrO₂ by transition, alkali, and alkaline-earth metal oxides for diesel soot oxidation." 742(12).

An, H., and McGinn, P. J. (2006). "Catalytic behavior of potassium containing compounds for diesel soot combustion." *Appl. Catal. B Environ.*, 62(1–2), 46–56.

Anantharaman, A. P., Gadiyar, H. J., Surendran, M., Rao, A. S., Dasari, H. P., Dasari, H., and Babu, G. U. B. (2018a). "Effect of synthesis method on structural properties and soot oxidation activity of gadolinium-doped ceria." *Chem. Pap.*, (123456789).

Anantharaman, A. P., Geethu, J., P, M. R., and Prasad, H. (2018b). "Ceria-samarium binary metal oxides: A comparative approach towards structural properties and soot oxidation activity." *Mol. Catal.*, 451(September 2017), 247–254.

Andana, T., Piumetti, M., Bensaid, S., Russo, N., and Fino, D. (2016a). "Nanostructured ceria-praseodymia catalysts for diesel soot combustion." *Appl. Catal. B Environ.*, 197, 125–137.

Andana, T., Piumetti, M., Bensaid, S., Russo, N., Fino, D., and Pirone, R. (2016b). "CO and Soot Oxidation over Ce-Zr-Pr Oxide Catalysts." *Nanoscale Res. Lett.*

Aneggi, E., Leitenburg, C. de, Dolcetti, G., and Trovarelli, A. (2008). "Diesel soot combustion activity of ceria promoted with alkali metals." *Catal. Today*, 136(1–2), 3–10.

Aneggi, E., Leitenburg, C. De, Dolcetti, G., and Trovarelli, A. (2006). "Promotional effect of rare earths and transition metals in the combustion of diesel soot over CeO₂ and

CeO₂-ZrO₂." *Catal. Today*, 114, 40–47.

Aneggi, E., Leitenburg, C. De, Dolcetti, G., and Trovarelli, A. (2007). "Promotion effect of surface lanthanum in soot oxidation over ceria-based catalysts." *Top. Catal.*, 42–43(1–4), 319–322.

Aneggi, E., Leitenburg, C. de, Llorca, J., and Trovarelli, A. (2012). "Higher activity of Diesel soot oxidation over polycrystalline ceria and ceria-zirconia solid solutions from more reactive surface planes." *Catal. Today*, 197(1), 119–126.

Aneggi, E., Wiater, D., Leitenburg, C. de, Llorca, J., and Trovarelli, A. (2014). "Shape-Dependent Activaity of Ceria in Soot Combustion." *ACS Catal.*, 4(1), 172–181.

Anjaneya, K. C., and Singh, M. P. (2017). "Synthesis and properties of gadolinium doped ceria electrolyte for IT-SOFCs by EDTA-citrate complexing method." *J. Alloys Compd.*, 695(18), 871–876.

Ansari, A. A. (2010). "Optical and structural properties of sol-gel derived nanostructured CeO₂ film." *J. Semicond.*, 31(5), 0530011–0530015.

Ansari, S. A., Khan, M. M., Ansari, M. O., Kalathil, S., Lee, J., and Cho, M. H. (2014). "Band gap engineering of CeO₂ nanostructure using an electrochemically active biofilm for visible light applications." *RSC Adv.*, 4(32), 16782–16791.

Artini, C., Pani, M., Carnasciali, M. M., Plaisier, J. R., and Costa, G. A. (2016). "Lu-, Sm-, and Gd-Doped Ceria: A Comparative Approach to Their Structural Properties." *Inorg. Chem.*, 55(20), 10567–10579.

Atribak, I., Bueno-López, A., and García-García, A. (2008). "Thermally stable ceria-zirconia catalysts for soot oxidation by O₂." *Catal. Commun.*, 9(2), 250–255.

Atribak, I., Bueno-López, A., and García-García, A. (2009). "Role of yttrium loading in the physico-chemical properties and soot combustion activity of ceria and ceria-zirconia

catalysts.” *J. Mol. Catal. A Chem.*, 300(1–2), 103–110.

Atribak, I., Such-Basanez, I., Bueno-López, A., and García-García, A. (2007). “Comparison of the catalytic activity of MO_2 (M=Ti, Zr, Ce) for soot oxidation under NO_x/O_2 .” *J. Appl. Phys.*, 250, 75–84.

Ayastuy, J. L., Gurbani, A., González-Marcos, M. P., and Gutiérrez-Ortiz, M. A. (2010). “CO oxidation on $\text{Ce}_x\text{Zr}_{1-x}\text{O}_2$ -supported CuO catalysts: Correlation between activity and support composition.” *Appl. Catal. A Gen.*, 387(1–2), 119–128.

Ayastuy, J. L., Iglesias-González, A., and Gutiérrez-Ortiz, M. A. (2014). “Synthesis and characterization of low amount tin-doped ceria ($\text{Ce}_x\text{Sn}_{1-x}\text{O}_{2-\delta}$) for catalytic CO oxidation.” *Chem. Eng. J.*, 244, 372–381.

Babitha, K. K., Sreedevi, A., Priyanka, K. P., Sabu, B., and Varghese, T. (2015). “Structural characterization and optical studies of CeO_2 nanoparticles synthesized by chemical precipitation.” *Indian J. Pure Appl. Phys.*, 53(September), 596–603.

Bharali, P., Thrimurthulu, G., Katta, L., and Reddy, B. M. (2012). “Preparation of highly dispersed and thermally stable nanosized cerium–hafnium solid solutions over silica surface: Structural and catalytic evaluation.” *J. Ind. Eng. Chem.*, 18(3), 1128–1135.

Boaro, M., Leitenburg, C. De, Dolcetti, G., and Trovarelli, A. (2000). “The Dynamics of Oxygen Storage in Ceria – Zirconia Model Catalysts Measured by CO Oxidation under Stationary and Cycling Feedstream Compositions.” *J. Catal.*, 193, 338–347.

Bond, T. C., Doherty, S. J., Fahey, D. W., Forster, P. M., Berntsen, T., Deangelo, B. J., Flanner, M. G., Ghan, S., Kärcher, B., Koch, D., Kinne, S., Kondo, Y., Quinn, P. K., Sarofim, M. C., Schultz, M. G., Schulz, M., Venkataraman, C., Zhang, H., Zhang, S., Bellouin, N., Guttikunda, S. K., Hopke, P. K., Jacobson, M. Z., Kaiser, J. W., Klimont, Z., Lohmann, U., Schwarz, J. P., Shindell, D., Storelvmo, T., Warren, S. G., and Zender, C. S. (2013). “Bounding the role of black carbon in the climate system: A scientific

assessment.” *J. Geophys. Res. Atmos.*, 118(11), 5380–5552.

Brezesinski, T., Smarsly, B., Iimura, K. I., Grosso, D., Boissière, C., Amenitsch, H., Antonietti, M., and Sanchez, C. (2005). “Self-assembly and crystallization behavior of mesoporous, crystalline HfO₂ thin films: A model system for the generation of mesostructured transition-metal oxides.” *Small*, 1(8–9), 889–898.

Bueno-López, A., Krishna, K., Makkee, M., and Moulijn, J. A. (2005). “Active oxygen from CeO₂ and its role in catalysed soot oxidation.” *Catal. Letters*, 99(February), 203–205.

Calvache-Muñoz, J., Prado, F. A., and Rodríguez-Páez, J. E. (2017). “Cerium oxide nanoparticles: Synthesis, characterization and tentative mechanism of particle formation.” *Colloids Surfaces A Physicochem. Eng. Asp.*, 529(May), 146–159.

Capdevila-Cortada, M., Vile, G., Teschner, D., Perez-Ramirez, J., and Lopez, N. (2016). “Reactivity descriptors for ceria in catalysis.” *Appl. Catal. B Environ.*, 197, 299–312.

Castoldi, L., Aneggi, E., Matarrese, R., Bonzi, R., Llorca, J., Trovarelli, A., and Lietti, L. (2015). “Silver-based catalytic materials for the simultaneous removal of soot and NO_x.” *Catal. Today*, 258, 405–415.

Castoldi, L., Matarrese, R., Lietti, L., and Forzatti, P. (2009). “Intrinsic reactivity of alkaline and alkaline-earth metal oxide catalysts for oxidation of soot.” *Appl. Catal. B Environ.*, 90, 278–285.

Cauda, E., Fino, D., Saracco, G., and Specchia, V. (2004). “Nanosized Pt-perovskite catalyst for the regeneration of a wall-flow filter for soot removal from diesel exhaust gases.” *Top. Catal.*, 30/31(1–4), 299–303.

Chavan, S. V., and Tyagi, A. K. (2006). “Investigations on ceria-hafnia system for phase analysis, and HT-XRD studies on a few cubic compositions.” *Mater. Sci. Eng. A*, 433(1–2), 203–207.

Chellappan, L., and Sanjeeviraja, C. (2014). “Rapid synthesis of nanocrystalline SnO₂ by a microwave-assisted combustion method.” *J. Adv. Ceram.*, 3(3), 171–176.

Chen, W., Ghosh, D., and Chen, S. (2008). “Large-scale electrochemical synthesis of SnO₂ nanoparticles.” *J. Mater. Sci.*, 43, 5291–5299.

Christensen, J. M., Grunwaldt, J. D., and Jensen, A. D. (2016). “Importance of the oxygen bond strength for catalytic activity in soot oxidation.” *Appl. Catal. B Environ.*, 188, 235–244.

Chudobova, D., Nejdil, L., Gumulec, J., Krystofova, O., Rodrigo, M. A. M., Kynicky, J., Ruttkay-Nedecky, B., Kopel, P., Babula, P., Adam, V., and Kizek, R. (2013). “Complexes of silver(I) ions and silver phosphate nanoparticles with hyaluronic acid and/or chitosan as promising antimicrobial agents for vascular grafts.” *Int. J. Mol. Sci.*, 14(7), 13592–13614.

CPCB. (2011). *Air quality monitoring, emission inventory and source apportionment study for Indian cities.*

Dai, F., Meng, M., Zha, Y., Li, Z., Hu, T., Xie, Y., and Zhang, J. (2012). “Performance of Ce substituted hydroxalcalite-derived mixed oxide catalysts Co_{2.5}Mg_{0.5}Al_{1-x}Ce_xO used for soot combustion and simultaneous NO_x-soot removal.” *Fuel Process. Technol.*, 104, 43–49.

Damyanova, S., Pawelec, B., Arishtirova, K., Huerta, M. V. M., and Fierro, J. L. G. (2008). “Study of the surface and redox properties of ceria–zirconia oxides.” *Appl. Catal. A Gen.*, 337(1), 86–96.

Dernaika, B., and Uner, D. (2003). “A simplified approach to determine the activation energies of uncatalyzed and catalyzed combustion of soot.” *Appl. Catal. B Environ.*, 40(3), 219–229.

Devaiah, D., Tsuzuki, T., Boningari, T., Smirniotis, P. G., and Reddy, B. M. (2015).

“Ce_{0.80}M_{0.12}Sn_{0.08}O_{2-δ} (M= Hf, Zr, Pr, and La) ternary oxide solid solutions with superior properties for CO oxidation.” *RSC Adv.*, 5(38), 30275–30285.

Du, Y., Zhu, X., Wang, H., Wei, Y., and Li, K. (2015). “Synthesis gas generation by chemical-looping selective oxidation of methane using Pr_{1-x}Zr_xO_{2-δ} oxygen carriers.” *J. Energy Inst.*, (May), 1–10.

Dupin, J., Gonbeau, D., Vinatier, P., and Levasseur, A. (2000). “Systematic XPS Studies of Metal Oxides , Hydroxides and Peroxides Systematic XPS studies of metal oxides , hydroxides and peroxides.” *Phys. Chem. Chem. Phys.*, 2, 1319–1324.

Duprez, D., Descorme, C., Birchem, T., and Rohart, E. (2001). “Oxygen storage and mobility on model three-way catalysts.” *Top. Catal.*, 16(1–4), 49–56.

Durgasri, D. N., Vinodkumar, T., Sudarsanam, P., and Reddy, B. M. (2014). “Nanosized CeO₂-Gd₂O₃ mixed oxides: Study of structural characterization and catalytic CO oxidation activity.” *Catal. Letters*, 144(6), 971–979.

Fan, L., Xi, K., Zhou, Y., Zhu, Q., Chen, Y., and Lu, H. (2017). “Design structure for CePr mixed oxide catalysts in soot combustion.” *RSC Adv.*, 7(33), 20309–20319.

Fang, P., Luo, M.-F., Lu, J.-Q., Cen, S.-Q., Yan, X.-Y., and Wang, X.-X. (2008). “Studies on the oxidation properties of nanopowder CeO₂-based solid solution catalysts for model soot combustion.” *Thermochim. Acta*, 478(1–2), 45–50.

Filtschew, A., Hofmann, K., and Hess, C. (2016). “Ceria and Its Defect Structure: New Insights from a Combined Spectroscopic Approach.” *J. Phys. Chem. C*, 120(12), 6694–6703.

Fino, D., Bensaid, S., Piumetti, M., and Russo, N. (2016). “A review on the catalytic combustion of soot in Diesel particulate filters for automotive applications : From powder catalysts to structured reactors.” *Appl. Catal. A, Gen.*, 509, 75–96.

Fino, D., Russo, N., Cauda, E., Saracco, G., and Specchia, V. (2006). “La – Li – Cr perovskite catalysts for diesel particulate combustion.” 114, 31–39.

Fino, D., Russo, N., Saracco, G., and Specchia, V. (2008). “Removal of NO_x and diesel soot over catalytic traps based on spinel-type oxides.” *Powder Technol.*, 180, 74–78.

Fujimori, H., Yashima, M., Sasaki, S., Kakihana, M., Mori, T., Tanaka, M., and Yoshimura, M. (2001). “Internal distortion in ceria-doped hafnia solid solutions: High-resolution x-ray diffraction and Raman scattering.” *Phys. Rev. B*, 64(13), 134104.

Gao, Y., Duan, A., Liu, S., Wu, X., Liu, W., Li, M., Chen, S., Wang, X., and Weng, D. (2017). “Study of Ag/Ce_xNd_{1-x}O₂ nanocubes as soot oxidation catalysts for gasoline particulate filters: Balancing catalyst activity and stability by Nd doping.” *Appl. Catal. B Environ.*, 203, 116–126.

Gardini, D., Christensen, J. M., Damsgaard, C. D., Jensen, A. D., and Wagner, J. B. (2016). “Visualizing the mobility of silver during catalytic soot oxidation.” 183, 28–36.

Getsoian, A. B., Zhai, Z., and Bell, A. T. (2014). “Band-gap energy as a descriptor of catalytic activity for propene oxidation over mixed metal oxide catalysts.” *J. Am. Chem. Soc.*, 136, 13684–13697.

Ghiasi, M., and Malekzadeh, A. (2015). “Synthesis, characterization and photocatalytic properties of lanthanum oxy-carbonate, lanthanum oxide and lanthanum hydroxide nanoparticles.” *Superlattices Microstruct.*, 77, 295–304.

Grasselli, R. K. (2002). “Fundamental principles of selective heterogeneous oxidation catalysis.” *Top. Catal.*, 21(1–3), 79–88.

Grover, V., and Tyagi, A. K. (2004). “Phase relations, lattice thermal expansion in CeO₂–Gd₂O₃ system, and stabilization of cubic gadolinia.” *Mater. Res. Bull.*, 39(6), 859–866.

Gu, H., Ran, R., Zhou, W., and Shao, Z. (2007). “Anode-supported ScSZ-electrolyte

SOFC with whole cell materials from combined EDTA-citrate complexing synthesis process.” *J. Power Sources*, 172(2), 704–712.

Guillén-Hurtado, N., Bueno-López, A., and García-García, A. (2012). “Catalytic performances of ceria and ceria-zirconia materials for the combustion of diesel soot under NO_x/O₂ and O₂. Importance of the cerium precursor salt.” *Appl. Catal. A Gen.*, 437–438(2), 166–172.

Guillén-hurtado, N., García-garcía, A., and Bueno-lópez, A. (2015). “Active oxygen by Ce – Pr mixed oxide nanoparticles outperform diesel soot combustion Pt catalysts.” *Appl. Catal. B Environ.*, 174–175(2), 60–66.

Guo, M., Lu, J., Wu, Y., Wang, Y., and Luo, M. (2011). “UV and visible Raman studies of oxygen vacancies in rare-earth-doped ceria.” *Langmuir*, 27(7), 3872–7.

Ho, M.-Y., Gong, H., Wilk, G. D., Busch, B. W., Green, M. L., Voyles, P. M., Muller, D. A., Bude, M., Lin, W. H., See, A., Loomans, M. E., Lahiri, S. K., and Räisänen, P. I. (2003). “Morphology and crystallization kinetics in HfO₂ thin films grown by atomic layer deposition.” *J. Appl. Phys.*, 93(3), 1477–1481.

Huang, H., Liu, J., Sun, P., Ye, S., and Liu, B. (2017). “Effects of Mn-doped ceria oxygen-storage material on oxidation activity of diesel soot.” *RSC Adv.*, 7(12), 7406–7412.

Hwang, N., and Barron, An. R. (1987). *Connexions BET Surface Area Analysis of Nanoparticles*.

Imanaka, N., Masui, T., Egawa, T., and Imadzu, H. (2009). “Novel catalysts for low-temperature combustion of diesel particulate matter.” *J. Mater. Chem.*, 19(2), 208–210.

International Energy Agency. (2016). *Energy and Air Pollution. World Energy Outlook*.

International Energy Agency. (2018). *Global Energy & CO₂ Status Report*.

Izu, N., Itoh, T., Shin, W., Matsubara, I., and Murayama, N. (2007). “The effect of hafnia doping on the resistance of ceria for use in resistive oxygen sensors.” *Sensors Actuators B Chem.*, 123(1), 407–412.

Jakubek, T., Kaspera, W., Legutko, P., Stelmachowski, P., and Kotarba, A. (2015). “Surface versus bulk alkali promotion of cobalt-oxide catalyst in soot oxidation.” *Catal. Commun.*, 71, 37–41.

Jampaiah, D., Venkataswamy, P., Tur, K. M., Ippolito, S. J., Bhargava, S. K., and Reddy, B. M. (2015). “Effect of MnO_x Loading on Structural, Surface, and Catalytic Properties of $\text{CeO}_2\text{-MnO}_x$ Mixed Oxides Prepared by Sol-Gel Method.” *J. Inorg. Gen. Chem.*, 641(6), 1141–1149.

Jayaraman, V., Sagadevan, S., and Sudhakar, R. (2017). “Studies on Optical and Electrical Properties of Hafnium Oxide Nanoparticles.” *J. Electron. Mater.*, 1–6.

Jiaxiu, G., Zhonghua, S., Dongdong, W., Huaqiang, Y., and Maochu, G. (2013). “Study of Pt – Rh/ $\text{CeO}_2\text{-ZrO}_2\text{-M}_x\text{O}_y$ (M = Y, La)/ Al_2O_3 three-way catalysts.” *Appl. Surf. Sci.*, 273, 527–535.

Katta, L., Reddy, B. M., Muhler, M., and Grunert, W. (2012). “Interfacial interaction driven CO oxidation: nanostructured $\text{Ce}_{1-x}\text{La}_x\text{O}_{2-\delta}/\text{TiO}_2$ solid solutions.” *Catal. Sci. Technol.*, 2(4), 745–753.

Katta, L., Sudarsanam, P., Thrimurthulu, G., and Reddy, B. M. (2010). “Doped nanosized ceria solid solutions for low temperature soot oxidation: Zirconium versus lanthanum promoters.” *Appl. Catal. B Environ.*, 101, 101–108.

Keramidas, V. G., and White, W. B. (1974). “Raman scattering study of the crystallization and phase transformations of ZrO_2 .” *J. Am. Ceram. Soc.*, 57(1), 2–4.

Khan, S. A., Gambhir, S., and Ahmad, A. (2014). “Extracellular biosynthesis of gadolinium oxide (Gd_2O_3) nanoparticles, their biodistribution and bioconjugation with

the chemically modified anticancer drug taxol.” *Beilstein J. Nanotechnol.*, 5(1), 249–257.

Kim, K., Yoo, J. Do, Lee, S., Bae, M., Bae, J., Jung, W. C., and Han, J. W. (2017). “A Simple Descriptor to Rapidly Screen CO Oxidation Activity on Rare-Earth Metal-Doped CeO₂: From Experiment to First-Principles.” *ACS Appl. Mater. Interfaces*, 9(18), 15449–15458.

Krishna, K., Bueno-López, A., Makkee, M., and Moulijn, J. A. (2007). “Potential rare earth modified CeO₂ catalysts for soot oxidation I. Characterisation and catalytic activity with O₂.” *Appl. Catal. B Environ.*, 75(3–4), 189–200.

Kumar, A., Das, S., Munusamy, P., Self, W., Baer, D. R., Sayle, D. C., and Seal, S. (2014). “Behavior of nanoceria in biologically-relevant environments.” *Environ. Sci. Nano*, 1, 516–532.

Kumar, E., Selvarajan, P., and Muthuraj, D. (2013). “Synthesis and characterization of CeO₂ nanocrystals by solvothermal route.” *Mater. Res.*, 16(2), 269–276.

Kuntaiah, K., Sudarsanam, P., Reddy, B. M., and Vinu, A. (2013). “Nanocrystalline Ce_{1-x}Sm_xO_{2-δ} (x = 0.4) solid solutions: structural characterization versus CO oxidation.” *RSC Adv.*, 3(21), 7953.

Kurnatowska, M., Mista, W., Mazur, P., and Kepinski, L. (2014). “Nanocrystalline Ce_{1-x}Ru_xO₂– Microstructure, stability and activity in CO and soot oxidation.” *Appl. Catal. B Environ.*, 148–149, 123–135.

Leistner, K., Nicolle, A., and Costa, P. Da. (2012). “Impact of the Catalyst / Soot Ratio on Diesel Soot Oxidation Pathways.”

Leitenburg, C. de, Trovarelli, A., Zamar, F., Maschio, S., Dolcetti, G., and Llorca, J. (1995). “A Novel and Simple Route To Catalysts With a High Oxygen Storage Capacity: the Direct Room-Temperature Synthesis of CeO₂-ZrO₂ Solid-Solutions.” *J. Chem. Soc. Commun.*, 2(21), 2181–2182.

Li, D., Meng, F., Yan, X., Yang, L., Heng, H., and Zhu, Y. (2013). "One-pot hydrothermal synthesis of Mn_3O_4 nanorods grown on Ni foam for high performance supercapacitor applications." *Nanoscale Res. Lett.*, 8(1), 1–8.

Li, Q., Wang, X., Chen, H., Xin, Y., Tian, G., Lu, C., Zhang, Z., Zheng, L., and Zheng, L. (2016). "K-supported catalysts for diesel soot combustion : Making a balance between activity and stability." *Catal. Today*, 264, 171–179.

Liang, Q., Wu, A. X., Xiaodi, A., Ae, W., and Weng, D. (2007). "Role of surface area in oxygen storage capacity of ceria–zirconia as soot combustion catalyst." *Catal. Letters*, 119, 265–270.

Liang, Q., Wu, X., Weng, D., and Xu, H. (2008). "Oxygen activation on Cu/Mn–Ce mixed oxides and the role in diesel soot oxidation." *Catal. Today*, 139(1–2), 113–118.

Lin, F., Wu, X., and Weng, D. (2011). "Effect of barium loading on CuO_x – CeO_2 catalysts : NO_x storage capacity, NO oxidation ability and soot oxidation activity." *Catal. Today*, 175(1), 124–132.

Lin, X., Li, S., He, H., Wu, Z., Wu, J., Chen, L., Ye, D., and Fu, M. (2018). "Evolution of oxygen vacancies in MnO_x – CeO_2 mixed oxides for soot oxidation." *Appl. Catal. B Environ.*, 223, 91–102.

Liu, J., Zhao, Z., Chen, Y., Xu, C., Duan, A., and Jiang, G. (2011). "Different valent ions-doped cerium oxides and their catalytic performances for soot oxidation." *Catal. Today*, 175(1), 117–123.

Liu, S., Wu, X., Liu, W., Chen, W., Ran, R., Li, M., and Weng, D. (2016). "Soot oxidation over CeO_2 and Ag/CeO_2 : Factors determining the catalyst activity and stability during reaction." *J. Catal.*, 337, 188–198.

Liu, S., Wu, X., Tang, J., Cui, P., Jiang, X., Chang, C., Liu, W., Gao, Y., Li, M., and Weng, D. (2017). "An exploration of soot oxidation over CeO_2 – ZrO_2 nanocubes: Do

more surface oxygen vacancies benefit the reaction?" *Catal. Today*, 281, 454–459.

Luo, M.-F., Yan, Z.-L., Jin, L.-Y., and He, M. (2006). "Raman spectroscopic study on the structure in the surface and the bulk shell of $Ce_xPr_{1-x}O_{2-\delta}$ mixed oxides." *J. Phys. Chem. B*, 110(26), 13068–71.

Ma, D., Lu, Z., Tang, Y., Li, T., Tang, Z., and Yang, Z. (2014). "Effect of lattice strain on the oxygen vacancy formation and hydrogen adsorption at CeO_2 (111) surface." *Phys. Lett. A*, 378(34), 2570–2575.

Malecka, M. A., Kępiński, L., and Miśta, W. (2007). "Structure evolution of nanocrystalline CeO_2 and $CeLnO_x$ mixed oxides (Ln=Pr, Tb, Lu) in O_2 and H_2 atmosphere and their catalytic activity in soot combustion." *Appl. Catal. B Environ.*, 74(3–4), 290–298.

Marbán, G., López, I., and Valdés-Solís, T. (2009). "Preferential oxidation of CO by CuO_x/CeO_2 nanocatalysts prepared by SACOP. Mechanisms of deactivation under the reactant stream." *Appl. Catal. A Gen.*, 361(1–2), 160–169.

Mario Birkholz. (2006). *Principles of X-ray Diffraction. Thin Film Anal. by X-Ray Scatt.*

Matarrese, R., Aneggi, E., Castoldi, L., Llorca, J., Trovarelli, A., and Lietti, L. (2016). "Simultaneous removal of soot and NO_x over K- and Ba-doped ruthenium supported catalysts." *Catal. Today*, 267, 119–129.

Mesnard, D., Mikulova, J., Ā, S. R., Ge, F., Kappenstein, C., and Duprez, D. (2006). "Properties of cerium – zirconium mixed oxides partially substituted by neodymium: Comparison with Zr – Ce – Pr – O ternary oxides." 179, 2511–2520.

Mia, M. N. H., Pervez, M. F., Hossain, M. K., Reefaz Rahman, M., Uddin, M. J., Mashud, M. A. Al, Ghosh, H. K., and Hoq, M. (2017). "Influence of Mg content on tailoring optical bandgap of Mg-doped ZnO thin film prepared by sol-gel method." *Results Phys.*, 7, 2683–2691.

- Mikhlin, Y., Likhatski, M., Karacharov, A., Zaikovski, V., and Krylov, A. (2009). "Formation of gold and gold sulfide nanoparticles and mesoscale intermediate structures in the reactions of aqueous HAuCl_4 with sulfide and citrate ions." *Phys. Chem. Chem. Phys.*, 11(26), 5445–5454.
- Miró, E. E., Ravelli, F., Ulla, M. A., Cornaglia, L. M., and Querini, C. A. (1999). "Catalytic combustion of diesel soot on Co, K supported catalysts." 53, 631–638.
- Montanari, R. (2004). "High-temperature XRD investigations on phase transformations." *Metall. Ital.*, 96(2), 23–30.
- Mukherjee, D., Rao, B. G., and Reddy, B. M. (2016). "CO and soot oxidation activity of doped ceria: Influence of dopants." *Appl. Catal. B Environ.*, 197, 105–115.
- Mukherjee, D., Rao, B. G., and Reddy, B. M. (2017). "Characterization of Ceria-Based Nano-Oxide Catalysts by Raman Spectroscopy." *Top. Catal.*, 60(19–20), 1673–1681.
- Mul, G., Kapteijn, F., Doornkamp, C., and Moulijn, J. A. (1998). "Transition Metal Oxide Catalyzed Carbon Black Oxidation: A Study with $^{18}\text{O}_2$." *J. Catal.*, 179(1), 258–266.
- Nascimento, L. F., and Serra, O. A. (2016). "Washcoating of cordierite honeycomb with ceria-copper mixed oxides for catalytic diesel soot combustion." *Process Saf. Environ. Prot.*, 101, 134–143.
- Neeft, J. P. A., Makkee, M., and Moulijn, J. A. (1996). "Metal oxides as catalysts for the oxidation of soot." *Chem. Eng. J.*, 64(2), 295–302.
- Nesbitt, H. W., and Banerjee, D. (1998). "Interpretation of XPS Mn(2p) spectra of Mn oxyhydroxides and constraints on the mechanism of MnO_2 precipitation." *Am. Mineral.*, 83(3–4), 305–315.
- Nezhad, E. H., Ghorbani, M., Zeinalkhani, M., and Heidari, A. (2013). "A New

- Technique to Absorb Yellow GX Anionic Pigments.” *Am. J. Chem.*, 3(3), 6–9.
- Nicholas, J. D., and Jonghe, L. C. De. (2007). “Prediction and evaluation of sintering aids for Cerium Gadolinium Oxide.” *Solid State Ionics*, 178, 1187–1194.
- Padma Kumar, H., Vidya, S., Saravana Kumar, S., Vijayakumar, C., Solomon, S., and Thomas, J. K. (2015). “Optical properties of nanocrystalline HfO₂ synthesized by an auto-igniting combustion synthesis.” *J. Asian Ceram. Soc.*, 3(1), 64–69.
- Palmisano, P., Russo, N., Fino, P., Fino, D., and Badini, C. (2006). “High catalytic activity of SCS-synthesized ceria towards diesel soot combustion.” *Appl. Catal. B Environ.*, 69(1–2), 85–92.
- Pan, C., Zhang, D., Shi, L., and Fang, J. (2008). “CTAB assisted hydrothermal synthesis, controlled conversion, and CO oxidation properties of CeO₂ nanorods, nanotubes, nanowires, and nanocubes.” *Eur. J. Inorg. Chem.*, 181(15), 2429–2436.
- Patel, S., and Pant, K. K. (2007). “Hydrogen production by oxidative steam reforming of methanol using ceria promoted copper–alumina catalysts.” *Fuel Process. Technol.*, 88(8), 825–832.
- Patra, H., Rout, S. K., Pratihari, S. K., and Bhattacharya, S. (2011). “Effect of process parameters on combined EDTA-citrate synthesis of Ba_{0.5}Sr_{0.5}Co_{0.8}Fe_{0.2}O_{3-δ} perovskite.” *Powder Technol.*, 209(1–3), 98–104.
- Piumetti, M., Bensaid, S., Russo, N., and Fino, D. (2015). “Nanostructured ceria-based catalysts for soot combustion : Investigations on the surface sensitivity.” *Appl. Catal. B Environ.*, 165, 742–751.
- Piumetti, M., Bensaid, S., Russo, N., and Fino, D. (2016a). “Investigations into nanostructured ceria-zirconia catalysts for soot combustion.” *Appl. Catal. B Environ.*, 180, 271–282.

Piumetti, M., Linden, B. van der, Makkee, M., Miceli, P., Fino, D., Russo, N., and Bensaid, S. (2016b). "Contact dynamics for a solid-solid reaction mediated by gas-phase oxygen: Study on the soot oxidation over ceria-based catalysts." *Appl. Catal. B Environ.*, 199, 96–107.

Prasad, D. H., Park, S. Y., Oh, E. O., Ji, H., Kim, H. R., Yoon, K. J., Son, J. W., and Lee, J. H. (2012). "Synthesis of nano-crystalline $\text{La}_{1-x}\text{Sr}_x\text{CoO}_{3-\delta}$ perovskite oxides by EDTA–citrate complexing process and its catalytic activity for soot oxidation." *Appl. Catal. A Gen.*, 447–448, 100–106.

Prasad, D. H., Son, J. W., Kim, B. K., Lee, H. W., and Lee, J. H. (2008). "Synthesis of nano-crystalline $\text{Ce}_{0.9}\text{Gd}_{0.1}\text{O}_{1.95}$ electrolyte by novel sol-gel thermolysis process for IT-SOFCs." *J. Eur. Ceram. Soc.*, 28(16), 3107–3112.

Prasad, H., Ahn, K., Park, S., Ji, H., Joong, K., Kim, B., Je, H., Lee, H., and Lee, J. (2013). "Hydrogen production from water-splitting reaction based on RE-doped ceria-zirconia solid-solutions." 8, 3–9.

Preda, G., and Pacchioni, G. (2011). "Formation of oxygen active species in Ag-modified CeO_2 catalyst for soot oxidation : A DFT study." *Catal. Today*, 177(1), 31–38.

"Printex ® U Properties Unit." (2009). *Appl. Technol. centre,NJ*.

Puigdollers, A. R., Schlexer, P., Tosoni, S., and Pacchioni, G. (2017). "Increasing oxide reducibility: The role of metal/oxide interfaces in the formation of oxygen vacancies." *ACS Catal.*, 7(10), 6493–6513.

Raitano, J. M., Khalid, S., Marinkovic, N., and Chan, S. W. (2015). "Nano-crystals of cerium-hafnium binary oxide: Their size-dependent structure." *J. Alloys Compd.*, 644, 996–1002.

Ramadoss, A., Krishnamoorthy, K., and Kim, S. J. (2012a). "Facile synthesis of hafnium oxide nanoparticles via precipitation method." *Mater. Lett.*, 75, 215–217.

Ramadoss, A., Krishnamoorthy, K., and Kim, S. J. (2012b). "Novel synthesis of hafnium oxide nanoparticles by precipitation method and its characterization." *Mater. Res. Bull.*, 47(9), 2680–2684.

Ranga Rao, G., and Sahu, H. R. (2001). "XRD and UV-Vis diffuse reflectance analysis of CeO₂-ZrO₂ solid solutions synthesized by combustion method." *J. Chem. Sci.*, 113(5–6), 651–658.

Rangaswamy, A., Sudarsanam, P., and Reddy, B. M. (2015). "Rare earth metal doped CeO₂-based catalytic materials for diesel soot oxidation at lower temperatures." *J. Rare Earths*, 33(11), 1162–1169.

Rao, G. R., and Mishra, B. G. (2003). "Structural, redox and catalytic chemistry of ceria based materials." *Bull. Catal. Soc. India*, 2, 122–134.

Reddy, B. M., Bharali, P., Gode, T., Saikia, P., Lakshmi, K., and Park, S.-E. (2008a). "Catalytic Efficiency of Ceria–Zirconia and Ceria–Hafnia Nanocomposite Oxides for Soot Oxidation." *Catal. Letters*, 123, 327–333.

Reddy, B. M., Bharali, P., Saikia, P., Park, S.-E., Berg, M. W. E. van den, Muhler, M., and Grünert, W. (2008b). "Structural Characterization and Catalytic Activity of Nanosized Ce_xM_{1-x}O₂ (M = Zr and Hf) Mixed Oxides." *J. Phys. Chem. C*, 112(31), 11729–11737.

Reddy, B. M., Thrimurthulu, G., and Katta, L. (2011). "Design of Efficient Ce_xM_{1-x}O_{2-δ} (M = Zr, Hf, Tb and Pr) Nanosized Model Solid Solutions for CO Oxidation." *Catal. Letters*, 141, 572–581.

Reed, K., Cormack, A., Kulkarni, A., Mayton, M., Sayle, D., Klaessig, F., and Stadler, B. (2014). "Exploring the properties and applications of nanoceria: is there still plenty of room at the bottom?" *Environ. Sci. Nano*, 1(58), 390–405.

Ruiz, M. L., Lick, I. D., Leguizamón Aparicio, M. S., Ponzi, M. I., Rodríguez-Castellón,

E., and Ponzi, E. N. (2012). “NO influence on catalytic soot combustion: Lithium nitrate and gold catalysts.” *Ind. Eng. Chem. Res.*, 51(3), 1150–1157.

Rushton, M. J. D., Chroneos, A., Skinner, S. J., Kilner, J. A., and Grimes, R. W. (2013). “Effect of strain on the oxygen diffusion in yttria and gadolinia co-doped ceria.” *Solid State Ionics*, 230, 37–42.

Sarkar, A., Loho, C., Velasco, L., Thomas, T., Bhattacharya, S. S., Hahn, H., and Djenadic, R. R. (2017). “Multicomponent equiatomic rare earth oxides with narrow band gap and associated praseodymium multivalency.” *Dalt. Trans.*, 46, 12167–12176.

Sethi, V., and Patil, R. S. (2008). *Development of Air Pollution Source Profiles – Stationary Sources*.

Setten, B. A. A. L. Van, Makkee, M., Moulijn, J. A., Setten, B. A. A. L. Van, Makkee, M., and Science, J. A. M. (2001). “Science and technology of catalytic diesel particulate filters.” *Catal. Rev.*, 43(4), 489–564.

Shangguan, W. (1998). “Promotion effect of potassium on the catalytic property of CuFe₂O₄ for the simultaneous removal of NO_x and diesel soot particulate.” *Appl. Catal. B Environ.*, 16(2), 149–154.

Shangguan, W. F., Teraoka, Y., and Kagawa, S. (1997). “Kinetics of soot-O₂ soot-NO and soot-O₂ -NO reactions over spinel-type CuFe₂O₄ catalyst.” *Appl. Catal. B Environ.*, 12, 237–247.

Shannon, R. D. (1976). “Revised effective ionic radii and systematic studies of interatomic distances in halides and chalcogenides.” *Acta Crystallogr. Sect. A*, 32(5), 751–767.

Shantilal Gangrade, A., Aditya Varma, A., Kishor Gor, N., Shriniwasan, S., and Tatiparti, S. S. V. (2017). “The dehydrogenation mechanism during the incubation period in nanocrystalline MgH₂.” *Phys. Chem. Chem. Phys.*, 19(9), 6677–6687.

Sharma, S., Jain, S., Goel, A., Mahtta, R., Kumar, A., Datt, D., Kundu, S., Aggarwal, P., and Sharma, P. (2014). *Advancement of Fuel Quality and Vehicle Emissions Norms to Improve Urban Air Quality in India*.

Shen, Q., Wu, M., Wang, H., He, C., Hao, Z., Wei, W., and Sun, Y. (2015). “Facile synthesis of catalytically active CeO₂ for soot combustion.” *Catal. Sci. Technol.*, 5(3), 1941–1952.

Shimizu, K., Kawachi, H., and Satsuma, A. (2010). “Study of active sites and mechanism for soot oxidation by silver-loaded ceria catalyst.” *Applied Catal. B, Environ.*, 96(1–2), 169–175.

Smith, E., and Dent, G. (2005). *Modern Raman Spectroscopy - A Practical Approach*. John Wiley & Sons Ltd.

Sobukawa, H. (2002). “Development of Ceria-Zirconia Solid Solutions and Future Trends.” *R&D Rev. Toyota CRDL*, 37(4), 1–5.

Soler, L., Casanovas, A., Escudero, C., Perez-Dieste, V., Aneggi, E., Trovarelli, A., and Llorca, J. (2016). “Ambient Pressure Photoemission Spectroscopy Reveals the Mechanism of Carbon Soot Oxidation in Ceria-Based Catalysts.” *ChemCatChem*, 8(17), 2735.

Su, C., and McGinn, P. J. (2014). “Application of glass soot catalysts on metal supports to achieve low soot oxidation temperature.” *Catal. Commun.*, 43, 1–5.

Sudarsanam, P., Hillary, B., Mallesham, B., Rao, B. G., Amin, M. H., Nafady, A., Alsalmeh, A. M., Reddy, B. M., and Bhargava, S. K. (2016). “Designing CuO_x Nanoparticle-Decorated CeO₂ Nanocubes for Catalytic Soot Oxidation: Role of the Nanointerface in the Catalytic Performance of Heterostructured Nanomaterials.” *Langmuir*, 32(9), 2208–2215.

Sudarsanam, P., Kuntaiah, K., and Reddy, B. M. (2014). “Promising ceria–samaria-based

nano-oxides for low temperature soot oxidation: a combined study of structure–activity properties.” *New J. Chem.*, 38, 5991–6001.

Sun, C., Li, H., and Chen, L. (2012). “Nanostructured ceria-based materials: synthesis, properties, and applications.” *Energy Environ. Sci.*, 5, 8475.

Sun, C., Li, H., Zhang, H., Wang, Z., and Chen, L. (2005). “Controlled synthesis of CeO₂ nanorods by a solvothermal method.” *Nanotechnology*, 16, 1454–1463.

Sun, X. L., Tok, A. I. Y., Huebner, R., and Boey, F. Y. C. (2007). “Phase transformation of ultrafine rare earth oxide powders synthesized by radio frequency plasma spraying.” *J. Eur. Ceram. Soc.*, 27, 125–130.

Tang, Q., Du, J., Xie, B., Yang, Y., Yu, W., and Tao, C. (2018). “Rare earth metal modified three dimensionally ordered macroporous MnO_x-CeO₂ catalyst for diesel soot combustion.” *J. Rare Earths*, 36(1), 64–71.

Tauc, J., Grigorovici, R., and Vancu, A. (1966). “Optical Properties and Electronic Structure of Amorphous Germanium.” *Phys. Status Solidi*, 15(2), 627–637.

Thrimurthulu, G., Komateedi, Rao, N., Devaiah, D., and Benjaram, Reddy, M. (2012). “Nanocrystalline ceria–praseodymia and ceria–zirconia solid solutions for soot oxidation.” *Res Chem Intermed*, 38, 1847–1855.

Tighe, C. J., Twigg, M. V, Hayhurst, A. N., and Dennis, J. S. (2016). “The kinetics of oxidation of Diesel soots and a carbon black (Printex U) by O₂ with reference to changes in both size and internal structure of the spherules during burnout.” *Carbon N. Y.*, 107, 20–35.

Trovarelli, A. (1996). “Catalytic Properties of Ceria and CeO₂ -Containing Materials.” *Catal. Rev.*, 38(4), 439–520.

Trovarelli, A. (1999). “Structural and oxygen storage/release properties of CeO₂-based

solid solutions.” *Comments Inorg. Chem.*, 20(4–6), 263–284.

Trovarelli, A., Leitenburg, C. De, Boaro, M., and Dolcetti, G. (1999). “The utilization of ceria in industrial catalysis.” *Catal. Today*, 50, 353–367.

Turishchev, S. Y., and Kashkarov, V. M. (2008). “XPS AND XANES studies of SnO.” 49(100), 80–91.

Vegard, L. (1921). “Die Konstitution der Mischkristalle und die Raumffüllung der Atome.” *Zeitschrift für Phys.*, 5(1), 17–26.

Venkataswamy, P., Jampaiah, D., Mukherjee, D., Aniz, C. U., and Reddy, B. M. (2016). “Mn-doped ceria solid solutions for CO oxidation at lower temperatures.” *Catal. Letters*, 1.

Vidal, H., Kašpar, J., Pijolat, M., Colon, G., Bernal, S., Cordon, A., and Perrichon, V. (2000). “Redox behavior of CeO₂–ZrO₂ mixed oxides II. Influence of redox treatments on high surface area catalysts.” *Appl. Catal. B Environ.*, 27, 49–63.

Vinodkumar, T., Durgasr Naga, D., and Reddy, B. M. (2013). “Design of transition and rare earth metal doped ceria nanocomposite oxides for CO oxidation.” *Int. J. Adv. Eng. Sci.*, 5(4), 224–231.

Vinodkumar, T., Mukherjee, D., Ch, S., and Reddy, B. M. (2018). “Investigation on the Physicochemical Properties of Ce_{0.8}Eu_{0.1}M_{0.1}O_{2-δ} (M= Zr, Hf, La, and Sm) Solid Solutions towards Soot Combustion.” *New J. Chem.*, 1–9.

Voutou, B., and Stefanaki, E.-C. (2008). *Electron Microscopy: The Basics. Phys. Adv. Mater. Winter Sch.*

Wagner, C. D., Riggs, W. M., Davis, L. E., and Moulder, J. F. (1978). *Handook of X-ray Photoelectron Spectroscopy.*

Wasalathanthri, N. D., SantaMaria, T. M., Kriz, D. A., Dissanayake, S. L., Kuo, C. H.,

Biswas, S., and Suib, S. L. (2017). “Mesoporous manganese oxides for NO₂ assisted catalytic soot oxidation.” *Appl. Catal. B Environ.*, 201(2), 543–551.

Weber, W. H., Hass, K. C., and McBride, J. R. (1993). “Raman study of CeO₂: Second-order scattering, lattice dynamics, and particle-size effects.” *Phys. Rev. B*, 48(1), 178–185.

Weckhuysen, B. M. (2004). “Ultraviolet-Visible Spectroscopy.” *In-situ Spectrosc. Catal.*, 255–270.

Wei, Y., Zhao, Z., Liu, J., Xu, C., Jiang, G., and Duan, A. (2013). “Design and synthesis of 3D ordered macroporous CeO₂-supported Pt/CeO_(2-δ) core-shell nanoparticle materials for enhanced catalytic activity of soot oxidation.” *Small*, 9(23), 3957–63.

Weng, D., Li, J., Wu, X., and Lin, F. (2008). “Promotional effect of potassium on soot oxidation activity and SO₂-poisoning resistance of Cu/CeO₂ catalyst.” *Catal. Commun.*, 9(9), 1898–1901.

WHO. (2018). *WHO ambient (outdoor) air quality database Summary results, update 2018*.

Wu, W. C., Huang, J. T., and Chiba, A. (2010a). “Synthesis and properties of samaria-doped ceria electrolyte for IT-SOFCs by EDTA-citrate complexing method.” *J. Power Sources*, 195(18), 5868–5874.

Wu, X., Liu, S., Lin, F., and Weng, D. (2010b). “Nitrate storage behavior of Ba/MnO_x-CeO₂ catalyst and its activity for soot oxidation with heat transfer limitations.” *J. Hazard. Mater.*, 181(1–3), 722–728.

Wu, X., Liu, S., Weng, D., Lin, F., and Ran, R. (2011). “MnO_x-CeO₂-Al₂O₃ mixed oxides for soot oxidation: Activity and thermal stability.” *J. Hazard. Mater.*, 187, 283–290.

Xiao, H. Y., and Weber, W. J. (2011). “Oxygen vacancy formation and migration in $\text{Ce}_x\text{Th}_{1-x}\text{O}_2$ solid solution.” *J. Phys. Chem. B*, 115(20), 6524–6533.

XiaodongWu, Lin, F., Wang, L., Weng, D., and Zhou, Z. (2011). “Preparation methods and thermal stability of Ba-Mn-Ce oxide catalyst for NO_x -assisted soot oxidation.” *J. Environ. Sci.*, 23(7), 1205–1210.

Yamazaki, K., Kayama, T., Dong, F., and Shinjoh, H. (2011). “A mechanistic study on soot oxidation over CeO_2 -Ag catalyst with ‘rice-ball’ morphology.” *J. Catal.*, 282(2), 289–298.

Yu, X., Li, J., Wei, Y., Zhao, Z., Liu, J., Jin, B., and Duan, A. (2014). “Three-Dimensionally Ordered Macroporous $\text{Mn}_x\text{Ce}_{1-x}\text{O}_8$ and $\text{Pt/Mn}_{0.5}\text{Ce}_{0.5}\text{O}_8$ Catalysts : Synthesis and Catalytic Performance for Soot Oxidation.” *Ind. Eng. Chem. Res.*, (53), 9653–9664.

Zaera, F., and Ma, Z. (2006). “Characterization of Heterogeneous Catalysts.” *Surf. Nanomolecular Catal.*, 1–38.

Zhan, S., Zhu, D., Qiu, M., Yu, H., and Li, Y. (2015). “Highly efficient removal of NO with ordered mesoporous manganese oxide at low temperature.” *RSC Adv.*, 5(37), 29353–29361.

Zhang, W., Niu, X., Chen, L., Yuan, F., and Zhu, Y. (2016). “Soot combustion over nanostructured ceria with different morphologies.” *Sci. Rep.*, 6, 1–10.

Zhao, H., Zhou, X., Wang, M., Xie, Z., Chen, H., and Shi, J. (2017). “Highly active MnO_x - CeO_2 catalyst for diesel soot combustion.” *RSC Adv.*, 7(6), 3233–3239.

Zhou, G., and Gorte, R. J. (2008). “Thermodynamic investigation of the redox properties for ceria-hafnia, ceria-terbia, and ceria-praseodymia solid solutions.” *J. Phys. Chem. B*, 112(32), 9869–9875.

Zhu, B., Tahara, Y., Yasunaga, K., Matsui, T., Hori, F., and Iwase, A. (2010). “Study on analysis of crystal structure in CeO₂ doped with Er₂O₃ or Gd₂O₃.” *J. Rare Earths*, 28(SUPPL. 1), 164–167.

Zhu, L., Yu, J., and Wang, X. (2007). “Oxidation treatment of diesel soot particulate on Ce_xZr_{1-x}O₂.” *J. Hazard. Mater.*, 140(1–2), 205–10.

PUBLICATIONS

International Peer Reviewed Journals (From Thesis)

Accepted

1. **Anjana P A**, Hari Prasad Dasari, Jong Ho Lee, Harshini Dasari, G Uday Bhaskar Babu, Soot Oxidation Activity of Redox and Non-Redox metal oxides synthesised by EDTA-Citrate method, 2017, *Catalysis letters*, 147 (12) 3004-3016 (IF 2.8)
2. **Anjana P A**, Hari Prasad Dasari, Harshini Dasari, G Uday Bhaskar Babu, Surface Morphology and Phase Stability effect of Ceria-Hafnia (CH_x) Binary Metal Oxides on Soot Oxidation Activity, 2018, *Applied Catalysis A: General* 566, 181-189 (IF 4.5)

Submitted

3. **Anjana P A**, Hari Prasad Dasari, Harshini Dasari, G Uday Bhaskar Babu, Study on Effect of Ionic Radius on Soot Oxidation Activity for Binary Metal Oxides, 2018, *Asia Pacific Journal of Chemical Engineering* (Minor Revision) (IF 1.2)
4. **Anjana P A**, Hari Prasad Dasari, Jong Ho Lee, Harshini Dasari, Effect of Multi Doping on Ce-Hf Oxides for Soot Oxidation Activity, 2018, *Applied Catalysis A: General* (Submitted) (IF 4.5)

Other Publications

5. **Anjana P A**, Geethu J, Mohammed Rishab P, Hari Prasad Dasari, Jong Ho Lee, Harshini Dasari, G Uday Bhaskar Babu, Ceria-Samarium Binary Metal Oxides: A Comparative Approach Towards Structural Properties and Soot Oxidation Activity, 2018, *Journal of Molecular Catalysis*, 451, 247-254 (IF 3.9)

6. **Anjana P A**, Hemanth J. Gadiyar, Mythili Surendran, A. Sumadhura Rao, Hari Prasad Dasari, Harshini Dasari, G Uday Bhaskar Babu, Effect of Synthesis Method on Structural Properties and Soot Oxidation Activity of Gadolinium-Doped Ceria, 2018, *Chemical Papers* <https://doi.org/10.1007/s11696-018-0532-5> (IF 1.2)
7. Zenab A, Mythili S, **Anjana P A**, Jidev P K, Harshini Dasari, Sudhakar Naidu N, Anandan S, Udhay Bhat K, Uday Bhaskar Babu G, Hari Prasad Dasari, Solubility limits of Ceria-Zirconia-Lanthanum Solid-Solutions, 2017, *Materials Today: Proceedings*, 4, 9360-9364
8. **Anjana P A**, S. Niju, K.M. Meera Sheriffa Begum, N. Anantharaman, Utilization of Limestone Derived Calcium Oxide for Biodiesel Production From Non-Edible Pongamia Oil, 2016, *Environmental Progress and Sustainable Energy*, 35 (6), 1758-1764 (IF = 1.6)
9. Anjana P A, S. Niju, K.M. Meera Sheriffa Begum, N. Anantharaman, R. Anand, D. Babu Studies on biodiesel production from Pongamia oil using heterogeneous catalyst and its effect on diesel engine performance and emission characteristics, 2016, *Biofuels*, 7 (4), 377-387

Patent

1. D. Hari Prasad, M P V Akhil, **Anjana P A**, “Solid Oxide Fuel Cell Anode Material As Soot Oxidation Catalyst” (C.000548). (Patent No: 201841028640)

BIODATA

Name : **Ms. Anjana P A**

PERSONAL DETAILS

Date of Birth 02/07/1991

Address Anjanam, Gokula Street, Keralapuram, Koduvayur. P.O,
Palakkad, Kerala
Pin-678501

Mobile +91-8754306539

Email id anjana.pa00@gmail.com

EDUCATION

2015 – Till Date **Ph.D. in Chemical Engineering**
National Institute of Technology Karnataka, Surathkal
Department of Chemical Engineering
Research topic: Catalysis, Nanomaterials, Energy and Environment
(CGPA 8.0)

2015-2013 **M-Tech in Energy Engineering**
National Institute of Technology Trichy
Department of Chemical Engineering
Research topic: Catalysis, Biodiesel, Energy and Environment
(CGPA 8.9)

2009-2013 **B-Tech in Chemical Engineering**
Government Engineering College, Kozhikode (Calicut University)
Department of Chemical Engineering
(CGPA 8.1)

CURRENT POSITION

Position **Assistant Professor**

Organization **SRM Institute of Science and Technology, Chennai**

Official email id **anjana.a@ktr.srmuniv.ac.in**

PUBLICATION DETAILS

International Journals	06 (Accepted) 01 (Minor Revision) 01 (Submitted)
International Conference	03
Conference Proceedings	01
Patent	01(Filed)